UC San Diego

UC San Diego Electronic Theses and Dissertations

Title

Fish-inspired adhesion with application to robotic manipulation and locomotion

Permalink

https://escholarship.org/uc/item/5jr6p69s

Author

Sandoval, Jessica Alexandra

Publication Date

2021

Peer reviewed|Thesis/dissertation

UNIVERSITY OF CALIFORNIA SAN DIEGO

Fish-inspired adhesion with application to robotic manipulation and locomotion

A dissertation submitted in partial satisfaction of the
requirements for the degree
Doctor of Philosophy

in

Materials Science and Engineering

by

Jessica A. Sandoval

Committee in charge:

    Professor Michael T. Tolley, Chair
    Professor Shengqiang Cai
    Professor Marc A. Meyers
    Professor Jennifer Taylor
    Professor Qiang Zhu

2021

The dissertation of Jessica A. Sandoval is approved, and it is

acceptable in quality and form for publication on microfilm

and electronically.

University of California San Diego

2021

DEDICATION

I dedicate this dissertation to my family. To my mom, dad, sisters, nieces, and

nephew, for their continued love and support throughout the course of my

academic career.

EPIGRAPH

It is a wholesome and necessary thing

for us to turn again to the earth

and in the contemplation of her beauties

to know the sense of wonder and humility.

—Rachel Louise Carson

TABLE OF CONTENTS

LIST OF FIGURES

LIST OF TABLES

ACKNOWLEDGEMENTS

I would like to acknowledge Professor Michael T. Tolley for his continued support, both as chair of my committee and as a mentor to my research. His guidance, positive demeanor, and encouragement to explore new research topics were essential to my development as a researcher.

I would like to extend my deepest gratitude to my committee–Professor Shengqiang Cai, Professor Marc Meyers, Professor Jennifer Taylor, and Professor Qiang Zhu–for their valuable feedback and support over the years.

I would like to thank Dr. Dimitri D. Deheyn at the Scripps Institution of Oceanography for his continued support and enthusiasm over the course of my PhD. It is through his lab that I was able to explore exciting topics in marine biology in pursuit of new engineering designs.

I would like to thank the wonderful individuals of the Bioinspired Robotics and Design Lab for the many happy memories both in and out of lab. Their friendship has made my experience as a PhD student researcher rich with laughter.

I would like to thank Dr. Dominique Rissolo for his enthusiasm to test out new prototypes in the field. I would like to thank Mr. Phil Zerofski from the Scripps Institution of Oceanography for his work in collecting live biological specimen. I would like to thank Dr. Shanglei Liu and Dr. Santiago Horgan from the UC San Diego Center for the Future of Surgery for their support in the trials of prototypes for surgical manipulation.

I would like to thank the many incredible undergraduate student researchers (Thomas Xu, Jade Sommers, Sarah Bartels) with whom I have worked over the course of my PhD.

I would like to thank my shipmates and friends aboard the E/V Nautilus, with special thanks to Mark DeRoche, Josh Chernov, and Allison Fundis, for the support and ocean-related adventures over the years.

Most importantly, I would like to thank my family for their continued love and support. I would like to extend special appreciation to my mother for always encouraging me to ask questions and for fostering my curiosity. It was from our walks through the forest and meanderings through

VITA

2015	B. S. in Biological Engineering, Massachusetts Institute of Technology
2018	M. S. in Mechanical Engineering, University of California San Diego
2021	Ph. D. in Materials Science and Engineering, University of California San Diego

PUBLICATIONS

J. A. Sandoval, T. Xu, M. T. Tolley, "Influence of stiffness on fluid channeling textures and their ability to grip soft, wet objects for application to surgical manipulators", in preparation for submission.

J. A. Sandoval, H. Quan, M. T. Tolley, M. A. Meyers, D. D. Deheyn. "Contribution of microstructures to underwater adhesion of the northern clingfish", in preparation for submission.

J. A. Sandoval, T. Xu, I. Adibnazari, D. D. Deheyn, M. T. Tolley. "Combining suction and friction to stabilize a soft gripper to shear and normal forces, for manipulation of soft objects in wet environments", submitted for publication.

J. A. Sandoval[*], M. Ishida[*], S. Jadhav, S. Huen, and M. T. Tolley. "Tuning the morphology of suction discs to enable directional adhesion for locomotion in wet environments", submitted for publication.

J. A. Sandoval, J. Sommers, K.R. Peddireddy, R. M. Robertson-Anderson, M. T. Tolley, and D. D. Deheyn, "Toward bioinspired wet adhesives: Lessons from assessing surface structures of the suction disc of intertidal clingfish", *ACS Applied Materials and Interfaces*, 12, 45460-45475, 2020.

J. A. Sandoval, S. Jadhav, H. Quan, D. D. Deheyn, and M. T. Tolley, "Reversible adhesion to rough surfaces both in and out of water, inspired by the clingfish suction disc", *Bioinspiration and Biomimetics*, 14, 066016, 2019.

[*] denotes equal contribution.

ABSTRACT OF THE DISSERTATION

Fish-inspired adhesion with application to robotic manipulation and locomotion

by

Jessica A. Sandoval

Doctor of Philosophy in Materials Science and Engineering

University of California San Diego, 2021

Professor Michael T. Tolley, Chair

Advances in reversible adhesives have proven critical in accomplishing novel robotic locomotion and manipulation tasks. However, reversible adhesives using previously reported methods have limited performance dependent on the surface type (i.e., surface roughness) to which they are being applied, and the surrounding environment (i.e., underwater). Bioinspiration, in which concepts from nature inspire synthetic designs, has furthered the development of provocative reversible adhesives. For this dissertation, I explored the topic of fish-inspired reversible adhesives to advance robotic manipulation and locomotion capabilities in wet and submerged environments. Specifically, I focused on the clingfish, an intertidal fish that attaches to rocky surfaces using a suction disc while sustaining high pull-off forces. This impressive ability

makes the clingfish an ideal model organism for the development of bioinspired adhesives. I performed investigations into the micro- and macro-scale components of the biological suction disc that are responsible for attachment. I analyzed the contribution of mesoscale surface structures using a custom algorithm to automate their detection and characterization. I applied the conclusions regarding the roles of each biological component to develop bioinspired suction discs that were capable of attaching to widely variable substrates while sustaining high pull-off forces. To minimize the need for active control of adhesion, I investigated the design parameters necessary for the suction discs to directionally adhere. By tuning their material and geometric characteristics, I developed discs that demonstrated morphological computation to achieve anisotropic adhesion in a wet environment. The morphologically programmed discs were applied to underwater locomoting robots, while minimizing the complexity of control. I lastly applied my conclusions regarding the impact of mesoscale surface structures of the clingfish to develop biomimetic textures to resist shear disturbances. I investigated the dependency of design parameters, such as stiffness, of the textures on the surface properties of the objects to be manipulated. The biomimetic textures were applied to the challenge of manipulating wet, delicate surfaces, with an explicit application to surgical manipulation. I lastly coupled the benefits of surface texturing and suction to develop a robotic manipulator to achieve a stable grasp of wet and lubricated objects against axial and shear disturbances. Overall, the exploration of fish-inspired adhesives presented in this dissertation yielded novel robotic capabilities when applied to the areas of manipulation and locomotion.

Chapter 1

Introduction

The development of reversible adhesives–i.e., adhesives that demonstrate the ability to attach to and detach from a surface without structural alteration-–is critical to enabling robots with novel capabilities [1]. Reversible adhesion encompasses the use of suction, magnetism, electrostatic attraction, and van der Waals forces, for example, and has been applied to a wide range of robotic applications, from surgical operations to manipulation of large objects in microgravity. Adhesion, however, is limited by the environment in which it is to be applied; adhesives that excel in dry environments, for example, are severely limited in performance in wet environments [2]. The environment type will also considerably impact the design of the adhesive. In terrestrial applications of adhesion, one of the predominant forces to counteract is gravity, which is of a predictable magnitude and direction. However, in an underwater domain, the variety of forces imparted by the environment, such as buoyancy and current, affects the dynamics of adhesion and thus the type of attachment strategy that would be successful. The type of substrate also greatly influences the mechanism of adhesion that is successful at attaching to the surface. For instance, attachment using magnetism only functions on ferrous surfaces, which limits the scope of use of this mechanism. Other forms of adhesion, such as suction, are generally limited to smooth surfaces as rough asperities can compromise attachment. The specificity of adhesion based on the

substrate and environment is therefore an important challenge to address when developing and applying adhesives.

Engineers have turned to nature to inspire the next generation of innovative reversible adhesives [3]. Through a process of bioinspiration, the development of adhesives takes design concepts and inspiration from all facets of life, from geckos to beetles to fish, to engineer novel attachment abilities [4]. This large repository of biological attachment processes encompasses both dry and wet adhesion, in air and underwater. One of the most well-studied forms of bioinspired reversible adhesives comes from studies of the toe pads of geckos. Geckos utilize dense arrays of setae, which are high aspect ratio microstructures terminating in highly branched spatulae, to achieve adhesion using van der Waals forces and contact splitting [5, 6]. It is important to note that a wide range of other organisms, including spiders [7], also use setae to achieve dry adhesion. The past two decades of research on biological dry adhesives has yielded considerable insights into the fabrication of high aspect ratio microstructures to take advantage of adhesion based on van der Waals forces [8]. Gecko-inspired adhesives have enabled gripping of irregular, challenging, or delicate objects, such as silicon wafers, with low contact stress and a high degree of repeatability. The impact of bioinspired dry adhesives on robotics has amounted to the accomplishment of novel tasks, from manipulating large space debris [9] to scaling glass walls [10].

Bioinspired reversible adhesives for use in a wet domain are comparatively less well studied. Wet adhesion, which encompasses attachment strategies that are mediated by viscous fluid, have been studied in tree frogs, newts, and insects [11, 12]. These organisms secrete a viscous fluid to form capillary bridges between the foot and/or toe pads and the surface, resulting in high normal adhesion [13]. Suction is also a useful tool, especially in aquatic settings, to attach onto surfaces [14]. The suckers of the octopus and the suction discs of fish have all drawn considerable interest in recent years from materials scientists and engineers. The octopus, for instance, has inspired the development of artificial suckers [15] which have been applied to soft

2

robotic arms for advanced underwater gripping applications [16].

Fish display an impressive variety of attachment devices to reversibly attach to underwater surfaces, which has begun to inspire novel adhesives. Fish have evolved innovative ways to thrive in environments with high-velocity, directional flow, such as in rivers, or in chaotic environments, such as in the intertidal, by use of suction discs. Suction discs are formed by modified fins, either pelvic and pectoral or dorsal, to ultimately attach onto surfaces using suction. Studies of the energetic cost and oxygen consumption of fish in high flow environments demonstrate that attachment using suction discs is energetically favorable and thus preferential for living in such challenging conditions [17]. The adaptations of the suction discs vary in design. For instance, the remora, a fish renowned for its hitchhiking abilities to whales, sharks, and dolphins, utilizes a dorsal suction disc to remain attached during the high-speed swimming of its host. The suction disc of the remora features arrays of hard protrusions called spinules to mechanically interlock with surface asperities to anchor its grip in high velocity, directional flows [18]. The remora has inspired the development of robotic suction discs, which use mechanically interlocking structures reminiscent of spinules and a fleshy sealing layer around the suction disc, to help underwater robots hitchhike by attaching to surfaces [19]. Other fish with innovative suction discs include the river loach [20] and gobies [21], which use a combination of suction, microstructures, and mechanical interlocking to secure themselves while accomplishing impressive feats, such as swimming upstream in rivers or climbing waterfalls.

For my dissertation, I sought to clarify as to how to reversibly adhere to challenging (i.e., rough, concave, or soft) surfaces while subjected to loads from highly variable directions. I focused my work on the clingfish, which demonstrates the impressive ability to grip onto rough surfaces in the intertidal while being subjected to highly variable fluid forces. The clingfish became instrumental in the development of reversible adhesives that extended into the fields of soft robotic manipulation and locomotion. The main questions that I addressed were 1) how to adhere to rough and irregular surfaces underwater? 2) How to stabilize adhesion to shear

3

dislodgement forces? And, 3) how to leverage these advances in reversible adhesion in soft robotics?
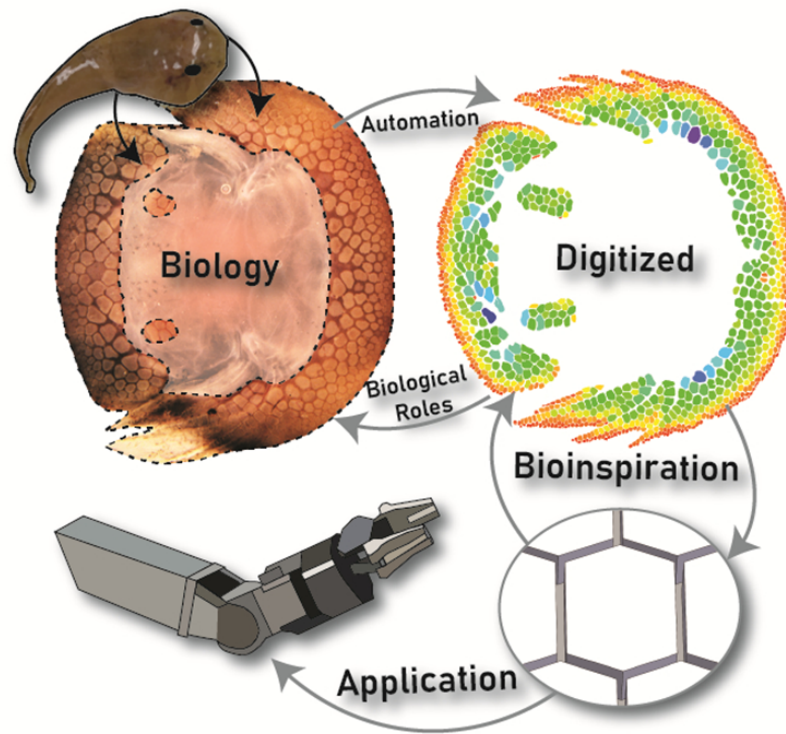
Figure 1.1: **Overview of fish-inspired adheison,** extending from biological models to bioin-spired designs and applications.

1.1 Overview

The components of this dissertation can be classified by their contributions to achieving stable attachment against either axial or shear loads. Thematically, I investigated the design and implementation of biomimetic suction discs (Chapters 2-4) and biomimetic surface textures (Chapters 5-6) for axial and shear loads. Suction discs provide strong adhesion given a disturbance perpendicular to a surface, yet do not demonstrate resistance to shear disturbances. On the other hand, the use of textures allows for resistance to shear loads, which act in parallel to a surface, but necessitate active engagement with an object to achieve a stable grasp. I review these two

topics in the following chapters and culminate the dissertation in the synthesis of the two modes of attachment to generate a stable, adhesive robotic gripper (Chapter 7).

In Chapter 2, we explore the biological structures responsible for successful attachment of the clingfish to rocky surfaces. We survey the structures using microscopy and force measurements taken at the microscale. Finally, we generalize these results in preparation for the following chapters regarding the design of biomimetic discs and textures.

In Chapter 3, we utilize the conclusions from the biological investigations to create a biomimetic suction disc that can be used to resist axial loads. The goal of this work was to design a device to reversibly adhere to rough objects of variable surface topologies in an underwater environment. In this chapter, we explore the use of soft elastomers and microstructures to seal the suction disc to surface asperities. We evaluate the impact of the geometric configuration of the disc in attaching to irregular topologies. We then demonstrate the use of the biomimetic disc in underwater gripping applications.

In Chapter 4, we explore the concept of morphologically programming the suction discs to display anisotropic adhesion in a wet environment. We tuned the structural parameters of the suction disc (i.e. material stiffness, geometry, symmetry) to successfully produce a directionally adhesive suction disc. The work was applied as a proof-of-concept to an array of linear actuators to demonstrate the utility for walking robots. We anticipate that the morphologically programmed suction discs will act to reduce the complexity of control for underwater walking robots.

In Chapter 5, we performed a biological investigation into the influence on adhesion of a predominant surface structure, referred to as papilla, which is found along the perimeter of the suction disc of the clingfish. The papillae influence the ability of the clingfish to resist shear and axial loads via viscosity-mediated adhesion. We created a custom image-processing software to quantify the geometric characteristics of the papillae across five sizes of clingfish. Using the results, we generated an "averaged" papilla, based on a survey of over 5,000 papillae, which served as the design for a biomimetic surface texture to be applied in engineering applications.

The geometric characteristics of the papillae of the clingfish demonstrated striking similarities to the toe pads of tree frogs, which also use a similar form of fluid-mediated, wet adhesion to attach to surfaces. These similarities potentially suggest a convergent evolution of wet adhesive structures.

In Chapter 6, we apply the "averaged" papilla to generate a biomimetic texture capable of withstanding shear loads in a wet environment. The overall goal of this work was to use shear textures to minimize loss of grip and damage of wet surfaces by robotic grippers, with specific application to surgical manipulation. When attempting to grip a soft surface that is lubricated in a fluid (i.e. secretions), the loss of friction between a grasper and the object leads to increased risk of over-compression of the surface and thus damage. We therefore evaluated the influence of design parameters (i.e. stiffness, channel spacing) of the textures on the successful attachment of the grasper to soft surfaces with a range of stiffnesses of three orders of magnitude. We modeled the effect of compression of these surface textures on the potential to cause tissue trauma. The frictional textures were applied to commercially available surgical graspers to achieve a stable grip while preventing tissue trauma and were demonstrated on *ex vivo* tissue. The textures were also applied to a soft robotic gripper to manipulate hydrogels.

In Chapter 7, we couple the benefits of the frictional textures and biomimetic discs to achieve a stable grasp of wetted, soft surfaces. The disc provided high axial adhesion while the frictional textures stabilized the manipulator to shear disturbances. We then applied the dual-adhesive gripper to a robotic arm for manipulation of wetted soft surfaces.

Overall, this dissertation embodies the essence of biomimetics, in which I worked between the fields of biology and engineering to address key challenges and limitations in currently existing adhesives. I began by studying central concepts and design components from an intertidal adhesive fish. I then approximated their contributions in synthetic analogs that I then applied to overarching engineering challenges, such as the lack of a gentle grip by robotic manipulators. In this process of developing biomimetic adhesives, I also addressed underlying biological hypotheses. This

6

cyclical nature of bioinspired design helped to uncover a plethora of innovative adhesive designs that impacted a range of fields spanning from underwater archaeology to surgical manipulation.

Chapter 2

Contribution of microstructures to underwater adhesion of the northern clingfish

Jessica A. Sandoval[1], Haocheng Quan[1], Michael T. Tolley[1], Marc A. Meyers [1], Dimitri D. Deheyn[2]

[1]Department of Mechanical and Aerospace Engineering, University of California San Diego, 9500 Gilman Dr., La Jolla, CA 92093

[2]Marine Biology Research Division, Scripps Institution of Oceanography, 9500 Gilman Dr., La Jolla, CA 92093

2.1   Abstract

The suction disc of the northern clingfish provides strong reversible adhesion to underwater surfaces while subject to turbulent wave action. The suction disc utilizes a dense array of fibrillar microstructures referred to as microfibrils that have been hypothesized to play a role in adhesion,

yet the extent of their role has yet to be quantified. Here, we analyzed the possible functions of microfibrils found across the suction disc, investigating whether their mechanical properties could ultimately contribute to the successful grip of underwater surfaces. Using a variety of imaging techniques, we surveyed the morphological characteristics of the microfibrils. We found that the microfibrils were expressed through a dense array of interconnected microchannels occurring throughout the cross-section of each papilla and were terminated at the surface by bifurcated heads and surrounded by secretions. Using Atomic Force Microscopy, we found that the microfibrils were about 3.4 times more adhesive than the associated secretions. From microindentation tests performed on AFM, we calculated the effective elastic modulus of the microfibrils to be between 1 and 2 MPa, which was used to ascertain their contribution to the adhesion of the overall suction disc. We then used image processing techniques to understand the extent of these microfibrils across the entirety of the disc margin, and therefore quantify their contribution to adhesion. Overall, this study brings together the adhesive and structural characteristics of microfibrils employed by the suction disc of the clingfish to yield conclusions regarding their respective utility in underwater adhesion.

2.2   Introduction

An underwater environment poses a unique set of challenges to adhesion in comparison to terrestrial environments. These challenges are ubiquitous between biological organisms and engineered adhesives. Underwater, forces from fluid flow, including turbulence and currents of varying direction and magnitude, influence adhesion, while in air, gravity poses the predominant constraint to adhesion [2]. Nature has evolved many impressive adhesive capabilities to temporarily attach to variable surfaces while subjected to disruptive forces. Explorations into the breadth of attachment adaptations used by organisms have yielded bioinspired principles to be utilized in the design of engineered adhesives to provide unprecedented attachment capabilities [4, 22, 1].

The different adhesion processes can be classified as either non-reversible or reversible [23, 24]. Non-reversible adhesion can be generally classified by the formation a permanent bond to a surface, such as the cementations used in barnacle adhesion or byssal threads for mussel attachment [25]. Reversible adhesion involves the ability to temporarily attach and detach in a switchable manner, without alteration of the surface to which adhesion occurs [23, 24, 26]. Reversibility is desirable in engineered adhesives with specific emphasis on robotic manipulation [27] and locomotion [10, 28]. Reversible attachment mechanisms employed by organisms are hierarchical in complexity and involve attachment strategies spanning across macro- and microscopic scales [29]. In addition to varying across the scales of size, the method of attachment also varies between wet and dry adhesion, and are often non-transferrable across environment type [2]. For instance, in air, adhesion via van der Waals forces are commonly used by terrestrial organisms ranging from arthropods – such as spiders [30], to reptiles – such as geckos [31, 5], to adhere onto dry surfaces.

Fibrillar or "hairy" microstructures [32], often referred to as setae, have been extensively described for terrestrial organisms, which use either dry or wet adhesion (via secretion to the substrate) to attach onto surfaces. Setae in terrestrial organisms are generally of a high aspect ratio (∼10) and are terminated in a variety of morphologies [33] that can include a single terminal element, as seen with insects [34], highly branched, as demonstrated in geckos [6], and flattened triangular shapes, as shown in spiders [30]. The terminations of the setae correspond to the type of adhesion for which they are used. Terrestrial organisms that exploit dry adhesion, such as geckos [5] and spiders [30], exhibit setae that are terminated in highly branched or flattened spatulae. For geckos, the use of highly branched spatulae results in a more intimate contact of the adhesive structure with a surface [35, 36]. Conversely, other terrestrial organisms combine microstructures and wet adhesion to attach onto surfaces. Flies [34] and beetles [37, 38, 39] are just two examples of organisms that use a combination of setae and secretions to attach onto surfaces using capillarity. Wet adhesion generally does not necessitate the use of fine

branching terminations since the fluid secreted by the organism is used to fill in surface asperities during attachment [34, 40]. Terminations have also been modified, for instance, to encompass an amphibious domain. As an example, diving beetles exhibit setae with microscopic suckers, allowing for adhesion in aquatic as well as terrestrial environments [41].

The microstructures of the aforementioned terrestrial organisms have become sources of bioinspiration for materials scientists and engineers for the fabrication of reversible adhesives [22]. Perhaps one of the most notable examples of artificial microstructured adhesives is the gecko-inspired adhesive, which exploits van der Waals adhesion and friction to attach onto objects. Such microscopic adhesives have been modified per their termination morphologies (i.e. hierarchies), body geometries (i.e. mushroom-shaped), and material composition (i.e., hydrogel-based) to improve adhesive performance [36, 42, 43]. Gecko-inspired adhesives have demonstrated their utility in the field of robotics [10, 28], and have been applied across a range of robotic tasks, from scaling glass walls [44] to grabbing objects in space [9]. The mushroom-shaped dry adhesives have been modified to terminate in a microscopic suction cup, similar to adaptations seen in nature, yielding adhesion in both wet and dry environments [45]. Advances in the understanding of microstructures of terrestrial organisms have resulted in the successful development of a diverse suite of microstructured adhesives which have started to transform engineering, with a specific emphasis in robotics.

However, the role of microstructures to adhesion is poorly understood for aquatic organisms. Fibrillar microstructures have been observed in the adhesive structures of the abalone, octopus, and clingfish, and yet little is understood of their mechanical properties and role in adhesion. In the abalone, the pedal foot is lined with branched microfibrils that are roughly 2 μm in diameter [46, 47]. The microfibrils of the abalone have been studied for their role in adhesion via van der Waals forces, in conjunction with suction and capillarity [46]. The octopus exhibits apically branched microfibrils within the acetabular protuberance of its sucker [48, 49]. The microfibrils have been proposed to increase the frictional footprint of the sucker. The use of

fibrillar microstructures in adhesion for these aquatic organisms is, in comparison to terrestrial organisms, considerably less studied and understood. Robust investigations of these fibrillar microstructures of aquatic organisms would therefore be pertinent to the development of novel underwater bioinspired adhesives.

The clingfish is one candidate for such study. The clingfish lives in intertidal environments and adheres to rough, irregular, and biofouled surfaces while being subjected to wave action and tidal surges [50, 51]. The ability of the clingfish to reversibly grip rough surfaces while subjected to powerful intertidal forces prompted our investigations into the components that are key to its successful grip.

The clingfish adheres to surfaces using a highly optimized suction disc, which is formed by the intersection of the modified pelvic and pectoral fins [50]. The suction disc functions by establishing a chamber of low pressure that is capable of sealing to surface irregularities, thereby sustaining pull-off loads that are up to 200 times the body weight of the clingfish [52, 53]. The disc margin, or the perimeter of the suction disc, is critical to the success of the grip of the clingfish. The disc margin is lined by rows of hexagonal pads, or marginal papillae, from which extend high aspect ratio, "hairy" microstructures consisting of extracellular cuticle [50, 52, 53]. We refer to the extracellular cuticle expressed by the papillae as microfibrils. Little is yet known of the mechanical properties of these microstructures.

To effectively develop bioinspired underwater adhesives, we must understand the adhesive role of the microfibrils found in underwater organisms. The goal of this work is to quantify the adhesive characteristics of the microfibrils found along the suction disc of the clingfish. We evaluated the contact density of the microfibrils based on Scanning Electron Microscopy and surveyed the transverse axis of a papilla using Transmission Electron Microscopy. We interrogated the microstructures using Atomic Force Microscopy to quantify the adhesive force of a single microfibril and determine its effective elastic modulus. By understanding the mechanical properties of the microfibrils of the clingfish, we aim to increase opportunities to better develop
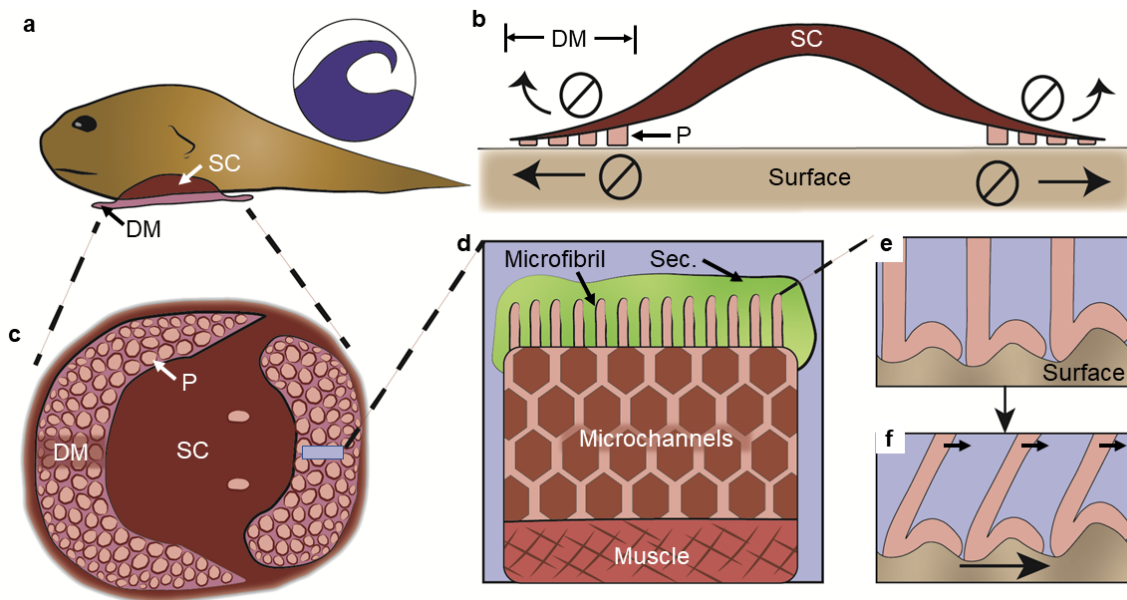
Figure 2.1: **Overview of the location and role of microfibrils in the adhesion of clingfish.**
a) A clingfish resides in high energy, intertidal environments. The clingfish uses a suction disc, composed of a suction chamber (*SC*) and disc margin (*DM*) to attach to surfaces. **b)** Overview of the contribution of microfibrils to adhesion. Microfibrils extend from papillae (*P*) located along the disc margin and are both soft and adhesive. The microfibrils prevent (1) the suction disc from slipping parallel along a surface and (2) the disc margin from flipping away from the surface. Both roles maintain the integrity of the seal of the suction chamber. **c)** Ventral view of the suction disc. **d)** Transverse view of a single papilla. Subsurface microchannels extend throughout the papilla. High aspect ratio microfibrils extend from the microchannels at the surface of the papilla. Secretions surround the papilla. The base of the papilla is composed of muscle tissue. **e)** Microfibrils conform to surface asperities. **f)** Deformation of the microfibrils when subjected to external forces.

microstructured adhesives for use in underwater environments.

2.3 Results

2.3.1 Papillae act as a network of fibrils

We investigated the internal and external structure of the papillae for their role as scaffolds for microfibrils. For such structural analysis, we performed Scanning Electron Microscopy (SEM) and Transmission Electron Microscopy (TEM).
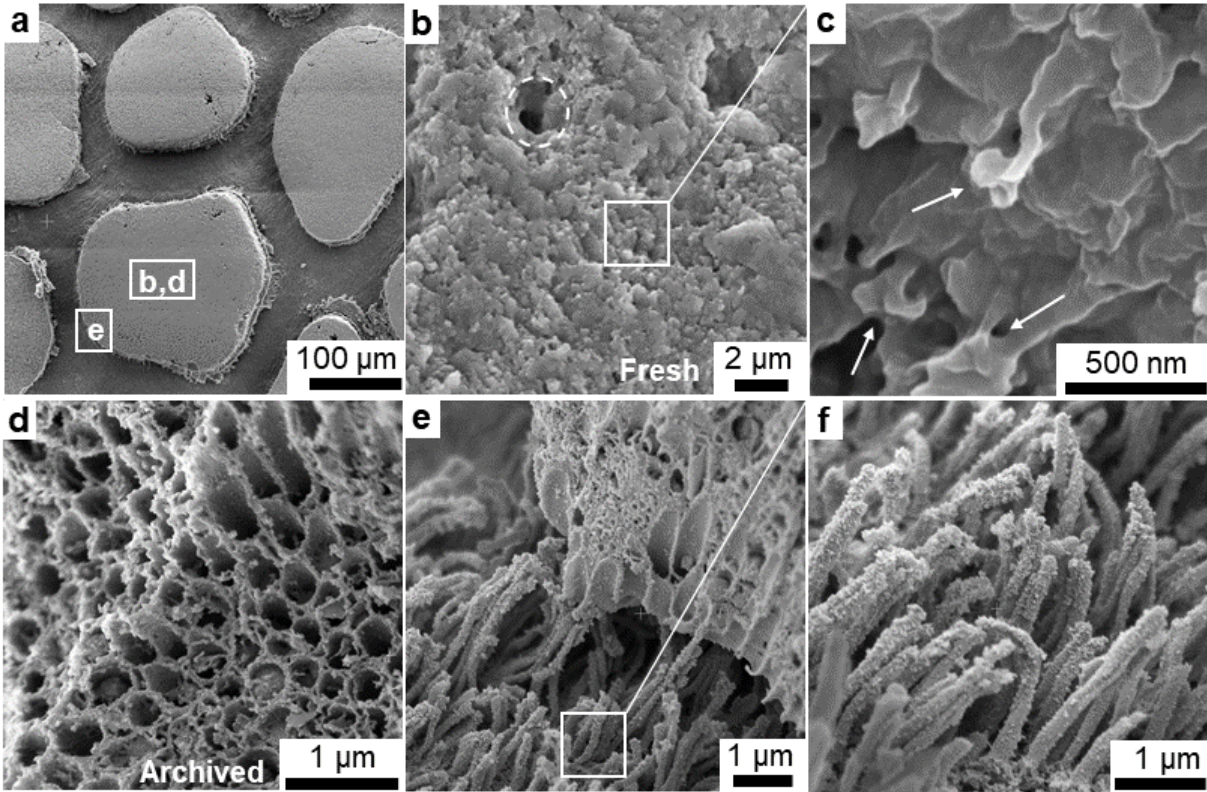
Figure 2.2: **Scanning Electron Microscopy (SEM) to image microscale features on the surface of papillae. a)** Papillae interdigitated across surface of the disc margin. Markers (b, d, e) provide a spatial reference to where the micrographs in subfigures (b, d, e) were sampled. **b)** Ventral view of the surface of a papilla, from a fresh tissue sample. Residual secretions were still present. Clumping of microfibrils (dashed, circle) observed sporadically across the papilla. **c)** Microfibrils observed with bifurcated heads (arrows) on the surface of papillae of the fresh tissue sample. **d)** Ventral view of the surface of a papilla of an archived clingfish specimen. Microchannels evidenced on surface. **e)** Fractured edge of a papilla from the archived specimen. Microfibrils observed to route through tubular microchannels. **f)** View of microfibrils on fractured edge.

SEM of both fresh and preserved samples revealed a highly complex structure on the surface of each papilla. Prior to imaging the fresh tissue sample, we eluted the secretions from the surface of the papillae by a series of ethanol washes. From the micrographs, we observed a dense array of microfibrils. These microfibrils were found to extend from the surface of the papillae through a series of microchannels (Fig. 2.2).

The terminations of the microfibrils differed between the specimen types. Samples from fresh specimen maintained the surface features terminating from the papillae. The microfibrils

of the fresh papillae were terminated by bifurcated heads (Fig. 2.2 b, c), although their extent was obscured by residual secretions. The microfibrils of the fresh specimen exhibited moderate, sporadic clumping, providing for the formation of gaps observed amongst the microfibrils (dotted line, Fig. 2.2 b).

The preserved specimen exhibited significantly less secretions covering the papillae, but also a lower abundance of intact microfibrils. We attributed the lack of intact microfibrils to the long-term preservation of the sample in isopropanol, which likely dehydrated the delicate microstructures, resulting in their degradation over time. However, the lack of microfibrils and secretions exposed an extensive network of microchannels that were expressed at the surface of each papilla (Fig. 2.2 d-f). These microchannels extended across the entirety of the ventral face of the papillae. We measured the microchannels to have an average diameter of 0.24 ± 0.05 μm ($n = 69$) and to be spaced 0.02 ± 0.009 μm ($n = 62$) apart. We measured the density of microchannels, which corresponded to the density of microfibrils. Via manual quantification of the SEM micrographs, we calculated that the microchannels, and thus microfibrils, were expressed at a density of 7.02 ± 0.82 microfibrils per μm^2. We observed that the microfibrils were orthogonally projected from the face of the papillae.

The microchannels acted as guides for softer fibrillar projections, as seen on a fractured edge (Fig. 2.2 e, f). These microfibrils were observed to project through the tubular microchannels (Fig. 2.2 e) to be expressed on the surface of the papilla. The microfibrils of the fractured edge lacked highly branched terminations yet were observed to have a consistent orientation in the SEM micrographs (Fig. 2.2 f). We considered the lack of terminations to be due to the fracture that led to the exposure of the internal microfibrils within the papilla.

Transmission Electron Microscopy of the papilla of a fresh tissue sample further supported the observation that throughout a papilla extends a network of microchannels to express the microfibrils at its surface (Fig. 2.3). Below the surface of a papilla, we observed a network of microchannels (Fig. 2.3 b) that extended for approximately 1.6 mm. These subsurface microchan-

15
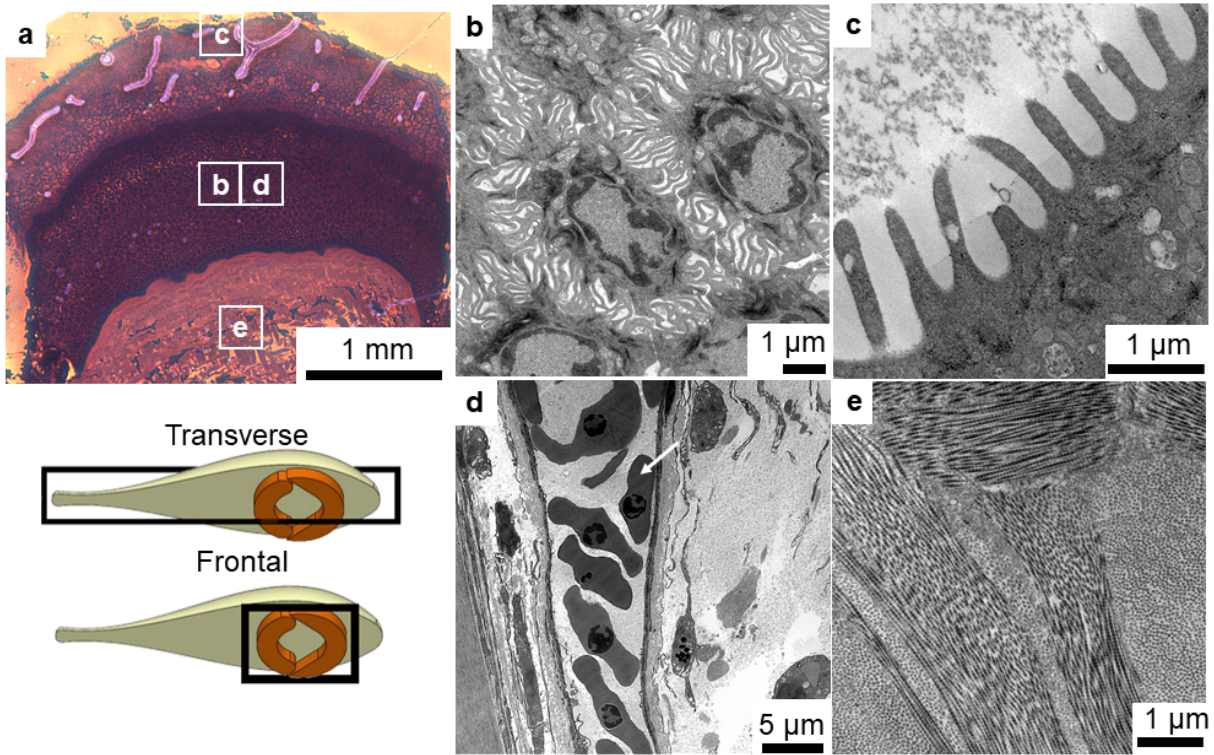
Figure 2.3: **Transmission Electron Microscopy (TEM) to visualize internal structures of papilla, from tissue of freshly euthanized specimen. a**) Semithin of a single papilla used for TEM, imaged under brightfield microscopy. Markers (b-e) provide reference of where spatially the micrographs in subfigures (b-e) were sampled. **b**) Hexagonal intersections of microchannels that extend for 1.6 mm from the surface of the papilla, observed from the transverse plane. **c** Microchannels shown to terminate at the surface of a papilla, observed from the transverse plane. **d**) Elongated cell bodies with nuclei, hypothesized to be the cell-bodies of nascent fibrils observed from the frontal plane. **e**) Arrangement of bundles of muscle fibers at the base of the papilla, observed from the transverse plane.

nels were measured to have a diameter of 1.4 ± 0.2 μm ($n = 7$). The subsurface microchannels interconnected with neighboring channels, forming hexagonal intersections that were approximately 4.5 μm in height and 2.5 μm in width, and of the internal angles of approximately 119° $\pm$ 9° ($n = 14$). These hexagonal intersections were ubiquitous across the network of subsurface microchannels.

The subsurface microchannels narrowed to terminate at the surface in a diameter of 0.4 ± 0.08 μm ($n = 8$; Fig. 2.3 c). The diameters of the surface microchannels measured from TEM were consistent with measurements of microchannels performed in SEM (Fig. 2.2 d).

16

We hypothesized that the subsurface microchannels transported bulk, nascent microfibrils to the surface (Fig. 2.3 d). From the TEM micrographs at the base of the papilla, we observed that the muscle fibers were routed in many non-uniform orientations (Fig. 2.3 e). Based on the less consistent orientations of muscle fibers, we suggest that the papillae may possess a dynamic response to stimuli from random, non-uniform orientations, which would be imperative in withstanding randomized environmental disturbances.

Overall, the observations made using TEM supported the hypothesis that the papillae act as a scaffold for microfibrils that protrude at the surface of the papillae.

2.3.2   Adhesive force of the microfibrils

To determine the adhesive properties of the microfibrils and secretions, we interrogated the surface of the papillae from a fresh clingfish specimen using Atomic Force Microscopy (AFM) (Fig. 2.4 a, b). The tissue was unaltered prior to experimentation, thereby preserving the integrity of the microstructures of the papillae. Secretions remained present on the tissue to prevent damage to underlying microstructures. To determine the adhesive properties of the secretions, we gently aspirated using a Pasteur pipette the secretion material from an untested region of the anterior disc margin and plated it on a glass slide. All tissue samples and isolated secretions remained hydrated in a droplet of filtered seawater for the entirety of the experimental procedure. We used filtered sea water to replicate the concentration of ions in solution, mitigating deleterious steric effects on the microstructures and their interaction with the environment. We therefore simulated environmental parameters during the interrogation with AFM to yield a more realistic understanding of the role in adhesion of microfibrils found in the marine environment. We interrogated the microfibrils, which we previously measured to have an average diameter of 240 nm, with an AFM tip of a nominal radius of 20 nm (Fig. 2.4 a). We therefore concluded that the AFM probe tip was sufficiently small enough to interrogate one fibril per test of adhesion.

We used AFM to test the adhesive force of the microfibrils and secretions of a freshly

17
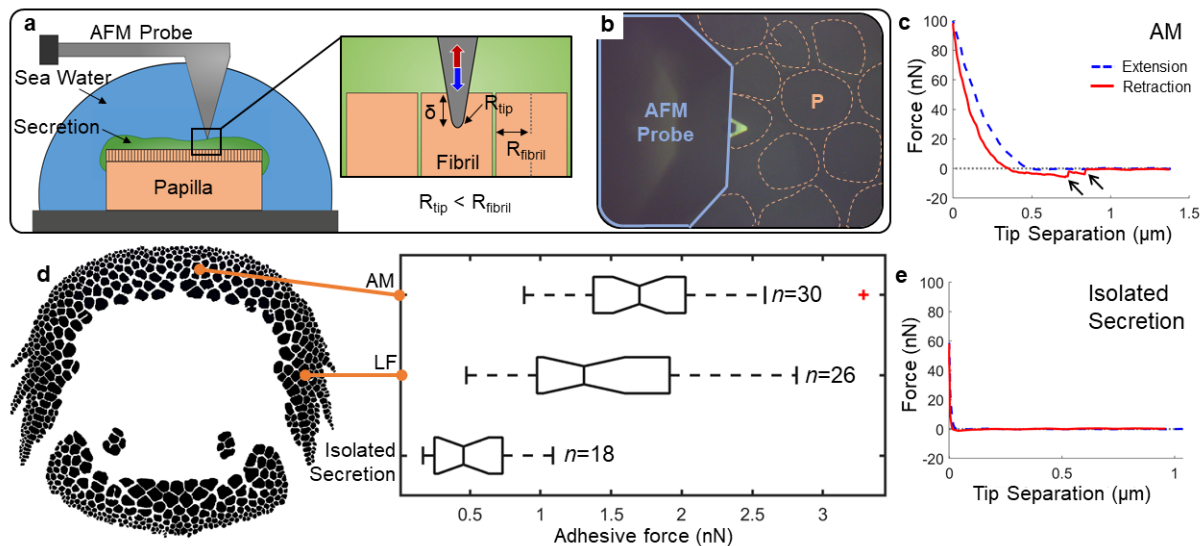
Figure 2.4: **Atomic Force Microscopy (AFM) to measure adhesive properties of microfibrils and secretions from fresh tissue samples. a)** Schematic of the experimental setup. AFM pull tests were performed in a droplet of filtered seawater. Secretions remained present at the site of the pull tests above the papilla to avoid damage to the microfibrils. Inset: Schematic of the interaction of the probe tip with the microfibril for both extension (blue arrow) and retraction (red arrow) of the AFM probe tip . Extension of the AFM probe tip resulted in a displacement (δ) and compression of the microfibril. The radius of the AFM probe (R_{tip}) was notably smaller than the radius of the microfibril (R_{fibril}). **b)** Image of the experimental setup. The AFM probe was aligned over the papilla (P) prior to tests. **c)** Example force curve from the interrogation of a papilla from the anterior margin. Unbinding events annotated with arrows. Extension allowing for compression of the AFM probe to the surface, blue dashed line. Retraction allowing for unbinding from the surface, red solid line. **d)** Average adhesive force of microfibrils from the papillae along the anterior (AM) and lateral (LF) disc margin, and of isolated secretions. **e)** Representative force curve from the interrogation of the isolated secretions on a glass slide.

euthanized clingfish specimen. The maximum adhesive force was calculated from the moment of a sharp vertical transition, or unbinding event, in the retraction force curve (Fig. 2.3 c). We observed that during interrogations of the papillae, the probe tip registered between one and two unbinding events. We suggest that the dual unbinding events may be a result of the probe tip interacting with the terminus of two neighboring fibrils. Such sharp vertical transitions indicative of unbinding events were not observed during the interrogations of the isolated secretions (Fig. 2.3 e).

From the force curves, we found that the fibrils were roughly three times more adhesive

than the isolated secretions (Fig. 2.3 d). The anterior and lateral components of the disc margin were measured with an average force of 1.75 nN $\pm$ 0.54 nN (n = 30) and 1.42 nN $\pm$ 0.59 nN (n = 26), respectively. In contrast, the secretions were measured with an average adhesive force of 0.51 $\pm$ 0.30 nN (n = 18). The location of the pull tests along the disc margin impacted the resulting adhesive force. The microfibrils from a papilla of the lateral component of the disc margin registered pull-off forces that were 20 percent lower than those of a papilla located along the anterior disc margin.

We used AFM to calculate the effective elastic modulus [54] of the microfibrils (Fig. 2.4 a, b). The measurement of effective elastic modulus is key for structured materials, as it accounts for the material composition, geometry, and hierarchy of microstrutcures [55]. We measured the effective elastic modulus of the microfibrils to understand their behavior under realistic loading conditions which helped us to understand their function. To calculate the effective elastic modulus (E), we used a Sneddon conical model to approximate the effective elastic modulus of the fibrils during compression of the AFM cantilever to the surface, as detailed in Equation (2.1) [56].

$$E = \frac{\pi}{2 tan\alpha} \frac{F}{\delta^2} (1 - \nu^2) \tag{2.1}$$

This model is dependent on the shape of the cantilever and conditions of the AFM interrogations. We performed all AFM interrogations with a triangular silicon nitride cantilever with a nominal tip half angle (α) of 18°. The modulus was calculated as a function of the force (F) given an indentation depth (δ). We approximated the Poisson ratio (ν) of the samples to be 0.3 [57]. A baseline correction was performed prior to our calculation of the effective elastic modulus. The effective elastic modulus was reported for Sneddon model approximations that have a significance value (R^2) greater than 0.8.

We found that the effective elastic modulus of the microfibrils differed based on the location of the papillae along the disc margin. Compression tests between the microfibrils of the anterior and lateral components of the disc margin exhibited an effective elastic modulus of

19
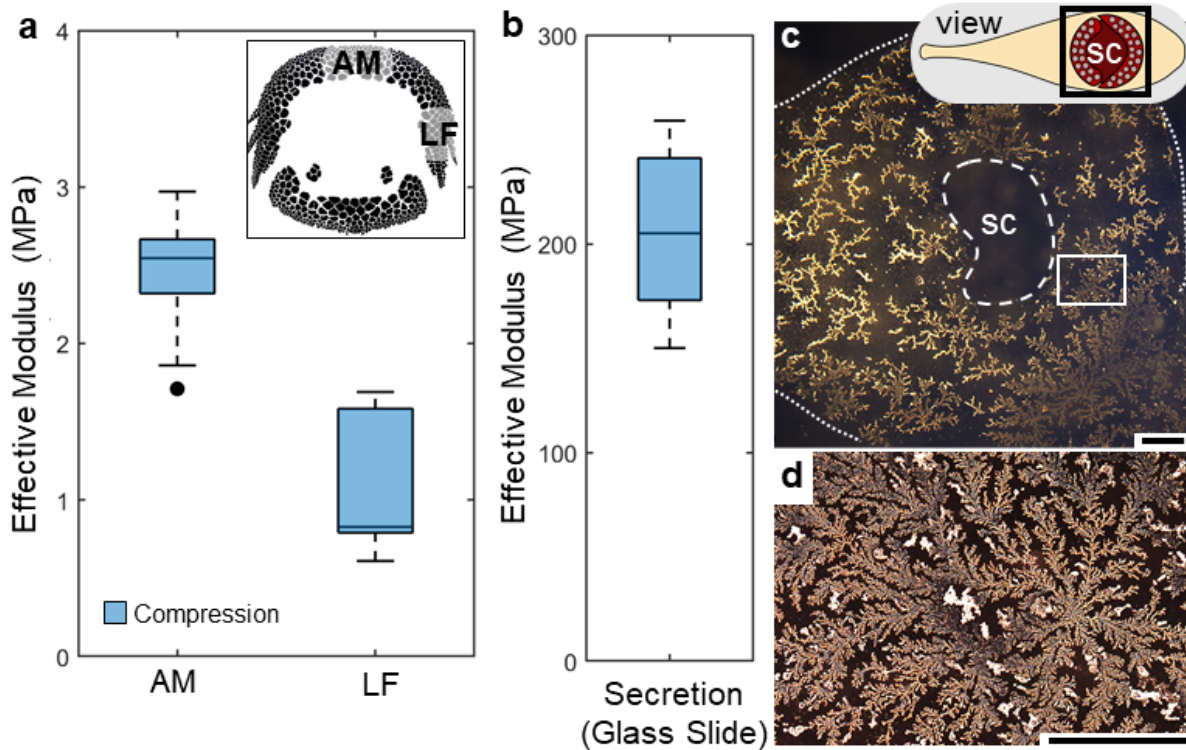
Figure 2.5: **AFM to measure the effective elastic modulus of the microfibrils. a)** Effective modulus (MPa) of the microfibrils of the anterior (*AM*) and lateral (*LF*) disc margin. Inset: Representative schematic of position of papillae along disc margin. **b)** Effective modulus of secretions that were plated on a glass slide, serving as a control. **c)** Brightfield micrograph of secretions that had been dried on a glass slide, to demonstrate a mucosal print of the clingfish. Suction chamber (*sc*) outlined in dashed line. Secretions were present within dotted line. Inset rectangle indicates view of subfigure (d). Scale bar, 1 mm. **d)** Brightfield micrograph of mucosal ferning, present along the anterior disc margin. Scale bar, 1 mm.

2.45 ± 0.31 MPa (*n* = 20) and 1.11 ± 0.42 MPa (*n* = 15), respectively. The microfibrils of the anterior disc margin were therefore 2.2 times stiffer than the microfibrils of the lateral disc margin. Overall, the effective elastic modulus of the microfibrils demonstrated their relative softness, which we hypothesize assist in conforming to surface asperities, thereby reinforcing the seal of the disc margin.

The isolated secretions that were interrogated on the glass slide exhibited an average effective elastic modulus of 205.50 ± 40.64 MPa (*n* = 6) in compression. We concluded that the effective elastic modulus of the secretions was dominated by the stiffness of the glass slide.

In visualizing the print of the secretions made by the clingfish, we observed branching and ferning patterns indicative of glycoproteinated mucous (Fig. 2.5 c, d) [58, 59]. We projected that the primary contribution to the secretions produced by the clingfish was mucosal. We hypothesized that the variability in the calculation of the effective elastic modulus of the secretions was in part due to an uneven layer of mucous across the glass slide, which would impact the thickness and thus stiffness of the layer.

2.3.3   Scaling impact of microfibrils across suction disc

To understand the prevalence of microfibrils across the disc margin, we investigated the total surface area and distribution of the papillae. Using microscopy and custom image processing protocols developed in previous work [60], we stitched together high magnification images of the disc margin to create a map of its papillae (Fig. 2.6 a, b). An individual papilla was automatically identified and its surface area was measured. The total surface area of the papillae accounted for about 65 percent of the total surface area of the suction disc. The heatmap of the papillae (Fig. 2.6 c) demonstrated their distribution based on surface area. The highest concentrations of small papillae were found along the outer edge of the disc margin, while the highest concentrations of large papillae were found towards the inner perimeter of the disc margin, consistent with previous studies [60]. The total surface area for the clingfish specimen we analyzed was counted to $3.55 \times 10^7 \ \mu\text{m}^2$.

Using the average contact density of 7.02 microfibrils per μm^2 that we had calculated from the SEM micrographs, we approximated the total count of microstructures across the disc margin. For this approximation, we assumed that all papillae expressed the same density of microfibrils. We calculated that across the entirety of the suction disc of our specimen, a total of 2.50×10^8 microfibrils were expressed. This approximation demonstrated a large prevalence of these microfibrils across the disc margin of the suction disc, which would substantially impact their role in adhesion.
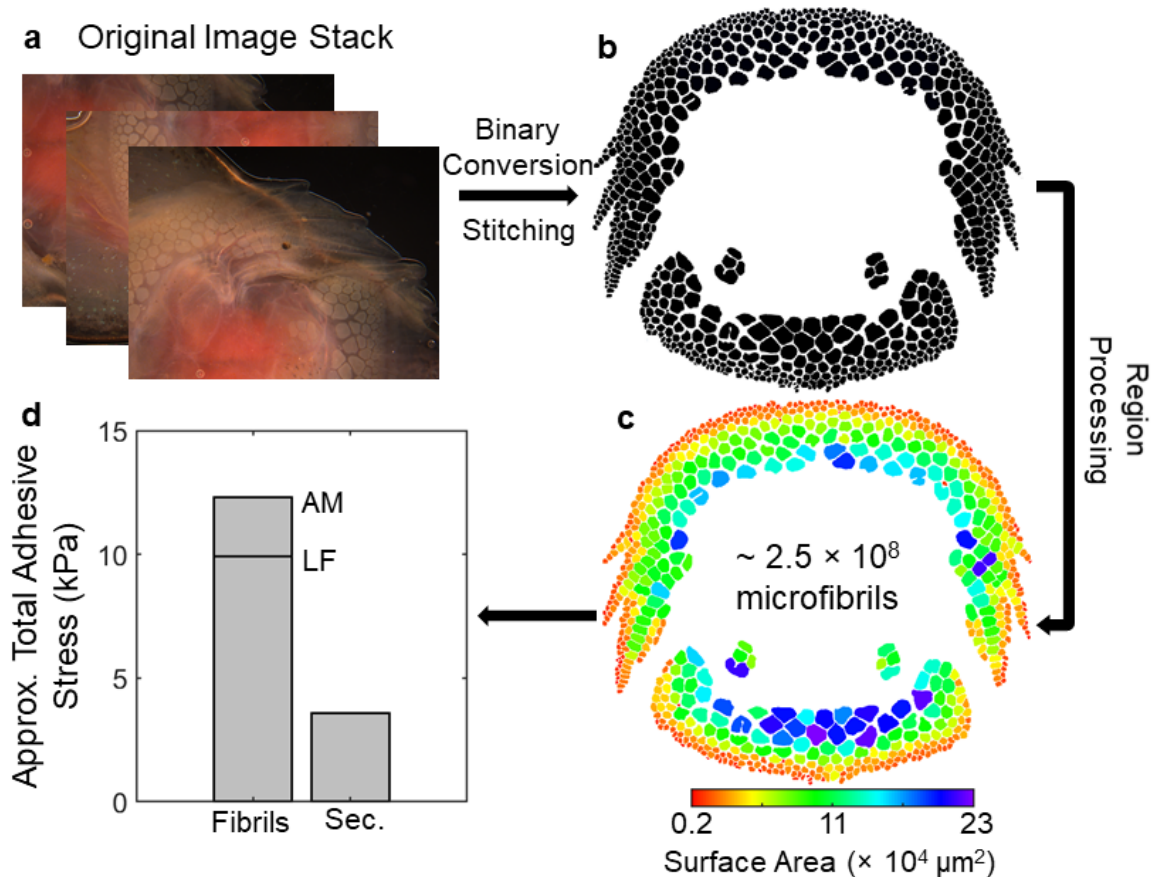
Figure 2.6: **Image processing to approximate the contribution of microfibrils to adhesion across the suction disc. a)** Original group of brightfield micrographs. **b)** Composite binary image generated by stitching together micrographs. **c)** Map of the papillae based on size across the suction disc. Largest papilla ($22.6 \times 10^4 \mu m^2$); Smallest papilla ($0.2 \times 10^4 \mu m^2$). **d)** Approximated adhesive stress (kPa) of the microfibrils, totaled across the entirety of the suction disc. Adhesive stress calculated from anterior and lateral disc margins were indicated by AM and LF, respectively. Approximated adhesive stress across the entire disc margin was also calculated for the isolated secretions (*Sec*).

Assuming that each microfibril resulted in an adhesive force of between 1.41 and 1.75 N, we scaled the total count of microfibrils by the adhesive force and normalized by the total surface area of all papillae. This calculation yielded an anticipated contribution to adhesive stress between 12.3 and 9.9 kPa, respectively (Fig. 2.6 d).

2.4 Discussion

The adhesion capabilities of the clingfish are hierarchical and involve multiple forms of adhesion on a range of size scales, from macro- to microscopic. The microfibrils emanating from the papillae are one example of the hierarchy of adhesive structures that enable attachment to surfaces. We found that the microstructures of the papillae were vastly abundant across the entirety of the disc margin of the clingfish. By understanding their mechanical properties, such as their adhesive characteristics and effective elastic modulus, we approximated their role in the adhesion of the clingfish in wet environments.

To start, a hierarchical combination of adhesion mechanisms have been reported in many other organisms, such as the limpet [46, 61], and provides a redundancy to prevent failure given environmental stresses. Previous work has attributed much of the success of the adhesion of the clingfish to the chamber of subambient pressure produced in its suction chamber [50, 53]. Recent studies have investigated the geometry of the papillae that aids in adhesion due to viscosity as a response to hydrodynamic forces [60]. Here, we have presented results suggesting that the microfibrils emanating from the papillae are also soft and adhesive and function to attach the disc margin to the surface, thereby preventing peeling, and reinforce the disc margin to shear forces. The low stiffness of the microfibrils, coupled with their adhesive qualities, combine to reinforce the seal of the suction disc, especially when confronted by highly chaotic wave surges.

2.4.1 Microscale morphology and comparison across taxa

The shape of the microfibrils of the clingfish that were observed in this study were of a high aspect ratio, terminating in bifurcated heads, consistent with previous studies in which the fibrils were terminated with filamented tips [53]. However, the terminations observed in SEM of the clingfish did not exhibit the same degree of branching at the terminus as the setae of lizards, for instance, which utilize the highly branched spatulae to greatly increase contact density.

Such highly branched protrusions have been suggested to be indicative of adhesive type. A high degree of branching has been posed to be indicative of dry adhesion for which a large density of terminal elements would allow for conformation to surface roughnesses [32]. Previous studies have concluded that the lack of fine terminal elements in animals that employ wet adhesion was due to the ability of fluid to fill small cavities formed on a substrate.

However, in comparison to other hairy adhesives found in nature and that are employed in wet adhesion, from flies ($\sim$0.1 setae per μm^2; [62]) and beetles ($\sim$8.5$\times$10^{-3} setae per μm^2; [37]), the contact density of the clingfish is markedly high ($\sim$7 microfibrils per μm^2). The contact density of the clingfish is of the same order of magnitude of larger organisms, such as lizards (10 setae per μm^2; [33]), that employ dry adhesion. Organisms that employ wet adhesion and that feature predominantly unbranched setae exhibit contact densities that are orders of magnitude less than that of the clingfish.

According to force scaling model, the density of hair-like microstructures increases with body size and likely correlates to adhesion type [33]. However, we suggest that this model and hypothesis only considers terrestrial organisms, and thus the scaling of body size may be different for aquatic organisms, such as the clingfish. Indeed, we do not anticipate that the contact density of aquatic organisms would scale with body mass, as described in terrestrial organisms. The anticipated force that adhesion must counteract for a terrestrial organism is gravity, which is a function of its weight, which is relatively stable or slow to change. For aquatic organisms, buoyancy greatly reduces the impact of gravity on adhesion; rather other dominating factors, such as fluid forces, would shape the adhesive microstructures. The high-density, bifurcated microfibrils would allow for a high-degree of intimate contact to be made between the clingfish and the surface on which it attaches. This high density would therefore conform to rough surfaces and secure the disc margin.

We observed that the fibrils emanate perpendicular from the papillae, guided by microchannels. This observation contrasted observations of microstructures in other animals, such

as the gecko, for which the setae exhibited a uniform angle indicative of preferential loading and peeling conditions [35]. We suggest that the angle of the microstructures in the clingfish are a function of the environmental conditions. Since the clingfish resides in a highly chaotic intertidal environment, the body of the clingfish would be subjected to a variety of forces of varying, non-uniform directions. Conversely, the main dislodgement force of terrestrial organisms such as the gecko is gravity, which is of a predictable direction. Therefore, we concluded that the perpendicular orientation of the microfibrils of the clingfish do not exhibit a preferential direction of loading and may be attributed to its intertidal environment.

2.4.2   Adhesion of the microfibrils

The microfibrils were roughly three times more adhesive when compared to their corresponding secretions. However, comparing the adhesive forces of the fibrils to that of a single seta of the gecko, the microstructures of the gecko exhibit a significantly larger adhesive force of approximately 40 μN [63]. Thus, the fibrils of the clingfish were found to be adhesive, but not to the same extent as previously reported values of land-dwelling organisms that rely on microstructures as the primary mode of attachment. The low values of adhesive force of the isolated mucosal secretions verified the hypothesis that the secretions are used for sealing, and do not serve to chemically bond the clingfish to a surface.

Although the adhesive force of each microfibril was found to be lower than terrestrial organisms, such as the gecko, the high abundance of the microfibrils along the disc margin scales their effect on adhesion. As reported in previous works [60], the total count of papillae and the surface area of papillae of the clingfish positively correspond to body size. Therefore, we expect that the number of microstructures to parallel this trend, resulting in a greater abundance of microstructures for larger body sizes. This positive correlation corresponds to a larger contribution of the microfibrils to adhesion.

We anticipate that the microfibrils adhere to local surface asperities, which helps to prevent

25

the disc margin from disassociating from a surface. Such disassociation events would compromise the subambient pressure of the suction chamber, which provides a large contribution to axial adhesion for the clingfish. Thus, by locally adhering to surface asperities, the disc margin can protect the seal of the suction disc on rough surfaces.

By measuring the adhesive force with secretions present, we believe we have provided a realistic assessment of the adhesive characteristics of the microfibrils. Given that these microstructures function in the presence of secretions in the natural environment, it was imperative to measure their adhesive force with secretions present.

2.4.3 Soft fibrils for sealing and regeneration

The microfibrils were observed to be of a high aspect ratio and were measured with a low effective elastic modulus of 1-2 MPa. A low effective modulus would in part be attributed to the high aspect ratio of the microfibril, in addition to its material composition. A low effective elastic modulus would allow for greater surface conformation, which would imply greater sealing capabilities of the suction chamber and a substantial increase in friction to prevent dislodgement of the disc margin. This finding was consistent with previous work. Hairy or fibrillar microstructures used in adhesion of terrestrial animals have been associated with the benefit of adapting to rough surfaces, thereby achieving intimate contact with asperities [32]. In terrestrial organisms, arrays of setae have been noted to have a low effective modulus, even though the setae were composed of a stiff material [55]. The setae of the gecko, for instance, is composed of β-keratin, with a measured elastic modulus of roughly 1.6 GPa [64]. However, tests of the effective modulus of an array of setae measured to 83 kPa during vertical compression [35]. Similarly, the setae of the beetle were measured with a cuticle modulus between 5 – 16 GPa, while the effective modulus dropped to 34 – 92 kPa [37]. The low effective modulus achieved by of the microstructures would therefore be in part due to their geometric arrangement, including a high aspect ratio. Due to the geometric configuration of setae in terrestrial organisms, microstructures composed of stiff

material behave in a soft manner.

Although we do not yet know the material composition of the extracellular cuticle of the microfibrils, the effective elastic modulus allowed us to hypothesize its function in sealing and increasing the frictional footprint of the clingfish to resist turbulent flow. Such softness of the microfibrils may make them subject to damage or possibly failure in reaction to turbulent forces [32], prompting the need for a mechanism of regeneration. The observation of wide hexagonal microchannels that expanded across the subsurface of a papilla led us to conclude that the subsurface microchannels play a role in microfibril regeneration at the surface. The wide subsurface microchannels may lead to faster regeneration of the microfibrils.

2.4.4   Biomimetic applications of microstructures for adhesion

This study provided a key to improve the design of underwater adhesives. The microfibrils of the clingfish were shown that not only were they adhesive, but that they function to secure the disc margin to a surface. We suggest that for adhesion underwater, a hierarchy of surface structures may be necessary to withstand unpredictable dislodgement forces of a large magnitude.

Our previous work has focused on mimicking key macroscopic elements of the clingfish suction disc to improve underwater manipulation [65]. The fibrils were approximated for their material stiffness as a soft layer of silicone, forming both micropillars and a thick layer of soft silicone, to seal against surface irregularities. Similar design methodologies were employed to provide adhesion to suction cups on rough surfaces [66]. Both studies demonstrated the need for a soft sealing layer to improve adhesion to rough surfaces. However, the use of synthetic microstructures analogous to the microfibrils requires further investigation. The synthetic microfibrils of previous works [65] were not optimized in geometry to densely pack the surface, nor were they representative of the same size scale as the microfibrils of the clingfish. By mimicking the microscale geometries, material properties, and termination geometries of the fibrils of the clingfish presented in this study, we hypothesize that these modifications would improve adhesion

27

to rough, submerged surfaces. The high density of soft microfibril contacts would yield advantageous sealing capabilities, which may aid in securing the disc to withstand a greater range of environmental disturbances.

The findings from the clingfish add to a growing repository of biological adhesive designs that have proven useful in advancing engineered adhesives. For instance, investigations of the microstructured adhesives of terrestrial organisms, such as the gecko, have been crucial in the development of dry adhesives. The bioinspired dry adhesives have begun to transform various aspects of robotic manipulation and locomotion to yield novel tasks that previously had not been achieved. Although the differences between the wet and dry environments are numerous, we suggest that a similar methodology of bioinspiration can be followed to yield novel, provocative adhesive designs in an underwater environment. By understanding the underlying mechanisms of adhesion of the clingfish, we can envision engineering biologically inspired adhesives for the underwater environment that allow for reversible binding. Enhanced adhesive capabilities that leverage microstructures could be transformative in the field of robotics in an underwater environment.

2.5   Materials & Methods

2.5.1   Collection of biological specimen

A live clingfish (n=1) was collected along the San Diego coastline under a collection permit to accredited organisms' collector, P. Zerofski from Scripps Institution of Oceanography. Animal care protocol IACUC #S11071 to D. Deheyn was used for fish euthanasia and fresh tissue was analyzed the day of animal sacrifice. SEM imaging was performed on a preserved clingfish specimen (n=1) from the Scripps Marine Vertebrate Collection, where specimen have been preserved in 50% isopropanol.

2.5.2   Imaging the microstructures of the papillae

Fresh and preserved tissue samples were imaged under Brightfield microscopy (Carl Zeiss AG, Germany) using a SMZ1500 Nikon camera. To image the secretions, we placed a live clingfish on a glass slide, inverted the surface, and subsequently removed the clingfish. Secretions from live specimen were dried prior to imaging under brightfield in transmittance (Nikon 50i microscope, get details). The anterior disc margins of the suction disc of both a freshly euthanized and preserved clingfish were imaged under the Scanning Electron Microscope FEI Apreo SEM (Thermo Fisher Scientific, Inc.). All tissue samples were dehydrated with an ascending series of ethanol (30, 50, 70, 90, 95, and 100 vol.%) prior to being coated with iridium using a sputter coater (Emitech K575X, Quorum Technologies Ltd.). The density of microfibrils was calculated by manually counting the number of microchannels expressed at the surface of papillae in SEM micrographs across 10 observation regions (area region, 1 μm^2). Transmission Electron Microscopy was performed on a single papilla of the posterior disc margin. Semithins were cut in the sagittal and frontal planes. All quantifiactions and measurements made on SEM and TEM micrographs were performed using ImageJ [67].

2.5.3   Atomic Force Microscopy

We used Atomic Force Microscopy to test material properties of the microfibrils that originated from the papillae. Fresh tissue samples were isolated from the anterior and lateral disc margin of a clingfish specimen, and all AFM measurements were taken within 5 hours of animal sacrifice. The papillae were interrogated with the Dimension Fast Scan Atomic Force Microscope using a silicon nitride triangular cantilever (ScanAsyst-Fluid probe; Bruker Nano Inc.) of spring constant 1.793 N·m^{-1} and a manufactured tip radius of 20 nm. All AFM tests were performed in a droplet of filtered seawater. Secretions were aspirated using a pipette from the surface of uninterrogated papillae from the anterior disc margin, plated onto glass, and hydrated in

a droplet of filtered saline prior to interrogation. Analysis of AFM interrogations were performed on NanoScope Analysis (Bruker Nano Inc.). With this software, we baseline corrected the force profiles and used the Sneddon conical model to approximate the effective elastic modulus of the sample.

2.5.4   Automated characterization of suction disc

We used the image processing protocol developed in previous work [60] to count the total surface area of the papillae across the suction disc. We first converted brightfield micrographs to a binary image and stitched together the images. We then labeled and processed every region of the suction disc, where a single papilla was considered one region. All image processing was performed in MATLAB (2018a, The MathWorks, Inc.).

2.6   Acknowledgments

Author Contributions: J.A.S., M.T.T, and D.D.D. conceived the project. M.A.M. provided guidance on materials characterizations of biological tissue. J.A.S. characterized the morphology of the clingfish suction disc and performed tissue preparations. H.Q. and J.A.S. performed SEM on the biological specimen, and D.D.D. performed TEM. J.A.S. prepared the initial draft of the manuscript and all authors provided feedback during revisions.

Chapter 2, in part, is currently being prepared for submission for publication of the

material. Sandoval, Jessica A.; Quan, Haocheng; Tolley, Michael T.; Meyers, Marc A.; Deheyn, Dimitri D. The dissertation author was the primary investigator and author of this material.

Chapter 3

Reversible adhesion to rough surfaces both in and out of water, inspired by the clingfish suction disc

Jessica A. Sandoval[1]*, Saurabh Jadhav[1], Haocheng Quan[1], Dimitri D. Deheyn[2], Michael T. Tolley[1]*

[1]Department of Mechanical and Aerospace Engineering, University of California San Diego, 9500 Gilman Dr., La Jolla, CA 92093

[2]Marine Biology Research Division, Scripps Institution of Oceanography, 9500 Gilman Dr., La Jolla, CA 92093

3.1   Abstract

Adhesion is difficult to achieve on rough surfaces both in air and underwater. In nature, the northern clingfish (*Gobiesox maeandricus*) has evolved the impressive ability to adhere onto substrates of various shapes and roughnesses, while subject to strong intertidal surges. The

suction disc of the clingfish relies on suction and friction to achieve and maintain adhesion. Inspired by this mechanism of attachment, we designed an artificial suction disc and evaluated its adhesive stress on rough surfaces and non-planar geometries. The artificial suction disc achieved adhesion strengths of 10.1 ± 0.3 kPa in air on surfaces of moderate roughness (grain size, 68 μm), and 14.3 ± 1.5 kPa underwater on coarse surfaces (grain size, 269 μm). By comparison, a commercially available suction cup failed to exhibit any significant adhesion in both scenarios. The roughly 2 g heavy clingfish-inspired suction discs gripped concave surfaces with small radii of curvature (12.5 mm) and supported payloads up to 0.7 kg. We correlated the effect of key bioinspired features (i.e. slits, a soft outer layer, and body geometry) to adhesion performance using contact visualization techniques and Finite Element Analysis. The suction discs were then tested on a Remotely Operated Vehicle (ROV) to demonstrate their utility in the soft manipulation of fragile objects.

3.2   Introduction

Non-destructive adhesion (i.e. reversible adhesion that does not damage or alter the substrate) to rough surfaces represents a challenge for robotic systems in both wet and dry environments. Many strategies for attachment in air (e.g. based on van der Waals forces [31, 68]) lose their effectiveness underwater and thus are specific to the type of environment [2]. Previous work has turned to nature to provide inspiration for the design of adhesive systems [1, 36]. Attachment mechanisms employed by organisms have been classified into the categories of mechanical interlocking [20], friction [6], chemical bonding [69, 70], dry adhesion (i.e. van der Waals forces) [31, 46, 71, 7], wet adhesion (i.e. capillary adhesion) [11], and suction (driven by a pressure differential) [72, 61]. Interlocking involves the use of structures, such as hooks and claws, to catch onto surface asperities or penetrate a surface [73]. Chemical adhesion involves the use chemical bonds to adhere to surfaces either permanently, such as in mussels [70], or temporarily,

33

as demonstrated in echinoderms such as sea stars [69]. Dry adhesion relies on van der Waals forces between microscopic structures along an adhesive pad and a surface. Adhesion relying on van der Waals forces is commonly used by terrestrial organisms ranging from arthropods such as spiders [7] to reptiles such as geckos [31, 5]. Wet adhesion leverages capillarity to form a liquid bridge between an attachment pad and a substrate [74]. Tree frogs, for instance, leverage wet adhesion by secreting mucus in between channels present on their toe pads to form a capillary meniscus, allowing for attachment to a substrate [11]. Insects employ a similar strategy to adhere to surfaces using an adhesive secretion that originates from the foot pads to take advantage of wet adhesion, as demonstrated in ants and flies [12, 75]. Friction as an attachment mechanism resists movement parallel to a surface [76] and can result from various mechanisms, one of which includes microscopic interlocking with surface asperities [73]. Lastly, suction is induced by the formation of a pressure differential between the surrounding environment and an adhesive disc [72, 61, 77, 78]. Organisms employ multiple types of these attachment strategies in order to adhere to surfaces.

Each environment type poses its own unique set of challenges to adhesion, resulting in new adaptations of these attachment devices [2]. For instance, an organism in an underwater environment may be subjected to disruption due to buoyancy or variable fluid flow, which would thereby influence the strategy for attachment. As an example, adhesion strategies utilized by organisms in wet environments less commonly employ van der Waals forces for adhesion. However, recent work on tree frogs [11] and abalone [46] suggest their use of van der Waals, in addition to capillarity, to adhere. Aquatic organisms commonly achieve reversible adhesion via suction in coordination with mechanical interlocking or friction [20]. The remora, a symbiotic fish that attaches to sharks, whales, and rays, uses a specialized dorsal suction disc with rigid spines to withstand highly directional flow while secured to the body of its host [77].

Attachment devices observed in nature inspire new adhesive designs in artificial systems as a form of biomimicry [3]. Bioinspired modes of attachment have been applied to the field

of robotics [79] to enhance locomotion [10, 80] and manipulation [81, 27]. Robotic footpads composed of gecko-inspired dry adhesives [79] and of spines and hooks [82] have provided robots with the ability to climb dry glass walls and fabric walls, respectively. Similarly, bioinspired, non-destructive adhesion methods are important for the growing field of soft robotics [83], such as for crawling robots that rely on anchoring to aid in elongation and contraction of the body [80].

Bioinspired attachment devices have also been used to enhance robotic manipulation [27]. In dry environments, gecko-inspired adhesives have been applied to soft robotic grippers to enhance their grasp of complex shapes [84] and manipulate large objects in microgravity [9]. Gecko-inspired adhesives have also been used in conjunction with a chamber of controlled subatmospheric pressure to achieve adhesion onto deformable surfaces [85].

Efforts have been made to improve adhesion in wet and damp conditions to enhance locomotion and manipulation. Bioinspired, microstructured adhesives, which have been traditionally used in dry environments, have been modified via chemical coating [86], material composition [87], and geometry [88, 89] to provide adhesion in wet conditions. The octopus has served as a source of inspiration for robotic grippers, including an actuated, soft-body continuum arm to grip around surfaces [90]. The suckers of the octopus have inspired the development of artificial suction cups with varying surface textures made of silicone, which have been tested on smooth surfaces [91]. A remora-inspired suction disc was developed, combining a suction chamber with actuated rigid spines to adhere onto surfaces of roughnesses up to 200 μm [19]. The examples listed above demonstrate the benefits of coupling bioinspired adhesion devices and the fields of materials science and robotics to provide enhanced attachment capabilities both in and out of water. However, further studies should be conducted to improve adhesion capabilities to rough surfaces in water while remaining passive or unactuated.

We sought inspiration from the clingfish to engineer a device to reversibly adhere to rough surfaces underwater. The clingfish (*Gobiesox maeandricus*) lives in intertidal habitats and clings to rocks while subject to continuous wave action of various forces and intensities.

Respiration tests have demonstrated that little sustained muscular exertion is required to maintain adhesion [50]. The passive nature by which the clingfish remains adhered to a substrate suggests a biomimetic analog may also need not be actuated to sustain adhesion. The ability of the biological specimen to cling and resist powerful intertidal forces is thanks to a ventral suction disc supported by the pelvic and pectoral girdles [50]. The suction disc functions by establishing a chamber of subatmospheric pressure that is capable of sealing to surface irregularities [53], thereby sustaining pull-off forces that are 80 to 230 times the body weight of the clingfish [52].

The clingfish accomplishes attachment via hierarchical mechanisms of adhesion, or multiple forms of adhesion on both micro- and macroscopic scales. Research has suggested that clingfish adhere by suction and maintain their grip via friction [52]. Capillary adhesion is also considered to play a role in attachment [53, 52]. Other mechanisms may also be at play, such as van der Waals forces, although this mechanism would be diminished in liquids as compared to air assuming a constant gap width. Involvement of van der Waals forces in adhesion may be non-nominal when the fibrils of the papillae are in close proximity to the substrate, a similar phenomenon being reported in tree frogs [11]. For this paper, we chose to investigate the impacts of the clingfish morphology and structure on two primary methods for attachment, via suction and friction.

On the macroscopic scale, the displacement of the surrounding fluid from the concavity of the clingfish disc induces suction by creating a chamber of sub-ambient pressure formed at the intersection of the pelvic and pectoral fins [50, 53, 52]. The disc margin, or the perimeter of the suction disc, acts to seal the suction chamber and is critical to the success of the grip of the clingfish. The disc margin is lined by rows of hexagonal pads, or marginal papillae [50], that aid in the sealing of the suction chamber. Previous work describes an extracellular cuticle that is secreted by the papillae [50]. We refer to this extracellular cuticle as "fibrils" in this work. These structures are hypothesized to play a role in increasing the frictional footprint of the clingfish, thereby conforming to surface asperities and preventing the slip of the disc margin.

Inspired by the ability of the clingfish to resist axial loads, we developed a non-destructive method of attachment that functions on rough and elaborate surfaces without necessitating complex fabrication or controlled actuation. We first investigated the macro- and microscopic structures involved in adhesion of the clingfish using Scanning Electron Microscopy (SEM). We then applied our findings to create artificial clingfish-inspired suction discs. These discs were composed of silicones of varying stiffnesses in specific molded geometries to tailor adhesion performance. The artificial suction discs were then applied to a manipulator of a Remotely Operated Vehicle (ROV) and tested for performance when handling delicate objects, as an example application of the technology.

3.3   Materials and Methods

3.3.1   Morphology of biological suction disc

In an effort to better understand the underlying mechanisms of attachment of the clingfish, we dissected and imaged the suction disc of both fresh and preserved clingfish specimen. Two live clingfish (*Gobiesox maeandricus*) were collected along the San Diego coastline under a collection permit to accredited organisms' collector, P. Zerofski from Scripps Institution of Oceanography. Animal care protocol IACUC #S11071 to D. Deheyn was used for fish euthanasia and fresh tissue was analyzed the day of animal sacrifice. Observations were also performed on preserved clingfish samples obtained from the Scripps Marine Vertebrate Collection. Clingfish were preserved in 70% ethanol and were therefore observed to be devoid of secretions and exhibited tissue dehydration from the preservation process.

Fresh and preserved tissue samples were imaged under brightfield microscopy (Carl Zeiss AG, Germany) using a SMZ1500 Nikon camera. The disc margin of the suction disc of the preserved clingfish was imaged under the Scanning Electron Microscope FEI Apreo SEM (Thermo Fisher Scientific, Inc.).

The brightfield micrographs were analyzed using ImageJ [67] to calculate the area of the disc margin relative to the entire suction disc surface area. The difference in surface areas between the disc margin and the entire suction disc was normalized to the surface area of the entire suction disc. We calculated that the disc margin comprised approximately 65% of the total suction disc footprint. These measurements were then used for the design of biomimetic suction discs.
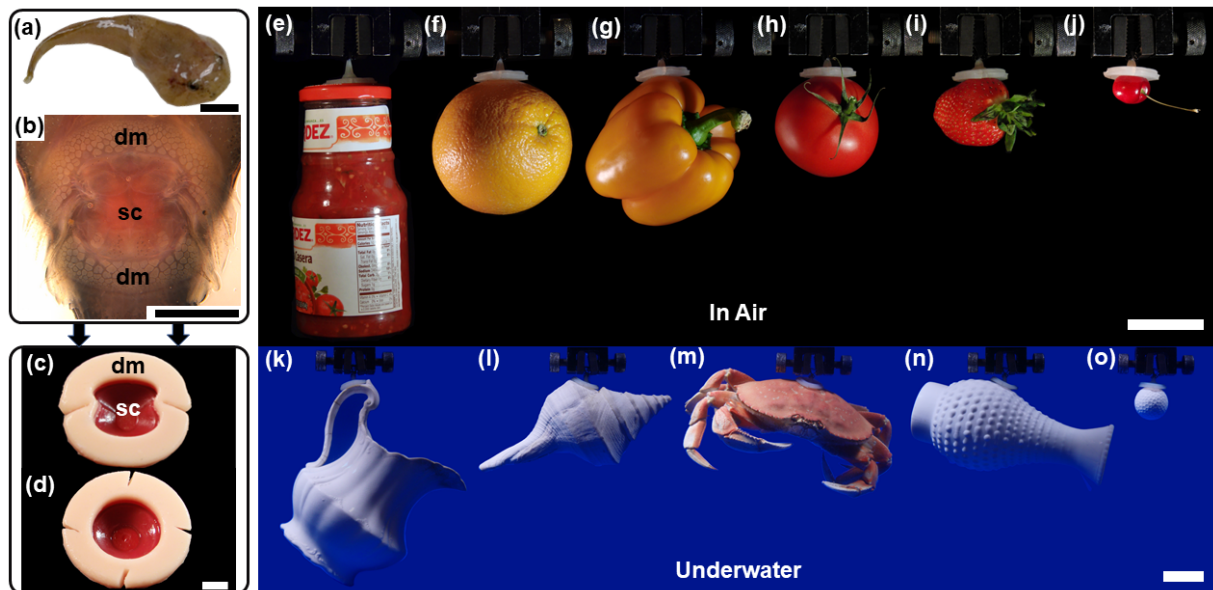
Figure 3.1: Suction disc clings to highly variable surfaces in air and underwater. **(a)** Clingfish (*Gobiesox maeandricus*) collected along the coast of Southern California. Scalebar, 10 mm. **(b)** Ventral view of clingfish suction disc imaged under brightfield microscopy. Disc margin (*dm*); Suction chamber (*sc*). Scale bar, 5 mm. **(c)** Bilaterally symmetric suction disc with two slits. The soft layer of the disc margin (*dm*) is composed of Ecoflex 00-30. The suction chamber (*sc*) is composed of Dragon Skin 20. Scale bar, 5 mm. **(d)** Radially symmetric suction disc with four slits in the disc margin. Scale bar, 5 mm. **(e-j)** Suction disc (radially symmetric, with soft layer, with four slits) adhering to food items in air. Scale bar, 50 mm. **(k-o)** Suction disc (radially symmetric, with soft layer, with four slits) gripping ceramic vase handle, calcareous shell, crab shell, textured vase, and golf ball in water. Scale bar, 50 mm.

3.3.2   Biomimetic suction disc design

We applied two key concepts of suction and friction to avoid slip while sealing the disc margin to create a bioinspired suction disc that successfully adhered onto textured surfaces and irregular shapes (Fig. 3.1). The low-pressure chamber of the artificial disc was composed of a silicone of shore hardness 20A, Young's modulus 1.11 MPa [92] (Dragon Skin 20, Smooth-On, Inc.) (Fig 3.2 (f),(g)). The soft fibrils originating from the papillae of the clingfish inspired the use of micropillars to line the disc margin (Fig. 3.2 (g),(h)). The dimensions of the synthetic micropillars were chosen to be the same order of magnitude as the biological fibrils. We compared the performance of suction discs with micropillars to that of discs without. For the latter, the soft fibrils of the clingfish were approximated as a thick layer of silicone of shore hardness 00-30, Young's modulus 125 kPa [93] (Ecoflex 00-30, Smooth-On, Inc.) (Fig. 3.2(f)). We will refer to the silicone layer lining the disc margin as "soft" and that of the suction chamber as "stiff" due to their relative stiffnesses (i.e. 125 kPa vs. 1.11 MPa, or about $9\times$ difference in stiffness).

We fabricated and tested a total of six prototypes, two with micropillars and four without, to evaluate the effect of three design parameters (disc geometry, a soft sealing layer, and slits) on adhesion of the disc to various surfaces (Fig. 3.3). Disc geometries were either bilaterally symmetric or radially symmetric. The bilaterally symmetric prototype was designed with two slits in the disc margin, analogous to the intersection of the pelvic fin and the posterior margin of the clingfish, described in previous work as a valve [50]. The bilaterally symmetric disc featured a soft layer in its disc margin. All five other prototypes were radially symmetric.

We fabricated two radially symmetric suction discs with micropillars (2 μm square cross-section, height 10 μm, spaced 1.5 μm apart) (figure 2(g),(h)) [94]. The disc margin overall was 0.8 mm thick. We tested two stiffnesses for the micropillars, changing the material composition of the micropillars to be either soft (125 kPa) or stiff (1.11 MPa) silicone.

We fabricated three radially symmetric suction discs without micropillars in the disc margin (Fig. 3.3). One prototype was designed with a soft layer of thickness 2 mm and with four
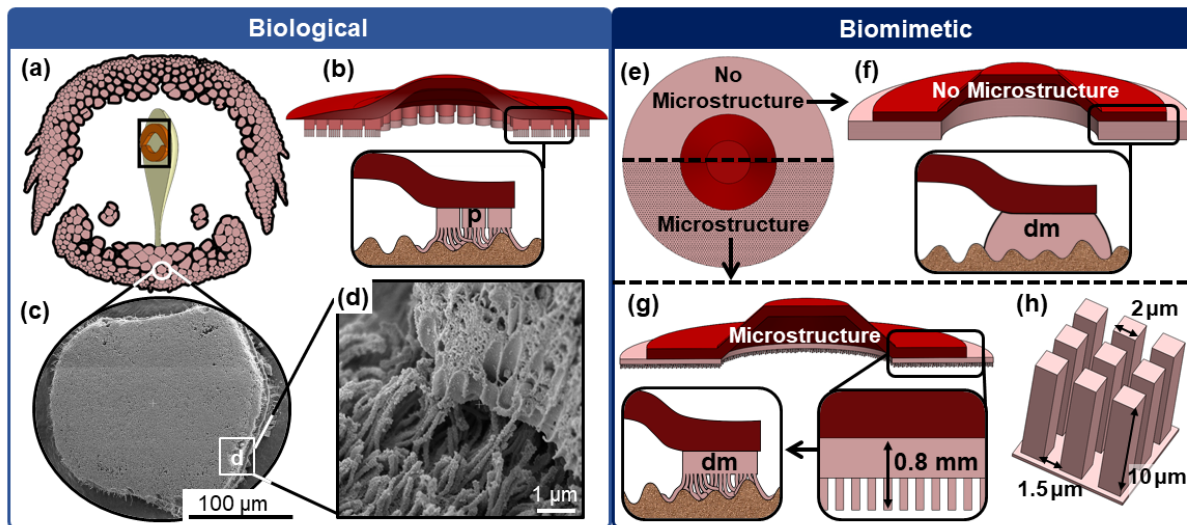
Figure 3.2: **Hierarchical mechanisms of adhesion in clingfish (*Gobiesox maeandricus*) and biomimetic suction discs. (a)** Footprint of clingfish disc margin. Generated from brightfield micrographs via image processing, outlining all papillae. Disc margin comprises about 65% of suction disc footprint. Inset: Schematic of ventral suction disc. **(b)** Schematic of the approximated biological methods of attachment. The pelvic girdle composes the suction chamber. The papilla (*p*) is represented as cylindrical, with densely packed fibrils that are used to conform to and seal surface asperities. **(c)** SEM micrograph of single papilla of the disc margin. **(d)** SEM of isometric view of papilla on fractured edge, fibril shown in lower left. Scale bar, 1 μm. **(e)** Bottom view of radially symmetric suction discs. **(f)** Schematic of the suction disc without microstructures. Inset: The soft layer of the disc margin (*dm*) conforms to surface irregularities. **(g)** Schematic of a suction disc with micropillars lining the disc margin. Disc margin thickness is 0.8 mm. Inset: Micropillars conform to surface irregularities. Note: microstructure dimensions have been exaggerated for illustrative purposes. **(h)** Schematic of micropillars of 2 μm square cross-section, height of 10 μm, and spacing of 1.5 μm.

equally spaced, radially symmetric slits, each angled 15 degrees from the radial direction (Fig. 3.1 (d)). We hypothesized that slits would improve sealing capabilities of the suction disc by providing geometric (in addition to intrinsic material) compliance to an irregular surface. Another prototype featured a 2 mm thick soft layer and did not have slits in the disc margin. We created a control design, referred to as a stiff disc, which was manufactured without slits and without a soft layer. Across all prototypes, the disc margin accounted for about 65% of the total suction disc footprint, congruent with our measurements of the biological specimen. All six types of suction discs created for this study were 25 mm in diameter and with a suction chamber depth of 4 mm.
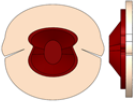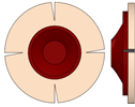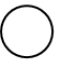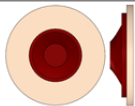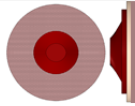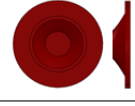
	Symmetry	Soft Seal	Slits	Micro-Struct
	Bilateral	●	●	○
	Radial	●	●	○
	Radial	●	○	○
	Radial	●	○	●
	Radial	○	○	○

Figure 3.3: **Schematics of different prototype designs.** **(row 1)** The bilaterally symmetric suction disc was fabricated with slits and a soft layer, without microstructures. **(row 2)** A radially symmetric disc was designed with 4 slits and a soft disc margin, without microstructures. **(row 3)** A radially symmetric disc was fabricated with a soft layer, without slits, and without microstructures. **(row 4)** A radially symmetric disc was designed with a soft layer, without slits, and with microstructures. **(row 5)** The stiff suction disc served as a control for the adhesion experiments. This disc did not have a soft margin, slits, or microstructures.

We detached the discs by either subjecting it to a shear force parallel to the attachment surface, or by lifting one side of the disc margin to relieve the subambient pressure within the suction chamber.

Fabrication of biomimetic disc

Artificial suction discs were designed using computer-aided design (Solidworks, Dassault Systems) and fabricated using molds that were manufactured from rigid material (VeroClear, Stratasys Inc.) on a multimaterial 3D printer (Objet350 Connex3, Stratasys Inc.) (Fig. 3.4). After printing, the rigid molds were aged in an oven at 40°C for 4 hours to ensure the part fully cured. Body geometries were either circular, or in the bilateral geometry of the clingfish suction disc in accordance to analysis as described in Section 3.3.1. The discs were molded with cylindrical
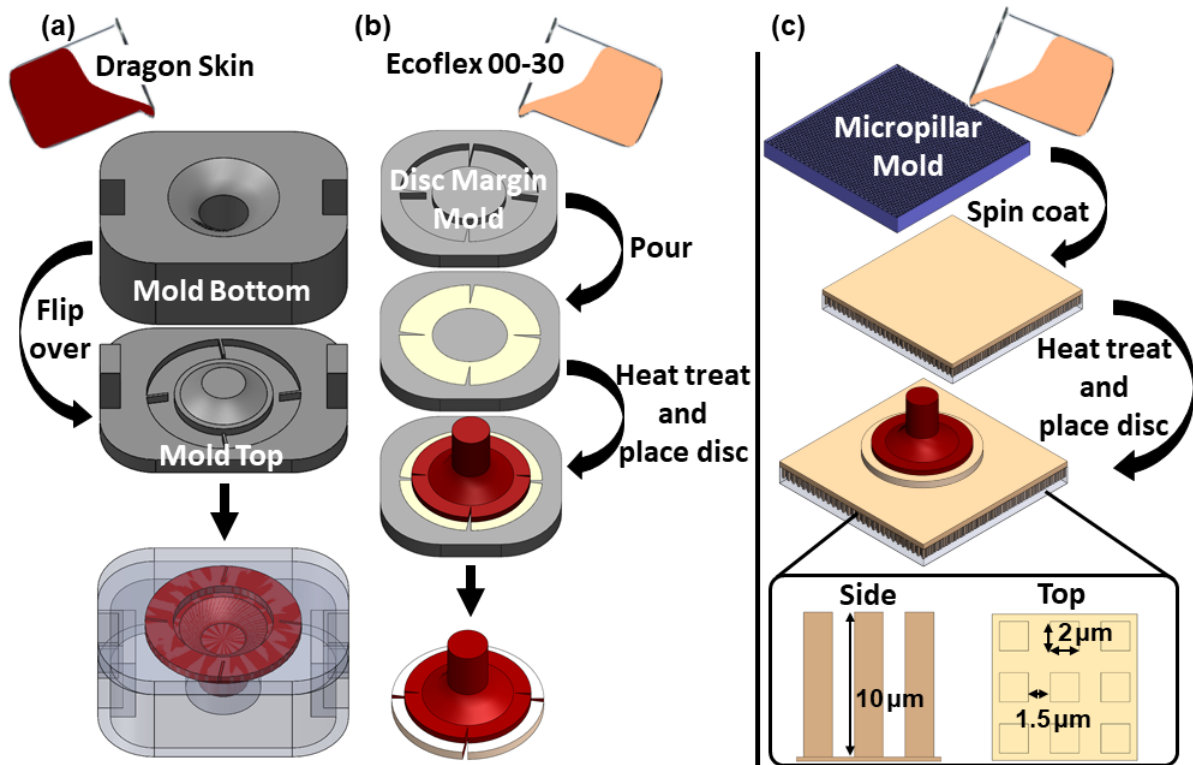
Figure 3.4: **Fabrication process of a suction disc.** **(a)** Stiff backing of the circular, radially slitted suction disc molded with DragonSkin 20 in custom, 3D-printed mold. **(b)** Soft layer of Ecoflex 00-30 added to stiff, radially symmetric backing in 3D-printed mold. **(c)** Fabrication of the micropillar array. Spin coat the mold for the micropillar array with silicone elastomer (either Ecoflex 00-30 or Dragon Skin 20). Place the suction disc to be coated in micropillars on heat-treated elastomer. Resulting micropillars are 2 μm squares with a height of 10 μm spaced 1.5 μm apart.

handles 8 mm in diameter, 10 mm in height to provide a gripping surface for a clamp during pull tests.

The suction chamber of each disc was 4 mm in depth, the walls of which were composed of Dragon Skin 20 (Dragon Skin 20, Smooth-On, Inc.) (Fig. 3.4). Molds of Dragon Skin were placed in a vacuum chamber for approximately 5 minutes to degas the silicone and then fully cured for 1 hour 30 minutes at 40ºC. Samples with a soft layer were coated with a 2 mm layer of Ecoflex 00-30 (Ecoflex 00-30, Smooth-On, Inc.). To apply the soft layer, a mold containing Ecoflex was partially cured at 40ºC for 3 minutes. The suction chamber composed of Dragon

Skin was then added to the partially cured mold of Ecoflex and set to cure for 1 hour at 30ºC.

Micropillars were fabricated using a mold provided by NASA Jet Propulsion Laboratory [94] by casting silicone elastomer (Ecoflex 00-30 or Dragon Skin 20) onto a wax mold with the microfeature geometry. The wax mold and silicone were spun at 800 rpm for 30 seconds and partially cured (40°C for 3 minutes). The remaining layers of the suction disc were then added on to the micropillar layer, and the entire assembly was cured at 40°C for 15 minutes.

3.3.3   Force measurements of biomimetic disc

We evaluated the performance of the suction discs on various surfaces using a mechanical testing system (3342, Instron Inc.; capacity 500 N; and 5965, Instron Inc.; capacity 5000 N) (Fig. 3.5 (a)-(c)). We then evaluated the performance of a commercially available suction cup (701477, Hillman Inc.; capacity 2.22 N, diameter 25 mm), to provide a comparison to the artificial suction discs. We chose a commercial suction cup with a diameter (and hence contact area) similar to our designs. We secured the suction discs to the mechanical testing setup by means of a clamp and pulled normally from a secured surface. All underwater trials occurred in a bath of tap water, bath depth 20 mm. All pull tests done in air were performed on dry surfaces. Suction discs were preloaded with 2 N, a force sufficient to collapse the chambers and generate subatmospheric pressure within the chambers when released. The load was held for <20 seconds prior to the start of the pull test. Pull tests were performed with a speed of retraction of 10 mm/s in triplicate for each substrate type.

To determine the effects of surface roughness on disc performance, experimental surfaces were fabricated with three textures: smooth (R_a = 0.2-1.2 μm [95]), moderate (grain size, 68 μm), and coarse (grain size, 269 μm) (Fig. 3.5 (d)-(f)). The smooth experimental surface was composed of a plate of acrylic. The rough experimental surfaces were fabricated by bonding sandpapers of grain size 269 μm (P60, 3M, Inc.) or grain size 68 μm (P220, 3M, Inc.) to an acrylic plate using an acrylic adhesive (VHB 4905, 3M, Inc.). Experimental textures were replaced
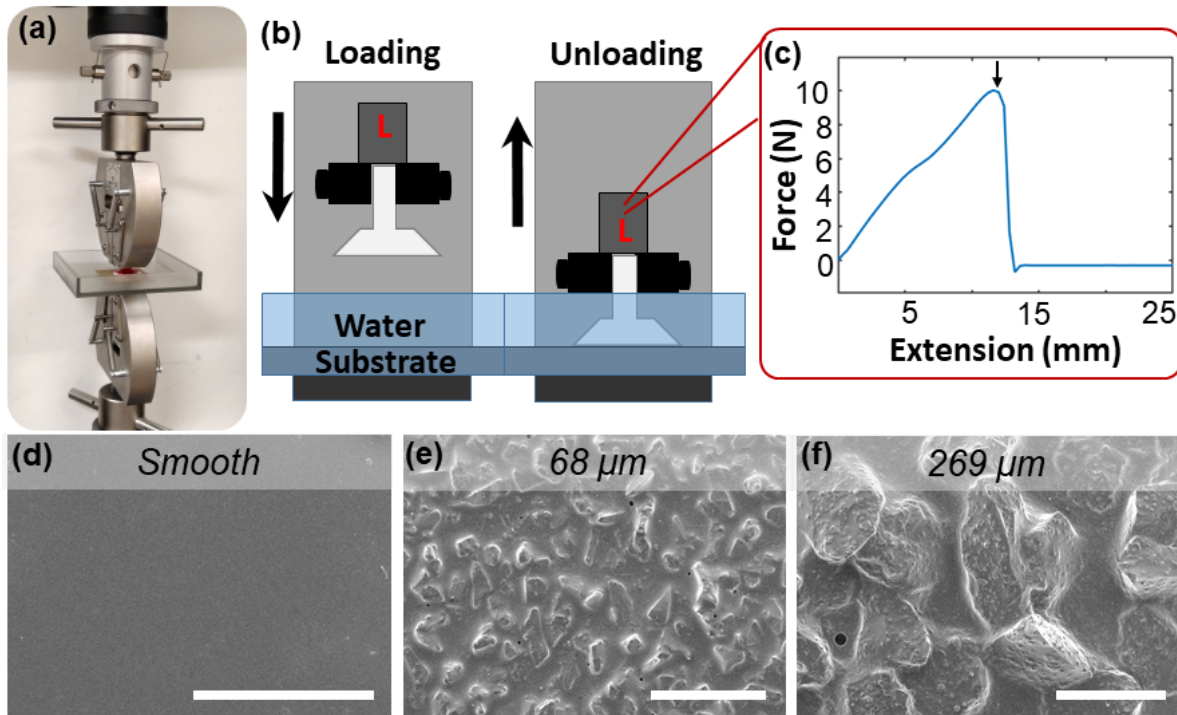
Figure 3.5: **Schematic depiction of adhesive force measurements using a mechanical testing system.** **(a)** Suction discs were secured in a clamp of a mechanical testing machine and engaged with a surface under a preload of 2 N. **(b)** Illustration of the loading and unloading of the suction disc. The force and displacement were recorded and used to calculate adhesive stress. Experimental surfaces were submerged in a bath of water for all underwater trials. **(c)** An example plot of force (N) and extension (mm) for the radially symmetric disc with a soft layer in disc margin. Arrow indicates maximum pull-off force achieved by the disc. **(d)** SEM micrograph of smooth experimental surface, scale bar 500 μm. **(e)** SEM micrograph of moderately rough (grain size, 68 μm) experimental surface, scale bar 500 μm. **(f)** SEM micrograph of coarse (grain size, 269 μm) experimental surface, scale bar 500 μm.

between disc trials.

The effect of surface concavity and convexity on disc performance was evaluated on smooth, semi-cylindrical surfaces (halved PVC pipes) of inner diameters: 60 mm, 48 mm, 41 mm, 25 mm, and 15 mm. Outer diameters of the PVC pipes were measured to be 70 mm, 58 mm, 50 mm, 33 mm, and 20 mm, respectively. To test adhesion of the disc to a rough, concave surface, an experimental surface was constructed by bonding sandpaper of grainsize 269 μm to the inner wall of a halved PVC pipe (41 mm diameter) using acrylic adhesive. All experiments involving

concave and convex surfaces were performed in triplicate and in a bath of water.

The effect of applying a preload was measured for both smooth and moderate (grain size, 68 μm) surface roughnesses using a mechanical testing system (5965, Instron Inc.; capacity 5000 N). Preloads of 0.5 N, 1.5 N, 2.0 N, 2.5 N, and 3 N were applied to the back of the suction disc prior to being pulled normal to the experimental surface. All trials occurred in a bath of fresh water and in triplicate per preload.
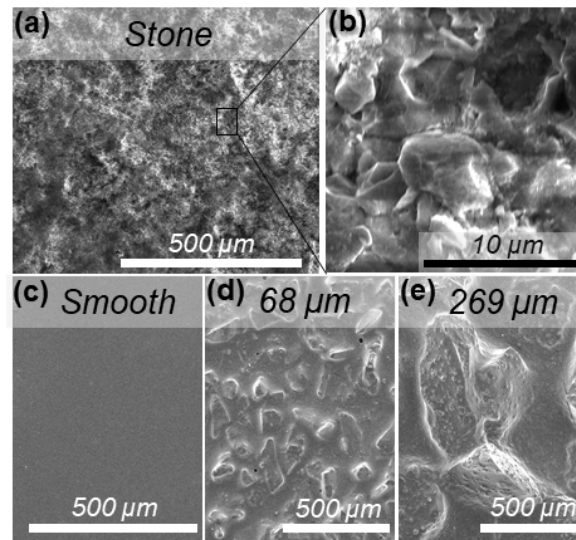
Figure 3.6: **Scanning Electron Microscopy (SEM) of stone surface used in longevity test.** **(a)** Micrograph of stone surface used in longevity experiments. Scale bar, 500 μm. **(b)** Enhanced zoom on micrograph of stone surface. Scale bar, 10 μm. **(c)** Micrograph of smooth experimental surface composed of acrylic, serves as comparison to stone surface. Scale bar, 500 μm. **(d)** Micrograph of experimental surface composed of sandpaper of moderate roughness (grain size, 68 μm). Scale bar, 500 μm. **(e)** Micrograph of experimental surface composed of sandpaper of coarse roughness (grain size, 269 μm). Scale bar, 500 μm.

3.3.4 Longevity of biomimetic disc

We evaluated the longevity of three suction disc types under various loads in air (Fig. 3.7 (a),(b)). Longevity tests were performed on (1) a radially symmetric disc with a soft layer and four slits, (2) a radially symmetric disc without slits and without a soft layer, and (3) a commercial suction cup. We pressed the discs to a smooth stone surface, to which we fixed a hook using epoxy.

45

The stone surface was water-worn, of low porosity, and rounded from weathering. Imaging with SEM provided a visual comparison of the stone surface to the experimental surfaces composed of sandpaper used during pull tests (Fig. 3.6 (a),(b)).
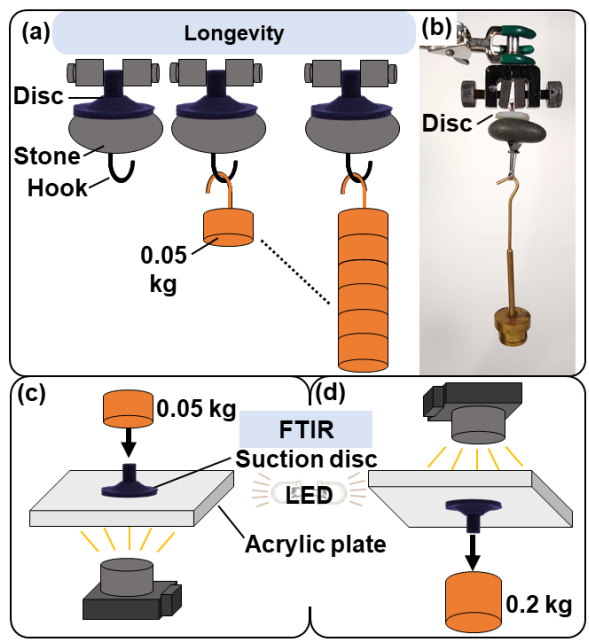
Figure 3.7: **Schematics of experimental setups for longevity and Frustrated Total Internal Reflection (FTIR). (a)** Schematic of the experimental setup for the longevity study. A suction disc (radial geometry, with soft layer and slits, without microstructures) adhered to a stone, and brass weights were added per trial to a hook attachment to increase the payload. Trials were timed and the payloads ranged between 0.82 kg to 0.482 kg. **(b)** Image of a suction disc adhered to the experimental payload (total weight in image: 0.282 kg). **(c)** Schematic of experimental setup for FTIR; the suction disc adhered to the imaging surface when a brass weight (0.05 kg) was applied to the back of the disc, resulting in a pushing force of 0.49 N. Imaged from below. **(d)** Schematic of second FTIR experimental setup in which a brass weight of 0.2 kg was used to pull the suction disc from the imaging surface, resulting in a pulling force of -1.96 N. Imaged from above.

We measured the diameters of protruding features on the stone surface to be between 1 and 5 μm. We measured the diameters of local depressions on the stone surface to range between 4 and 10 μm. The weight of the stone and hook totaled 82.5 g. We then increased the total payload every trial by adding brass weights to the hook of the stone. The trials were timed from the moment the loads were applied until the moment of failure, which occurred when the disc dropped the load. Discs remained undisturbed for the length of the trial. Experiments were run in

triplicate and monitored via webcam (640×360 pixels, frame captured every 20 s; Logitech, Inc.).

3.3.5   Contact area measurement
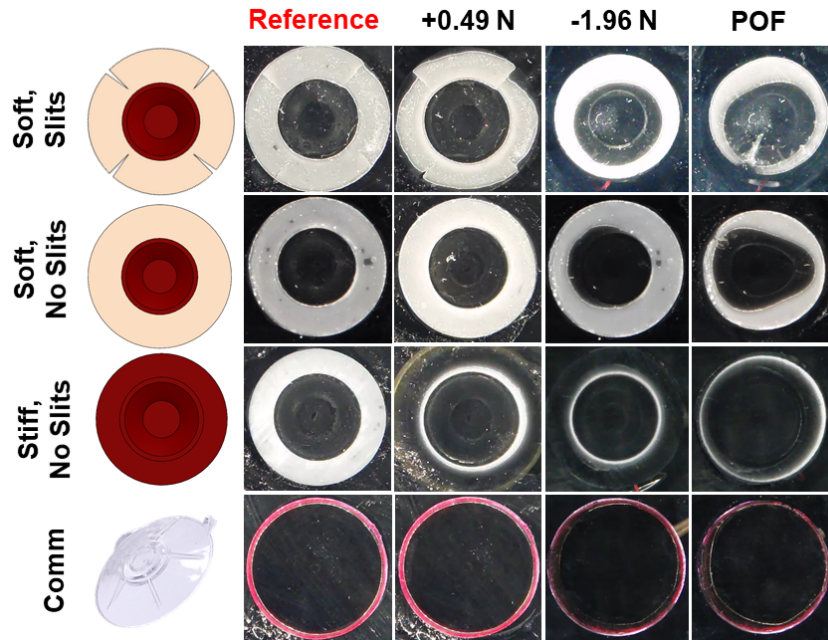
Figure 3.8: **Original images from Frustrated Total Internal Reflection (FTIR).** Original images from FTIR, prior to image processing. Disc at rest ("Reference"). A load of 0.05 kg was applied to push the disc to the imaging surface ("+0.49 N"). A load of 0.2 kg was applied to pull the disc from the imaging surface ("-1.96 N"). The point of failure ("POF") was the moment prior to failure of the disc. FTIR used to evaluate footprints of three radially symmetric discs and commercial suction cup ("Comm").

We measured the contact area of the disc to a surface using Frustrated Total Internal Reflection (FTIR). The setup for FTIR experiments was custom-built [96] (Fig. 3.7 (c),(d)). The station was constructed with a 3D printed mount, 9.7 mm thick acrylic, and natural white LEDs (3528-24VDC, Super Bright LEDs, Inc.). The light emitted from the diodes was internally reflected within the acrylic. The acrylic was wetted with water during wet trials. To visualize the contact area, the suction discs were dyed black using silicone pigment (Silc Pig, Smooth-On, Inc.) during the molding process. Contact with the acrylic plate allowed light to escape from the surface of the acrylic, which was then imaged with a camera (1280×780 pixels, 140 pixels·cm^{-1},

40 frames per second; EXILIM EX-FH25, Casio Computer Co., Ltd.).

The discs were either pushed or pulled from the imaging surface. Loads were applied by brass weights to the backing of the suction disc. A load of 0.05 kg applied to the back of a disc generated a force of 0.49 N to push the disc to the imaging surface. A load of 0.2 kg applied to the back of the disc generated a force of 1.96 N to pull the disc from the imaging surface. Discs were then pulled manually to the point of failure (*POF*). We considered the last frame of the suction disc in contact with the imaging surface to be the POF.

The images from FTIR were post-processed by increasing the contrast by 100% and sharpness by 10% and reducing the brightness by 20%. The color temperature of the image was also set to 1500 K. The original images are provided in the supplemental materials (figure S2).

3.3.6   Finite Element Analysis of disc

To understand the effect of incorporating slits in the disc margin on the total strain energy and stress distribution, we performed Finite Element Analysis (FEA) on two disc types, one with and one without radial slits (both without a soft layer). We measured the equivalent stress and total strain energy of the system subject to a constant vertical compression of 2 mm (Fig. 3.9 (a)). We selected the vertical displacement to be 2 mm, or half the height of the suction chamber, suggesting that the deformation simulated in FEA would be analogous to evacuating half of the suction chamber to engage with a surface.

Finite Element Analysis was conducted and analyzed using ANSYS 19.2. We experimentally determined the material properties of DragonSkin 20 by performing a tensile test using a mechanical testing setup (3342, Instron Inc.). The data was best fit to the Yeoh 3rd order hyperelastic model. Parameters for the model (C10, C20, C30, D1, D2, D3) were 99161 Pa, -1604 Pa, 1065.2 Pa, 0 Pa^{-1}, 0 Pa^{-1}, and 0 Pa^{-1}, respectively.

We used 20-node Brick elements to mesh the suction disc model (Fig. 3.9 (b)). The FE model had 2698 and 2634 elements for the case with slits and without slits, respectively. Element
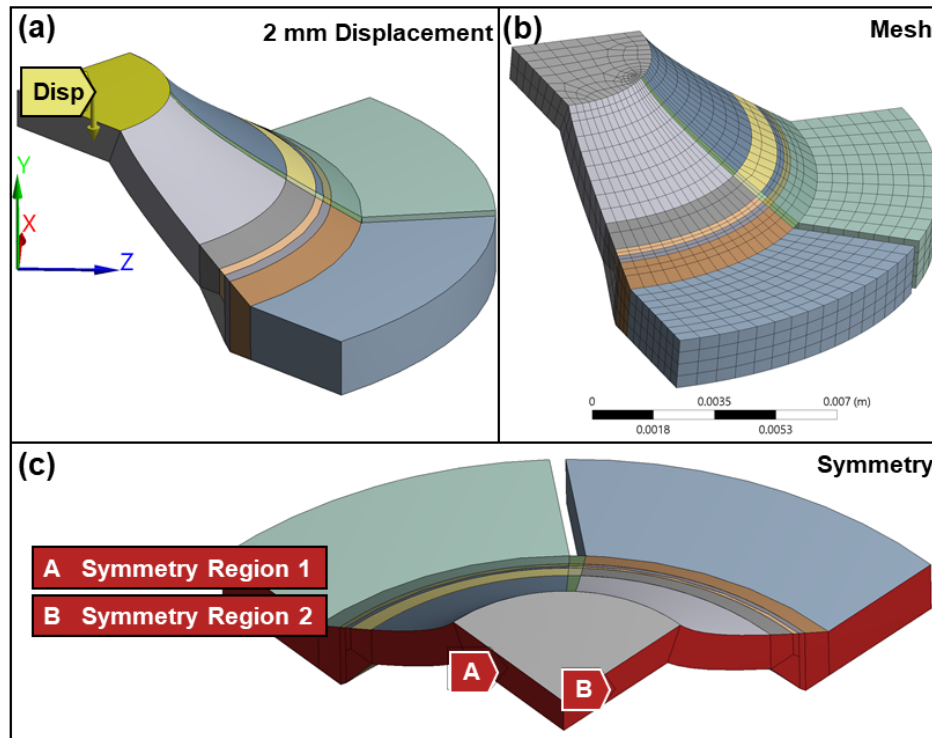
Figure 3.9: **Setup of Finite Element Analysis (FEA) of a suction disc. (a)** Representation of a 2 mm displacement ("Disp") on the back of the suction disc. **(b)** Representation of the 20-node Brick elements used to mesh the model of the suction disc. **(c)** Representation of the regions of symmetry specified in the FE model geometry. Two regions of symmetry are shown, labeled "A" and "B". Due to symmetry, the suction disc was modeled as a quarter of a suction disc to reduce time for computation.

shapes with an aspect ratio close to one are highly desirable in FE analysis for better accuracy and convergence. In our FE model for all cases, more than 60% of the total elements had an aspect ratio between one to two. The average aspect ratio of the elements was 2.87 ± 1.08, while the average skewness was 0.194 ± 0.14.

Due to radial symmetry of the design, we chose to model a quarter of the suction disc in FEA to reduce time required for computation (Fig. 3.9 (c)). The total strain energy of the quadrant was multiplied by 4 to represent the entire disc. We did not account for surface energy, friction, or vacuum and neglected the contribution of a soft layer in the simulation. We varied one boundary condition of constraining deformation of the disc margin in the axial direction. The

surface was assumed to be frictionless. A constant, 2 mm displacement in the axial direction was imparted on the back of the suction chamber. We compared the results for deformation, Von-Mises stress, and elastic energy from each case.

3.4 Results

3.4.1 Adhesion mechanisms of the clingfish suction disc

The clingfish has an impressive grip when subject to normal loads, yet the same is not true for tangential forces. Manipulations of a euthanized clingfish demonstrated that the suction disc does not resist shear motion when moved across a glass slide using dissection forceps (Movie S1). However, when pulled perpendicular to the surface of the glass slide, the euthanized clingfish resisted the axial load, thereby causing the glass slide to lift from the benchtop. Using image processing of brightfield micrographs of the suction disc of a clingfish, we calculated that the disc margin accounts for about 65% of the total suction disc footprint of the clingfish (Fig. 3.2 (a)).

When a fractured edge of a papilla was imaged under SEM, one can observe that densely-packed, presumably soft fibrils emanate from channels (0.25 μm diameter, at a spacing of 0.02 μm) (Fig. 3.2 (d)). Fibrils shown in SEM micrographs lack a consistent orientation, contrary to other adhesive structures seen in nature for other organisms, such as the directional setae of the gecko [31, 5].

The soft fibrils increase the frictional footprint of the clingfish by conforming to surface asperities. By doing so, the fibrils resist an inward slip of the disc margin and seal the suction chamber. Suction and friction are two methods of attachment that act in combination to successfully adhere the clingfish to rough substrates (Fig. 3.2 (b)).
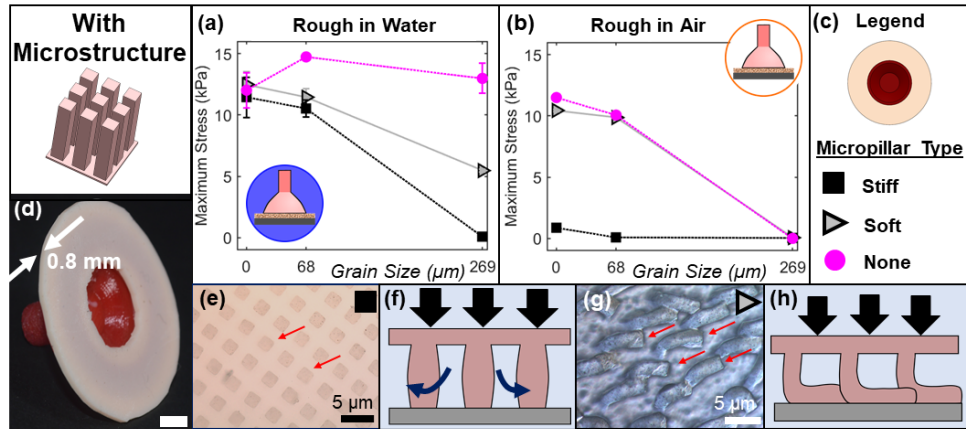
Figure 3.10: **Maximum adhesive stress for discs with micropillars on rough surfaces. (a)** Discs with micropillars, average (n=3; ± Std Dev) maximum adhesive stress across flat surfaces of roughnesses: 0 μm, 68 μm, and 269 μm, in water. **(b)** Discs with micropillars, average maximum adhesive stress across flat, rough surfaces in air. **(c)** Legend containing schematic of prototype body geometry (radially symmetric, with a soft layer, without slits). Prototypes vary by presence and material stiffness of micropillars. Disc with micropillars composed of stiff silicone, dark square. Disc with micropillars composed of soft silicone, grey triangle. Disc without micropillars, pink circle. **(d)** Image of a suction disc with a layer of micropillars; arrows indicate the disc margin thickness, which was measured to be 0.8 mm. Scale bar, 5 mm. **(e)** Brightfield micrograph of top view of micropillars composed of stiff silicone, subject to a glass slide sheared parallel to the surface. Arrows indicate individual micropillars, shown with a square cross-section. **(f)** Illustration of stiff micropillars allowing fluid to pass between columns. Vertical arrows illustrate a force exerted on the micropillars. Curved arrows illustrate the passage of fluid in between micropillars. **(g)** Brightfield micrograph of top view of micropillars composed of soft silicone, subject to shear force. Arrows indicate individual micropillars, which bend when subject to external force. **(h)** Illustration of soft micropillars deforming and intermeshing when subject to a load. Load indicated by vertical arrows.

3.4.2   Performance of the micropillars

We compared the effect of micropillars and their stiffness on the adhesive capabilities of the suction disc to flat, rough surfaces both in air and underwater. To quantify the effect on adhesion, we measured the maximum adhesive stress (σ; $\sigma = F_{ad}/A$, where F_{ad} represents the maximum pull-off force, and A represents the surface area of the biomimetic disc) to evaluate adhesion of the suction disc on three types of surface roughnesses – smooth (R_a = 0.2-1.2 μm [95]), moderate (grain size, 68 μm), and coarse (grain size, 269 μm).

In air and underwater, the best performing suction disc with microstructures was covered

51

with soft micropillars (12.4±1.1 kPa smooth, 11.4±0.7 kPa moderate, 5.5±0.1 kPa coarse, wet; 10.4±0.1 kPa smooth, 9.9±0.1 kPa moderate, dry) (Fig. 3.10 (a), (b)). Suction discs with micropillars composed of the stiffer silicone failed to adhere to the dry surfaces, regardless of surface roughness. Additionally, on submerged surfaces of a coarse roughness, the suction discs with soft micropillars were capable of adhering to the testing surface whereas those with stiff micropillars were not.

We imaged the micropillars and observed how they behaved when subject to load. We pressed a glass slide atop the micropillars to observe their deformation. The micropillars composed of stiffer silicone deformed less when subject to a compressive and shear load (Fig. 3.10 (e),(f)). The micropillars composed of softer silicone were visibly able to bend and fold to the glass slide (Fig. 3.10 (g),(h)). When a shear load was not applied, the micropillars of soft silicone would clump and bundle. We concluded that the pillars of soft silicone intermeshed together to better seal the perimeter, in comparison to the pillars of stiff silicone.

However, for moderate and coarse surfaces in water, the best performing suction discs with soft micropillars performed 1.3 and 2.4 times worse, respectively, in comparison to the suction disc without micropillars (Fig. 3.10 (a),(b)). Thus, we found that for both of these designs, the microstructures reduced the performance of the suction disc when compared to its analog without microstructures.

3.4.3 Adhesion without micropillars to rough substrates

Using suction discs without micropillars, we evaluated the effect of body geometry and slits on how they impact adhesion to rough surfaces. All three clingfish-inspired suction discs with a soft silicone disc margin outperformed commercial suction cups on rough surfaces both in and out of the water. In air, the biomimetic disc supported dynamic loads up to roughly 305 times its weight (2.3 g disc; 0.7 kg load, brass weights) (Fig. 3.11 , Movie S2).

On flat, rough underwater surfaces, the circular suction disc with radial slits and a soft
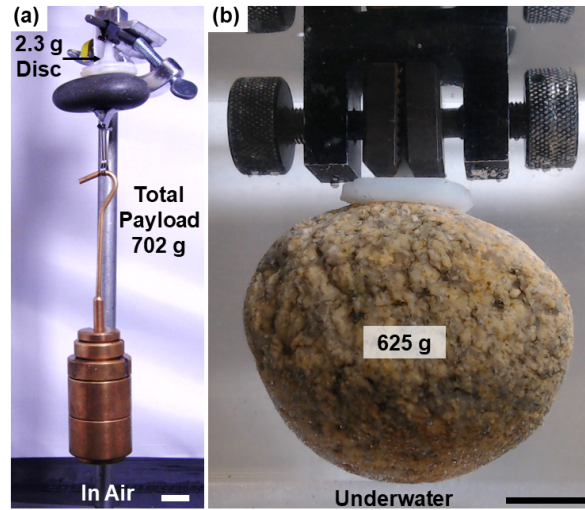
Figure 3.11: **Demonstration of a suction disc supporting a payload. (a)** A suction disc with soft layer, with slits shown attached to river stone suspended in air. Brass weights were added to the stone. The maximum payload weight supported (stone and brass weights) was 702 g. The suction disc weight was 2.3 g. **(b)** A suction disc with a soft layer and slits adhered to granite payload, 625 g, suspended in water. Scale bars, 20 mm.

layer outperformed all other prototypes and a commercially available suction cup (Movie S3). In our underwater trials, this top-performing suction disc achieved adhesive stresses of 13.7±0.4 kPa (smooth), 18.3±0.4 kPa (moderate), and 14.3±1.4 kPa (coarse) (Fig. 3.12 (a)). By comparison, while the commercially available suction cup achieved a high adhesive stress on smooth surfaces (63.6±2.3 kPa), it performed poorly on rough surfaces, reaching 2.8±0.3 kPa on a moderate roughness. The commercial suction cup failed to adhere to the coarse surface.

Conversely, in air, a circular disc with a soft layer and without slits outperformed (10.1±0.2 kPa) all other prototypes and a commercially available suction cup on dry surfaces of a moderate roughness (Fig. 3.12 (b)). Despite being the top performing design in the underwater trials, the disc with slits showed weaker adhesion in the dry trials, with a roughly 1.6 times decreased (6.2±0.2 kPa) suction ability as compared to the discs with a continuous soft layer. The commercial suction cup failed to adhere to both moderate and coarse surfaces in air. All the suction discs tested failed to adhere to coarse surfaces in air.

The disc geometry affected adhesion capabilities in both wet and dry trials; the radially
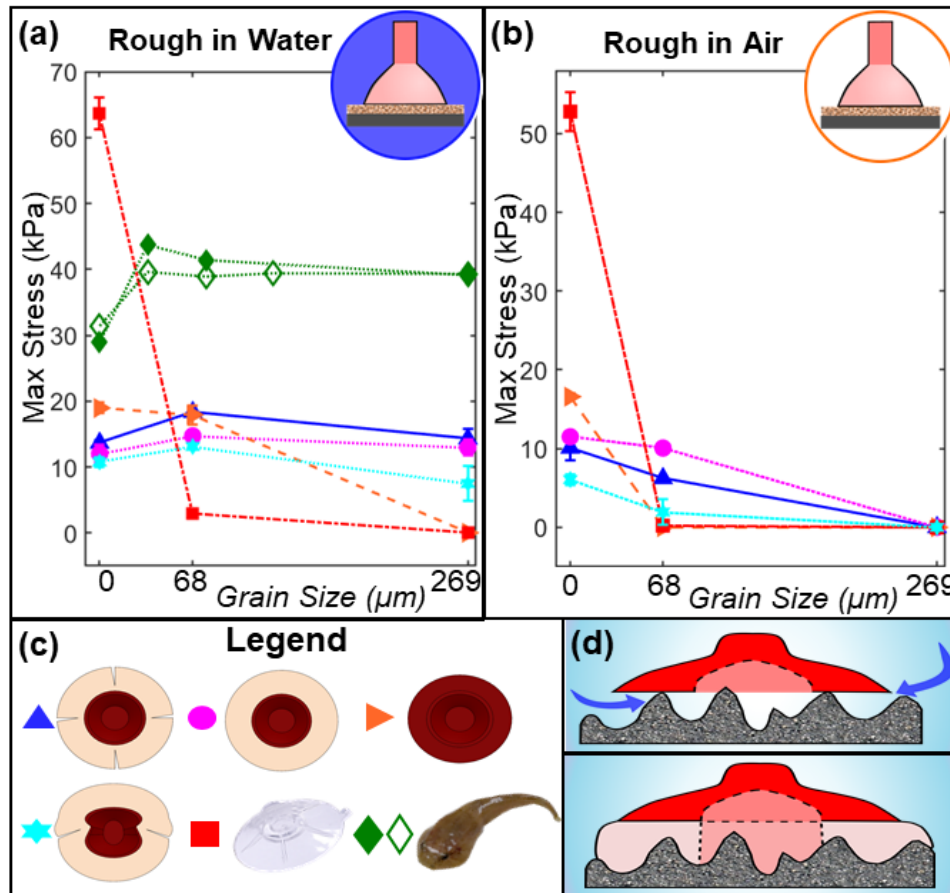
Figure 3.12: **Adhesion to rough surfaces of discs without micropillars.** **(a)** Disc without micropillars, average (n=3; ± Std Dev) maximum adhesive stress across flat, rough surfaces in water. **(b)** Disc without micropillars, average maximum adhesive stress across flat, rough surfaces in air. **(c)** Legend containing schematics of prototypes (bottom view) and their corresponding symbol within the adhesive stress curves. Soft layer of Ecoflex (light colored), stiff silicone backing of suction chamber (dark colored). Suction disc variants (no micropillars): Radially symmetric with four slits and soft layer (blue triangle); Radially symmetric with soft layer and without slits (pink circle); Radially symmetric with stiff disc margin (orange triangle); Bilaterally symmetric with soft layer (light blue star); Commercially available suction cup (red square). Clingfish adhesive stress, median values shown, data from Wainwright *et al.* 2013 [52] (solid green diamond), data from Ditsche *et al.* 2014 [53] (white diamond). **(d)** Schematic of the effects of the soft layer in the disc margin on sealing to surface irregularities. Stiff backing (dark colored), soft silicone (light colored).

symmetric disc geometry achieved adhesive stresses about 1.9 times stronger underwater and about 5.2 times stronger in air than the bilaterally symmetric disc on rough surfaces.

The presence of a soft layer in the disc margin improved adhesion capabilities in both wet and dry trials. To understand this effect, we compared the performance of the circular suction discs, both without slits and with and without a soft layer. The stiff disc achieved higher adhesive stresses on smooth surfaces (18.9± 0.8 kPa, wet; 16.6± 0.4 kPa, dry), in comparison to the disc with a soft layer (12.0±1.4kPa, wet; 11.5± 0.2 kPa, dry). However, while a stiff disc margin enhanced performance on smooth surfaces, it compromised performance on textured surfaces. For instance, the prototype with a soft layer in the disc margin achieved an adhesive stress of 13.0±1.2 kPa on a coarse surface underwater, while the prototype with a stiff disc margin failed to adhere. The stiff disc performed 6.4 times better than the commercial suction cup at a moderate surface roughness under water, as the material of the stiff suction disc was still more compliant than the commercial suction cup. Thus, the stiffer the material in contact with a surface, the less effectively it can conform to irregularities and maintain the suction chamber sealed (Fig. 3.12 (d)).

3.4.4 Adhesion to irregular shapes

Much like the intersection of the pelvic and pectoral fins of the clingfish, slits in the disc margin of the biomimetic discs provided a geometric compliance to the body. Slits thereby impacted the adhesive performance of the disc to irregular shapes. We measured adhesive stress of the disc to concave and convex surfaces, normalizing the radius of curvature of the surface by the radius of the suction disc (ρ; $\rho = R_{surface}/R_{disc}$, where $R_{surface}$ represents the radius of curvature of the surface, and R_{disc} represents the radius of the suction disc). To understand the effect of slits on adhesion to irregular surfaces, we performed experiments on only the radially symmetric suction discs, which removed the effect of body geometry on adhesive performance.

The artificial suction disc with four slits and a soft layer outperformed all other prototypes
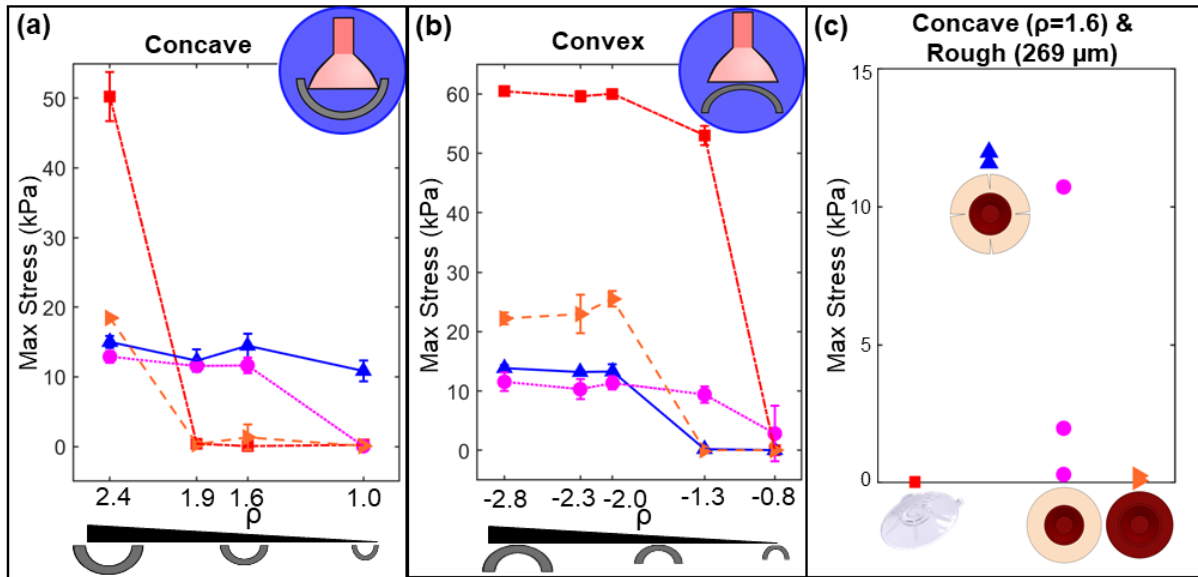
Figure 3.13: **Adhesion to irregular shapes of discs without micropillars. (a)** Disc without micropillars, average (n=3; ± Std Dev) maximum adhesive stress across concave surfaces, underwater. Concavity represented as the dimensionless ratio (ρ) of radius of curvature of the surface to the radius of suction disc. Suction disc variants (no micropillars): Radially symmetric with four slits and soft layer (blue triangle); Radially symmetric with soft layer and without slits (pink circle); Radially symmetric with stiff disc margin (orange triangle); Commercially available suction cup (red square). **(b)** Disc without micropillars, average maximum adhesive stress across convex surfaces, underwater. **(c)** Adhesive stress of suction discs to a rough (grain size, 269 μm), concave ($\rho = 1.6$) surface, underwater. Three trials were performed per disc type.

and the commercial suction cup on concave surfaces with small radii of curvature ($\rho < 1.9$) (Fig. 3.13 (a)). The disc with slits performed consistently across all tested concavities, with an average adhesive stress of 13.2±1.9 kPa across all four surfaces. Slits improved performance about 1.24 times on moderate (ρ=1.6) surface concavities. Slits coupled with a soft layer in the disc margin adhered to the smallest surface concavity (ρ=1.0) (Movie S4), with an adhesive stress of 10.9±1.5 kPa, while all other disc prototypes and the commercial suction cup failed to adhere. All suction discs were unable to adhere to a surface concavity of ρ=0.6, as the suction discs were too large for the radius of curvature and were physically unable to fit within the pipe to create a sealed chamber of subambient pressure. Overall, we observed that slits provided a geometric compliance that resulted in the capability to better conform and seal to concave surfaces.

We also observed that the soft layer in the disc margin aided in adhesion to concave surfaces. The soft silicone layer yielded adhesion strengths of 11.6±0.6 kPa (ρ=1.9) and 11.7±1.2 kPa (ρ=1.6), greatly outperforming the disc with a stiff disc margin, which failed to adhere to the moderate surface concavities. The stiff suction disc and commercial cup both lost all adhesive capabilities, at moderate concavities (ρ=1.6). We therefore concluded that the soft silicone filled gaps between the suction chamber and concave surface, improving adhesion performance.

We observed that the soft layer in the disc margin reduced adhesive capabilities of the suction disc to convex surfaces for all but the smallest radii of curvature ($|\rho| < 1.3$) (Fig. 3.13 (b)). Slits also reduced adhesion to convex surfaces with a small radius of curvature, observed when comparing the performance of discs with and without slits (0.2±0.2 kPa, 9.4±1.4 kPa, respectively; ρ = -1.3).The stiffness of the disc margin was observed to be most influential to adhesive strength for discs on convex surfaces. The commercial suction cup and stiff suction disc were able to withstand greater pull off forces on larger surface convexities ($|\rho| > 2.0$) in comparison to the discs with a soft disc margin. A threshold convexity, or a convexity at which the discs failed to adhere, was observed as an abrupt decrease in performance, occurring at moderate convexities (ρ = -2.0) for the radial disc with slits and for the disc without a soft layer, and at higher convexities for the commercial suction cup (ρ = -0.8).

Coupling concavity and surface roughness, we tested adhesion of the disc to a rough (grain size, 269 μm), concave (ρ = 1.6) surface (Fig. 3.13 (c)). The radial suction disc with a soft layer and slits (no microstructures) achieved consistently higher adhesive stresses (averaged to 11.7±0.2 kPa) in comparison to the commercial suction cup and the suction discs without slits (one with and one without a soft layer). The stiff discs were unable to adhere across the trials. The disc with a soft layer and without slits was less consistent in its performance, achieving adhesive stresses ranging from 0.3 kPa to 10.7 kPa. We attribute part of the inconsistent performance to the absence of slits from the disc with a soft layer, suggesting that the disc was less able to radially expand when pressed to the surface due to the rough texture. The disc without slits would

therefore be less able to fill the gaps caused by the concave surface due to the rough texture. The consistency and high adhesive stresses resulting from the disc with a soft margin and slits led us to conclude that this design performed best for rough, concave surfaces in comparison to all other prototype designs.
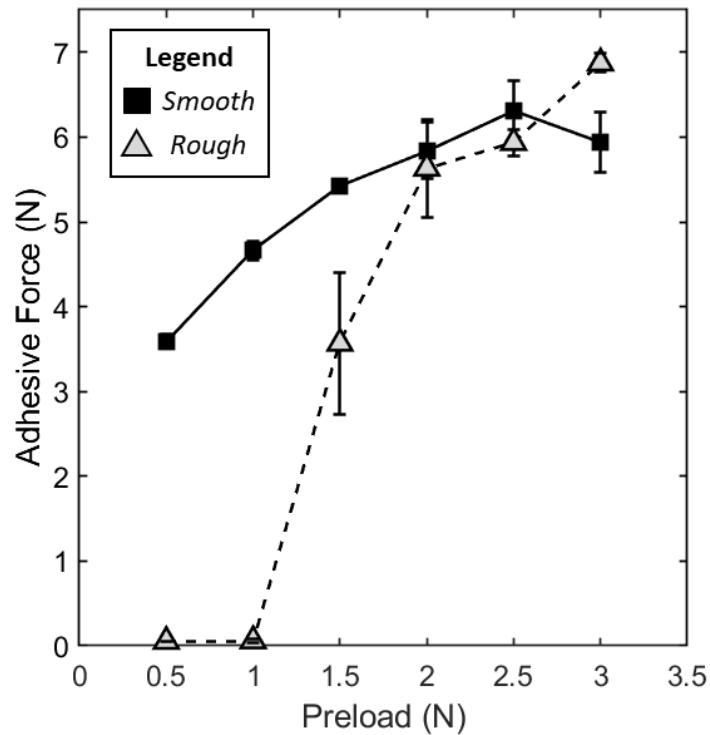
Figure 3.14: **Adhesive force based on preload and surface roughness.** Average (n=3; ± Std Dev) force of adhesion of a disc (radially symmetric, soft layer, no slits, no microstructures) for a range of preloads. Trials performed on a smooth surface represented as dark squares. Trials performed on a rough surface (grain size, 68 μm) represented as light triangles.

3.4.5 Effect of preload on adhesive performance

A minimum preload was required to initiate attachment of the suction disc to experimental surfaces. To smooth surfaces, preloads of 0.5 N were capable of initiating attachment and resisting 3.6±0.1 N of pull of force until separation from the surface (Fig. 3.14 (a)). However, the adhesive performance of the suction disc seemed to stabilize around 5.8±0.3 N given a preload of 2 N.

Conversely, for moderately rough surfaces (grain size, 68 μm), a minimum preload of 1.5 N was required to attach the disc to the experimental surface, generating an adhesive force of 3.6±0.8 N (Fig. 3.14 (b)). Applying a preload of 1.5 N yielded an inconsistent adhesive performance, resulting in an inability to adhere to the moderately rough experimental surface in some instances. Increasing the preload to 2 N increased the adhesive force of the suction disc to 5.6±0.6 N, and allowed for reliable and consistent adhesion to the experimental surfaces. Overall, the minimum preload required for attachment of the suction disc was higher for rougher surfaces.
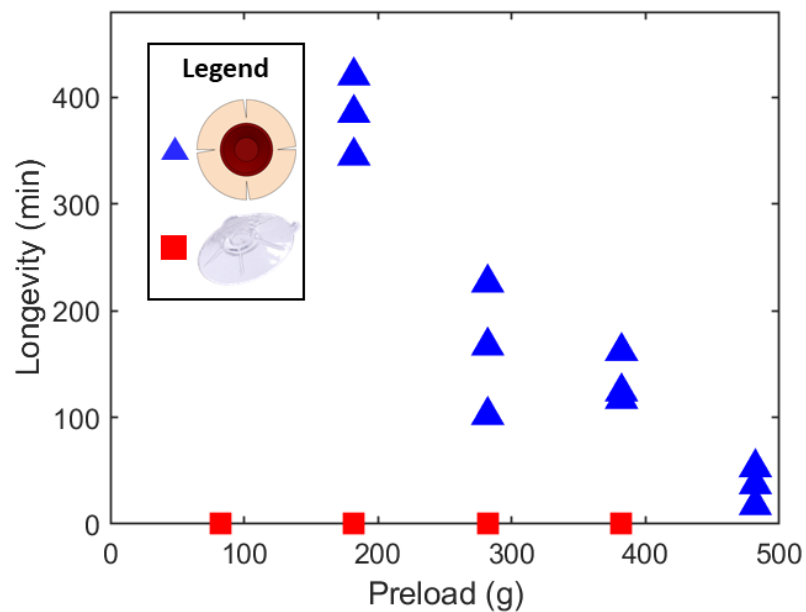
Figure 3.15: **Longevity of a disc bearing a payload.** Timed trials of longevity (minutes) of suction discs supporting a payload (g). The results shown in the plot were for the radially symmetric disc with four slits and soft layer (blue triangle) and the commercially available suction cup (red square). The radially symmetric disc without a soft layer was also tested but unable to adhere

3.4.6 Longevity of biomimetic disc

We performed longevity tests on 1) a suction disc with a soft layer and four slits, 2) on a suction disc without a soft layer, and 3) on a commercial suction cup. The suction disc with a soft

layer and four slits greatly outperformed the suction disc without a soft layer and the commercial suction cup (Fig. 3.15). The suction disc without a soft layer was unable to support any of the tested payloads. The commercial suction cup was consistently able to attach to the payloads for only about 1 second across all trials and payloads. The successful suction disc (radially symmetric with a soft layer, without microstructures, without slits) was successful at attaching to all payloads tested. Payloads of 182 g, 282 g, 382 g, and 482 g were supported for an average time of 383±38 min, 165±62 min, 134±24 min, and 35±18 min, respectively, by the suction disc with a soft layer and four radial slits. Therefore, the suction disc with a soft layer and slits was capable of maintaining adhesion for a significantly longer duration of time, in comparison to the stiff suction disc and the commercial suction cup.

3.4.7 Visualizing surface contact of discs

We used a contact imaging technique based on Frustrated Total Internal Reflection (FTIR) to visualize how the different suction disc designs interacted with a wet surface when subject to external loads during adhesion. All suction discs used in FTIR did not have micropillars lining the margin. For each load, we measured the area of the disc margin in contact with the imaging surface and normalized it to the total surface area of the suction disc of the reference image.

A stiff disc margin resulted in a low effective area of contact to the wetted imaging surface (Fig. 3.16, third row from the top). When applying a load of 0.05 kg to adhere the stiff disc to the imaging surface, the outer margin of the disc raised off the surface, resulting in an inverted configuration (Fig. 3.18 (c)), and significantly reducing the area in contact with the imaging surface (down to 12% of the total area under the disc, from 59% in the unloaded state). When pulling on the adhesive disc without a soft layer with a load of 0.2 kg normal to the imaging surface, the disc reverted from the inverted configuration, but maintained a small footprint (Fig. 3.16, third row from the top). The area in contact remained at 8% but then shifted radially to the outer perimeter when the disc was pulled to failure. As a result, the stiff adhesive disc without
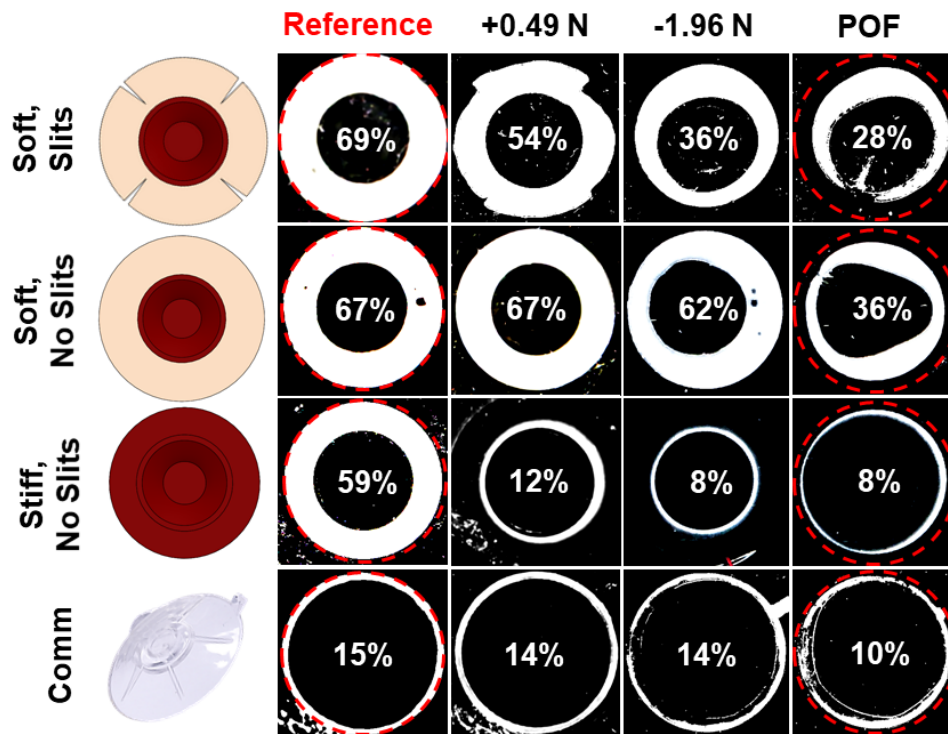
Figure 3.16: **Representative FTIR images of disc footprint.** Disc at rest ("Reference") when placed upon the wetted imaging surface. A load (0.05 kg) was applied to push the disc to the imaging surface ("+0.49 N"). A load (0.2 kg) was applied to pull the disc from the imaging surface ("-1.96 N"). The point of failure (*POF*) was the moment prior to failure of the disc. The dashed circular lines in POF represent the initial size of the disc in the reference state. The percentages are calculated from the area of contact of the disc per load normalized to the total disc area measured in the reference frame. FTIR used to evaluate footprints of three radially symmetric discs and commercial suction cup ("Comm").

a soft layer had about 4.5 times smaller effective contact area at the moment prior to failure, in comparison to those with a soft layer. Furthermore, the commercial suction cup also maintained a small area of contact, ranging from 15% at rest to 10% at the moment prior to failure (Fig. 3.16, bottom row). Thus, in general a stiffer material resulted in a smaller effective area of contact with the imaging surface.

Conversely, the disc with a soft layer had a larger contact footprint both when pushed to and pulled from the wetted surface. The disc margin of the prototype without slits and with a soft layer remained in full contact with the imaging surface when pushed and only experienced

a 5% reduction in contact when pulled (-1.96 N; Fig. 3.16, second row from the top). At the moment prior to failure, we observed that about 36% of the disc margin remained in contact with the surface. The soft layer provided a relatively larger effective area of contact with the imaging surface, thereby increasing the frictional footprint of the biomimetic disc.

The presence of slits also affected the disc footprint during adhesion. The outer perimeter of the disc with slits lifted when the disc was pushed onto the wet imaging surface (Fig. 3.16, top row). When pulled from the surface, the disc margin changed from this flared state with a discontinuous perimeter to a closed, continuous perimeter. We hypothesize that the transition between discontinuous to continuous disc margin provides the opportunity to "regrip" surfaces when pulled. Additionally, when a 0.2 kg load was applied, the percentage of the total area under the disc in contact with the surface reduced by roughly 33% in comparison to its reference. By contrast, the disc without slits only experienced a <5% reduction in contact area.
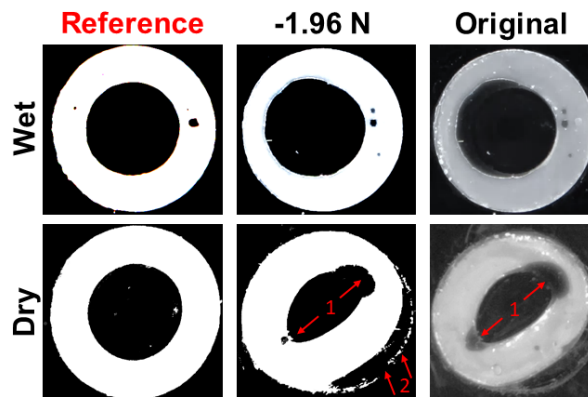
Figure 3.17: **Surface contact of a disc on wet and dry surfaces.** Disc (with soft layer, without slits) at rest ("Reference") when placed upon the imaging surface. A load was applied to pull the disc from the imaging surface ("-1.96 N"). Surface contact visualized with FTIR. Original, preprocessed image shown for the disc loaded with -1.96 N ("Original"). (row 1) Surface contact of the suction disc on a wet surface. (row 2) Surface contact of the disc on a dry surface. Arrows distinguish (1) a cavity formed inside of the suction disc, and (2) residue from the silicone denoting the original footprint of the disc margin prior to loading.

We compared the surface contact of one disc (with a soft layer, without slits) on dry and wetted imaging surfaces (Fig. 3.17). The disc was pulled with a force of -1.96 N in both

cases. On a wet imaging surface, the perimeter of the suction disc remained circular. On a dry imaging surface, the disc elongated to an ellipse. We concluded that this elongation was caused by the anchoring of the disc margin to the dry acrylic plate. In the process of elongation, a cavity was formed along the major axis of the ellipse. The elongation of the disc would result in the propagation of the cavity which could inevitably compromise the seal of the disc. We concluded that the suction disc on a wet surface was better able to prevent elongation due to the presence of a thin fluid film between the disc and the imaging surface.

3.4.8   Modeling geometric compliance

Finite Element Analysis (FEA) on two disc types, one with and one without radial slits (both without a soft layer), provided insight on how incorporating slits in the disc margin affected stress and strain energy of the total system. We measured the equivalent stress and total strain energy of the system subject to a constant vertical compression of 2 mm representing the displacement applied to engage the adhesive disc (Fig. 3.18 (a),(b)). The total strain energy is the mechanical energy that is stored reversibly within the elastic material [97]. A greater total strain energy stored within the body corresponds to higher internal stresses that attempt to restore the original shape. We assume that the primary effect of these stresses during compression onto a flat surface is to resist the compression, which negatively impacts adhesion. Thus, these predictive models allow us to better understand the impact of design parameters on the total strain energy of a system, which affects the adhesive performance of a disc when subject to deformation.

For the simulation, we only considered the effects of deformation to the stiff backing, as the structural integrity of the stiff suction chamber significantly influenced the ability to maintain subambient pressure within the disc. We axially constrained deformation of the disc margin in two of the four simulations. By constraining the disc, we modeled the elastic energy that was stored within the system due to deformation. As modeled under the condition of constrained axial deformation at the disc margin, the total strain energy of the disc with slits (632 μJ) was lower
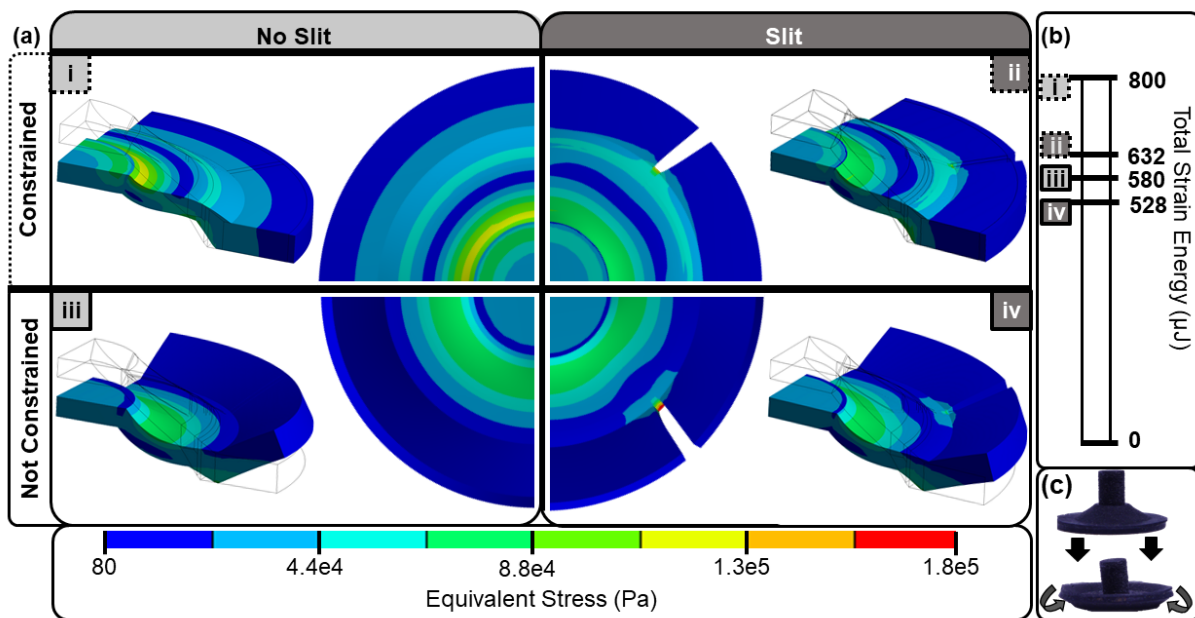
Figure 3.18: **Finite Element Analysis to understand disc behavior when subject to vertical compression. (a)(i-ii)** Simulation of equivalent stress (Pa). Axial displacement of disc margin was constrained in simulation for no slit and slit conditions, respectively. **(iii-iv)** Representation of equivalent stress (Pa). Axial displacement of disc margin was unconstrained for no slit and slit conditions, respectively. Scale bar consistent. **(b)** Total strain energy (μJ) calculated per trial. **(c)** Demonstration of the outer perimeter of the suction disc lifting from a surface, resulting in an inverted configuration.

than that of the disc without (800 μJ), when subject to vertical compression (Fig. 3.18 (b)).

In the simulation that allowed for axial displacement in the perimeter of the disc, it lifted, congruent with what was observed in experimental trials (Fig. 3.18 (c)). The disc without slits experienced about a 28% reduction in total strain energy and 42% reduction in maximum equivalent stress between constrained and unconstrained boundary conditions. The disc with slits, by contrast, experienced about a 17% reduction in total strain energy and a 17% increase in maximum stress between constrained and unconstrained conditions. The lifted configuration expanded the slits, thereby increasing local stress at the separation node within the disc margin.

3.4.9 Application to amphibious manipulation

We demonstrated that the suction discs can be successfully applied to robotic manipulation. We focused our efforts to adhering to delicate specimen, such as fresh produce (Fig. 3.1 (e)-(j), (k)-(o)), and to enhancing the capabilities of currently existing manipulators, such as those employed by Remotely Operated Vehicles (ROVs) (Fig. 3.19). These applications suggest that the capabilities of the bioinspired disc could extend across a wide range of manipulation tasks.
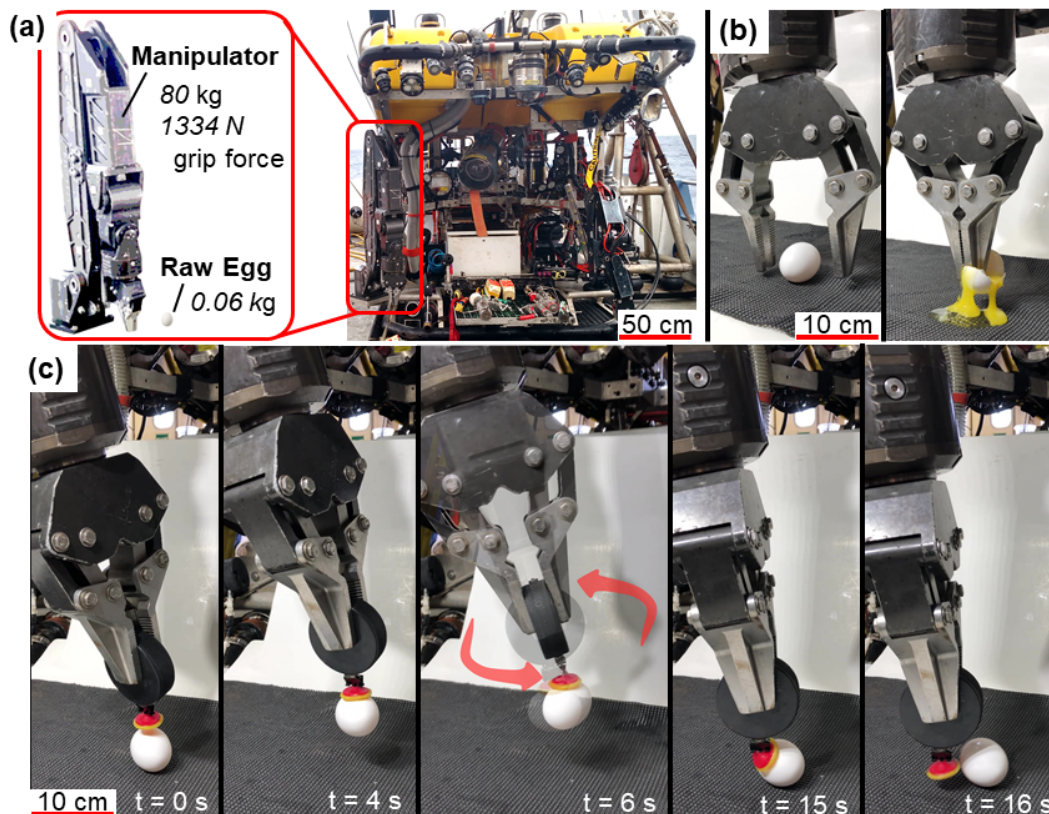
Figure 3.19: **Providing soft touch to an ROV manipulator.** **(a)** Overview of the subsea manipulator used by ROV Hercules. **(b)** Unsuccessful attempt to grip a raw egg without use of suction disc. **(c)** Manipulator using a suction disc to successfully grip, rotate ($\times 3$) and replace raw egg without damage.

We demonstrated successful adhesion of the biomimetic disc to household items (Fig. 3.1 (e)-(j), (k)-(o)), where surface geometries, textures, and weights varied. While suspended in air, the suction disc supported bottles of preserved goods (450 g, mass in air) and fresh produce,

including oranges (250 g), bell peppers (240 g), tomatoes (210 g), strawberries (38 g), and cherries (9 g). While suspended in water, the suction disc gripped ceramic pitchers (320 g, mass in water), calcareous shells (210 g), a Dungenous crab (2 g), a textured ceramic vase (320 g), and a golf ball (6 g). Deformation of the biomimetic disc was the only method of initiating suction in both air and water trials. No additional actuation was required to sustain grip. The ability to deform to the variable surfaces and maintain a vacuum in the suction chamber yielded success at picking up and holding the objects of interest.

To further the application of manipulation, we sought to provide a soft touch to the manipulators of ROVs, which are designed for industrial applications but are also used for subsea recovery of specimen and archaeological artifacts. Manipulators used by the ROVs, such as the Kraft Predator (80 kg, 1334 N maximum grip force) [98] (Fig. 3.19 (a)), do not have a soft touch; this fact increases the risk of damaging delicate artifacts. We addressed this challenge by designing a passive adaptor equipped with a suction disc for use by the manipulators of underwater vehicles. As a proof of concept, two experienced pilots attempted to manipulate a raw egg both with and without the suction disc using the robotic manipulator (Movie S5). By fixing the disc to a hard handle, we were able to successfully adhere to, pick up, perform three full rotations, and place a raw egg (0.06 kg) back on a surface without damage (Fig. 3.19(c)). We disengaged the biomimetic disc by moving the manipulator tangential to the egg surface. By comparison, trials without the use of a suction disc were unsuccessful at manipulating the egg without significant damage to the fragile object (Fig. 3.19(b)). Although the trials were performed using a subsea manipulator in air, we were able to demonstrate the capability of the manipulator to successfully manipulate a delicate raw egg using our suction disc.

3.5   Discussion

By combining insights from engineering and biology, we developed an artificial mimic of the suction disc of the northern clingfish. Upon initial experimentation with the biological specimen, we observed that a euthanized clingfish can withstand normal loads yet was unable to resist shear forces against a wet glass surface. We therefore engineered a mimic of the clingfish with the ability to withstand normal loads on rough and irregular surfaces while being passive in mechanism.

The biological mechanisms of adhesion of the clingfish are highly complex. However, we hypothesize that similar adhesion can be achieved with a simplified design consisting of a suction chamber with a soft layer covering the disc margin to allow for sealing to irregular surfaces. Our observations support the previous conclusion that the soft fibrils that originate from an extensive network of papillae provide one of the primary mechanisms by which the low-pressure chamber is sealed [50].

We mimicked the microfeatures of the suction disc of the clingfish and also approximated their function. In order to mimic the fibrils of the clingfish originating from the papillae, we fabricated artificial discs lined with microscopic silicone pillars. Overall, the discs with micropillars that were composed of a soft silicone were better capable at adhering to surfaces in comparison to the prototypes with pillars of stiff silicone. The soft micropillars were capable of intermeshing together, the overlap thereby sealing in gaps of the disc margin that could otherwise compromise the chamber of subatmospheric pressure. A similar mechanism of sealing may occur in the clingfish where the fibrils of the papillae intermesh to generate a thicker, seemingly continuous soft layer of the disc margin.

Our preliminary work demonstrated that the suction discs with micropillars performed worse in comparison to suction discs without micropillars, most notably on rough surfaces underwater. However, the suction disc with soft micropillars were more successful at adhering to

all surfaces in air and underwater, in comparison to the disc with stiff micropillars. This finding coupled with micrographs of the artificial micropillars suggests that the soft micropillars acted to intermesh together, generating a seemingly thicker soft disc margin. The intermeshing behavior would thereby more effectively seal the suction chamber. We acknowledge that in this study, the micropillars were approximated but not optimized in geometry or spacing, and could therefore be improved to better mimic the microscale geometry of the fibrils of clingfish, which may lead to greater sealing performance.

Our bioinspired suction discs outperformed commercial suction cups on rough textures and concave surfaces. In air, the discs with a soft layer, without micropillars, and without slits performed best on dry, rough surfaces. The biomimetic discs also supported large payloads both in and out of the water. In water, the discs with a soft layer and slits (without micropillars) outperformed all other prototypes and a commercially available suction cup on moderate and coarse surfaces. The biomimetic discs sustained higher adhesive stresses in water than in air. We coupled these results with the comparison of wet and dry surface contact, as visualized by FTIR. The suction disc was able to retain a circular shape of its perimeter when subject to load on a wet surface. Conversely, when the disc was subjected to the same load on a dry surface, the perimeter elongated to an ellipse. Elongation was hypothesized to be the result of the disc margin anchoring to the dry surface. We concluded that the suction disc on the wetted surface would be lubricated by a thin fluid film, resulting in the retention of the circular shape of the perimeter and thus a more even distribution of stress within the body when subjected to a load. The observations made by comparing FTIR results corresponded with the force measurements performed on surfaces in air and underwater. Thus, the higher adhesive stresses achieved by the suction disc in water may be in part due to boundary lubrication by a thin fluid film and a more even distribution of stress within the body cavity.

The performance of our suction discs on coarse surfaces underwater (grain size, 269 μm; 14.3±1.4 kPa) was comparable to the performance of a biomimetic suction disc inspired by the

remora (R_a = 200 μm, 15.8 ± 0.1 kPa, [19]). However, contrary to the remora-inspired disc, our design was unactuated, simplistic in fabrication, and passive in its ability to maintain adhesion.

Three components were identified as critical to improving adhesion: body geometry, a soft layer in the disc margin, and the presence of slits. Body symmetry affected adhesive capabilities of the suction disc. The bilaterally symmetric body performed worse in all occasions in comparison to the radially symmetric body. We concluded that the radial body geometry was capable of better distributing stress across the circumference of the body, allowing for improved adhesion, in comparison to the bilaterally symmetric body.

A soft layer in the disc margin improved performance on concave and rough surfaces. While the stiff silicone backing functioned to maintain the integrity of the internal suction chamber, a soft compliant layer of silicone in the disc margin greatly enhanced sealing capabilities to rough surfaces, similar to the hypothesized role of the soft fibrils originating from the papillae of the clingfish. As visualized using FTIR, the soft layer increased the effective area of contact between the disc and a surface. The relatively large area in contact with the imaging surface increased the frictional footprint of the biomimetic disc, thereby enhancing its capabilities for sealing and sustaining a chamber of low pressure.

The results from the longevity study also demonstrated the ability of the biomimetic disc with a soft layer to maintain a seal for a long period of time while bearing a payload. The suction disc with a soft layer and slits was more successful at bearing a load over an extended amount of time in comparison to the disc without a soft layer or to the commercial suction cup. The soft layer aided in the sealing of the suction chamber. The friction of the soft disc margin helped to prevent the inward slip of the perimeter of the suction disc, which would otherwise lead to failure of attachment. These two factors allowed for a larger payload to be supported by the disc and for a longer period of time, in comparison to the discs without a soft layer. The ability of a 2 g suction disc to bear a payload that is 191 times its mass for well over 100 minutes suggest that the disc may prove useful in load-bearing applications, such as in manipulation or semi-permanent

fixtures.

Geometric and material compliance impacted adhesive capabilities to irregular surfaces. Adhesive discs with slits were considered more geometrically compliant in comparison to their counterparts without slits. Geometric compliance yielded better conformation of the disc to concave shapes to prevent the loss of vacuum from the low-pressure chamber. However, slits were less successful in comparison to material stiffness at maintaining adhesion to convex surfaces. Overall, adhesion to convex surfaces was positively influenced by stiffness of the disc margin and negatively influenced by slits. This trend was opposite that observed for concave surfaces, in which adhesion was positively influenced by slits and negatively influenced by stiffness of the disc margin. Coupling shape with roughness, discs with a soft margin and slits were most successful at adhering to rough, concave surfaces. The results from the rough, concave experimental surface demonstrated the combined effect of slits and a soft layer, which are individually most successful at maintaining adhesion to concave and rough surfaces, respectively.

We investigated the minimal preload required to achieve attachment to two substrates with different values of surface roughness. The minimal preload to attach a disc to the smooth surface was 0.5 N and 1.5 N to the moderately rough surface (grain size, 68 μm). A greater preload suggested a more substantial deformation of the suction disc, thereby expelling a greater amount of fluid from the chamber, resulting in the storage of strain energy within the structure. The combination of a greater amount of expelled fluid and higher stored strain energy, subject to limitations, allowed for a larger pressure differential between internal and external environments. We hypothesize that a greater preload required for rough surfaces may also act to more forcibly conform the soft layer of the suction disc to surface asperities, thereby sealing the suction chamber. Greater conformation to the rough surface would result in an increased resistance to slip in the disc margin which would help to seal the low-pressure chamber.

The results from studying the minimal preload required for attachment suggested possible applications of the suction disc. Given that the preloads to achieve attachment were relatively low

in comparison to other work on robotic grippers intended for delicate gripping tasks [99, 100] this could lead to applications that include manipulation of fragile objects. However, we only explored the preloads required for substrates with two values of surface roughness on exclusively hard surfaces. Future work could therefore explore the effect of preloads on non-rigid surfaces or under a variable environmental conditions.

The results from FEA suggested that the inverted state of the suction discs was energetically favored in all simulated cases when we applied a load of vertical compression. This finding corresponded with the behavior that we observed in FTIR when the suction disc without a soft layer inverted from the surface. We also observed that the presence of a soft layer impacted the tendency of a disc to invert. As demonstrated in FTIR, the disc with a soft layer did not invert, whereas a disc without a soft layer did invert.

We also used FEA to evaluate the impact of slits on the total strain energy of the system. The results from FEA showed that the discs with slits had a lower total strain energy in comparison to the discs without slits. The work done by the initial compression is either stored in the body as elastic potential energy or performs work on the fluid within the suction chamber, evacuating the chamber, and forming a vacuum. Therefore, for a given amount of work to engage the suction disc, we concluded that designs with lower energy storage will experience greater work done on the fluid, suggesting a higher adhesive force. When a force of detachment is applied to the disc, the total energy of the system consists of not only the stored elastic energy in the deformed body, but also the potential energy from the load applied to the disc and the interfacial surface energy used to separate a unit area of the disc from a surface [101]. Our models were used to understand deformation of the suction discs and do not account for other factors such as surface energies, friction, or vacuum, which are also important to adhesion.

Coupling observations from FEA and the experiments of preload, a higher preload resulted in a higher total stored elastic energy of the system. Given that we were only comparing the effect of preload on adhesive capabilities of one disc design (radially symmetric, with soft layer,

without slits), the work done to the body of the suction disc was stored reversibly within the disc. We expect there to exist a trade-off of the magnitude of preload to adhesion. That is, a larger preload would result in a greater stored elastic potential energy and thus a greater restoring force. The preload would therefore have a threshold value that, when surpassed in magnitude, would be counterproductive to adhesion, resulting in a high restoring force that would lead to detachment of the disc from a surface via an elastic restoration to its original shape.

While the biomimetic discs worked well on adhering to concave shapes, coarse surfaces underwater, and moderately rough surfaces in air, they had limited performance on coarse surfaces in air and convex shapes with small radii of curvature. The performance of the suction discs was half of that reported for the biological specimen in previous studies on rough surfaces [52]. Additionally, the artificial suction discs were less successful at adhering to convex surfaces with comparison to concave. However, the clingfish is found to live on intertidal rocks, which we would suggest have both locally convex and concave features. We hypothesize that the ability of the clingfish to actively adjust its suction disc may influence its ability to adhere to irregular surfaces. Our artificial suction discs did not have an active mechanism by which to adjust its seal, which may contribute to its decreased adhesive capabilities to convex surfaces in comparison to the biological specimen. We suggest that while we were mimicking key components of the suction disc, such as geometry, we have left other components of adhesion, such as secretions, to future work. The clingfish is hypothesized to use secretions [52], much like gastropods [102], to increase the viscosity of the fluid beneath the organism, thereby increasing the contribution of Stefan adhesion to surface attachment.

The clingfish and the commercial suction cup achieved higher adhesive pressures on flat, smooth surfaces in comparison to the biomimetic discs. The pelvic girdle of the clingfish and the commercial suction cup are both stiffer than the bioinspired discs, thereby preventing deformation of the suction chamber when subjected to external pulling forces. Therefore, the stiffness in the backing also plays a role in achieving higher adhesive pressures. 3D reconstructions of the

clingfish could therefore be used to inform designs of the suction disc to achieve higher adhesive stresses in future work.

In evaluating the adhesive performance of the prototypes, we only performed pull tests that were normal to the experimental surface, analogous to the pull tests performed on clingfish specimen. Our suction discs, much like the euthanized clingfish, are much less capable of resisting shear forces while on wet glass surfaces. We did not test the combination of shear and normal forces on neither the clingfish nor the artificial suction discs, which we leave for future work. Applications in which high normal adhesion and low resistance to shear forces could be favorable include pick-and-place manipulations or adhesive footpads for robotic locomotion.

Future work could explore the modification of the suction disc geometry, size, composition, and surface structure of the disc margin to tailor its use to specific surfaces and external disturbances, such as fluid flow, for use in applications not explored here. Tailoring micropillar materials in the disc margin may also aid in adhesion in an underwater environment, as demonstrated by microstructured hydrogels to yield amphibious adhesion [87].

In sum, we created a suction disc that functions in and out of water to grip rough and irregular surfaces without necessitating sustained actuation. Our system is effective at gripping textured surfaces while being relatively simple and inexpensive to fabricate. The bioinspired design has many potential applications, including robotic manipulation. We demonstrated its capabilities on handling delicate objects, such as fresh produce, of varying weights and textures. With the suction disc, we can also provide a delicate touch to the seemingly ungentle, such as subsea manipulators. As demonstrated in this study, the suction disc gave a manipulator commonly used in subsea operations the ability to delicately maneuver a raw egg. Given these demonstrated capabilities, future iterations of the clingfish-inspired suction disc could markedly improve manipulation while being cost-effective for fabrication.

3.6 Acknowledgements

Author Contributions: J.A.S., M.T.T, and D.D.D. conceived the project. J.A.S. characterized the morphology of the clingfish suction disc. H.Q. performed Scanning Electron Microscopy on the biological specimen. J.A.S. designed and fabricated the clingfish-inspired disc. J.A.S. performed and analyzed tests of adhesion of the biomimetic discs. S.J. performed Finite Element Analysis of the suction discs. S.J. performed longevity and preload experiments. J.A.S. conducted robotic manipulation experiments. J.A.S. prepared the initial draft of the manuscript and all authors provided feedback during revisions.

Competing Interests: Invention disclosure UCSD# SD2019-160 (to J.A.S., D.D.D., M.T.T.) has been filed describing fabrication and performance testing of the clingfish-inspired adhesive disc.

Chapter 3, in full, is a reprint of the material as it appears in Bioinspiration & Biomimetics, 2019. Sandoval, Jessica A.; Jadhav, Saurabh; Quan, Haocheng; Deheyn, Dimitri D.; Tolley, Michael T., IOP Publishing, 2019. The dissertation author was the primary investigator and author of this paper.

Chapter 4

Tuning the morphology of suction discs to enable directional adhesion for locomotion in wet environments

Jessica A. Sandoval[1]*, Michael Ishida[1]*, Saurabh Jadhav[1],

Sidney Huen[1], and Michael T. Tolley[1]

[1]Department of Mechanical and Aerospace Engineering, University of California San Diego,

9500 Gilman Drive, La Jolla, CA, 92093 USA

*These authors contributed equally to this work.

4.1   Abstract

Reversible adhesion provides robotic systems with unique capabilities, including wall climbing and walking underwater, and yet the control of adhesion continues to pose a challenge. Directional adhesives have begun to address this limitation, by providing adhesion when loaded in one direction, and releasing easily when loaded in the opposite direction. However, previous work

has focused on directional adhesives for dry environments. In this work, we sought to address this need for directional adhesives for use in a wet environment by tuning the morphology of suction discs to achieve anisotropic adhesion. We developed a suction disc that exhibited significant directional preference in attachment and detachment without requiring active control. The suction discs exhibited morphological computation—i.e. they were programmed based on their geometry and material properties to detach under specific angles of loading. We investigated two design parameters - disc symmetry and slits within the disc margin - as mechanisms to yield anisotropic adhesion and through experimental characterizations, we determined that an asymmetric suction disc most consistently provided directional adhesion. We performed a parametric sweep of material stiffness to optimize for directional adhesion and found that the material composition of the suction disc demonstrated the ability to override the effect of body asymmetry on achieving anisotropic adhesion. We modeled the stress distributions within the different suction disc symmetries using Finite Element Analysis, yielding insights into the differences in contact pressures between the variants. We experimentally demonstrated the utility of the suction discs in a simulated walking gait using linear actuators as one potential application of the directional suction disc.

4.2   Introduction

Reversible adhesion, the ability to attach to and detach from a surface in a controlled manner, has gained specific interest in the field of robotics, ranging from manipulation to locomotion [1]. In the area of robotic locomotion, adhesion can be advantageous for generating traction (i.e. for maintaining contact between a robot and a surface throughout a walking gait cycle). Reversible adhesion can therefore enable unprecedented locomotion capabilities, such as scaling glass walls [44].

The adhesive strategies of animals have inspired a new generation of bioinspired adhesives

to be paired with locomotion [10]. Many organisms employ adhesion to effectively locomote across a surface or to counter environmental disturbances. Animals ranging from lizards [5] to insects [40] use adhesive foot pads to walk on a wide variety of surfaces, including inverted surfaces. By coupling adhesion and locomotion, animals can attain novel locomotion strategies while countering high disruptive forces. For instance, sea stars locomote using hundreds of tube feet to contact and chemically adhere to a substrate [69]. This distribution of adhesion across a large quantity of attachment points allows echinoderms to locomote and remain attached to a substrate all the while countering wave surges, currents, and other marine disturbances. The coordination of a highly distributed network of actuators and adhesion allows sea stars to achieve a steady crawling locomotive gait [103]. Our goal is to develop a directional adhesive that could in the future enable sea star inspired locomotion while minimizing the complexity of control.

Reversible adhesives developed for use in engineered systems include microstructured dry adhesives, interlocking devices, electroadhesives, magnetism, phase-change based adhesives, vibration-based adhesives, and negative static pressure devices (e.g. suction cups). Microstructured dry adhesives (i.e. gecko-inspired adhesives) take advantage of van der Waals forces to attach to a surface [26]. Previous work has used these adhesives to endow robots with wall-climbing capabilities [44, 104]. Roboticists have also explored the use of attachment devices composed of interlocking structures, ranging from rigid hooks [82] to *ex vivo* shark skin [105], on the foot pads of locomoting robots to provide greater frictional resistance to slippage while walking. Such interlocking devices may however limit the surface type to which locomotion would be successful. Electroadhesion based on electrostatic attraction between two surfaces has been used to achieve robotic locomotion [106], including on inverted and vertical surfaces [107]. However, the presence of water generally leads to weak electrostatic adhesion due to Debye shielding [108]. Adhesion using magnetism provides strong attachment during locomotion, yet is limited to ferromagnetic surfaces [109, 110]. Adhesion mediated by a material such as gallium that changes phase from solid to liquid at a temperature just above the robot's normal

operating temperature allows for switchable attachment dependent on temperature [111]. Such adhesion occurs when a phase-change material partially covers and solidifies to an object once its temperature is decreased. Use of phase-change material to adhere requires control of its local temperature and may result in the deposition of residue. Additionally, adhesion generated by the vibration of a thin flexible membrane near a surface has recently been demonstrated for adhesion by mobile robots to curved, vertical, and inverted surfaces [112]. This vibration-based adhesion functions by forming a low-pressure region in a lubricating air film beneath the vibrating disk. However, this form of adhesion requires constant energy expenditure to attach and remain adhered to a surface and has not been shown to work in incompressible fluids (e.g. underwater). The use of suction has been explored in wall-climbing tasks in legged [113], tracked [114], and soft, inchworm-inspired [115] robots for use in air and underwater. However, suction discs currently used in locomoting robots are generally limited to use on smooth, flat surfaces and require active control for attachment and detachment [116].

In addition to reversibility, controllability of an engineered adhesive is critical for robotic applications [117, 118]. Control can be achieved by including an actuator to engage with and detach from a surface or by morphologically programming the structure of the adhesive. Active actuation requires an energetic input to achieve attachment and detachment, thereby adding complexity to a design that could potentially reduce the scalability of a design to smaller sizes or larger number of adhesion points. An alternative form of adhesive control includes the use of morphological computation [119] to encode the conditions for attachment and detachment into the physical body of the adhesive. Morphological computation leverages the shape, design, and material composition to offload computational complexity into a physical structure of an object while producing a predictable behavior [120, 121, 122]. The use of morphological computation for adhesive control is not unique to engineered solutions but is also found in naturally occurring adhesive systems [119, 123]. For instance, geckos utilize a dense array of branched, anisotropic microstructures [124] to adhere via van der Waals forces [63]. Moreover, the setae of the gecko

demonstrate sensitivity to angle such that once a threshold in angle is reached, the setae detach with minimal pull-off force [5, 63, 125]. Similarly, gecko-inspired adhesives developed with anisotropic profiles, such as angled stalks or wedges, result in directional adhesion in artificial systems [126, 94]. Pads expressing gecko-inspired adhesives can therefore be removed from a surface by peeling when adhesion is only required in one direction (e.g. in the case of climbing against gravity) [126]. The morphological computation exhibited by these microstructures therefore creates controllable adhesion without necessitating additional methods of actuation to attach to and detach from a surface [117].

Directional, microstructured adhesives which enable novel robotic locomotion are limited by the environment in which they are applied. Dry adhesives are most effective for adhering in dry environments and are significantly less effective in a wet environment. A thin, lubricating layer has been reported to form between a substrate and the tip of a dry adhesive microstructure when submerged in a water, leading to 50% lower pull off forces [127]. Modifications of the dry microstructured adhesives, such as the use of polymer coatings [128], changes to the material composition [87], and incorporation of cupped terminations [45], have been used to adapt the microstuctures for wet environments. These advances in microstructured adhesives have yielded strong normal and shear adhesion in a wet environment, yet lack anisotropy for directional adhesion or a controllable mechanism for detachment.

Many underwater creatures employ some form of reversible adhesion [129], including the use of chemical secretions in echinoderms [69], mechanical interlocking in the remora [130], and suction in the octopus [131] and intertidal fish [53]. Inspiration from these biological systems yield promising steps towards the development of successful engineered adhesives for use underwater [132]. Mechanical interlocking has been coupled with suction in the development of a biomimetic suction disc that is capable of withstanding high shear detachment forces [19]. Inspired by the clingfish, we have previously demonstrated the ability to modify the material composition of a suction disc to adhere to rough substrates [65, 66]. Soft artificial suckers

inspired by the octopus [15] and an array of vacuum-driven suckers have demonstrated the utility of suction for underwater manipulation and locomotion [133].

However, these previous approaches to suction-based adhesion necessitated a separate, actively controlled mechanism to reversibly attach to and/or detach from a surface. In these studies, detachment required a separately controlled set of actuators to disengage the suction disc from a surface [134, 135]. For instance, detachment of the suction cups via peeling requires the outer perimeter of the disc to be lifted using tendons, thereby releasing the seal of the suction cup [113]. Other works have explored actively controlling the shape of the suction cup [115] or controlling pressure in a suction cup with a separate vacuum line for attachment and detachment, adding to the complexity of the pneumatic circuitry [136].

Here, we introduce a reversible suction disc that leverages morphological computation to detach at predetermined angles without necessitating a separate mechanism for detachment. Such a design would advance the field of directional adhesives, achieving anisotropic adhesion in a wet domain. We demonstrate that the detachment angle can be encoded into the body of the disc through a combination of factors - geometric asymmetry, disc margin morphology, and material stiffness. We generalized the types of design factors that yield directional adhesion in suction discs and by applying the directional adhesives to linear actuators, we demonstrated their utility in sea-star inspired walking. To the extent of our knowledge, this work presents the first directionally adhesive suction disc to be reported and demonstrated for use in multi-legged robotic locomotion.

4.3   Results and Discussion

4.3.1   Testing two mechanisms for directional adhesion

We designed suction discs to achieve passive, reversible adhesion with adhesive strength based on the angle of applied tensile loading. We considered a sea star inspired walking scenario

in which we attached the disc to the end of a linear actuator which was mounted to a body constrained to move parallel to the surface (Fig. 4.1b). To achieve translation of the body, we desired high adhesion at what we defined as a negative angle of the tube foot-inspired actuator relative to the body (angle, $< 0°$), corresponding to a tube foot that had reached out and engaged its suction disc with a horizontal surface. After pulling on the surface to move the body forward, causing the actuator to pass through the neutral axis (angle, $0°$), we desired low adhesion allowing the suction disc to release at a positive angle of the tube foot relative to the body (angle, $> 0°$).
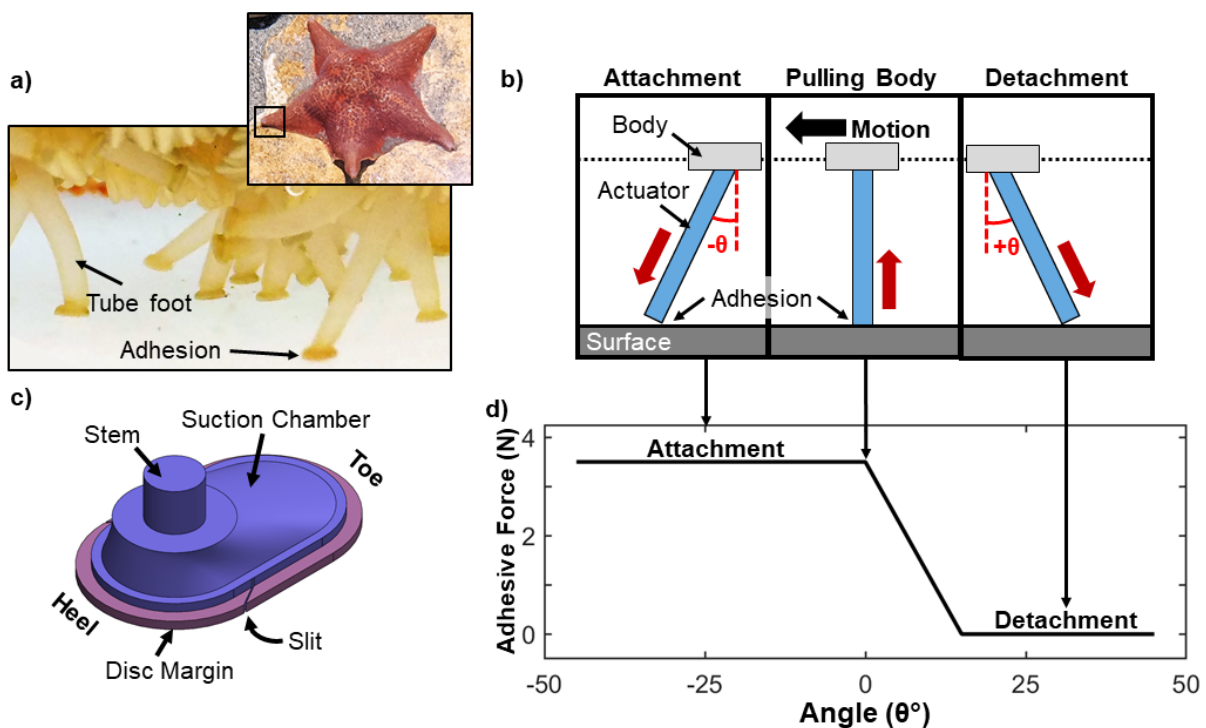
Figure 4.1: **Tuning morphology for directional adhesion. Design parameters of a suction disc cause an adhesive force that is highly dependant on the direction of loading.** a) Sea star inspired locomotion. Sea stars use an array of tube feet coupled with adhesive secretions to adhere and pull/push themselves along a surface. b) Schematic demonstrating idealized, angle-dependent attachment and detachment conditions for sea star inspired locomotion. c) Computer-generated rendering of suction disc, with key features labeled. d) Model of the idealized performance of a suction disc with adhesion mechanically "programmed" as a function of the angle of an applied tensile load (relative to vertical).

A suction disc was composed of a suction chamber that was lined by a disc margin (Fig. 4.1c), a design that we found previously to adhere well to surfaces with a variety of

roughnesses in air and in water [65]. The disc margin was composed of silicone that was softer than that of the body cavity and served to seal the suction chamber against the substrate. A load was applied to the suction disc through a stem located at the top of the suction chamber. For all disc designs, the width of the disc (w) was twice the radius of the suction chamber (r) and the length of the disc (l) was four times the radius (Fig. 4.2a).

To compare various approaches to achieve directional adhesion, we investigated the role of two parameters – symmetry and slits within the disc margin – to achieve anisotropic adhesion (Fig. 4.2a-d). We then performed a parametric sweep of the material stiffness of the disc to optimize anisotropic performance.

Parameter I: Symmetry for anisotropic adhesion

In the first set of prototypes, we varied the symmetry of the body of the disc. Symmetry was dependent on the location of the applied load, which we indirectly controlled with the position of the stem along the body of the disc. We then applied either a tensile or compressive load to the stem. We hypothesized that an uneven distribution of load across the body of the suction disc would adversely affect the seal around the disc margin for some (i.e. positive) angles of applied load relative to the surface, thereby reducing the adhesive stress. Accordingly, we hypothesized that a greater offset of the load would result in a more pronounced asymmetric performance of adhesion.

The load placement ranged from the center of the disc (Body Type C) to offset from the center (Body Types A and B). For body types A and B, a load was applied to the stem which was offset by a distance of half the radius, ($r/2$, Body Type B) or by one radius (r, Body Type A) from the center of the disc (Fig. 4.2a). We refer to the positions of the load as either symmetric, for the centered condition, or asymmetric, for the offset conditions, about the transverse axis. To evaluate how the adhesive force generated by the discs varied with the direction of the applied load, we performed pull tests with a universal mechanical testing machine across the sets of
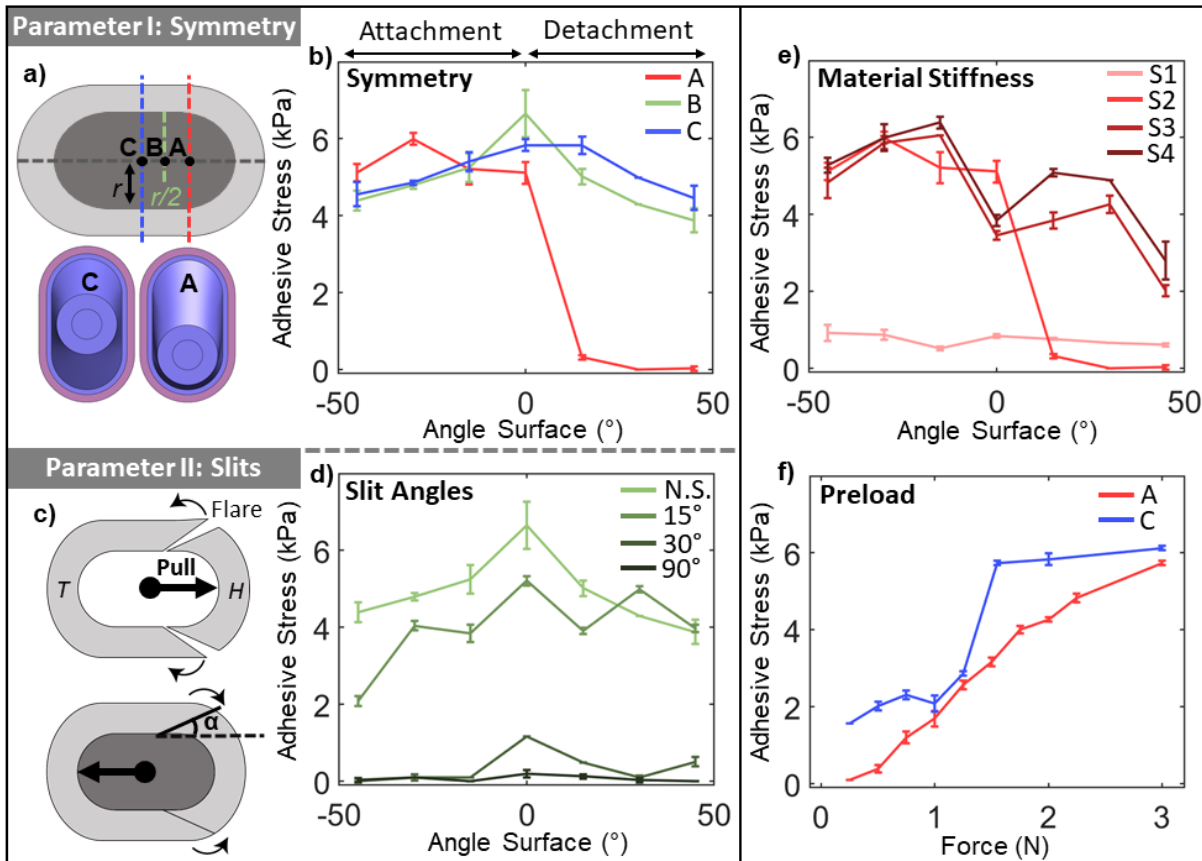
Figure 4.2: **Experimental investigation into the morphological parameters for anisotropic adhesion.** a) Investigations into the first parameter, disc symmetry, on anisotropic adhesion. We tested three possible load placements for suction discs: discs A and B were asymmetric, with loads offset from the center and discs C were symmetric, with a load applied to the center of the disc. b) Effect of disc symmetry on adhesion, where adhesive stress (kPa) is plotted with respect to the angle of the surface. c) Investigations into the second parameter, slits within the disc margin, on anisotropic adhesion. A schematic demonstrates the function of the slits. Top: Slits flare when the disc is pulled towards the heel, breaking the seal of the suction chamber. Bottom: Slits come together, forming a continuous seal, when the disc is pulled towards the toe. Representation of slit placement in the disc margin, angles with respect to the longitudinal axis. d) Effect of slit angle on adhesion (body type, B), where adhesive stress (kPa) is plotted with respect to the angle of inclination of the surface. The discs with slits were compared to a disc without slits (*N.S.*). e) Effect of material stiffness on adhesion for an asymmetric body type (A). Materials tested with platinum cured silicone with a moduli of elasticity at 100% strain of 68.9 kPa (S1, light red), 338 kPa (S2), 593 kPa (S3), and 662 kPa (S4, dark red). f) Effect of the magnitude of preload (N) on adhesion (kPa). Experiment performed on A and C body types (no slits). The angle of the surface relative to the discs was zero degrees for preload tests. All pull tests were performed in triplicate, error bars indicate standard deviation.

83

suction disc variants. We changed the angle of the substrate with respect to the direction of travel of the mechanical testing machine.

We found that the symmetry of the body significantly affected adhesive stress as a function of angle (Fig. 4.2b). At negative angles of inclination in which attachment was desired, all three discs body types (A-C) exhibited significant adhesion (> 5 kPa), with only small differences in adhesive stress. All of the discs maintained adhesion across the neutral axis, perpendicular to the surface. However, the discs varied greatly on their performance at positive angles of inclination where detachment was desired.

The most asymmetric body type (A) with the largest offset had the largest difference in adhesive stress from attachment to detachment angles. Body Type A demonstrated nearly zero adhesive force in the angles associated with detachment. Conversely, the suction discs with a centered (Body Type C) and mildly offset load (Body Type B) maintained their adhesive strength (> 4 kPa) in positive angles of inclination, corresponding to the desired detachment orientations. Overall, a high degree of asymmetry resulted in a dependence on the angle of the loading (i.e. in directional adhesion).

Parameter II: Slits in the disc margin for anisotropic adhesion

In the second set of disc variants, we evaluated the effect of slits in the disc margin to yield anisotropic adhesion. The incorporation of slits in the disc margin was inspired by the clingfish, an intertidal fish that uses a ventral suction disc to attach to rocky surfaces [53]. The adhesive disc of the clingfish is formed by the union of the pelvic and pectoral fins, resulting in the formation of two bilateral slits in the disc margin. The clingfish can moderate the amount of suction by modifying the position of its fins [50], effectively changing the angle of the slits in its disc margin. Inspired by the clingfish, we included two slits in the disc margin to passively achieve directional adhesion. The slits were intended to flare (Fig. 4.2c) thereby disrupting the seal of the disc margin when pulled or loaded from specific angles. We varied the angles of the

slits with respect to the longitudinal axis of the disc from 15° to 90° for a moderately offset body type (B).

Similar to our tests of adhesion based on disc symmetry, we tested the discs with slits with a universal mechanical testing machine at a variety of angles of loading relative to the surface to determine whether the slits contributed to anisotropic adhesion. We hypothesized that the addition of slits would act as a valve to facilitate direction-dependent adhesion. To answer this hypothesis, we compared designs with slits (angles; 15°, 30°, 90°) to the design without slits (0°) for body type B (Fig. 4.2d).

Overall, we found that the addition of slits did not yield the intended directional adhesion. The disc variant with a 15° slit in the disc margin adhered in an angle-dependent manner, but opposite of the anticipated adhesive curves. We observed that while the slits (15°) flared as anticipated while experiencing a compressive load, they did not fully close when pulled to form a completely continuous disc margin in the attachment orientation. The variant with slits of 15° exhibited directional adhesion, where the adhesive stress increased from 2.09 ± 0.12 kPa at -45° inclination to 3.98 ± 0.09 kPa at 0° and 45° inclinations. The magnitude of the dependency on the angle of the surface, however, was small. Thus while we were able to produce an anisotropic adhesive response in a disc with slits, the difference in adhesive stress between a negative and positive angle of the surface was lower than alternative disc variants (i.e., changing the symmetry of the disc).

The variant with a slit of 30° achieved lower adhesive stresses in comparison to the disc with slits of smaller angles (15°). The slits of 15° exhibited more overlap in the disc margin, in comparison to the 30° variant. Our interpretation of these results is that the greater amount of overlap corresponded to a better seal and thus higher adhesive stress. This trend continued for the suction disc with a slit of 90°, for which no adhesion was achieved across all angles of inclination. We attributed the ineffective adhesion of the 90° slits to the inability of the disc margin to seal the suction chamber.
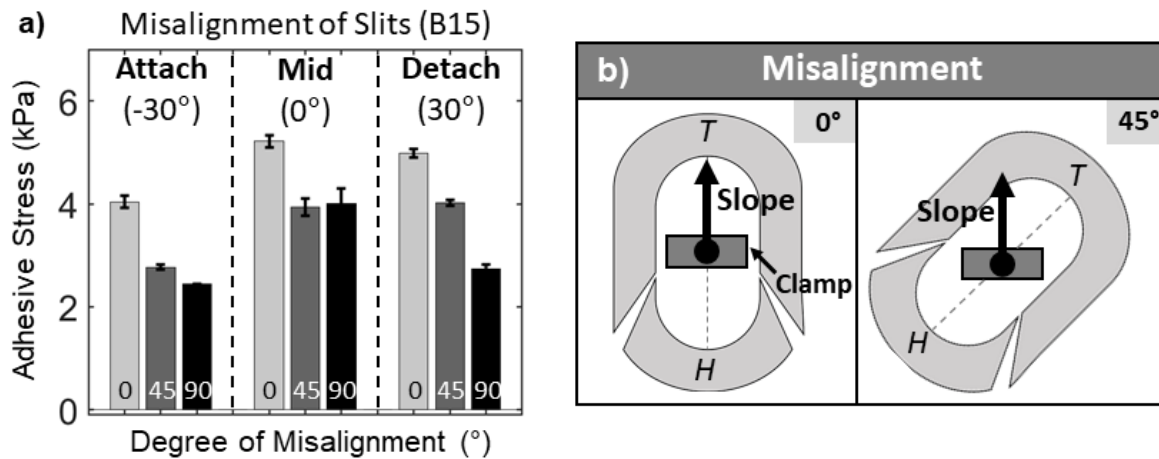
Figure 4.3: **Effect of misalignment of the suction disc with slits on adhesive stress. a)** We evaluated the performance of a suction disc (Body Type B, slit angle 15°) that was misaligned by either 45° (dark gray) or 90° (black) to the slope of the surface. For comparison, the disc was also inline with the slope (0° misalignment, light gray). We evaluated the effects of misalignment for the attachment (angle of surface, -30°), midstance (angle of surface, 0°) and detachment (30°) orientations. **b)** Schematic demonstrating the effect of alignment of the suction discs that were either inline (0°) or 45° misaligned with the slope of the surface. The clamp from the load cell is represented in dark gray.

The incorporation of slits was a less reliable design parameter than asymmetry and was therefore less practical for applications in locomotion. During detachment, the slits were intended to flare open, dependent on the angle and direction of the pulling force (Fig. 4.2c), thereby reducing adhesion. However, the slits were more sensitive to the initial loading conditions, such as the alignment of the disc with respect to the surface and with respect to the clamp from the load cell. Suction discs that were misaligned to the slope of the experimental substrate would result in an uneven flaring of the slits (Fig. 4.3). This inconsistent behavior left slits either partially or fully closed, thereby keeping the suction chamber sealed during detachment.

We performed a quantification of the effect of misalignment on the overall adhesive stress of a disc (Body Type B) with slits (15 °). This disc was either inline (0°) or misaligned by 45° or 90° to the slope of the surface (Fig. 4.3 b). Given that the surface and the load cell were fixed in position, we created a misalignment by rotating the disc within the clamp of the load cell. The degree of misalignment directly affected the adhesive stress, where a 45° misalignment resulted

in up to a 31% drop in adhesive stress (2.77 ± 0.05 kPa), in comparison to the disc when inline with the slope of the surface (4.04 ± 0.12 kPa). A 90° misalignment resulted in up to a 45% drop in adhesive stress (2.73 ± 0.07 kPa), when compared to the disc inline with the slope (4.99 ± 0.07 kPa). Thus, the adhesive performance of the discs with slits was highly dependent on its alignment with the slope of the surface.

We clarified how the performance of the disc was affected by its misalignment with respect to the clamp by testing against a flat surface without a slope (0°; Fig. 4.3 a). A misalignment (45° and 90°) of the suction disc relative to the clamp resulted in a ~24% reduction in adhesive stress for the disc against a flat surface. We attributed this to an uneven distribution of compressive stress across the body of the disc caused by its misalignment with the clamp (Fig. 4.3 b). Misalignment would non-uniformly deform the suction chamber of the disc. We observed that this uneven distribution of stress caused by misalignment with the clamp resulted in an uneven flaring of the slits and therefore a reduced adhesive stress.

The considerable sensitivity of the slits to alignment made them less reliable for practical implementation in a locomoting robot. Future work could explore the use of different materials or geometries of the slits to yield more predictable flaring that is less sensitive to misalignment. We anticipate that we could modify the location of the slits and orientation (i.e., 180° to their current orientation) to help tune their anisotropic adhesive performance.

In conclusion, of the design parameters investigated (symmetry and slits), the modification of the symmetry of the suction disc yielded the most predictable, repeatable anisotropic adhesion. We therefore chose to use a suction disc with a large geometric asymmetry (Body Type A) without slits for further experiments.

Impact of stiffness on anisotropic adhesion

We investigated the impact of material stiffness of the suction chamber on adhesion of a highly asymmetric suction disc (Body Type A), in which the offset load has already demonstrated

the ability to yield anisotropic adhesion (Fig. 4.2e). We hypothesized that increasing the stiffness of the body of the suction disc would help to maintain the integrity of the suction chamber when deformed, allowing for greater adhesive stresses to be achieved. We changed the stiffness of the suction chamber while maintaining a constant stiffness of the disc margin. The types of silicone used spanned across one order of magnitude of stiffness (moduli of elasticity at 100% of strain of 68.9 kPa for S1, 388 kPa for S2, 593 kPa for S3, and 662 kPa for S4).

We tested the discs of different stiffnesses on the universal mechanical testing machine by applying loads at different angles relative to the surface to determine how stiffness of the disc affects anisoitropic adhesion. The relatively stiff elastomers, such as S4, adhered more strongly to a substrate in comparison to the softest elastomer tested (S1). However, stiff elastomers (S3 and S4) adhered with adhesive stresses greater than 5 kPa and 2.5 kPa for negative and positive angles of the surface, respectively. We considered this behavior to be insufficient anisotropy as we desired minimal adhesion at positive angles with respect to the surface.

We found that by decreasing the stiffness of the suction chamber, the disc was able to preferentially, directionally adhere. We found that an intermediate stiffness (S2) of 338 kPa (100% modulus) demonstrated adhesion that corresponded to the angle of the surface (Fig. 4.2e). S2 adhered with a high adhesive stress ($>$ 5 kPa) at negative angles and did not adhere (0 kPa) at positive angles, corresponding to the desired attachment and detachment orientations, respectively. However, we observed a limit to this trend as the disc composed of the softest of the silicones tested (S1) adhered with the lowest adhesive stress ($<$ 1 kPa) across all angles of the surface. Thus, intermediate stiffnesses (0.38 MPa, S2) created directional adhesion, while the stiffest ($>$ 0.5 MPa, S3 and S4) and softest ($<$ 0.06 MPa, S1) elastomers did not produce both high adhesion at negative angles and low adhesion at positive angles. These results show that optimization of directional adhesion in suction discs requires a balance of material properties and geometric asymmetry.

We concluded that the differences in adhesive performances of the prototype variants

resulted from the deformation experienced by the suction chamber. Decreasing the stiffness of the disc resulted in a reduced resistance to deformation, and a low structural integrity that compromised the suction chamber, resulting in low adhesive stress at all load angles. In contrast, increasing the material stiffness of the disc reduced the deformation under the same compressive load, avoiding the collapse of the suction chamber.

This is consistent with previous work [137], which found that increased stiffness of the suction chamber increased the adhesive force of the disc. However, to create directional adhesion, the disc must create minimal adhesive forces under certain loading conditions, dependent on the angle of the surface. A disc composed of high stiffness material would thereby create high adhesion forces at all angles of detachment. For predictable, directional adhesion, the suction chamber must be of an intermediate stiffness to be compliant enough to collapse the front of the suction chamber during detachment while being stiff enough to maintain its integrity during attachment. We envision that additional optimizations of the structure of the discs could be used to combine the effects of shape and material stiffness on the directionality of the adhesion.

Impact of preload on symmetric and asymmetric discs

Lastly, we tested the effects of preload on the adhesion of symmetric and asymmetric discs using a universal mechanical testing machine to first load the disc against a surface perpendicular to the axis of travel of the machine and then pull the disc away from the surface.

The geometric asymmetry affected the amount of force that should be applied as a preload to achieve the maximum adhesive force (Fig. 4.2f). The preload caused the disc to deform, which forced fluid out from the enclosed chamber and created a pressure differential responsible for adhesion. As the force of the preload increased, the adhesive stress increased until the disc was fully deformed and the maximum pressure differential was reached. After this point, a further increase to the preload resulted in a minimal increase of the adhesive stress, as demonstrated in the symmetric suction disc. Conversely, the increasing preload for the asymmetric disc led to a

89

gradually decreasing slope, resulting in a point of inflection in the curve around 3 N.

We observed that the symmetric disc achieved an inflection point in the maximum adhesive stress at about half the preload required by the the asymmetric disc (1.5 N for Body Type C, 3 N for Body Type A; Fig. 4.2f). We concluded that the reduced preload required by the symmetric disc was due to a more uniform deformation of the disc. Conversely, the asymmetric disc required a greater amount of force to fully evacuate the suction chamber as the shorter heel of the disc was more resistant to deformation.

4.3.2   Contact mechanics at discrete angles during loading

To understand why different discs demonstrated orientation-dependent adhesion, we imaged the contact made between the suction disc and a surface during preload and pull-off conditions using frustrated total internal reflection (FTIR; Fig. 4.4a). FTIR is a contact-visualization technique in which light is internally reflected within a sheet of acrylic [96]. Contact with the acrylic sheet allows light to escape, which can then be imaged by a camera and serves as an indicator of contact with a surface. However, FTIR does not provide the magnitude of the contact pressure, only whether or not there is contact with the surface.

During FTIR, both asymmetric (A) and symmetric (C) discs were imaged under a 2 N compressive load when the imaging surface was rotated to $-30°$, $0°$, and $30°$ with respect to the suction disc. We then imaged the contact at the point of failure (*PoF*) of the suction disc when pulled from the imaging surface at a displacement rate of 150 mm/min.

As visualized during compressive trials using FTIR, the symmetric disc always maintained a seal between the disc margin and the substrate, irrespective of the angle of the surface (Fig. 4.4a). At both $-30°$ and $30°$ rotations, a full preload of 2 N caused the outer perimeter of the disc margin to flare upwards, thereby reducing the area in contact with the imaging surface but still retaining the seal around the perimeter of the disc. This flaring behavior was not observed in the zero degree condition, suggesting a more uniform distribution of stress along the perimeter of the disc
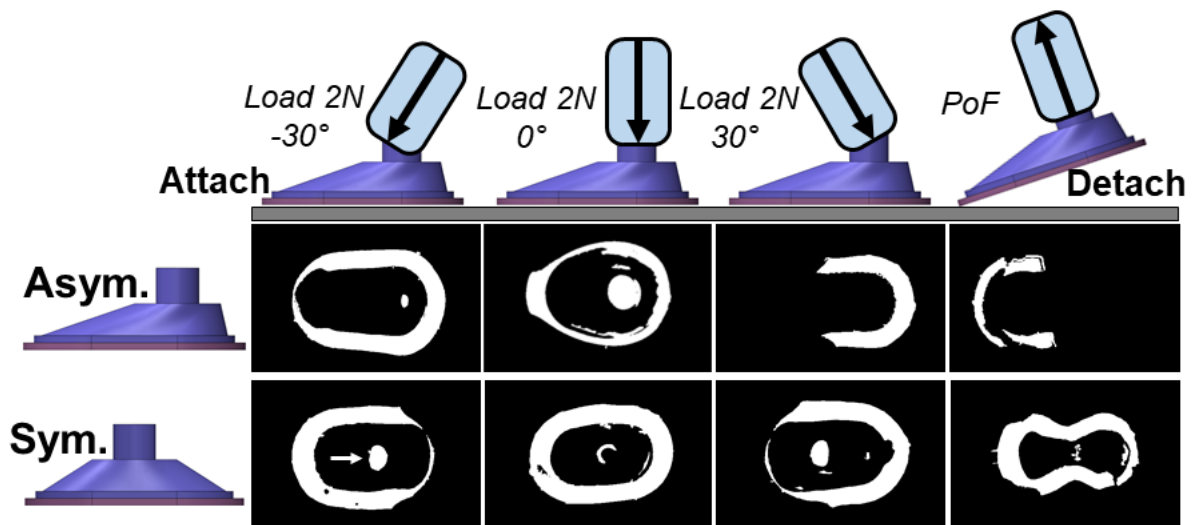
Figure 4.4: **Visualizing the contact between a suction disc and a surface.** a) Visualization of the contact area of the asymmetric disc (Body Type A, top row) and symmetric disc (Body Type C, bottom row) for four angles of contact using frustrated total internal reflection (FTIR). Column 1: a compressive load of 2 N was applied to the suction disc on a surface at an angle of -30°. Column 2: a compressive load of 2 N was applied to a disc perpendicular to a surface. Column 3: a compressive load of 2N was applied to a disc at an angle of 30°. Column 4: the suction disc was then pulled away from the surface (angle, 30°), FTIR images correspond to the point of failure (PoF), or the moment before the disc detached from the surface. For all FTIR images, the white regions indicate contact with the imaging surface.

margin. Additionally, a compressive preload of 2 N caused the suction chamber to deform such that the inner surface of the top of the suction chamber (beneath the stem) contacted the imaging surface, shown as a circle in the frames from FTIR (arrow; Fig. 4.4a). We interpreted the contact of the top of the suction chamber with the imaging surface to be indicative of the strain in the disc; that is, a larger area of contact with the upper cavity implied a larger deformation of the disc.

The behavior of the asymmetric disc when in contact with the surface differed from the symmetric disc. At a negative angle of inclination, the asymmetric disc completely sealed its suction chamber. However, when loaded in compression from a positive angle (the low adhesion orientation), the asymmetric disc did not maintain a full seal. When loaded by a compressive force in this orientation, the front of the disc lifted from the surface, while the heel was still in contact with the surface. As the suction disc was gradually pulled away from the surface in this orientation (first decreasing the magnitude of the compressive force to zero, then increasing the tensile load), the contact of the asymmetric disc would roll from heel to toe. Thus, at positive angles of inclination, the asymmetric disc did not adhere because the suction chamber was not sealed and hence did not maintain a pressure differential.

The FTIR results showed that a compressive preload concentrated about the heel of the asymmetric suction disc resulted in adhesion to a surface. However, as the compressive load changed to being centered about the toe, the front of the disc would lift and thereby break the seal of the suction chamber. We concluded that asymmetry resulted in an uneven distribution of stress across the disc, corresponding to reduced adhesion at angles associated with detachment in a locomotive gait cycle. On the other hand, symmetry yielded high adhesion, irrespective of if the load was centered over the heel or the toe.

4.3.3   Modeling mechanics and contact throughout a gait cycle

The FTIR results provided an understanding of the behavior of the discs when loaded at discrete angles against an imaging surface. However, when in use during a walking gait, the disc

would be subjected to loading under a continuous change of angles relative to the surface (see Fig. 4.1). To examine the behavior of the disc during a gait cycle, we used finite element analysis (FEA) to model the effects of body symmetry (Types A and C) on the mechanics due to loading while cycling from an angle of -30° to an angle of 30°. (Fig. 4.5). To simulate the angle change, we loaded the suction discs to a virtual surface that rotated about an axis orthogonal to the stem and the long axis of the suction disc. The simulations neglected environmental conditions and effects of the fluid in the suction cavity and focused on how contact with the surface affected the mechanics of the disc.

Distribution of stress within the body of the discs

The distribution of stress within the body of the suction disc differed between the body types (Fig. 4.5a). The symmetric disc (C) exhibited a symmetric distribution of stress with respect to the angle of the applied preload. Furthermore, the symmetric disc experienced a symmetric change in internal volume across angles tested in the simulation (Fig. 4.5b). Conversely, the asymmetric disc (A) experienced a greater concentration of stress within the body (> 175 kPa) during the angles associated with attachment ($<0°$) than in comparison to the angles associated with detachment ($>0°$). The stress was concentrated at the heel when loaded at -30°, which was distributed throughout the body of the suction disc when rotated. The asymmetric disc experienced the greatest reduction in internal volume at angles associated with detachment ($>0°$; Fig. 4.5b). A low internal volume corresponded to the collapse of the front of the asymmetric suction disc ($>0°$; Fig. 4.5a).

Distribution of contact pressure along the disc margin

We simulated the spatial distribution of contact pressure around the disc margin for the asymmetric (Body Type A) and symmetric (Body Type C) discs (Fig. 4.5c-e). The minimum contact pressure around the inner perimeter of the suction chamber provided a measure of the
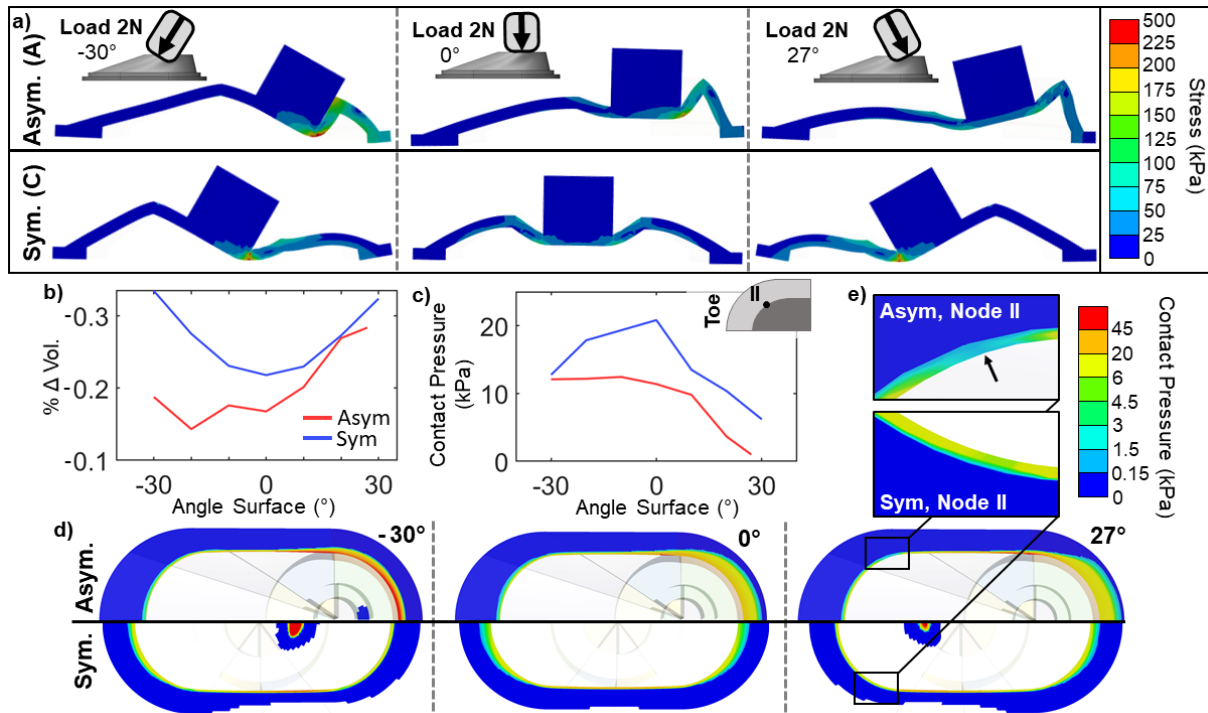
Figure 4.5: **Finite Element Analysis to model the mechanics of adhesion of a suction disc while attached at various angles of attachment and detachment.** a) Top panel: Visualization of the distribution of Von Mises stress (kPa) across a vertical cross-section through the center of suction discs A. Stress plotted when a load (2 N) was applied at an angle of -30°, 0°, and 30°. Bottom panel: Stress plotted for a symmetric suction disc C when a load (2N) was applied at an angle of -30°, 0°, and 30°. b) Plot of percent reduction in the internal volume within the suction chamber with respect to the internal volume for the case of no preload, as a function of the angle of the surface. Measurement of internal volume performed at seven angles during the simulation. c) Plot of the contact pressure (kPa) of node II, located along the innermost perimeter of the disc margin, with respect to the angle of the surface. Measurement performed at seven angles during the simulation for both asymmetric (red) and symmetric (blue) discs. d) Results from FEA visualizing contact pressure (kPa) of the suction disc with respect to angle of the surface. e) Inset images of Node II for the asymmetric (top) and symmetric (bottom) discs. Node II was determined to be the location of lowest contact pressure for the asymmetric disc.

integrity of the seal of the suction chamber [137] (i.e. localized points of low contact pressure indicate a low adhesive strength). The asymmetric disc experienced a contact pressure that was nonuniform across the inner perimeter of the disc margin. A compressive preload on the asymmetric disc generated a high contact pressure on the heel of the disc and lower contact pressure at the toe, which was a consistent trend across all angles tested (Fig. 4.5d). In contrast, the symmetric suction disc demonstrated a more uniform distribution of contact pressure across the inner perimeter of the disc margin for all angles of inclination of the surface.

To quantify the integrity of adhesion throughout the motion simulated, we probed five nodes along the inner perimeter of the disc margin, ranging in position from the toe to the heel. We found that the node along the arc transitioning from the toe to the middle of the suction disc (Node II) experienced the lowest contact pressure (0.9 kPa) for the asymmetric suction disc at $27°$ inclination of the surface (Fig. 4.5c). Visually, this region of localized low contact pressure can be compared between the symmetric and asymmetric disc cases (Fig. 4.5e). The minimum contact pressure of the asymmetric disc dropped from 3.6 kPa at a $20°$ inclination to 0.9 kPa at $30°$ of inclination. In comparison, all nodes for the symmetric disc experienced a contact pressure that was greater than 5 kPa across all angles of inclination of the surface. The symmetric disc had a comparatively higher minimum contact pressure (5.6 kPA) across all angles of the simulation in comparison to the asymmetric disc, and most notably during positive angles of inclination. Overall, we concluded that angles of inclination of the surface $>20°$ were shown through simulation to be predictive of low adhesion for the asymmetric disc due to localized points of low contact pressure.

Modeling to inform anisotropic adhesion

To successfully predict directional adhesion of a suction disc using a computational model, we found it important to characterize both the internal stresses and contact pressures of a disc rather than the change in internal volume. From our FEA model, we found that a change in

volume, which is generally a predictor for adhesion using suction cups, was not a good indicator of directional adhesion. Adhesion of a suction cup is caused by a pressure differential between the internal suction chamber and the ambient fluid. The maximum limit of adhesion would correspond to when all the fluid is expelled from the internal chamber during preload. By this logic, a suction disc would adhere better given a larger decrease in internal volume during preload.

However, we found this that this heuristic did not accurately predict adhesion due to directional loading. In our FEA model, the asymmetric suction disc had its greatest change of internal volume at angles that were experimentally determined to result in no adhesion to the surface. Predicting suction disc performance by the change in internal volume would oversimplify the mechanics involved in directional adhesion. As previously found, adhesion is also dependent on the contact pressure between an adhesive and a surface [137]. For a suction disc, contact pressure is a function of various parameters, including geometry, deformation due to preload, material stiffness, and size. Thus, investigating the differences in spatial distribution of contact pressure between the discs in simulation allowed us to better predict their behaviors.

From the combination of the results from FTIR, FEA, and pull test experiments, we concluded that a disc would detach when the minimum contact pressure along the innermost perimeter of the disc margin in contact with a surface dropped to near zero. As demonstrated by the asymmetric disc, although it underwent large internal changes in volume, the disc did not adhere due to a low contact pressure around the rim of the disc. Given that the quality of the seal is only as strong its weakest point, when the contact pressure around the innermost perimeter of the disc margin dropped to near zero, this corresponded to a compromised seal, allowing the pressure of the fluid inside the suction chamber to equilibrate with the surrounding fluid. An understanding of the changes in internal volume (determines theoretical maximum adhesion) coupled with changes in contact pressure distribution (determines ingress of fluid into the disc) were required to provide a more complete understanding of the anisotropy of adhesion. Using this information, we can design a disc to have a nonuniform contact pressure to design for greater

96

directionality in suction discs.

4.4   Conclusion

Directional adhesives that exhibit morphological computation can reduce the complexity of control in robotic systems. In this paper, we presented a way to design directional adhesives to adhere based on angle in a wet environment. We demonstrated that we can tune the performance of the suction disc by modifying the symmetry of the body, material composition, and incorporation of slits in the disc margin. Careful selection of body asymmetry, in coordination with material stiffness of the suction discs, produced the most successful and repeatable form of directional, anisotropic adhesion.

By tuning the morphology of the adhesives, we incorporated behaviors (i.e. attachment/detachment at appropriate points in a gait cycle) into the body of the suction disc that would otherwise necessitate controlled actuation. Based on the approach and analyses presented here, future work could use these anisotropic suction discs to enable sea star inspired robots capable of robust locomotion in wetted and submerged environments to achieve traction and novel gaits with minimum system complexity.

4.5   Materials and Methods

4.5.1   Fabrication of the discs

We designed the suction discs using computer-aided design (Solidworks, Dassault Systems). We modified the disc symmetry, material stiffness, and presence of slits in the disc margin to determine which were successful in yielding directional adhesion. Across all prototype variants, the constraining dimensions of the body remained constant. The footprint of the suction chamber was an oval of 16 mm diameter, 28 mm length. The suction chamber was terminated by a disc

margin that was 1 mm thick, 1.5 mm offset from the footprint of the suction chamber. The height

of the suction chamber was 5.5 mm across all variants. We designed the discs to have cylindrical

handles of 5 mm height, 6 mm diameter to provide a gripping surface during adhesive pull tests.

For experiments varying the symmetry of the discs, we fabricated two asymmetric discs (Body

Type A and B) and a symmetric disc (Body Type C). The asymmetric discs varied by degree

of asymmetry. Body type A had the largest degree of asymmetry, where the upper cavity was

centered at one full radius from the center of the suction disc (Fig. 4.6c) . The upper cavity of

Body Type B was centered at one half the radius from the center of the suction disc. The upper

cavity of Body Type C was located directly above the center of the suction disc.

We manufactured the suction chamber using a platinum cured silicone with an elastic

modulus at 100% strain of 338 kPa (Dragon Skin 20, Smooth-On, Inc.), which we dyed with

silicone pigment (Silc-Pig, Smooth-On, Inc.). The main body of the suction discs across all

prototypes were composed of this silicone, except for those manufactured to test the impact of

material stiffness on adhesion, in which case we fabricated a suction disc of Body Type A with

a suction chamber composed of silicone of 100% modulus of 662 kPa (MoldStar 30, Smooth-

On, Inc.), 593 kPa (Dragon Skin 30, Smooth-On, Inc.), 338 kPa (Dragon Skin 20, Smooth-On,

Inc.), or 68.9 kPa (Ecoflex 00-20, Smooth-On, Inc.). Each silicone was dyed with a pigment

corresponding to its stiffness. Lastly, we varied the presence and angle of slits in the disc margin.

The slits were angled at either 15°, 30°, or 90° with respect to the longitudinal axis. For each disc

variant, we fabricated the molds using a rigid, photocurable resin (VeroClear, Stratasys Inc.) in

a multimaterial 3D printer (Objet350 Connex3, Stratasys Inc.). To ensure the parts were fully

cured, we aged the molds in an oven at 40°C for 4 hours. The molds containing uncured silicone

were degassed in a vacuum chamber for 10 min and then fully cured in an over for 1 h 30 min at

40°C (Fig. 4.6a). We then added a soft layer of silicone to the disc margin to provide a sealing

layer, following the approach described in previous work [65]. To apply a soft layer, we first

partially cured a mold of the elastomer (Ecoflex 00-30, Smooth-On Inc.) at 40°C for 3 min, then
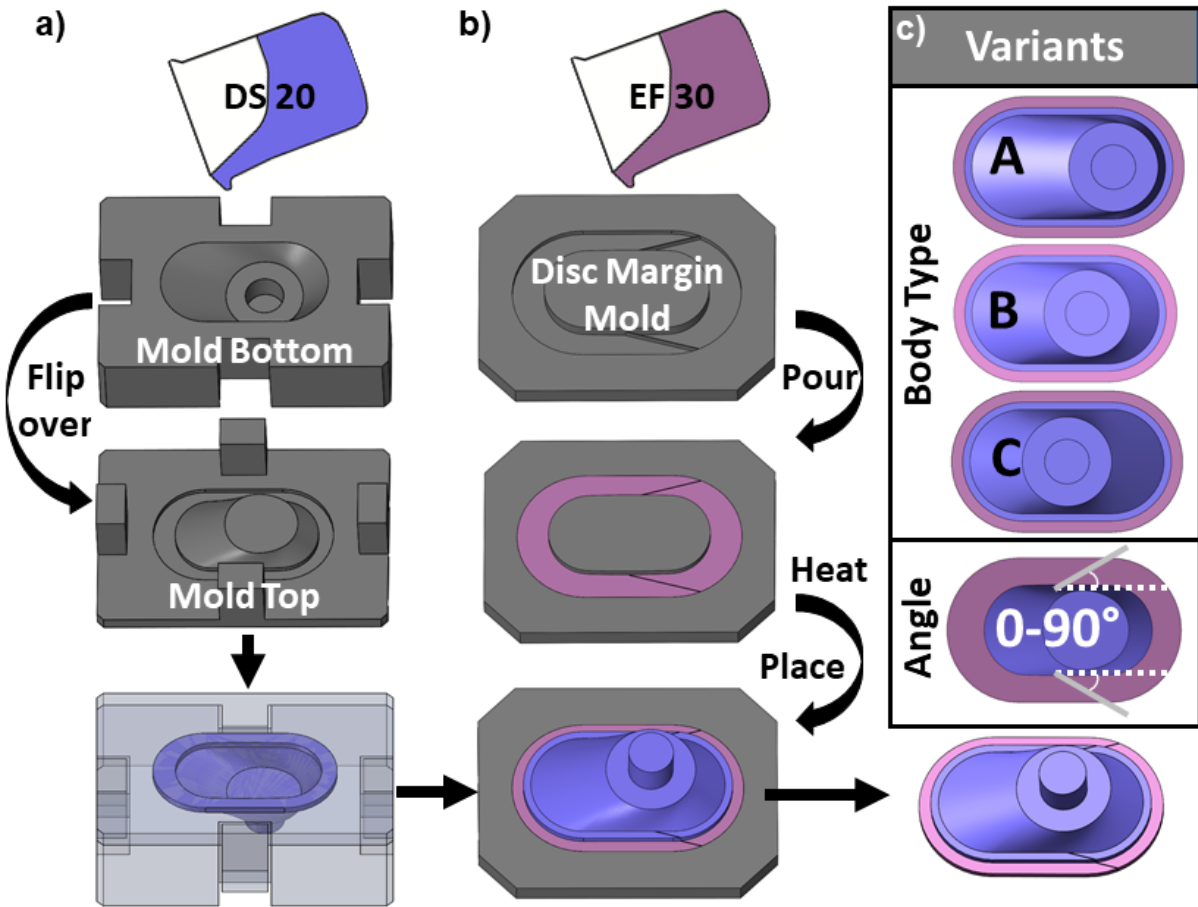
Figure 4.6: **Fabrication of the suction discs.** a) Molding process of the suction chamber using Dragon Skin 20. b) Molding process of the disc margin, using EcoFlex 20. c) Variations of the suction disc based on body type and angle of slits in the disc margin.

applied the suction disc backing to the mold (Fig. 4.6b). We then fully cured the assembly for 1 hr at 40°C.

4.5.2   Experimental evaluation of adhesion

We experimentally tested the adhesives at a fixed velocity. We conducted the pull tests using a universal tensile testing machine (force gauge, 100 N limit, 0.02 N resolution; M7-20, Mark-10 Co.). We mounted the handles of the discs into a clamp that was then held in the upper grips of the tensile testing machine. All pull tests were performed against an angled acrylic plate (angles; 0°, 15°, 30°, 45°) in a tank of water (Fig. 4.7). We engaged the suction disc to the acrylic surface with a preload of 2 N. We performed the pull tests in triplicate, using a rate of retraction of 150 mm· min^{-1} for all prototypes and trials. The adhesive stress was calculated by normalizing the adhesive force by the surface area of the footprint of the suction disc. We evaluated the effect of preload on the different body symmetries. We varied the preload between 0.25 N and 3 N for body types A and C at angles of inclination of -30° and 0°.

4.5.3   Imaging contact

We imaged the contact of the suction disc with a surface using FTIR [96]. The setup of the FTIR station was custom-built, where a 9.7 mm thick acrylic plate internally reflected the light emitted from diodes (natural white light-emitting diodes, 3528-24VDC, Super Bright LEDs, Inc.) that were mounted along the perimeter of the plate. The FTIR plate was statically angled at either -30°, 0°, or 30° to visualize contact throughout three distinctive phases of the gait cycle.

To remove background noise, we dyed the suction discs black using silicone pigment (Silc Pig, Smooth-On, Inc.). We imaged the acrylic surface using a camera (1280 X 780 pixels, 140 pixels cm^{-1}, 40 frames per second, EXILIM EX-FH25, Casio Computer Co., Ltd.). The suction discs were engaged with the surface to a preload of 2 N, and the surface was wetted during the

100
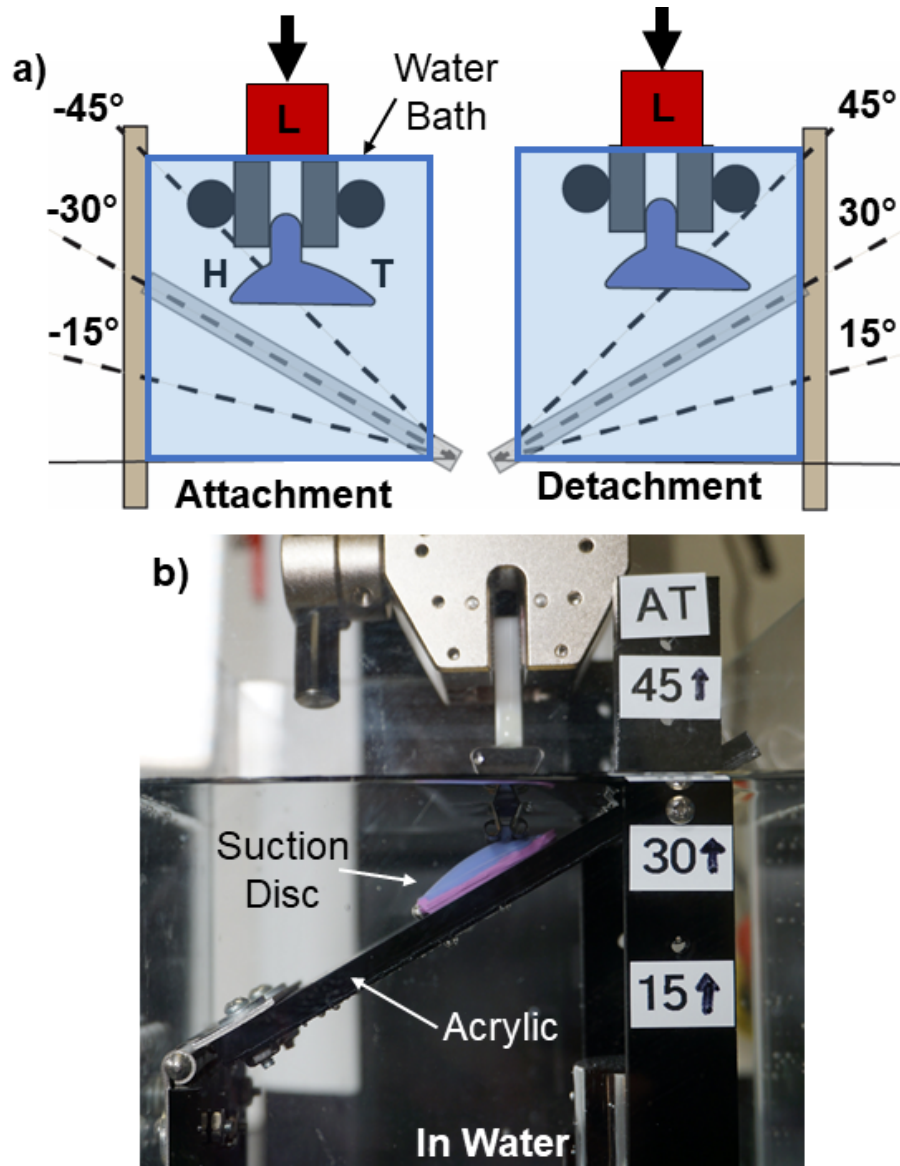
Figure 4.7: **Experimental setup for characterization of adhesion.** a) Schematic demonstrating that each adhesion test was performed in a water bath against an acrylic surface. H denotes heel, T denotes toe of the suction disc. b) Image of experimental setup.

FTIR trials. When the surface was angled to 30° of inclination, we retracted the upper grip of the mechanical testing setup at a rate of 150 mm·min^{-1}, thereby pulling the suction disc from the imaging surface. The point of failure (PoF) was determined to be the last frame of the image sequence during which the suction disc was adhered to the imaging surface.

4.5.4   Modeling the mechanics of directional adhesion

Finite Element Analysis (FEA) was performed using ANSYS Mechanical Version 2019R1. We experimentally determined the material properties of Dragon Skin 20 by performing a tensile test (3342, Instron Inc.) and fitting the Yeoh 3rd order hyperelastic model to the experimental data. Parameters for the Yeoh 3rd order model (C10, C20, C30, D1, D2, D3) were 99 161 Pa, -1604 Pa, 1065.2 Pa, 0 Pa^{-1}, 0 Pa^{-1}, and 0 Pa^{-1}, respectively. Due to the bilateral symmetry of the suction discs, we modeled half of the suction disc using symmetry boundary conditions in FEA to reduce the computation time. The suction discs were predominantly meshed using 20-node brick elements with an average element size of 0.5 mm. The suction discs were preloaded on an inclined steel plate to obtain a vertical reaction force of ≈ 0.28 N. Frictionless contact was assigned between the suction discs and the steel plate. We neglected the effects of the change in fluid pressure inside the cavity of the suction disc as the plate was rotated. We performed a quasi-static simulation and neglected the effects of surface energy and friction at the interface of the suction discs and the steel plate.

Simulating the attachment of the suction disc at a -45° angle of the plate, corresponding to the angle of the surface in the of the experimental setup, is complex due to the large-scale deformation, in addition to the contact and material non-linearities required to model the physics of the suction disc. The simulation for the attachment of the suction disc at an angle of the plate of -45° was unable to converge in our case. Hence, we simulated the suction disc to attach to a plate that rotated from -30° (attachment) to 30° (detachment). . The angle of inclination for the steel plate was then varied from -30° to 30° with the horizontal (with +10° increments) and the

response of the suction discs was recorded. The vertical reaction force, strain energy, Von-Mises stress, deformed shape, contact pressure, and contact status was recorded for variation in the angle of the steel plate between -30° to 30° with 10° increments. The volume of the internal cavity of the suction disc as the plate was rotated was calculated numerically. The internal surface of the suction disc cavity was extracted using Meshmixer 3.3. This extracted surface was then imported to Unity 5.6.7f1 and the volume enclosed by the cavity was numerically calculated.

We quantified the contact pressure of five nodes along the inner perimeter of the suction disc. We probed the contact pressure at the nodes along the plane of symmetry intersecting the inner perimeter, the node along the axis of rotation of the plate intersecting the inner perimeter, and the nodes where the geometry of the inner perimeter transitions from a straight line to a circular arc.

4.6 Acknowledgements

Chapter 4, in part, has been submitted for publication of the material as it may appear in Soft Robotics, 2022. Sandoval, Jessica A.; Ishida, Michael; Jadhav, Saurabh; Huen, Sidney;

Tolley, Michael T. The dissertation author was a primary investigator and co-first author of this paper.

Chapter 5

Towards Bioinspired Wet Adhesives: Lessons from assessing surface structures of the suction disc of intertidal clingfish

Jessica A. Sandoval[1], Jade Sommers[2], Karthik R. Peddireddy[3], Rae M. Robertson-Anderson[3], Michael T. Tolley[1,4], Dimitri D. Deheyn[5]

[1]Materials Science and Engineering Program, Department of Mechanical and Aerospace Engineering, University of California San Diego, 9500 Gilman Dr., La Jolla, CA 92093

[2]Department of Mechanical Engineering, San Diego State University, 5500 Campanile Dr., San Diego, CA 92182

[3]Department of Physics and Biophysics, University of San Diego, 5998 Alcala Park, San Diego, CA 92110

[4]Department of Mechanical and Aerospace Engineering, University of California San Diego, 9500 Gilman Dr., La Jolla, CA 92093

[5]Marine Biology Research Division, Scripps Institution of Oceanography, 9500 Gilman Dr., La Jolla, CA 92093

5.1 Abstract

The clingfish attaches to rough surfaces with considerable strength using an intricate suction disc, which displays complex surface geometries from structures called papillae. However, the exact role of these structures in adhesion is poorly understood. To investigate the relationship between papillae geometry and adhesive performance, we developed an image processing tool that analyzed the surface and structural complexity of papillae, which we then used to model hydrodynamic adhesion. Our tool allowed for the automated analysis of thousands of papillae in specimens across a range of body sizes. The results led us to identify spatial trends in papillae across the complex geometry of the suction disc and to establish fundamental structure-function relationships used in hydrodynamic adhesion. We found that the surface area of papillae changed within a suction disc and with fish size, but that the aspect ratios and channel width between papillae did not. Using a mathematical model, we found that the surface structures can adhere considerably when subjected to disturbances of moderate to high velocities. We concluded that a predominant role of the papillae is to leverage hydrodynamic adhesion and wet friction to reinforce the seal of the suction disc. Overall, the trends in papillae characteristics provided insights on bioinspired designs of surface microstructures for future applications in which adhesion is necessary to attach to diverse surfaces, in terrestrial or aquatic environments, even when subjected to disturbance forces of randomized directionality.

5.2 Introduction

Adhesion involves highly complex and hierarchical structures in nature, and by under-standing the biological intricacies of such adhesive structures, one can improve engineered adhesives [1]. The role of reversible adhesion in both the natural world and in engineering is to temporarily bind to a surface, providing the opportunity to detach and re-attach as needed [1, 24]. In nature, animals use attachment to enhance their fitness, thereby taking advantage of

beneficial opportunities, such as decreased instances of competition and predation or an increased abundance of resources, that would otherwise not be attained [3]. In robotics, reversible adhesion enables improved manipulation [27] and locomotion [10, 28] by managing contact at the interface between the robot and its environment.

Adhesion can be broadly categorized into either dry (i.e., via van der Waals interactions [43]) or wet [138]. Narrowing our focus to wet adhesion, this form of attachment takes advantage of viscous fluids, such as mucosal secretions (whether from terrestrial or aquatic organisms), found between an adhesive pad and a surface [139]. Wet adhesion encompasses both capillarity [140], which is dependent on the surface tension of the fluid, and hydrodynamic forces [138]. Hydrodynamic adhesion, also called Stefan adhesion, is due to viscous forces and is dependent on the rate at which an adhesive structure is pulled from a surface [141]. Both capillarity and hydrodynamic adhesion are responsible for attachment in a variety of organisms, ranging from tree frogs [139, 11] to insects [34] such as ants [12]. The range of wet adhesive performances is related to the properties of the viscous fluids themselves, which have been found to be tunable in certain organisms. As demonstrated in the adhesives of spiders [142] and bee pollen [143], humidity significantly influences its viscosity and subsequently its adhesive strength.

The performance of adhesives is dependent on surface properties (i.e., roughness and lubrication) and environmental conditions (i.e., wetness and disruptive forces) [2]. An increase in surface roughness has been demonstrated to greatly reduce attachment performance in synthetic adhesives [2, 144]. For instance, devices such as suction cups [52] or microstructured adhesives [144] function optimally on flat, smooth surfaces. Modifications to the geometries of the microstructured adhesives, such as the addition of hierarchical structures, have been shown to improve adhesive performance to rough surfaces via enhanced surface conformation [145].

Attachment performance varies based on environmental conditions [2]. Wetness and humidity have been shown to compromise adhesive performance due to the presence of water between the contacting surfaces, excluding dry adhesives from functioning in a wet domain [2].

However, recent developments to synthetic dry adhesives, including modifications to the material composition [128, 87] and structure, such as the addition of cupped microstructures [45], have conferred the ability to adhere to wet surfaces. In addition to wetness, the dislodgement forces per environment type also shape the adhesive devices that can be applied [2]. In a terrestrial environment, gravity—of a predictable direction and magnitude—plays a substantial role in dislodgement. However, in a wet environment, fluid flow—often of unpredictable direction and magnitude—becomes a predominant mode of dislodgement. Adhesive strategies to be employed underwater must be resilient to these more randomized and dynamic disturbances.

The adhesive structures of biological organisms have inspired engineers to develop new designs to improve adhesion [1, 14]. In considering the methodology, previous work in characterizing adhesive surface structures in biological specimens has primarily involved observations and manual quantification of often a small sample size [146]. Manual quantification is a time-intensive process that quantifies a relatively small percentage of adhesive structures across the entire surface used in attachment by an organism. By automating the analyses of surface patterns, we can more efficiently quantify structures involved in adhesion to gain insights that enable us to mimic their designs.

With inspiration from nature, engineers have developed a range of bioinspired adhesives with impressive capabilities [3]. For instance, the use of gecko-inspired, microstructured adhesives has expanded robotic capabilities for applications ranging from manipulating objects with irregular surface topologies [84] and large objects in microgravity [9], to climbing vertical walls [44]. Tree-frog-inspired surface structures have been developed to enable the delicate manipulation of soft tissue during surgery [147]. Remora-inspired adhesion has yielded hitchhiking and manipulation capabilities for underwater robots [19, 148]. In previous work, we have also developed a synthetic suction disc inspired by the clingfish with improved adhesion to various shapes and surface roughnesses [65]. However, the hierarchical mechanisms of adhesion for application to clingfish bioinspired suction discs remained relatively unexplored.

108

Echinoderms [69], octopuses [15, 49], and abalone [46] are just a few examples of organisms that have been investigated for their approaches to reversibly adhere to submerged surfaces. Furthermore, fish, such as the remora [18], cisorid catfish [149, 150], river loach [20], and clingfish [52, 50, 53], have been studied for their adhesive suction discs. The northern clingfish (*Gobiesox maeandricus*) has become an impressive candidate for bioinspired adhesion due to its ability to adhere to rough surfaces while supporting large loads, up to 230 times its body weight [52]. Euthanized specimens have been reported to adhere with an adhesive stress of approximately 40 kPa against coarse (grain size, 269 μm) surface textures [53]. These impressive abilities make the clingfish an ideal candidate for identifying designs to produce high-performance bioinspired adhesives.

The ability of the clingfish to attach to rough surfaces stems from its highly evolved suction disc formed by its modified pelvic and pectoral fins [50]. The suction disc forms a cavity, considered the suction chamber (*SC*), and is lined by a disc margin (*DM*) (Fig. 1 b). The suction chamber maintains subambient pressure, while the disc margin acts to secure and seal its perimeter. A prominent feature of the disc margin is an extensive layer of papillae (*P*), which are geometric, flattened epithelial protrusions (Fig. 1 c). In this study, we focus on clarifying the role of papillae in adhesion.

Papillae have been the subject of only limited studies on their potential role in sealing the suction chamber [53]. Previous work has proposed that the papillae leverage viscous forces that can be used to oppose axial disturbances, thereby securing the perimeter of the disc to the surface [52]. The papillae act to reinforce the disc margin on irregular surfaces, in part by resisting shear and axial dislodgement forces. The papillae come in a diversity of sizes, shapes, and distributions across the suction disc, which had yet to be thoroughly characterized and quantified. By understanding the surface patterns of papillae across the disc, we aim to gain a clearer understanding of their added role in adhesion and to approximate their structure in a biomimetic analog.

To complete this objective, we developed an approach based on image processing software to assess structural complexity in the suction discs of clingfish. This technique employed image processing algorithms used in computer science applications, ranging from fingerprint matching to vehicle traffic monitoring [151], to understand the attributes and extent of the geometric biological structures involved in adhesion. We automated the characterization and quantification of papillae, which provided us with a more complete picture of their geometric characteristics within a given suction disc and across different sizes of suction discs. We used these results to model the impact of the papillae on adhesion due to viscous forces. With the results of the geometric characterizations, we also computed the average shape and size of the papillae, which we then used to design and fabricate biomimetic surface textures. Ultimately, a profound understanding of the inherent complexity—i.e., shapes, sizes, distribution—of papillae would serve to inspire future biomimetic designs of high-performance wet adhesive devices.

5.3 Results

Our analyses combined experimental measurements with image processing techniques and modeling to address the role of papillae in biological adhesion. Our analysis across size in the clingfish highlighted key geometries of the adhesive structures, which we found to be shared by other organisms in the animal kingdom. The geometry of the papillae helps to leverage hydrodynamic forces for rate-dependent adhesion, which would be crucial in the turbulent intertidal habitat of the clingfish. Accordingly, we have replicated these structures in an artificial surface texture and experimentally validated their importance to resisting shear forces.

5.3.1 Visualizing complex surface structures of live specimen

We imaged a live clingfish specimen on an inverted surface using Frustrated Total Internal Reflection (FTIR) [96] contact measurement to visualize the components of the fish involved
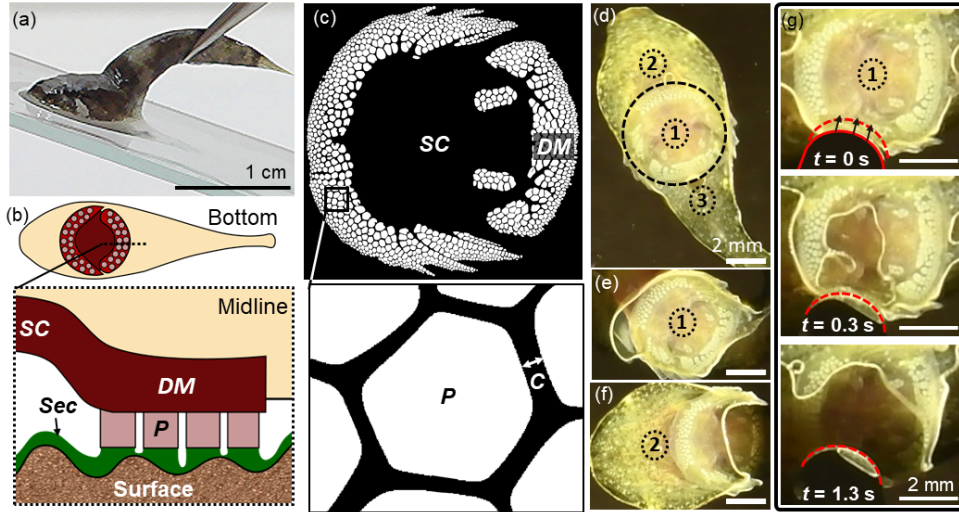
Figure 5.1: **Visualization of the suction disc of the clingfish.** **a)** Image of the profile of a euthanized clingfish adhered to a glass surface. Scale bar, 1 cm. **b)** Schematic of the ventral view of the clingfish. The suction disc is indicated in dark red. Inset: Schematic of the midline view of a suction disc, illustrating the position and role of various components. The suction chamber (*SC*) forms a cavity of subambient pressure that is lined along its perimeter by a disc margin (*DM*), from which extend papillae (*P*). The papillae act to reinforce the disc margin on irregular surfaces and during large disruptive forces. Secretions (*Sec*) are released by the clingfish to coat the attachment surface. We propose that the secretions act to bridge the papillae to the surface. Schematics not drawn to scale. **c)** Binary image of the suction disc of the clingfish, for which only the papillae are shown. Inset: Channels (*C*) form between papillae and are hypothesized to channel fluid from the contact area of a papilla and thus aid in hydrodynamic adhesion. **d)** Frustrated Total Internal Reflection (FTIR) images for visualization of contact between a live clingfish and a flat surface. The imaging surface was transparent and wetted with salt water during the experiment. The clingfish was inverted during imaging, and the FTIR surface was imaged from above. Markers 1-3 denote the isolated chambers that we hypothesize are used to maintain subambient pressure. Chamber 1 is the suction disc (outlined by a dashed line). **e)** Isolation of Chamber 1 by using a blunt spatula to physically detach Chambers 2 and 3 from the wetted surface. **f)** Isolation of Chamber 2 on the wetted surface. **g)** Time series visualizing contact of the clingfish when the suction chamber was disrupted. Disruption occurred by a gentle prodding with a blunt spatula at the intersection of the pelvic and pectoral fins. Spatula, outlined with a solid red line, moved to the final position, denoted by the dashed red line.

with adhering to a surface (Fig. 5.1 b). We observed the formation of three distinctive chambers in which a pressure differential was formed (Fig. 5.1 d-f). The chamber of the suction disc (1) was formed by the union of the modified pelvic and pectoral fins. Two additional cavities formed anterior (2) and posterior (3) to the suction disc. We successfully isolated two of the three cavities involved with providing some contribution of suction (Fig. 5.1 e, f). Although the suction disc (1) is considered the main attachment organ of the clingfish, we hypothesize that the two auxiliary cavities formed anterior and posterior of the suction disc may provide a supplemental contribution to adhesion via suction.

We disrupted the seal of the suction disc by gently prodding the intersection of the pelvic and pectoral fins (Fig. 5.1 g), referred to in previous work as a "vent" [50]. When we disrupted the suction chamber (t = 0 s), the disc remained adhered using other modes of adhesion that therefore excluded suction. As the disc margin detached from the surface (t > 0.3 s), the papillae were the last in contact with the imaging plane. The fish specimen detached itself by peeling its body laterally from the surface. Overall, the ability of the papillae to remain attached to the imaging surface after suction was removed suggested additional adhesive capabilities associated with the papillae, supplementary to sealing the suction chamber.

5.3.2 Suction disc diameter correlates to body size

We conducted our study of suction disc morphologies across five preserved specimens (*Gobiesox maeandricus*) of different sizes, denoted as Size I – V, ordered by increasing body size. The specimens ranged from a body length of 37 mm (Size I; 0.54 g, weight) to 69 mm (Size V; 4.29 g, weight) (Table 5.1). The diameter of the suction disc linearly corresponded to both body size and weight of the clingfish (Fig. 5.2 a).

The total count of papillae per specimen exhibited a positive correlation with body length (Fig. 5.2 b). The fewest number of papillae, which totaled 800, was counted for the smallest specimen (Size I). The greatest number of papillae, 1179, was counted for the largest specimen
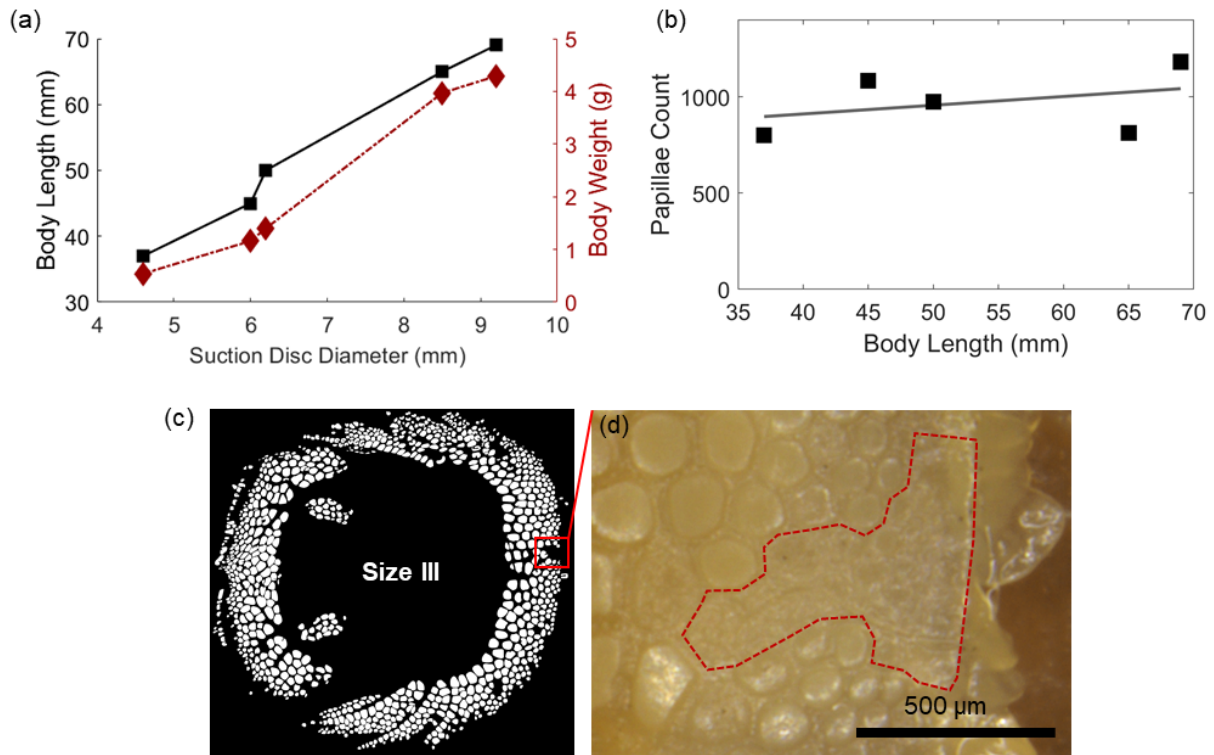
Figure 5.2: **Suction disc diameter corresponded to body size and was dependent on state of preservation. a)** Body length (mm) and weight (g) linearly correlated to the diameter of the suction disc (mm). **b)** Total papillae count across the suction discs positively correlated to body size. Linear fit of the data, solid line. **c)** Binary image of the suction disc of Size III, which was considered to have the greatest degree of deterioration across all suction discs. **d)** Brightfield micrograph of the anterior disc margin. Region outlined by red, dashed line demarcates a region of significant deterioration, which as a result was not represented on the binary image of the suction disc. Scale bar, 500 μm. Quality of preservation was indicated by the visual state of deterioration of the epithelial cells. Preservation primarily affected the papillae along the outer radius and lateral regions of the suction disc. From our observations of the micrographs of the papillae, Size III exhibited the greatest state of visible deterioration of its papillae, primarily along the outer perimeter of the suction disc. Despite its deterioration, we were able to identify and count 974 papillae for Size III.

Table 5.1: **Sizes and weights of the clingfish specimen.** Specimens were measured and weighed prior to imaging.

Size	Weight (g)	Body Length (mm)	Suction Disc Diameter (mm)
I	0.54	37	4.6
II	1.16	45	6.0
III	1.40	50	6.2
IV	3.97	65	8.5
V	4.29	69	9.2

(Size V). The quality of preservation varied across specimens, leading to a limited uncertainty on the count of papillae (this uncertainty was estimated to <7% based on the extent of damaged areas; Fig. 5.2 c, d).

Table 5.2: **Computed values of geometric attributes of papillae.** The contents are as follows: The body length (col. 2); Total papillae count (col. 3); Maximum area of a papilla (col. 4); Minimum area of a papilla (col. 5); Average area computed across all papillae (col. 6); Average aspect ratio computed across all papillae (col. 7); Average minimum channel width (col. 8).

Size	Len. (mm)	Total Pap. (Count)	Max Area ($\times 10^4 \mu m^2$)	Min Area ($\times 10^4 \mu m^2$)	Avg. Area ($\times 10^4 \mu m^2$)	Asp. Rat. ($\pm$ SD)	Min. Width (μm)
I	37	800	5.68	0.086	1.27$\pm$0.85	1.36$\pm$0.36	9.10$\pm$2.73
II	45	1084	4.60	0.041	0.80$\pm$0.58	1.25$\pm$0.25	7.12 $\pm$ 1.92
III	50	974	3.65	0.036	0.86$\pm$0.61	1.37$\pm$0.33	8.73$\pm$2.63
IV	65	813	11.83	0.198	2.38$\pm$1.58	1.33$\pm$0.29	9.34$\pm$3.10
V	69	1179	9.83	0.060	2.08$\pm$1.56	1.36$\pm$0.33	5.94$\pm$1.34

5.3.3 Surface area of papillae scales with body size

We investigated the influence of body size on the surface area of an individual papilla (Fig. 5.3 a). The average area of an individual papilla increased from $(1.27 \pm 0.85) \times 10^4$ μm^2 for the smallest specimen (Size I, $n = 800$ papillae) to $(2.08 \pm 1.56) \times 10^4$ μm^2 (Size V, $n = 1179$ papillae; Table 5.2). We modeled the power-law relationship between the surface area of an individual papilla (A) and body length (l), with a scaling exponent (m) and constant (k) [152].

$$A = k \cdot l^m \tag{5.1}$$
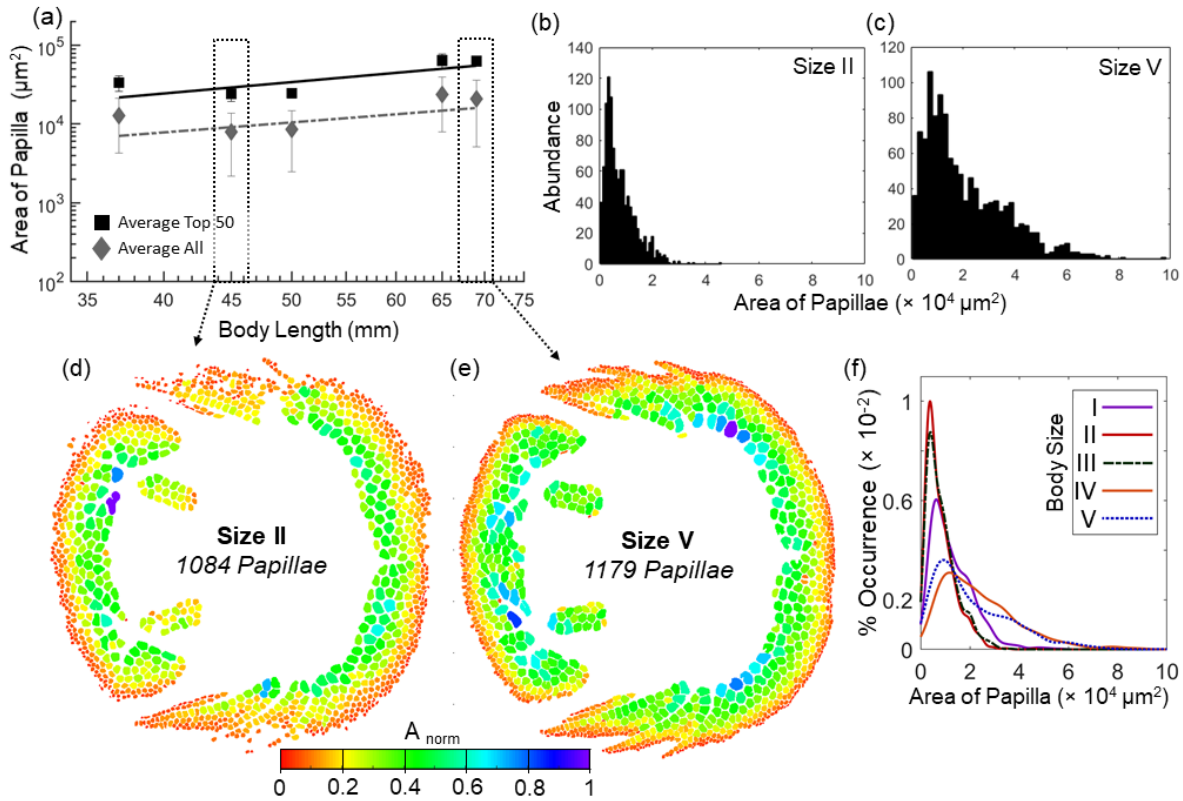
Figure 5.3: **Characterizing the surface area of individual papillae across the suction disc.**
a) Power-law relationship of the surface area (μm2) of all papillae ($n = 4850$; gray diamond) and the 50 largest papillae ($n = 250$; black square) to the length of the clingfish body (mm), represented on a double-logarithmic plot. **b)** Abundance of papillae with respect to the surface area, for Size II. **c)** Abundance of papillae with respect to the surface area, for Size V. **d)** Map for Size II of the distribution of 1084 papillae based on area normalized by the largest papilla (A_{norm}). **e)** Map for Size V of the distribution of 1179 papillae based on A_{norm}. **f)** Kernel probability distributions of surface areas of papillae across all five clingfish body sizes (I-V).

To calculate the scaling exponent and constant, we log-transformed the data and performed a linear regression.

$$log(A) = m \cdot log(l) + log(k) \tag{5.2}$$

We determined that the relationship between the surface area of a papilla and body length was defined by a scaling exponent of 1.3, when considering data from all papillae across all specimens (Fig. 5.3 a; $n = 4850$; $p = 0.13$; r^2-value, 0.60). Given the large variability in the

115

surface areas across the entirety of the suction disc, we also quantified this trend considering only the 50 largest papillae of each individual (Fig. 5.3 a). We observed a more defined relationship between the body length and surface area of the 50 largest papillae, with a scaling exponent of 1.5 ($n = 250$; $p < 0.05$; r^2-value, 0.81). The scaling exponent between 1.3 and 1.5 signified that the body size has a positive, nonlinear effect on the size of the papillae.

Other groups of clingfish, such as the much larger Chilean clingfish (*Sicyases sanguineus*), demonstrated a similar relationship with body size and surface area. For instance, in samples of preserved Chilean clingfish (body length, 29.4 cm; disc diameter, 11.6 cm), the papillae measured to surface areas of roughly $1.9 – 3.0 \times 10^7$ μm^2, two orders of magnitude greater than the papillae of *Gobiesox maeandricus* (Fig. 5.4).

Figure 5.4: **Example of large papillae in Chilean clingfish.** Preserved specimen (*Sicyases sanguineus*) demonstrated the influence of body size on the surface area of the papillae. The body length was measured to 29.4 cm, and disc diameter was measured to 11.6 cm. The surface areas of the papillae, labelled as 1, 2, 3, and 4, were measured to be 2.226, 3.02, 1.91, and 2.23 $\times 10^7$ μm^2, respectively. Specimen was loaned from the Scripps Marine Vertebrate Collection and originally collected from Viña del Mar, Chile.

5.3.4   Surface area of papillae decreases radially

We analyzed the distributions of papillae based on the surface area across the entirety of each suction disc (Fig. 5.3 b, c). We observed that the distributions of surface area exhibited a right-skewed asymmetry, and thus a larger concentration of smaller papillae across every size of the suction disc (Fig. 5.5 and 5.3 b, c). The Kernel probability distributions of the surface area also showed a right-skewed asymmetry across all body sizes (Fig. 5.3 f). Therefore, the suction disc of the clingfish favors a larger density of smaller papillae, and this trend is independent of body size.
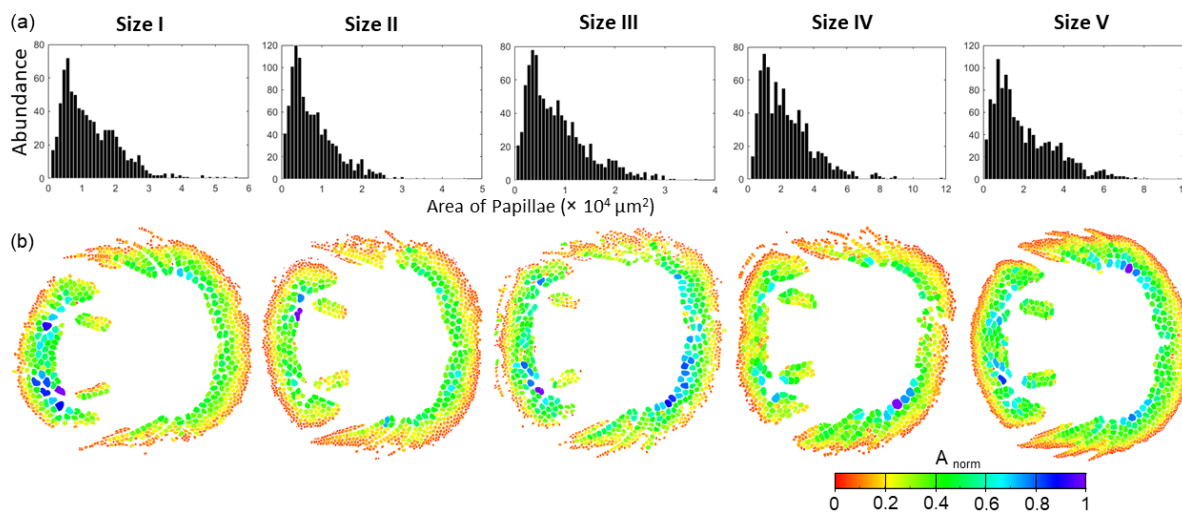
Figure 5.5: **Surface area of papillae across all body sizes. a)** Abundances based on surface area of individual papilla (μm^2). Sizes I-V in order of increasing body length. **b)** Normalized surface area distributed as heat map for all body sizes.

To understand the spatial distribution of papillae based on area, we normalized (A_{norm}) the surface area of an individual papilla (A_i) to that of the largest papilla (A_{max}) for each suction disc ($A_{norm} = A_i/A_{max}$). We chose to normalize the surface area to elucidate trends in papillae distribution across different body sizes (Fig. 5.5). For each of the five suction discs, the distribution of A_{norm} was mapped to a binary image [151], which was generated by isolating the papillae, or regions of interest, from the original micrographs. To demonstrate spatial trends

across the range of body sizes, we showed representative examples of small (Size II) and large (Size V) body sizes (Fig. 5.3 d, e).

As demonstrated in Sizes II and V, a clear trend existed in the distribution of papillae when considering their surface area. We observed a decrease in the surface areas of the papillae when extending from the center of the disc along the radius to the outermost perimeter. The largest papillae ($A_{norm} > 0.80$) were found to be located along the innermost radius of the anterior and posterior regions of the suction disc. Conversely, the smallest papillae ($A_{norm} < 0.20$) were located consistently along the outermost radius of the disc. On average, eight rows of papillae were expressed in both the anterior and posterior regions of the suction disc, irrespective of body size. The lateral regions of the disc margin exhibited a greater concentration of small papillae ($A_{norm} < 0.20$), with comparison to both anterior and posterior regions. These trends were consistent across all five body sizes of the clingfish specimen (Fig. 5.5).

We sought to understand the probability density functions of papillae based on location along the suction disc. We segmented one suction disc (Size V) based on region, differentiating between the anterior, posterior, and lateral components of the disc margin. Of the anterior and posterior, we deconstructed the disc into the components of "inner" (three rows, innermost radius) and "outer" (two rows, outermost radius). We also isolated the lateral components of the disc margin (Fig. 5.6 a, d-f).

A total of 357, 184, and 408 papillae were counted for the outer, inner, and lateral components, respectively. We superimposed the Kernel probability distributions of the isolated regions (Fig. 5.6 c). Similar to the heat maps, the outermost regions contained the greatest abundance of small papillae, with an average area of $(1.00 \pm 0.50) \times 10^4$ μm^2 (Fig. 5.6 g). The innermost regions contained the greatest abundance of large papillae, with an average area of $(4.27 \pm 1.40) \times 10^4$ μm^2 (Fig. 5.6 h). Along the radius, the papillae increased in size roughly 4.2 times from the outermost to the innermost rows. The distributions of size were symmetric for both the inner and outer regions of the anterior and posterior disc margins (Fig. 5.6 c). Conversely, we
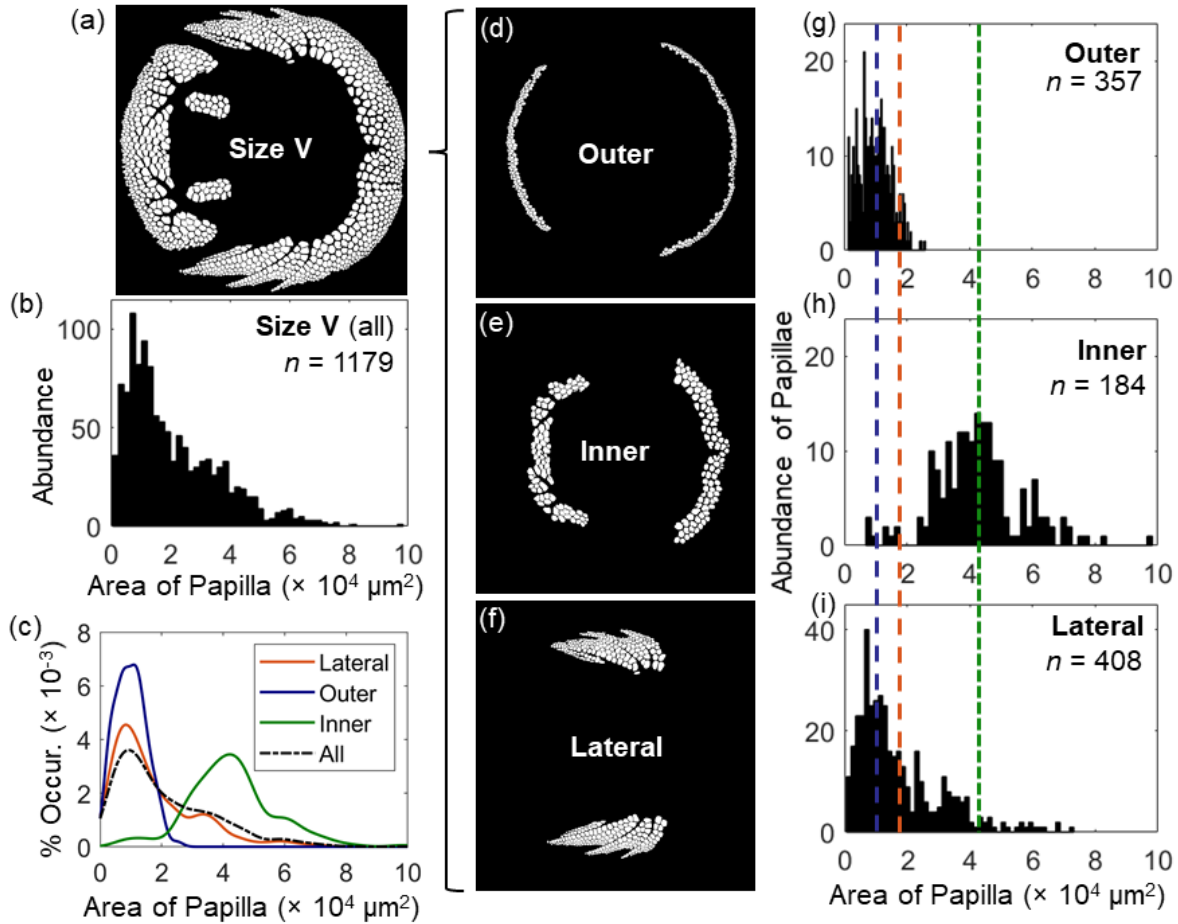
Figure 5.6: **Segmentation of the suction disc for analysis of the spatial distribution of papillae based on size. a)** Binary image of the suction disc of Size V. **b)** Abundance of papillae based on surface area (μm^2). **c)** Kernel probability distribution of the surface area of papillae (μm^2). Distributions of lateral components, orange; outer, blue; inner, green; and across all papillae of the suction disc, dashed black. **d)** Binary image of the outer rows of the disc. **e)** Binary image of the inner rows of the disc. **f)** Binary image of lateral components. **g)** Abundance of papillae based on the surface area for the outer disc margin. The mean is represented as the blue dashed line, centered at $1.00 \times 10^4 \mu m^2$. **h)** Abundance of papillae based on the surface area for the inner disc margin. The mean is represented as the green dashed line, centered at 4.27 $\times 10^4 \mu m^2$. **i)** Abundance of papillae based on the surface area for lateral components. The mean is represented as the orange dashed line, centered at $1.74 \times 10^4 \ \mu m^2$.

observed a right-skewed asymmetry in the distribution of surface area for the lateral fin regions, consistent with a greater, but nonhomogenous, concentration of small papillae (Fig. 5.6 i).

5.3.5 Aspect ratio of papillae independent of body size

We generated an image processing procedure to automatically calculate the aspect ratio across all papillae of the suction disc. The aspect ratio is a measure of the elongation of a papilla. To perform this calculation, our program automatically detected each papilla and drew the minimum bounding box around the region of interest (*ROI*) such that all sides and vertices were included. We then calculated the aspect ratio as the division of the longest side (*l*) of the bounding box by the shortest side (*w*, aspect ratio $= l/w$).

The average aspect ratio of the papilla was consistent across the body sizes, centered around 1.3 (Fig. 5.7 a). We therefore concluded that the aspect ratio of the papillae was independent of the body size of the clingfish. Comparing the specimen, the lowest average aspect ratio was calculated to be 1.25 ± 0.25 (Size II, $n = 1084$), whereas the largest ratio was 1.37 ± 0.33 (Size III, $n = 974$). To compare, a regular hexagon (*RH*) has an aspect ratio of 1.15. Therefore, we concluded that the papillae are elongated structures (Fig. 5.7 e), which are consistent across body sizes.

We then mapped the aspect ratio to the binary image of the suction disc for all body sizes. We noted a greater concentration of elongated papillae along the outer perimeter of the suction disc and along the lateral fin regions (Fig. 5.7 b and 5.8). Conversely, we observed less elongated papillae along the anterior, innermost region of the suction disc. Furthermore, we found a high abundance of elongated papillae at the innermost region of the posterior margin. The anterior and posterior papillae therefore exhibited divergent behaviors. Thus, the distribution of elongated papillae differed depending on the location along the suction disc.

The orientation of an elongated papilla was also dependent on its location (Fig. 5.7 b). The outermost papillae of the anterior disc margin were elongated laterally, parallel to the contour
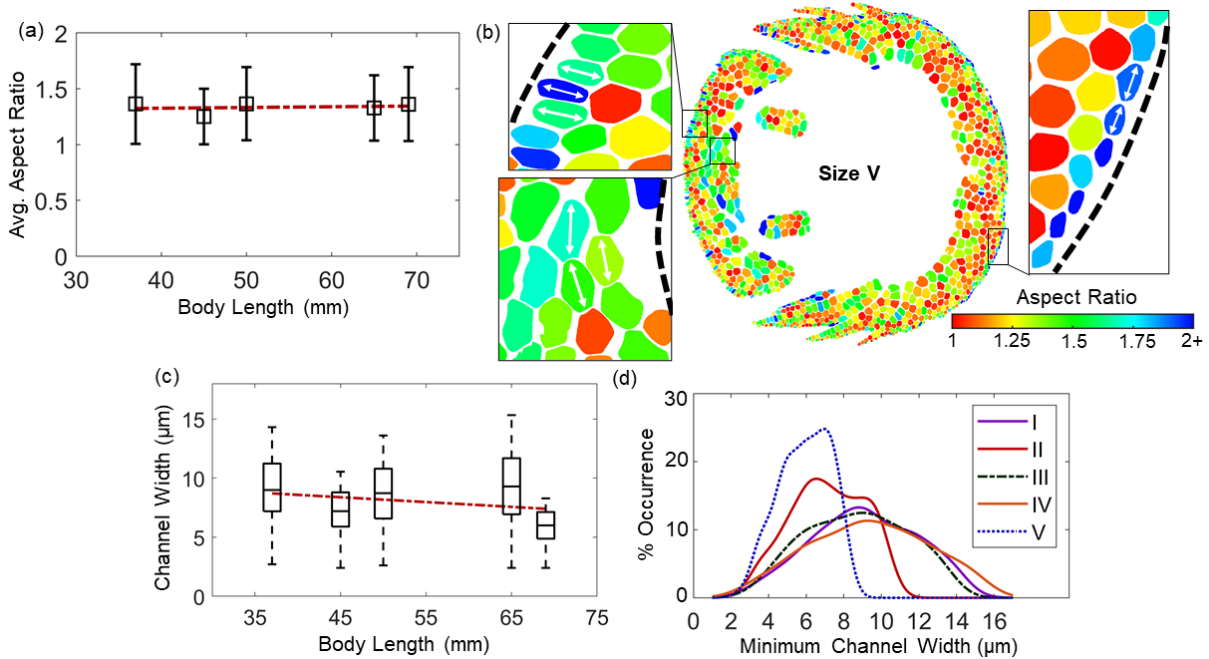
Figure 5.7: **Characterizing aspect ratio and channel width to inform an idealized, average papilla. a.)** Aspect ratio averaged across all papillae per specimen. Linear fit of data, red dashed line. All averages centered around a ratio of 1.3. **b)** Aspect ratio mapped to the suction disc for Size V. Aspect ratio ranges between 1 and 2. Inset, top left: Papillae (Aspect ratio ¿ 1.3) elongated anteroposteriorly along the outer posterior disc margin, indicated by arrows. Elongation perpendicular to the contour of the outer disc margin (dashed line). Inset, bottom left: Papillae along the inner posterior disc margin elongated laterally, tangent to the contour of the inner disc margin (dashed line). Inset, right: Papillae elongated laterally along the outer anterior disc margin, parallel to the contour of the outer disc margin (dashed line). **c)** Box plot of the minimum channel width (μm) for all five body sizes. Linear fit of data (dashed red line; slope: -0.04; y-intercept: 10.2). **d)** Kernel probability distributions of the minimum channel widths for body sizes I-V.

of the outer disc margin. In contrast, the outermost papillae of the posterior disc margin were elongated anteroposteriorly, perpendicular to the contour of the outer disc margin. The innermost papillae of the posterior margin exhibited lateral elongation, tangent to the contour of the inner disc margin. The observations in elongation and orientations were consistent across body sizes (Fig. 5.8). We hypothesize that the differences in orientations may play a role in reinforcing the perimeter of the suction chamber.

121
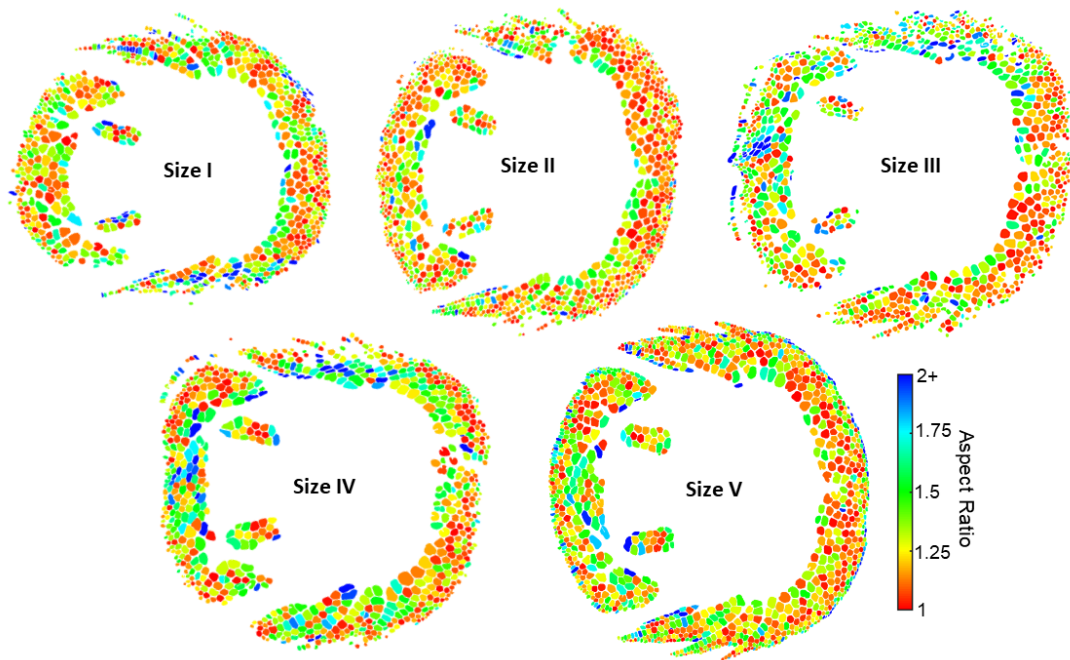
Figure 5.8: **Aspect ratio of papillae across all body sizes.** Aspect ratio was represented as a heat map, where red denoted an elongation of 1, and blue an elongation of 2 or greater. A larger aspect ratio indicated a more linear papilla.

5.3.6   Channels between papillae direct fluid from the contact area

We hypothesized that the channels between the papillae function to shuttle fluid from the contact area, thereby reducing the distance of separation and lowering the papillae to the surface. Previous work has demonstrated that microchannels surrounding surface structures used in wet adhesion channel fluid from beneath the biological adhesive pads, thus reducing the distance of separation between the epithelium to the surface on which the animal is attached [147].

To understand the microchannels used by the clingfish, we created a separate processing technique to calculate the minimum channel width between papillae. For this computation, we calculated for every pixel along the circumference of a papilla, the distance to its nearest neighboring papilla. We averaged across the five smallest distances per papilla to report the minimum distance to its neighbor, which we considered to be the minimum channel width. This computation was performed across the entirety of the suction disc, and the average per disc was

then calculated.

We found that the minimum channel spacing between papillae was consistent and of the same order of magnitude, ranging between $9.1 \pm 2.7\ \mu m$ (Size I) and $5.9 \pm 1.3\ \mu m$ (Size V) for the smallest and largest body sizes, respectively (Fig. 5.7 c). The largest body size (V) exhibited the smallest average channel width, whereas the smallest body size (I) exhibited the second largest channel width, resulting in a negatively sloped trend line (Fig. 5.7 c). The probability distributions of the channel width were symmetrical and did not exhibit skewness (Fig. 5.7 d).

We noticed that the channel width was affected by the degree of degradation of the specimen. A more degraded disc exhibited a loss of papillae along the outer perimeter, which by observation had narrower channels. Therefore, specimens, such as Size V, that were better preserved generally had a smaller average channel spacing. Taking this into account, we concluded that overall the channel width was independent of body size, and centered around an average spacing of $8.05\ \mu m$ across the five specimens (Fig. 5.7 c).

5.3.7   Geometric shape of papilla predominantly hexagonal

We characterized the predominant shape of the papilla for the largest clingfish specimen (Size V) and labelled a binary image by assigning colors to represent the number of sides of the structures (Fig. 5.9 a). We performed this task manually by referring to the original micrographs, where the number of sides was clearly delineated. The binary image, by contrast, exhibited smoothing of the vertices of the shapes, rending subtle side lengths indistinguishable to automated image processing techniques.

Of the papillae in Size V, we found that 52% were hexagonally shaped (Fig. 5.9 c, d and 5.10). The second most abundant shape was pentagonal, representing 38.3% of all papillae (Fig. 5.9 b, d). The prevalence of other shapes fell considerably to 4.8 and 4.3% for heptagons and quadrilaterals, respectively (Fig. 5.9 e). We considered 85 of the papillae to be too deteriorated to yield a definitive conclusion on shape.

123
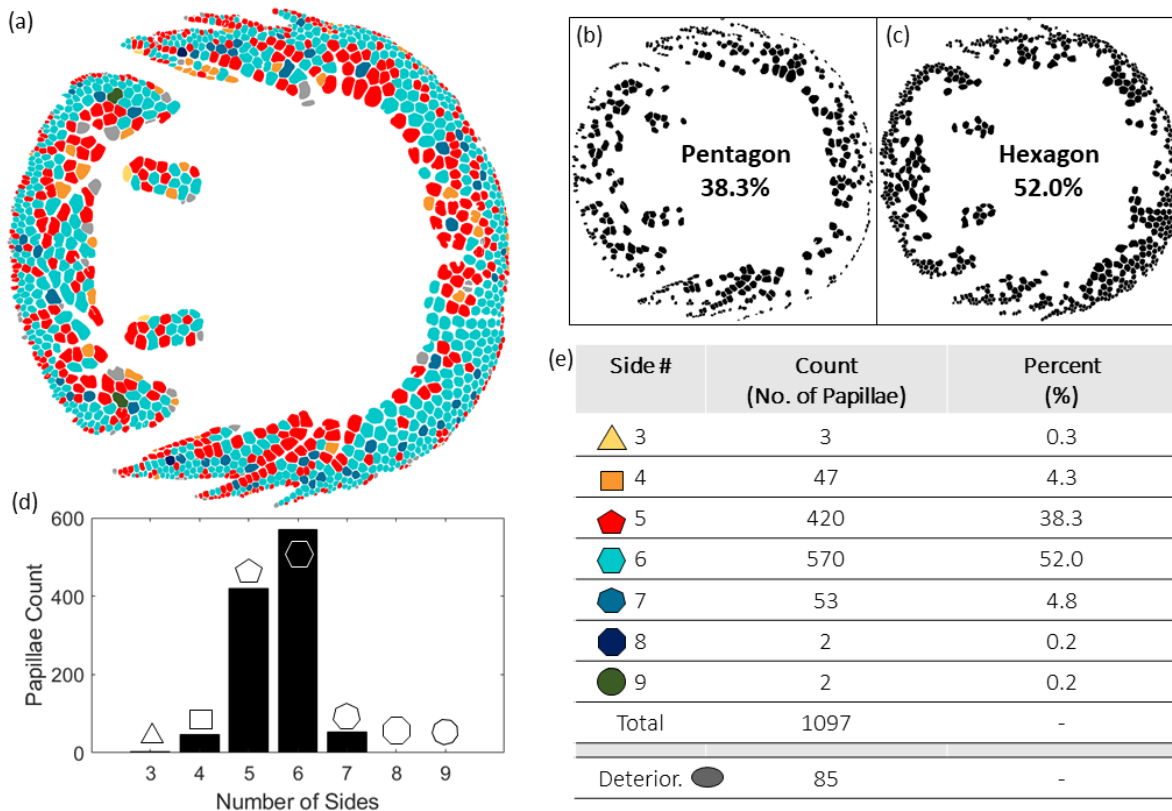
Figure 5.9: **Geometric shape of papillae across the suction disc for Size V. a)** Map of the distribution of papillae, based on the number of sides. Color coordination is as follows: three sides (light yellow), four sides (light orange), five sides (red), six sides (light turquoise), seven sides (navy blue), eight sides (dark blue), nine sides (dark green), deteriorated (gray). **b)** Binary image of only pentagonal papillae. **c)** Binary image of only hexagonal papillae. **d)** Abundance of papillae based on the number of sides. **e)** Table detailing the abundance and percent occurrence of the different shapes. Papillae that were considered too deteriorated to be quantified for the number of sides are indicated by "Deterior."

In the map detailing the distribution of shapes, higher concentrations of pentagons were found along the inner and outermost perimeters of the suction disc and also along the lateral fin rays (Fig. 5.9 a). Conversely, hexagonal structures were most prevalent, filling in the space between the inner and outer perimeters. We observed an appreciable presence of shapes that have less than five sides or greater than six. We suggest that the prevalence of such shapes aided with packing the non-uniform surface of the disc margin of the clingfish.
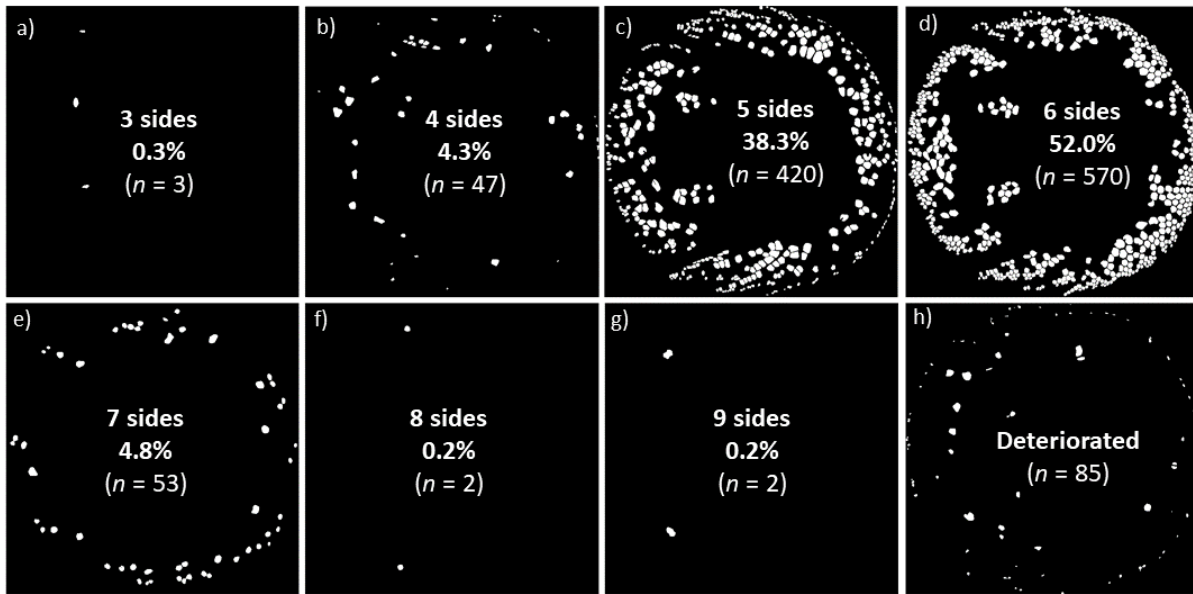
Figure 5.10: **Binary maps of papillae based on number of sides for clingfish Size V.** White regions of interest represented the location of papillae with the specified number of sides. Count of papillae, *n*. **a) – g)** Papillae with 3-9 sides, respectively. **h)** Papillae that were considered to be too deteriorated to be quantified for their number of sides.

5.3.8   Characterization of the secretion

We investigated the linear viscoelastic properties of the secretions found beneath the suction disc (Fig. 5.11 a-c). As demonstrated using optical microscopy, the secretions when dried crystallized into a ferning pattern, indicative of a mucosal contribution to its composition (Fig. 5.11 b) [58, 59]. We performed passive microrheological measurements of the clingfish secretion to determine the elastic modulus (G'(ω)), viscous modulus (G"(ω)), and viscosity. We found that the viscous modulus was over an order of magnitude larger than the elastic modulus at all explored frequencies (Fig. 5.11 c). This finding indicated that the secretion behaves as a viscous, not viscoelastic, fluid at nano- and microscales of interaction [153]. The viscosity of the secretion was calculated to be 6.5 ± 1 mPa·s; by comparison, the viscosity of water is 1 mPa·s. The value of viscosity calculated from the microrheological experiments was then used to model its impact on hydrodynamic adhesion across the entirety of the suction disc.
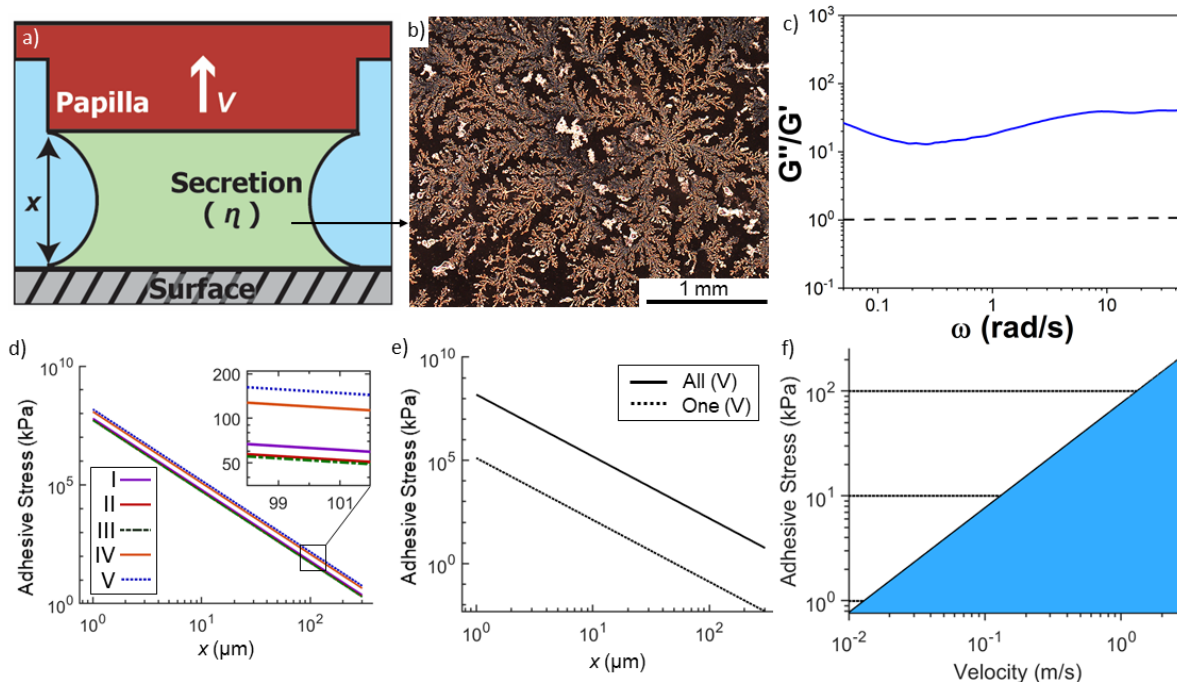
Figure 5.11: **Modeling the contribution of papillae to Stefan adhesion. a)** Schematic representing the papillae as a parallel plate above a surface, separated by a distance (x). Secretions of viscosity (η) fill the spacing between the two faces. The papilla is pulled perpendicular to the surface with a velocity (V), which is representative of external disturbances. **b)** Ferning pattern indicative of the mucosal content observed under microscopy of the secretion. **c)** Ratio of the viscous modulus ($G''(\omega)$) to the elastic modulus ($G'(\omega)$), i.e., the loss tangent, of the isolated secretion. Secretion determined to be viscous as G''/G' is 20-30 over the entire frequency range. **d)** Double-logarithmic plot of the model of Stefan adhesion across a range of separation distances, for all five clingfish specimens. Velocity of disturbance, 2 m/s in simulation. Viscosity of secretion, 6.5 mPa·s. Total surface area per specimen was used to compute the adhesive stress. **e)** Double-logarithmic plot of the model of Stefan adhesion for Size V only. The adhesive stresses were modeled for one papilla of average surface area ($2.08 \times 10^4 \mu m^2$, "One," dashed line) and across all papillae for Size V (total, $2.46 \times 10^7 \mu m^2$, "All," solid line). **f)** Double-logarithmic plot modeling Stefan adhesion across all papillae for Size V, varying the velocity of disturbance from 0 to 3 m/s. This range encompasses the fluid flow velocities that the clingfish is known to withstand in nature. Distance of separation: 100 μm. The shaded region indicates the contribution due to Stefan adhesion. The dotted line represents the adhesive stresses of 1, 10, and 100 kPa at 0.01, 0.13, and 1.31 m/s, respectively.

126

5.3.9 Modeling the contribution of hydrodynamic adhesion

With an understanding of the geometric characteristics of the papillae and microrheological properties of the secretion, we estimated their contributions to hydrodynamic adhesion. The secretions produced by live clingfish fill the space between the papillae and a surface and would resist axial separation. Hydrodynamic adhesion perpendicular to the surface (Stefan adhesion, F_{Stef}) can be modeled for the case of two parallel, rigid, circular plates of radius (r) separated from each other by a distance (x) (Fig. 5.11 a) [146]. A fluid layer of viscosity (η) fills the space between the two plates, which separate with a relative velocity ($V = \delta x / \delta t$) The resistance to separation is the rate-dependent adhesive force. We generalized the calculation of Stefan adhesion to Equation (5.3), to consider the surface area of the papilla (A), which accounted for noncircular surface geometries [146].

$$F_{Stef} = \frac{3\pi r^4 \eta}{2x^3} \cdot \frac{\delta x}{\delta t} \approx \frac{3A^2 \eta}{2\pi x^3} \cdot \frac{\delta x}{\delta t} \tag{5.3}$$

By Equation (5.3), when pulled axially, Stefan adhesion is directly proportional to the rate of the disturbance, viscosity of the secretion, and surface area of the papillae. Adhesion is inversely related to the distance of separation between a papilla and the surface to which it is adhered. Therefore, by reducing the distance of separation, the papillae can increase the contribution of adhesion due to viscous forces.

Using Equation (5.3), we modeled the influence of papillae on adhesion, varying either their distance of separation or the velocity of an axial disturbance. Adhesive stress (σ_{Stef}) was calculated as the amount of resistance to separation due to hydrodynamic forces (F_{Stef}) as a function of the contact surface area (A) ($\sigma_{Stef} = F_{Stef} / A$). In the models, we set the viscosity of the secretion to be 6.5 mPa·s, as determined from the microrheological experiments.

We modeled how varying the distance of separation to a surface impacted adhesion. We evaluated the adhesive stress for a range of separation distances, varying from 1 to 300 μm.

We chose this range based on the previous literature in tree frogs, which reported a distance of separation that varied between 5 and 300 μm [11]. For this study, we also used a velocity of disturbance of 2 m/s. We chose this velocity from an estimate of the forces experienced by the clingfish in its natural habitat [51]. The adhesive stresses across the five body sizes all exhibited exponential decay given an increasing distance of separation from the surface (Fig. 5.11 d). That is, the greater the distance to the surface, the less of a role the papillae have in adhesion. Additionally, the largest of the clingfish body sizes (V) was modeled to have between 2.5 and 3 times greater adhesive stress than the smallest of body sizes (I, II).

We modeled the cumulative effect of papillae on adhesion for one specimen (Size V; Fig. 5.11 e). The surface area of the single papilla, labelled as "one," was the average surface area computed for Size V, 2.08×10^4 μm^2. The total surface area of Size V was calculated to be 2.46×10^7 μm^2. Adhesive stress across all of the papillae of Size V was three orders of magnitude greater than that of a single papilla, hence the linear relation to area (Fig. 5.11 c). In high abundances, the papillae greatly increase their collective surface area, thereby increasing their impact on Stefan adhesion.

We modeled the impact of velocity on adhesion, given a disturbance acting perpendicularly on a clingfish (Size V; Fig. 5.11 f). For this study, we fixed the distance of separation to 100 μm, an intermediate value from our previously reported range. We modeled the range of axial velocities from 0 to 3 m/s. We chose this range since the body of a clingfish is projected to withstand disturbances between 2 and 3 m/s in the intertidal, while their habitat has registered wave surges up to 8 m/s [51]. Turbulent fluid flow would result in an axial lift of the body of the clingfish. We approximated the axial velocity due to turbulence to be roughly equal to the velocity of the fluid in the environment.

Given that Stefan adhesion scales linearly with velocity, we found that flow velocities of 0.01, 0.13, and 1.31 m/s resulted in adhesive stresses on the order of 1, 10, and 100 kPa, respectively. We represented this linear relationship on a logarithmic plot to emphasize the

contribution of Stefan adhesion at velocities of different orders of magnitude. In sum, the velocity of an axial disturbance greatly influenced the adhesive stress achieved by the papillae. Stefan adhesion provided by the papillae would therefore be most beneficial in instances of disturbances of moderate to high velocities on the order of or greater than 0.1 m/s. The papillae could therefore act as a fail-safe to the suction disc, such that at higher vertical velocities of the clingfish due to a disturbance, the papillae would adhere with greater strength to a surface of the rocky intertidal. Adhesion of the papillae would ensure that the edge of the disc margin does not detach from its substrate, which would compromise the subambient pressure of the suction chamber.

5.3.10   Development of a surface pattern mimicking the papillae

We developed a biomimetic surface pattern to empirically test the effect of the geometry of the papillae when subjected to shear forces (Fig. 5.12). From the results of the automated characterizations, we computed an "average" papilla, which resulted in an elongated hexagon (*EH*, aspect ratio, 1.3) which was consistent with the averages computed across all body sizes of clingfish (Fig. 5.12 a, d). The surface area of the individual biomimetic structure was designed to be equal to the average area of an individual papilla (Size V), scaled by a factor of 10 (total surface area, 0.21 mm^2). The biomimetic surface pattern was compared to a pattern of regular hexagons (*RH*) and a pattern of squares (*S*), both with the same surface area. We varied the orientation of the elongated hexagon, such that the hexagon was either oriented along (*EH*) or orthogonal to (*EH90*) the axis of elongation (Fig. 5.12 c). The control was devoid of surface structures. The surface patterns were composed of silicone and were pulled in shear along an acrylic surface lubricated with glycerol (viscosity, 1.4 Pa·s), which was used as an approximation of the secretions.

We found that the averaged, biomimetic papillae (*EH*) experienced the greatest shear stress, in comparison to all other geometries. The biomimetic texture resulted in a shear stress that was roughly twice that of either the regular hexagon or square textures and 80 times that of
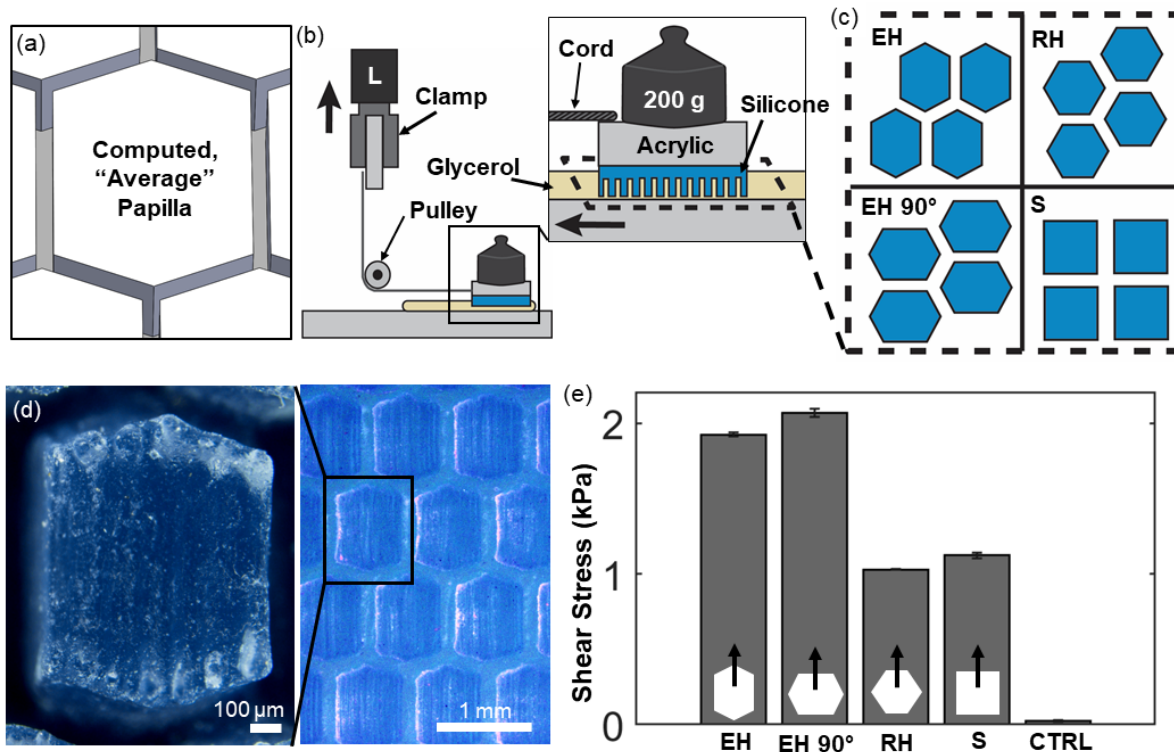
Figure 5.12: **Experimentally validating the effect of the geometry of the surface patterns on resistance to shear disturbances.** **a)** Computer-generated rendering of an "average" papilla, based on the average shape, channel width, surface area, and aspect ratio. **b)** Experimental setup to validate the effect of the surface structures on shear stress. The surface structures were composed of silicone (dyed in blue to ease visualization) that were then bonded to a stiff acrylic backing. An inextensible cord was applied to the acrylic backings and routed through a frictionless pulley to a clamp connected to a load cell of a universal testing machine. A preload of 200 g was applied to the backing. **c)** Schematic of the patterns tested, consisting of either elongated hexagons (*EH*), regular hexagons (*RH*), elongated hexagons oriented orthogonal to the direction of motion (*EH90*), or squares (*S*). All structures were designed with the same surface area. **d)** Biomimetic surface structure (*EH*). All structures were composed of silicone. Scale bar, 100 μm. Inset: scale bar, 1 mm. **e)** Performance of the surface structures when pulled in shear on a glycerol-lubricated surface. Control was a silicone surface devoid of surface structures. All trials performed in triplicate.

the control. All surface textures outperformed the control, demonstrating the need for surface structuring to maintain attachment while subjected to shear forces.

Additionally, the orientation of the elongated hexagon when compared to the direction of motion only marginally impacted the shear stress of the surface structure (2.07 ± 0.03 kPa to 1.92 ± 0.01 kPa, for *EH90* and *EH*, respectively). We therefore did not notice an orientation preference

of the biomimetic structure.

These experimental results demonstrate the utility of surface structures in resisting shear forces on lubricated surfaces. This experiment also supports the conclusion that an elongation of a surface structure best improves attachment performance.

5.4   Discussion

The suction disc of the clingfish is highly complex and employs a variety of attachment processes at multiple scales to optimally adhere to rough surfaces underwater. The papillae of the clingfish that we examined exhibited distinctive morphological trends (surface area, channel spacing, shape, and elongation), most of which were independent of body size. In this work, we highlighted the importance of the geometric arrangements and characteristics of the papillae, which aided in attachment via hydrodynamic adhesion. We concluded that these structures, coupled with the properties of the secretions, have the capabilities to reinforce the disc margin by preventing a leak in the seal of the suction chamber. These surface structures are therefore vital at resisting both axial and shear dislodgement forces and are viable candidates for replication in biomimetic analogs. We implemented an "averaged" papilla in a biomimetic surface texture to experimentally validate our hypotheses and demonstrate a potential use application.

5.4.1   Geometric shape helps to resist shear forces

The papillae of the clingfish were predominantly hexagonal, followed by pentagonal, in shape. Theoretical models of epithelial cell division to fill an irregular global shape found that the distribution of epithelial cells converged to hexagonal (46.4%), pentagonal (28.9%), and heptagonal (20.8%) when driven by stochastic cell division alone [154]. The similarities in the ratios of shapes between the theoretical model and the clingfish may suggest a function of the shapes of the papillae. Hexagons would be used to effectively pack of the surface, while other

shapes would be used to compensate for the irregular topologies of the disc margin [154].

We have experimentally demonstrated that the shape of the surface structure affected its resulting shear stress. Elongated hexagons, of the same aspect ratio of the averaged papillae, were the best-performing shape in shear. This finding is consistent with previous work, in which textures with elongated hexagonal shapes were found to increase the coefficient of friction to wet surfaces in comparison to other polygonal shapes [147].

We experimentally demonstrated that the orientation of the elongated papillae did not significantly impact shear stress. This finding contrasts with previous studies that have demonstrated that sliding in the direction of elongation improved the coefficient of friction of a surface structure [147]. Previous work attributed the orientation-dependent behavior on the flow of fluid around the surface structures. Accordingly, a greater amount of fluid was reported to be flushed onto the contact area when sliding in the direction perpendicular to elongation, thus reducing the coefficient of friction [147]. It is most likely that the designs of our prototype and experiment may have resulted in the contrasting behavior to previous work. Indeed, our prototype was designed with channels that were roughly 10 times greater than that of previous work, which may have resulted in a much greater fluid channeling capacity [147]. Thus, it appears that the difference in the designs between our study and the literature may have reduced the potential for fluid to flush into the contact area during trials, resulting in the reduced impact of orientation on shear stress.

The distribution of elongated hexagonal papillae could be used to understand how to reinforce a disc margin when confronted with shear loads from random directions. For instance, the papillae of the outermost rows were greatly elongated, spanning laterally for the front of the disc and anteroposteriorly for the back. The elongations of papillae along the outer rim of the disc margin, and their nonuniform orientations, would act to counter shear loads from random, nonuniform directions, which would prove particularly beneficial for a clingfish given its rocky shoreline environment. Lessons from the spatial arrangement of elongated papillae could be used to inform the development of adhesive surface textures that are resistant to randomized shear

disturbances.

Previous work reported that from each papilla extends a dense array of microscopic extracellular cuticle [50] terminated with nanofilaments at the tips [52, 53]. The cuticle was hypothesized to spread and seal against surface asperities, leading to an increased area of contact and coefficient of friction [65, 53]. Although our study primarily focuses on how the macroscopic geometries of the papillae affect adhesive performance, these microscopic structures cannot be overlooked in their contributions to resisting dislodgement via an increased coefficient of friction.

5.4.2 Papillae provide crack tolerance during adhesion to rough surfaces

We propose that structuring the surface of the disc margin helps to make attachment to rough surfaces feasible. The shape and spacing of papillae in the disc margin resulted in an increased occurrence of fluid channeling through a dense network of microchannels and greater conformation to surface asperities. Fluid channeling could reduce the overall distance of separation between the papillae and a surface. Increased fluid channeling would therefore exponentially increase the contribution of papillae to Stefan adhesion. The presence of channels would also provide a form of geometric compliance within the disc margin, such that it can better adapt to rough surfaces and improve its seal.

Surface structuring would function to arrest cracks at the interface of the suction disc and a surface, similar in function to the segmented adhesive pads of other organisms, such as the bush cricket [155]. The structural discontinuities provided by the papillae would prevent the propagation of a crack within the seal of the disc margin that would otherwise compromise the chamber of subambient pressure. We suggest that this function partially explains the radial trend in the size of the papillae. Specifically, the dominant presence of small papillae along the outer perimeter of the disc margin would provide greater instances of surface discontinuities that could be used to arrest the propagation of cracks that begin around the outer rim of the disc. We anticipate that this crack prevention mediated by the arrangement of papillae is vital to successfully

adhering to rough surfaces in turbulent environments. We suggest that understanding such patterns in the spatial arrangements of papillae should be further considered while implementing the design of bioinspired surface structures, which could yield more versatile adhesion capabilities.

5.4.3 Rate-dependent adhesion for turbulent environments

The velocities of a disturbance common in an intertidal environment considerably influenced the resulting adhesive stress. We found that the adhesion of the papillae would be greatest during considerable disturbances, such as a wave surge, to which clingfish are routinely subjected in their natural habitat. Turbulent fluid flow would generate considerable lift of the body of the clingfish, resulting in a large, instantaneous load perpendicular to a surface. The wave-swept rocky habitats in which the clingfish resides register peak flow velocities from 5 to 8 m/s [51]. The individual bodies of the clingfish are expected to withstand flow velocities of 2 – 3 m/s, which encompasses both laminar and turbulent characteristics [51]. The chaotic water flow of the intertidal habitat therefore subjects the clingfish to a variety of external disturbances, which consist of high normal and shear loads from nonuniform directions.

Based on our analysis, we concluded that the adhesion of the suction disc of the clingfish was dependent on the environmental stimulus. In scenarios of low-frequency disturbances, this analysis indicates that suction would play the predominant role in attaching to surfaces. In conditions of high-frequency disturbances, our analysis leads us to conclude that both suction and hydrodynamic adhesion play critical, yet somewhat separate, roles in remaining attached to a substrate. Suction would provide significant adhesion against axial loads. Hydrodynamic adhesion would serve to reinforce the seal of the suction chamber. Maintaining the disc margin attached to a surface is therefore critical to the success of the suction chamber and adhesive disc as a whole. Considering that the potential for dislodgement is greatest during disruptive, high-frequency disturbances, the clingfish would need to employ multiple adhesion processes to secure attachment in variable and unpredictable environments.

One important consideration in experimentally evaluating the adhesive stress of the clingfish is the rate of dislodgement. Previous work measured the adhesive stress of clingfish at low rates of disturbance (0.017 m/s), yielding a tenacity of 29 kPa (smooth surface, unfouled) [53]. We hypothesize that the low linear velocity of the experimental setup would have rendered negligible the contribution of hydrodynamic forces to adhesion, and thus, the tenacity reported was predominantly due to suction. We would therefore suggest testing adhesion at a higher range of linear velocities to understand the effects of hydrodynamic adhesion in a biological specimen.

The model of Stefan adhesion used in this study served to understand the impact of surface structures on adhesion. This model, however, approximated the papillae as rigid, which observationally is not the case for the clingfish. An additional factor to consider in our model of hydrodynamic adhesion would be the material stiffness of the papillae [156]. Our model of the adhesive stress would be impacted by the deformation of the papillae experienced when in contact with a surface. We recognize that there are also likely other types of forces involved in attachment, including viscous friction or potentially a nonzero contribution of van der Waals forces [11]. Therefore, our investigation into the adhesion of the suction disc primarily identifies and considers the role of predominant surface structures in adhesion while subjected to disturbances of high velocities, thus likely underestimating the true performance of this highly complex adhesive disc.

5.4.4   Analytical tools advance understanding of complex geometries

Our use of both imaging techniques and processing provided novel insights into the interfacial behavior and characteristics of the papillae. FTIR allowed for visualization of a live clingfish and its contact with an imaging surface. Using this technique, we observed that the papillae were last to remain engaged with an imaging surface, even when suction was removed. The rate of detachment was slow, and thus, FTIR did not demonstrate the rate-dependent effect on the adhesive capabilities of the papillae. However, we were able to gain an understanding of the interfacial behavior of the papillae in a live specimen.

Our use of image processing made it possible to elucidate trends in the geometries of surface structures involved in adhesion. We were able to analyze the suction disc in a quantifiable manner, which made it possible to tease out geometric characteristics that might have otherwise been overlooked. These geometric attributes have significant implications on modes of attachment, other than suction, that are employed by the disc. The attachment of the suction disc therefore cannot be represented as purely suction-based, but rather a combination of attachment processes that are dependent on the disturbances they act to resist.

Using an image processing analytical tool, we reduced possible human biases that could otherwise be introduced in the quantification of the papillae characteristics. Our use of image processing allowed for a higher degree of accuracy and rapid quantifications of the surface structures, providing for a large-scale, in-depth analysis of patterns. We propose that the automation of image processing for biology will yield considerable insights into the mechanisms that may otherwise be overlooked due to the labor-intensive nature of quantification. This would be especially applicable in analyzing the adhesive structures and patterns of other organisms, for which understanding the surface geometries and distributions on a broad scale may yield considerable insights into attachment.

Our image processing tool can be improved by automating the conversion of the original micrographs to a single binary image. We can envision the further improvement of image processing procedures by implementing machine learning algorithms to detect surface structures. Use of such machine learning algorithms could be used to further quantify the suction disc to yield perhaps even more novel or nuanced findings with regards to surface patterns. The synthesis of computer science, biology, and materials science is a step in advancing our understanding and applications of biological adhesives.

5.4.5 Scaling effects of geometry, for biomimetic applications

Our analysis allowed us to design a biomimetic papilla, based on the averages calculated across all five clingfish specimens. The biomimetic surface structures were experimentally most resistant to shear loads, in comparison to other surface textures. The biomimetic surface structures can be applied to improve adhesion for wet environments. This could, in the case of the suction disc, inspire biomimetic designs of a smart suction cup, which can attach to rough surfaces and under a range of frequencies of disturbances. Previous work has been performed to mimic the clingfish to engineer suction devices to attach onto rough surfaces [65, 66]. In the previous work, the contributions of the papillae and extracellular cuticle were approximated as a soft sealing layer lining the disc margin. Engineered geometric structures analogous to the papillae could be coupled with soft sealing and suction to design a hierarchical and complex suction disc that can successfully adhere to irregular surfaces given highly variable external forces. Such geometric structures could therefore enhance the attachment of biomimetic suction discs by their contributions to hydrodynamic adhesion and wet friction. We can envision scaling the extent or geometries of these engineered papillae structures to tailor them to the application. The use of such bioinspired structures to improve adhesion to wet or submerged surfaces would advance the fields of underwater manipulation and locomotion in unstructured environments, in which attachment is critical to success.

5.4.6 Geometry of surface structures convergent across evolution

We compared the surface patterns of clingfish to tree frogs, which also adhere using hydrodynamic adhesion and exhibit similar geometric epithelial cells that are hierarchical in structure [157, 158, 159]. The tree frog secretes a mucus to increase the viscosity of the fluid beneath its toe pads [76]. The structure of the toe pads leverages the viscous secretion to adhere and enable locomotion on inclined and vertical surfaces [11, 160, 161].
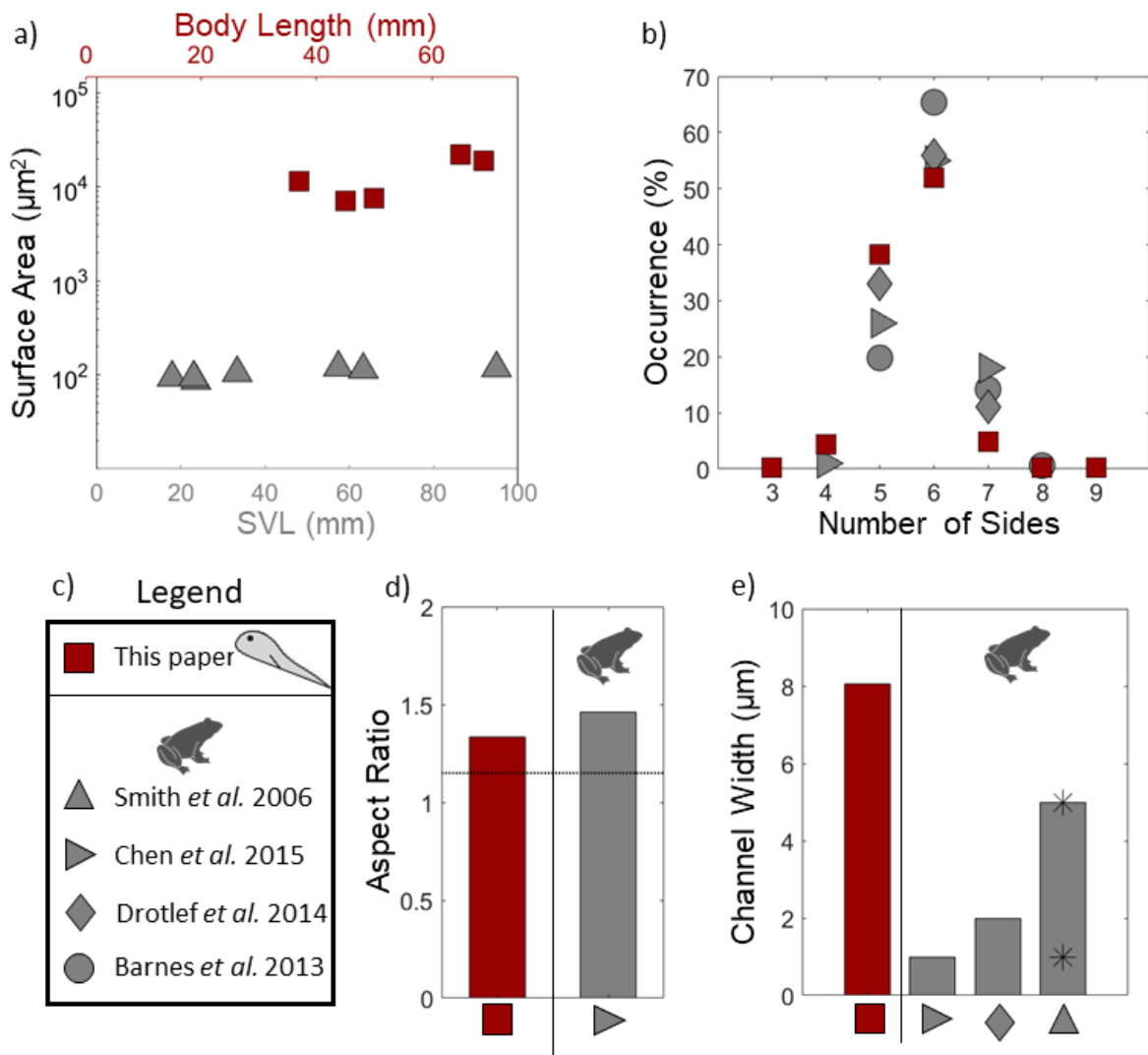
Figure 5.13: **Geometric similarities between the toe pads of tree frogs and the suction disc of the clingfish. a)** Comparison of the surface areas of the individual epithelial protrusions between species. Tree frog data (gray triangle) from Smith *et al.* 2006 [146]. Clingfish data represented as red squares. Body length (mm) of the clingfish was measured snout to tail. Snout-vent length (*SVL*) was reported for the body length of the tree frog, measured snout to anus. **b)** Comparison of the occurrence of different shapes of the epithelial projections. Gray, right-pointing triangle, data from Chen *et al.* 2015 [147]. Gray diamond, data from Drotlef *et al.* 2014 [162]. Gray circle, data from Barnes *et al.* 2013 [158]. **c)** Legend denoting the symbols and referenced sources for the data presented in the subfigures. **d)** Comparison of the aspect ratio of the papillae of clingfish and projections from the toe pads of tree frogs. **e)** Comparison of the channel width (*μ*m) between epithelial projections. The star indicates the maximum and minimum bounds of the data presented in Smith *et al.* 2006 [146].

We found overlapping similarities in the geometric attributes between clingfish and tree frogs (Fig. 5.13). The surface areas of the papillae of the clingfish were on average two orders of magnitude greater than those of the epithelial cells of tree frogs (Fig. 5.13 a). This finding suggests that tree frogs have a greater density of channels across their toe pads. However, we found that the width of the channels in the tree frogs and clingfish were of the same order of magnitude, despite the significant difference in surface areas of the pads [147, 158, 162]. Overall, the width of the channel did not change across body size or species. We suggest that the width of the channel may be optimized for directing viscous secretions while mitigating the loss of surface area due to channeling. Fluid channeling would therefore reduce the distance of separation of the adhesive pad from a surface in both tree frogs and clingfish. This reduced distance would allow for the organisms to exploit normal adhesion due to hydrodynamic forces and would also increase the contribution of wet friction to help counteract dislodgement.

The overall distribution of shapes between the tree frog and clingfish is notably similar (Fig. 5.13 b). Most of the surface patterns for both species are hexagonal in shape, while the second most prevalent structure is pentagonal. The use of hexagonal structures in tree frogs is similar in role to its hypothesized function in clingfish. The hexagonal structure would be critical in densely packing an irregular surface, optimizing contact area and channel density. The hexagonal epithelial cells in both tree frogs and clingfish would therefore increase the frictional footprint of the organism when subjected to shear disturbances.

Tree frogs and clingfish express similar aspect ratios of their epithelial cells (1.47 for tree frogs, Chen *et al.* 2015; 1.33 for clingfish; Fig. 5.13 d) [147]. In frogs, the orientation of the elongated hexagons resists the shear loads experienced when climbing surfaces [147]. Therefore, the friction of the elongated toe pads in frogs is predominantly used to counteract the effect of gravity. For the clingfish, we concluded that the elongated papillae are used to reinforce the outer perimeter of the disc margin via friction. However, the clingfish is less affected by gravity, as experienced by tree frogs, and is rather subjected to intertidal forces that vary greatly

139

in direction, frequency, and magnitude. The differences in environmental forces may account for the differences in orientations of the elongated epithelial cells between the tree frog and clingfish. The tree frog experiences predicable dislodgement forces, due to gravity, whereas the clingfish experiences unpredictable dislodgement forces, due to its intertidal habitat. However, the elongated epithelial cells would serve the same function of stabilizing the attachment of the organisms.

Overall, our comparison of the structure of the clingfish to the tree frog has reinforced our conclusions that the geometric properties of the papillae play considerable roles in adhesion. The noticeable similarities between tree frogs and clingfish lead us to propose a convergent evolution of their structures that leverage attachment due to hydrodynamic adhesion and friction.

5.5   Conclusion

The suction disc of the clingfish provides a model for bioinspired adhesion to wet, rough surfaces under nonuniform loading conditions. Our results suggest that the papillae function to seal the suction disc using hydrodynamic adhesion and wet friction during high-frequency disturbances. The automated characterization of surface structures made possible the visualization of spatial trends of papillae across the disc margin. Future work could use similar automated techniques to assess the geometric characteristics of other structured adhesives found in nature. An "average" papilla was computed across all 4853 papillae surveyed in this study to be an elongated hexagon, similar to that observed in the surface structure of tree frogs [162]. The computed papilla was used to design a biomimetic surface structure which could be used for future applications in engineered wet adhesives.

5.6   Methods

5.6.1   Biological sample preparation

Two live clingfish (*Gobiesox maeandricus*) were collected along the San Diego coastline under a collection permit to accredited organisms' collector, P. Zerofski (Scripps Institution of Oceanography). Animal care protocol IACUC #S11071 was issued to D. Deheyn. The live clingfish was imaged using FTIR.

We collected the secretions of a live specimen for microrheological analysis. The specimen was placed on a dry glass slide to reduce the presence of seawater in the sample. A pipette was used to probe and collect secretions at the intersection of the suction disc and the glass slide. Between 10 to 20 μL of secretion were collected per sampling period. Sampling occurred over four days with at least 12 hours between collection events. Secretions were stored at -20°C prior to microrheological analysis. Previous work indicated that storage up to 30 days at -20°C does not change the viscoelastic properties of mucosal secretions [153]. To image the secretions, we placed and removed a live clingfish on a dry glass slide. The secretions on the glass slide were dried and imaged using an optical microscope (Eclipse 50i, Nikon Co.).

We imaged the suction discs of the preserved clingfish (Gobiesox maeandricus) specimen available from the Scripps Marine Vertebrate Collection. Preserved specimens were collected from San Luis Obispo, CA and maintained in 50% isopropanol. We chose specimens of five different body sizes for the same species. The specimens were measured for body length from snout to tail and weight both prior to imaging (Table 5.1). The diameter of the suction disc was measured using ImageJ [67].

5.6.2   Frustrated Total Internal Reflection (FTIR)

The setup for the FTIR experiment was custom-built [96]. The imaging station consisted of a 3D printed mount, 9.7 mm thick plate of acrylic, and natural white light-emitting diodes

(LEDs) (3528-24VDC, Super Bright LEDs, Inc.). Light from the diodes was internally reflected within the acrylic, and contact with the imaging plate allowed for the illumination of the suction disc. The acrylic was wetted with a thin layer of seawater for all FTIR trials. The clingfish was placed on the inverted imaging surface, which was imaged with a camera (1280 × 780 pixels, 140 pixels $\cdot$ cm^{-1}, 40 frames $\cdot$ s^{-1}; EXILIM EX-FH25, Casio Computer Co., Ltd.). Different components of the suction chamber were isolated. Disruption of the suction disc was induced by a gentle prodding with a blunt spatula at the intersection of the pelvic and pectoral fins.

5.6.3 Passive Microrheology

For passive microrheology measurements, a trace amount of 1 μm carboxylated polystyrene microspheres (Polysciences, Inc.) was added to clingfish secretion. Beads were coated with Alexa-488 bovine serum albumin (BSA) to minimize adsorption and enable fluorescence visualization. This coating confers a no-stick boundary condition between the beads and the surrounding solution. Diffusing microspheres were visualized using an Olympus IX73 microscope with a 20× objective and high-speed CMOS camera (Hamamatsu Orca Flash 2.8). For each sample, 10 time-series of 1920×1440 (181 nm $\cdot$ pixel^{-1}) images consisting of ~50 beads $\cdot$ frame $^{-1}$ were recorded for 20 seconds at 45 fps. A custom-written Python code was used to extract the trajectories of diffusing beads and calculate the mean-squared displacements (MSD) in the x and y directions. MSDs (Fig. 5.14) shown consist of ~500 particles and are an average of MSDs in the x and y directions, denoted as $< \Delta r^2(t) >$. Linear viscoelastic moduli (G'(ω), G"(ω)) were determined via the generalized Stokes-Einstein relation [163]:

$$G^*(\omega) = G^{'}(\omega) + iG^{''}(\omega) = \frac{k_B T}{i\omega < \Delta r^2(\omega) > \pi R)} \tag{5.4}$$

where k$_B$ is Boltzmann's constant, T is the absolute temperature, $< \Delta r^2(\omega) >$ is the Fourier transform of $< \Delta r^2(t) >$, and R is the radius of the beads. The Fourier transform of $< \Delta r^2(t) >$

is obtained by [164]:

$$-\omega^2 <\Delta r^2(\omega) >= (1 - e^{-i\omega t_1}) \cdot \frac{<\Delta r^2(t_1)>}{t_1} + 2De^{-i\omega t_N}$$
$$+ \sum_{k=2}^{N} (\frac{<\Delta r^2(t_k)> - <\Delta r^2(t_{k-1})>}{t_k - t_{k-1}})(e^{-i\omega t_{k-1}} - e^{-i\omega t_k}) \quad (5.5)$$

where 1 and N in the equation represent the first and last points from the oversampled MSD data, respectively. Oversampling is done using the PCHIP MATLAB function. More details about the data analysis can be found in Ref. [165].
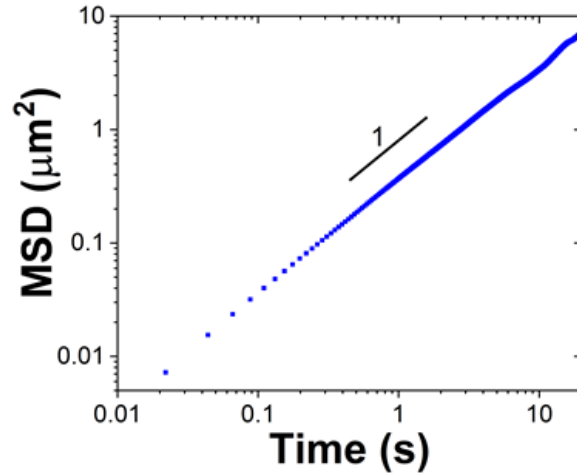
Figure 5.14: **Mean-squared displacements (MSD) of diffusing beads in clingfish secretion,** used to determine the viscoelastic moduli and viscosity of the secretion in experiments.

5.6.4 Preparation of micrographs for binary image

Preserved specimens were imaged under brightfield microscopy (SMZ18 Stereo Microscope; DS-F13 Camera, Nikon) at $2\times$ magnification. We imaged the circumference of the disc with a 25% overlap of content in the micrographs (Fig. 5.15 a). The papillae in each micrograph were manually outlined in a graphics software (Illustrator, Adobe Inc., 2019; Fig. 5.15 c). We

used the vectorized outlines of the papillae to generate a binary image in which white regions represented individual papillae and black represented the background. All binary images of the micrographs were manually stitched together by orienting the overlapping regions (Fig. 5.15 d). The conversion of micrographs to binary images was performed for all five different body sizes of clingfish (Sizes I – V).

To understand the trends in region properties across various parts of the suction disc, we also manually segmented the binary image for one suction disc (Size V) into three components using a graphics software. We segmented the disc into three binary images containing one of the following: two rows of the outermost radius of the anterior and posterior regions of the disc, three rows nearest the innermost radius of the anterior and posterior, and the lateral fin regions of the suction disc.

5.6.5 Automated region detection of papillae across entire disc

We developed an image processing sequence to automatically characterize of the binary image of the clingfish suction disc (Fig. 5.15). All image processing was performed in MATLAB (2018, The MathWorks, Inc.). The computer program labeled and characterized each papilla, which was labeled in the program as a region of interest (ROI). The regions of interest underwent a thresholding filter dictating that the area of each ROI must be larger than 20 pixels, to exclude noise present in the data. Each ROI was defined by a discrete boundary and was assigned a unique identity, where all pixels included within that region shared that identity.

Using image processing toolboxes native to MATLAB, we extracted region properties about each individual papilla, thereby calculating surface area (μm^2), perimeter (μm), and orientation of each papilla across the disc (Fig. 5.15 e). This region processing was performed on all clingfish body sizes (I – V), allowing for rapid characterization of the entire suction discs. The region processing code was also performed across all body segments for the Size V segmentation study. All plots were generated using MATLAB.

144
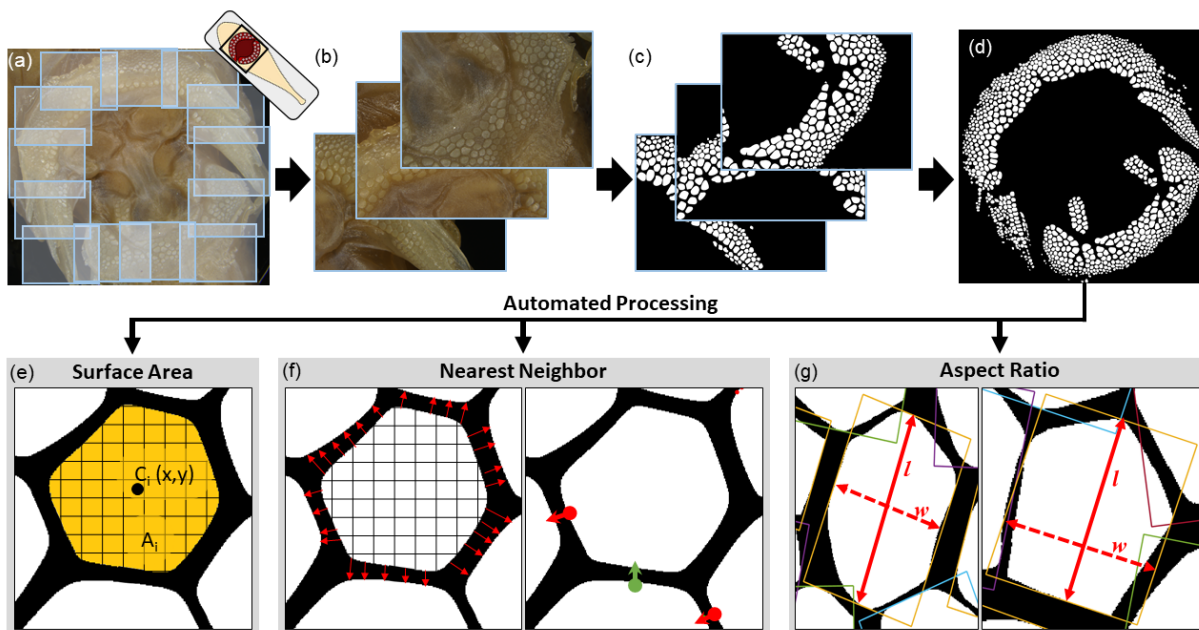
Figure 5.15: **Methodology for the quantification of the papillae. a.)** Overview of the imaging sequence. Images to overlap by 25%. **b)** Example micrographs to be processed. **c)** Individual papillae were outlined manually, creating a binary image of the original micrograph. **d)** Binary images were stitched together at overlapping regions. **e)** Image processing automatically detected and characterized the resulting binary image. Each papilla was considered by the program as a region of interest (ROI). Surface area was computed for every papilla as the sum of the pixels in the ROI. C(x,y) denoted the center of the ROI, which served as an identifier and was used in future mapping functions. **f)** Determination of the channel width by calculation of the nearest neighbor. (left) For every papilla, each pixel along its perimeter was used to calculate its nearest neighbor. (right) We averaged the five shortest distances to the nearest neighbor and considered that to be the minimum channel spacing of that individual papilla. The result of such computation is shown with red and green bold lines. The arrows point from the interrogated papilla to its nearest neighbor at the site with the smallest channel spacing. **g)** Determination of the aspect ratio of each individual papilla. A bounding box was computed for each papilla, accounting for all vertices and the orientation of the ROI. The length (*l*) and width (*w*) of the box were used to compute the aspect ratio.

145

5.6.6 Automated characterization of area of papillae

With the resulting data from our region detection procedure, trends in surface area were mapped based on ROI location to the original binary image. To understand the distribution of papillae based on size across this binary map, we normalized the surface area of an individual papilla (A_i) to that of the largest papilla (A_{max}) per suction disc (normalized area, $A_{norm} = A_i/A_{max}$). The binary map was converted into a heat map, where color was used to represent the normalized surface area. Such heat map provided insight into trends in the size of papillae along the suction disc.

5.6.7 Automated characterization of aspect ratio

We automatically computed the aspect ratio of each ROI across the suction disc, which represented the elongation of the papillae. This computation defined the minimal bounding rectangle around a set of points [166]. A bounding box was computed to contain the major and minor axes and all vertices of the ROI (Fig. 5.15 g). The bounding box was rotated to the orientation of the ROI, and the aspect ratio (R_{aspect}) was calculated to be the ratio of the length (l) to width (w) of the bounding box $R_{aspect} = l/w$.

5.6.8 Automated characterization of channel width

We automated the calculation of the width of the channel formed between neighboring papillae. This computation calculated the shortest distance between ROIs [167]. For each point along the perimeter of the ROI, the minimum distance to the neighboring ROI was computed, thus reporting the nearest neighbor of each point along the circumference of the ROI (Fig. 5.15 f). The program then averaged the five points along the circumference of the ROI that have the minimum distance to a neighboring ROI. The average of the minimum distance to a neighboring ROI was considered the minimum channel width per papillae. Only one averaged minimum
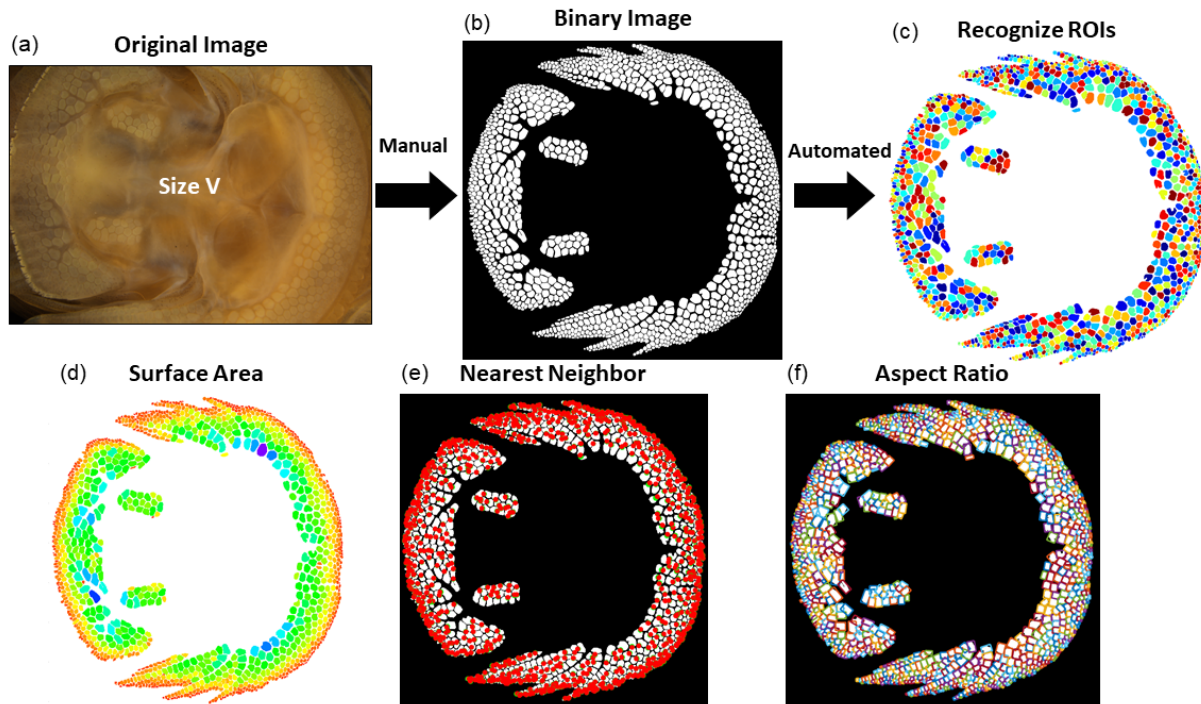
Figure 5.16: **Demonstration of the image processing protocol for Size V. a)** Original bright-field micrograph. **b)** Resultant binary image of the suction disc, after manual conversion and image stitching. **c)** Representation of the individual regions of interest (ROI) of the suction disc that were recognized by the computer. **d)** Representation of the suction disc, with respect to the normalized surface area. **e)** Representation of the results of the nearest neighbor computation.**f)** Representation of the bounding boxes surrounding the ROIs across the entirety of the suction disc.

distance was calculated per papilla. The calculation of channel width was performed across the entirety of the suction disc.

5.6.9   Manual characterization of papilla shape

We manually characterized the shape of papillae across the disc margin of the largest clingfish, Size V. We chose to manually count the number of sides of each papilla instead of automating its characterization. The finer edges of the papillae were smoothed in the process of vectorizing and compressing the binary image. This smoothing made it difficult for a computer program to be developed to resolve the finer edges and thus accurately count the number of sides.

Therefore, we visually inspected the original brightfield micrographs and manually counted the number of sides of each papilla in the micrograph. We then labeled the corresponding papillae in the binary mask, tagging each ROI with different colors to indicate the number of sides of the individual. Papillae that were considered too damaged to discern the number of sides were labeled as deteriorated. We created a program to count the abundance of each labeled region based on color, thereby quantifying the prevalence of shapes across the suction disc.

5.6.10 Fabrication of the biomimetic surface structures

We designed the biomimetic surface structure in a computer-aided design program (Auto-CAD, Autodesk Inc.). We fabricated the mold of the surface structures by engraving the designs into acrylic using a laser machining system (PLS6MW, Universal Laser Systems). The surface patterns were either elongated hexagons (aspect ratio, 1.3), regular hexagons, or squares, all of the same surface area, 0.21 mm^2. The channel spacing between the surface structures was 150 μm. The total footprint of the surface texture was 30 mm $\times$ 30 mm.

We prepared the silicone (Young's modulus, 1.1 MPa [92]; Dragon Skin 20, Smooth-On, Inc.) with a blue silicone pigment (Silc Pig, Smooth-On, Inc.) for better visualization. We degassed the silicone in a vacuum chamber for 5 min and poured the mixture into the molds. The molds were then degassed for 15 min to prevent the accumulation of bubbles in the microscale features of the surface textures. We partially cured the silicone for 5 min at 45°C. We applied a stiff backing composed of acrylic (30 mm $\times$ 30 mm) to the surface texture. A silicone adhesive (0.5 mm thickness; ARclad IS-7876; Adhesives Research, Inc.) provided the interface between the acrylic and the silicone mold. The assembly was then fully cured.

To prepare for the test of shear stress, we applied an inextensible nylon cord (25 cm length) to the back of the acrylic using cyanoacrylate adhesive (Loctite Super Glue Gel, Henkel Corporation).

5.6.11 Testing performance of the biomimetic surface structures

We experimentally tested the effect of the surface structures on resistance to shear dislodgement forces. We performed these experiments on a mechanical testing system outfitted with a force gauge of a maximum force and a resolution of 100 N and 0.02 N, respectively (M7-20, Mark-10 Co.). Shear tests were conducted using a motorized test stand (ESM303, Mark-10 Co.) at a speed of retraction of 50 mm/min.

The inextensible cord stemming from the acrylic backing of the surface structure was routed through a frictionless pulley to the upper clamp of the motorized stage. The surface on which the test was performed was composed of smooth acrylic and lubricated with glycerol (viscosity, 1.4 Pa · s; Vegetable Glycerin, Essential Depot, Co.). A preload of 200 g was applied to the acrylic backing. Shear tests were initiated upon retraction of the upper clamp. The force reported in the shear stress was determined to be the steady-state value of force across the duration of the test. The force was normalized to the total surface area and reported as shear stress (kPa). Experiments were performed in triplicate.

5.7 Acknowledgements

performed the manual binary conversions of the micrographs. J.A.S. programmed the automation procedures to quantify the papillae. K.R.P. performed the microrheological experiments and analysis. J.A.S. performed the mathematical modelling of the papillae and comparisons to tree frogs. J.A.S. designed, fabricated, and tested the biomimetic surface textures. J.A.S. prepared the initial draft of the manuscript, and all authors provided feedback during revisions.

Chapter 5, in full, is a reprint of the material as it appears in ACS Applied Materials and Interfaces, 2020. Sandoval, Jessica A.; Sommers, Jade; Peddireddy, Karthik R.; Robertson-Anderson, Rae M.; Tolley, Michael T.; Deheyn, Dimitri D., American Chemical Society Publications, 2020. The dissertation author was the primary investigator and author of this paper.

Chapter 6

Influence of stiffness on fluid channeling textures and their ability to grip soft, wet objects for application to surgical manipulators

Jessica A. Sandoval[1], Thomas Xu[2], Michael T. Tolley[1]

[1]Materials Science and Engineering Program, Department of Mechanical and Aerospace Engineering, University of California San Diego, 9500 Gilman Dr., La Jolla, CA 92093, United States

[2]Department of Mechanical Engineering, Carnegie Mellon University, 5000 Forbes Ave, Pittsburgh, PA 15213, United States.

6.1 Abstract

The use of excessive force on organ tissue during surgical manipulation risks causing damage to the tissue. The challenge of manipulating organs is typically exacerbated by their soft nature and the presence of mucus on their surfaces. We have previously shown that bioinspired, hexagonal textures improve the friction of the contact between a gripper and a wet surface. In this article, we present a thorough investigation into the effects of the stiffnesses of both a hexagonally textured manipulation surface and of the surface of an organ to understand their influences on the shear stress and wet friction between the two. Using experimental approaches to quantify friction and visualize the contact, we found that the elastomeric hexagonal textures with specific stiffnesses were successful at maintaining grip of objects with stiffness falling within specific ranges: Stiff elastomeric textures achieved a high coefficient of friction based on a form of mechanical interlocking with a soft surface ($\sim$0.001 MPa); Conversely, soft textures achieved the greatest friction to stiffer surfaces ($\sim$0.01-0.1 MPa), via deformation and contact spreading. We found that the use of textures to channel fluid was essential to maintain a stable grip by removing the interfacial, lubricating layer between a gripper and a wet object. Using Finite Element Analysis, we modeled the impact of texture stiffness on the contact stress experienced when compressed to a soft surface, the stiffness of which ranged over three orders of magnitude. The simulation was used to predict potential tissue trauma. We then applied the elastomeric textures to a soft, pneumatically actuated robotic gripper. The textured soft gripper successfully grasped soft, wet, and deformable surfaces, including hydrogels without causing noticeable damage. Enhancing the friction of the surface of the soft gripper was vital for obtaining a stable grasp of wet, delicate surfaces while minimizing the risk of trauma.

6.2 Introduction

Achieving a stable grasp to soft, wet surfaces presents a considerable challenge during surgical procedures. Surgical manipulation of organ tissue increases the potential for tissue damage and thus necessitates careful operation. The development of minimally invasive surgery (MIS) has transformed surgical practices due to the favorable outcomes including reductions in duration of hospitalization, recovery time, and scarring, in comparison with traditional open surgery [168]. The advances of MIS, however, are not without their limitations. MIS provides limited haptic feedback, which increases the potential use of excessive force on tissue, resulting in trauma and damage [169, 170, 171]. Surgeons must manipulate delicate organ tissue that is lubricated by viscous secretions, which lowers the coefficient of friction of the grasp. Use of excessive force on the tissue during manipulation procedures leads to damage, including the formation of hematomas and hemorrhages [171]. In this work, although we specifically focused on manipulation for surgical applications, we recognize that the challenge of manipulating soft, wet surfaces extends beyond surgery to other applications in robotics, such as in the areas of manufacturing and agriculture. Solutions to delicately grip wet and soft surfaces would therefore be critical to a variety of use cases.

The primary challenge to gripping wet surfaces is the presence of fluid, such as water or secretions, that lubricates the interface between the manipulator and the object to be gripped. Interfacial lubrication dramatically reduces the friction achieved between the object and the manipulator, which may therefore compromise the grasp [172, 173]. As with the human hand, a gripper exerts a grip force on an object, perpendicular to the surface, to maintain its grasp [174]. The grip force is related to the amount of friction between the gripper and the object being manipulated [175]. For grippers with high coefficients of friction, the grip force required to maintain a stable grasp is reduced, allowing for more delicate manipulation [175, 176]. Conversely, low coefficients of friction may lead to exertion of greater grip forces to maintain a stable grasp, which

may in turn damage the tissue. Another confounding factor of surface lubrication is the dissimilar stiffnesses between the surgical grasper and the organ, which also influences the potential for damage [177]. Given that traditional surgical graspers are typically composed of metal alloys that are orders of magnitude stiffer than the viscoelastic, soft tissue that they manipulate, the differences in stiffness increase the potential for damage. The use of a soft layer, such as PDMS [147] or silicone rubber [178], to line the jaws of surgical graspers provides a soft interface to reduce the potential for damage.

The addition of patterned textures has become an effective mechanism to enhance the friction of a gripper to a lubricated surface. Textures act to shuttle fluid from beneath the area of contact into channels between the textures, resulting in an improved coefficient of friction and more intimate contact with a surface [13]. In addition, textures enable wet adhesion mediated by capillarity to help stabilize a grip to the axial components of a disturbance force [179]. This challenge of successfully gripping wet surfaces is not unique to engineering but extends to the natural world. Animals such as amphibians and fish exploit wet adhesion mediated by surface texturing to attach to surfaces. The geometries of the textures found on the toe pads of frogs [158] and newts [180] and the suction discs of clingfish [60, 181] have all been explored during the development of biomimetic textures to enable successful attachment to wet surfaces. While the size and scale of the species vary, the shape of the features of the textures were similar across species, where elongated hexagons of high aspect ratios were the most prevalent texture geometry used by frogs and clingfish [60]. These biological patterns in both amphibians and fish have been the focus for materials scientists and engineers in the design of successful biomimetic textures to leverage the advantages of wet adhesion and friction [182].

In the field of biomimetic and micropatterned textures, geometric constraints, such as shape and orientation, were found to strongly influence frictional performance. Elongated, frog-inspired hexagons outperformed triangular and square textures when fabricated out of PDMS [147]. The geometric arrangement of the textures to allow for continuous, uninterrupted

154

fluid channeling was also critical to preventing hydroplaning (to achieve a higher coefficient of friction), in comparison to the formation of fluid pockets from discontinuous geometries [183]. The direction of the shear disturbance was also shown to impact performance, where pulling along the direction of elongation resulted in the greatest coefficient of friction and pulling orthogonal resulted in the lowest [147]. The function of using surface textures to channel fluid and thus increase friction has been reported across a range of size scales that encompasses the microscopic [147] and macroscopic [172, 60].

The bioinspired textures can be tuned and modified to yield better resistance to shear loads. For instance, while many previously reported micropatterns were composed of PDMS, modifications to the material composition have increased the effectiveness of the frictional pads. As an example, a composite micropatterned array of frog-inspired, hexagonal structures composed of PDMS embedded with stiff micropillars was shown to achieve a higher coefficient of friction over an array of soft hexagons alone [180, 184]. The addition of convex structures resemblant of octopus-inspired suction cups have also been added to the face of the frog-inspired textures, thereby coupling the effects of fluid channeling, wet adhesion, and suction to increase the adhesive stress when compared to textures without convex structures [185]. To address the challenge of lubrication during manipulation of wet objects, previous work has turned to the integration of frog-inspired textures onto surgical grippers [139]. Frog-inspired textures were applied to commercially available surgical graspers to increase fluid channeling and thus the coefficient of friction of the grip [147]. Increasing the coefficient of friction between the gripper and the surface would reduce the gripping force required to manipulate a delicate object.

In addition to the use of patterned textures to achieve a successful grip of a wet surface, soft robotic grippers, composed entirely of compliant materials, have been explored as an avenue to minimize the damage caused to delicate surfaces during manipulation [27, 186]. For surgical applications of soft robotics, the materials, such as silicone, that constitute the body of a soft robotic gripper are more comparable to the stiffnesses of the organ tissue that they

aim to manipulate and would therefore deform before damaging the object [187]. Soft grippers encompass a wide range of designs and include three-fingered [188, 189] and multi-directional tentacle-inspired grippers [16]. Soft grippers also vary in the method of actuation, from the use of pneumatic networks (PneuNet) [190] to the use of granular jamming to provide variable stiffness to the manipulator [191, 192]. The use of soft actuators minimizes the risk of damage, yet still encounters the issue of lubrication when gripping a wet surface. The addition of surface textures, such as pneumatically actuated patterns, to soft robotic actuators shows considerable promise to yielding tunable friction for robotic manipulation and locomotion [193]. The application of adhesives, such as gecko-inspired adhesives, to soft gripping systems presents a way to achieve high loads while minimizing contact pressures [85, 84]. However, dry adhesives have been predominantly used in application to soft robotics, with fewer instances of using wet adhesives. Two of the use cases of wet adhesives in soft robotics were the use of fluid-channeling textures to enable the successful grip of commercial items of interest, from oil-lubricated objects [172] to tofu [194]. Building on the previous approaches, here we present an exploration combining wet adhesives, surface texturing, and soft robotics to yield advancements to delicate gripping with specific application to surgical manipulation.

The human body is composed of a variety of tissues exhibiting a wide range of stiffnesses. The stiffness of living tissue varies by orders of magnitude, from tens of pascals to gigapascals [195]. For this study, we focused on soft abdominal tissue, which constitutes most abdominal organs (i.e. the kidney and liver) and has stiffnesses on the order of submegapascals. In this work, we investigated the influence of the stiffness of an organ on the fluid channeling capabilities and the manipulation shear stress of biomimetic textures. We investigated the relationship of the stiffness of the textures and the estimation of compressive stress during manipulation using finite element simulation. We then applied the surface textures to a soft robotic gripper to manipulate hydrogels as a demonstration of the ability of the grippers to handle wet, fragile surfaces without causing damage to the hydrogels.

6.3   Results

6.3.1   Design of the textures and organ-mimicking surfaces

We developed frictional textures that were composed of an array of bioinspired, elongated hexagons (aspect ratio, 1.3), which we found in previous work to have a high coefficient of friction when subjected to shear loads [60]. We fabricated the textures using elastomeric rubber that varied by an order of magnitude in stiffness. We created a soft elastomeric texture (S2; $E_{texture}$, 0.0167 MPa) and compared its performance to a stiff elastomeric texture (S5; $E_{texture}$, 0.445 MPa). The hexagons were designed with a width of 1.6 mm, length of 2.1 mm, and a height of 1 mm. The channel widths were varied across trials (0.2, 0.3, 0.4, 0.5 mm) to determine how the optimal spacing of the textures was influenced by their stiffnesses.

In both experiments and simulation, we tested the textures across a range of surfaces that mimicked soft tissue. We considered the range of stiffnesses of organs–the kidney, liver, bladder, and heart–to establish a range of tissue stiffnesses. The kidney is comparatively the softest of the four organs, with a stiffness of 3.5 kPa [196]. The liver has been reported with a stiffness around roughly 5.5 kPa [197] in healthy adults. The bladder has a stiffness that varies from roughly 50 kPa when empty to 100 kPa when full [198]. The heart has been reported with a range of stiffnesses, but with an average around 500 kPa [199]. Based on the properties of these organs, we chose a range of stiffnesses from 0.001 to 0.1 MPa. We used this range to develop organ "mimics" on which we tested the textures in both experimental settings and in Finite Element Analysis (FEA). The experimental surfaces ranged from soft to stiff, and were of the following stiffnesses: 0.0065 MPa (S1), 0.0167 MPa (S2), 0.165 MPa (S3), 0.231 MPa (S4), and 0.445 MPa (S5).
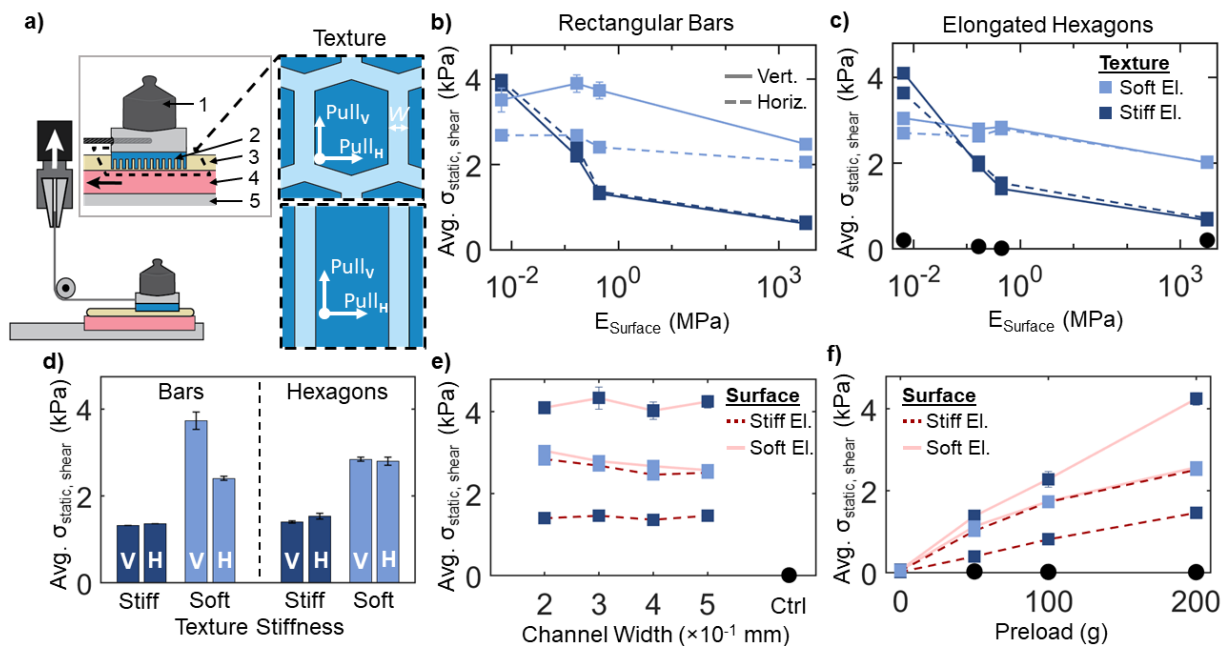
Figure 6.1: **Wet friction of textures varied by surface stiffness. a)** Schematic of the experimental setup to test the resistance to shear disturbances of the textures. Inset: A texture (2) was placed on a soft surface (4) which was lubricated in glycerol to approximate the presence of secretions and was supported by a rigid plate (5). The texture was preloaded to the surface by a weight (1) and pulled in shear using a universal testing machine. The textures were either hexagonal (top) or rectangular (bottom). The textures were pulled in a direction parallel (Pull$_V$) or perpendicular (Pull$_H$) to the direction of elongation of the structures. (W) indicates the width of the channels in each texture. **b)** The average static shear stress (σ, kPa) of the rectangular textures of both soft (light blue) and stiff (dark blue) stiffnesses, and with a channel width of 0.2 mm. Solid line denotes that the texture was vertically aligned to the direction of motion. Dashed line denotes that the texture was horizontally aligned. **c)** The average static shear stress (kPa) of the hexagonal textures (channel width, 0.2 mm) was dependent on the stiffness of the surface. Black circles indicate the performance of the control, which was devoid of textures. **d)** Example of the differences in performance of the hexagonal and rectangular textures against a stiff (S5, 0.445 MPa) surface for a channel width of 0.2 mm. **e)** Impact of channel width on the average static shear stress, depending on the stiffness of the texture and stiffness of the surface (stiff, dark red, dashed line; soft, light red, solid line). **f)** Effect of the stiffness of the texture (hexagonal; channel width, 0.5 mm) on the preload (g) required to maximize the shear stress. Trails were conducted on the softest (light red; S1, 0.0065 MPa) and stiffest (dark red; S5, 0.445 MPa) surfaces. All trials were conducted in triplicate. Error bars represent standard deviation per trial type.

6.3.2 Friction dependent on relationship between texture and surface stiffness

We experimentally measured the maximum shear stress achieved by the textures while varying the stiffness of the surface. We tested the parameters of structure type (elongated hexagon vs. rectangular bar), orientation, stiffness, and channel width. The friction pads were preloaded with a weight of 200 g (1.96 N) and pulled in parallel along a surface lubricated with glycerol. The use of glycerol approximated the presence of viscous secretions that would be found along the surfaces of organ tissue within the body. The surface was composed of either a silicone elastomer with a range of stiffnesses (S1: 0.0065 to S5: 0.445 MPa) or acrylic. We tested the orientation of the textures, where we defined a vertical orientation to be a texture that was elongated in-line with the direction of the shear pull. Textures that were horizontally oriented were pulled orthogonal to the direction of elongation of the hexagons (Fig. 6.1 a).

Overall, we found that the friction of the texture was highly dependent on the stiffness of the surface on which it was being pulled. This interplay of stiffness on friction was consistent for both the barred (Fig. 6.1 b) and hexagonal (Fig. 6.1 c) textures. At a low stiffness of the surface ("softest" surface, S1: 0.0065 MPa), stiff textures yielded the highest resistance to shear pulls, in comparison to soft textures. In this regime, the stiffness of the texture was 68.5 times stiffer than the surface.

However, as the stiffness of the surface increased, the stiff elastomeric texture performed increasingly worse in comparison to the soft elastomeric texture. For instance, when considering a stiff elastomeric surface (S5; $E_{surface}$, 0.445 MPa), the texture composed of vertically aligned, rectangular bars of a soft stiffness achieved static shear stresses that were 2.8 times greater than their stiff counterparts. This trend was consistent across both bar and hexagonal geometries. Therefore, for surface stiffnesses greater than 0.0065 MPa (S1), a soft elastomeric texture would generate higher friction and would therefore be preferred over stiff textures.

The shape type and its orientation also significantly influenced the resulting friction, most notably for soft textures. Specifically, a soft texture composed of rectangular bars had friction dependent on its orientation with respect to the direction of the shear load. Horizontal rectangular bars that were oriented orthogonal to the direction of motion achieved shear stresses that were 1.55 times lower (2.4 ± 0.05 kPa; soft texture on a stiff surface; S5, 0.445 MPa) than the vertically aligned rectangular bars (3.7 ± 0.2 kPa). This orientation dependence was observed across all trials involving rectangular bars.

On the other hand, the hexagonal texture (both soft and stiff) demonstrated less dependence of friction on its orientation with respect to the direction of motion (Fig. 6.1 c-d). Although the elongated hexagons were not as highly performant in comparison to the vertically, aligned soft rectangular bars at select surface stiffnesses, the relative indifference of the hexagonal structures with respect to the direction of the shear load made this design more desirable for future characterizations and applications to organ manipulation.

We evaluated the impact of the channel width between the hexagonal structures on the resulting shear stress achieved by the texture. The channels ranged from 0.2 to 0.5 mm in width, which corresponded to 20 to 50% of the width of the hexagons. We found that the stiff texture was relatively indifferent to the width of the channel between the hexagonal features (Fig. 6.1 e). On the other hand, the soft hexagonal texture demonstrated a negative correlation between channel width and shear stress (channel of 0.2 mm, stress of 3.05 ± 0.08 kPa; channel of 0.5 mm, stress of 2.58 ± 0.09 kPa).

We evaluated the effect of the stiffness of the texture on the preload required to adequately engage the texture with a surface. We calculated the average static shear stress and monitored the change in the slope as we increased the preload, where the point of inflection in the graph was considered to be the preload required to engage the texture with a surface. We found that the soft texture achieved points of inflection in shear stress between the preloads of 100 to 200 g for both the soft and stiff surfaces (Fig. 6.1 f). Conversely, the stiff texture maintained a consistent

slope past the preload of 200 g, suggesting that the stiff texture would require a higher preload to achieve a point of inflection in shear stress.
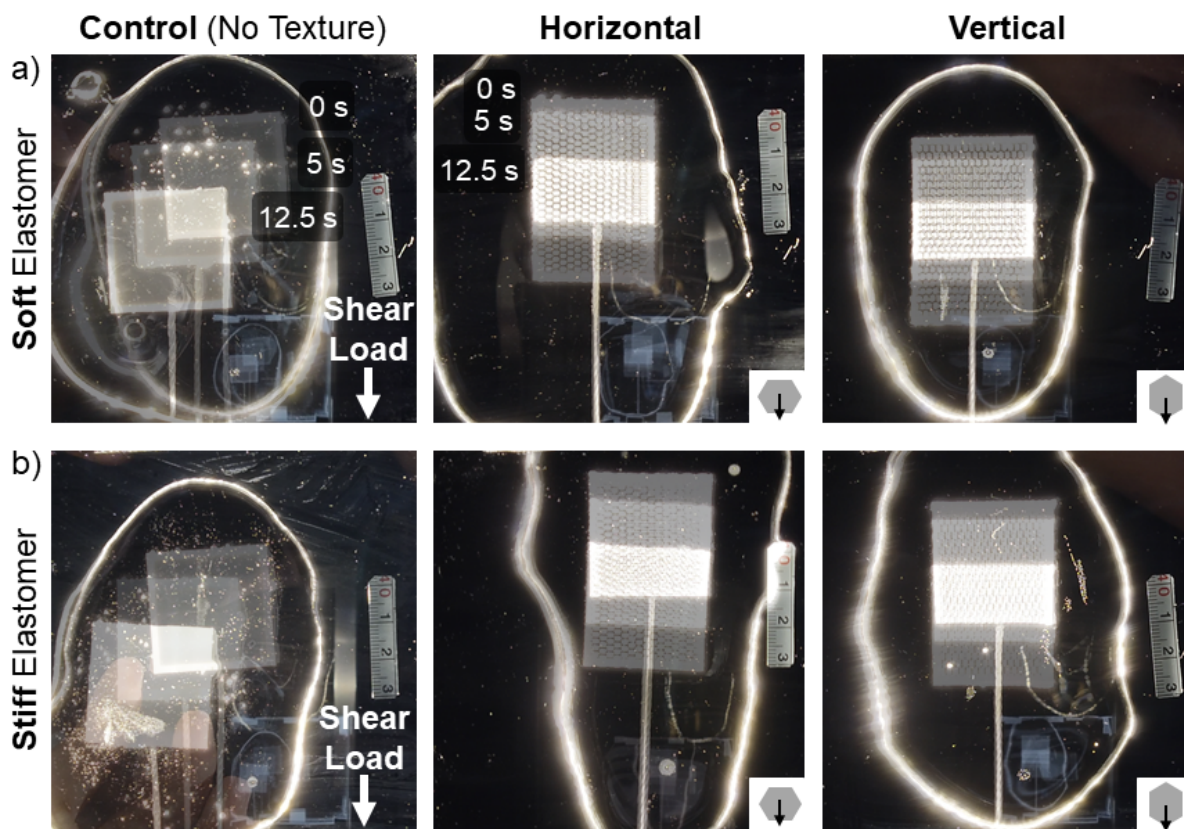
Figure 6.2: **Position control of surface textures when pulled in shear along a surface lubricated in glycerol, as visualized in FTIR. a)** Time series of the drift for textures composed of soft elastomers. The trials demonstrated the drift of the control (left) and position stability of the horizontally aligned (middle) and vertically aligned (right) hexagonal textures. **b)** Time series of the drift for textures composed of stiff elastomers. The trials were for the control (left) and the horizontally aligned (middle) and vertically aligned (right) hexagonal textures.

6.3.3   Position control dependent on texture

To assess how stiffness of a texture affected its ability to maintain a stable position during a shear motion, we visualized the contact made between it and an imaging surface using Frustrated Total Internal Reflection (FTIR). FTIR is a visualization technique in which light is internally reflected within a sheet of acrylic. When a surface texture contacts the acrylic, light escapes at
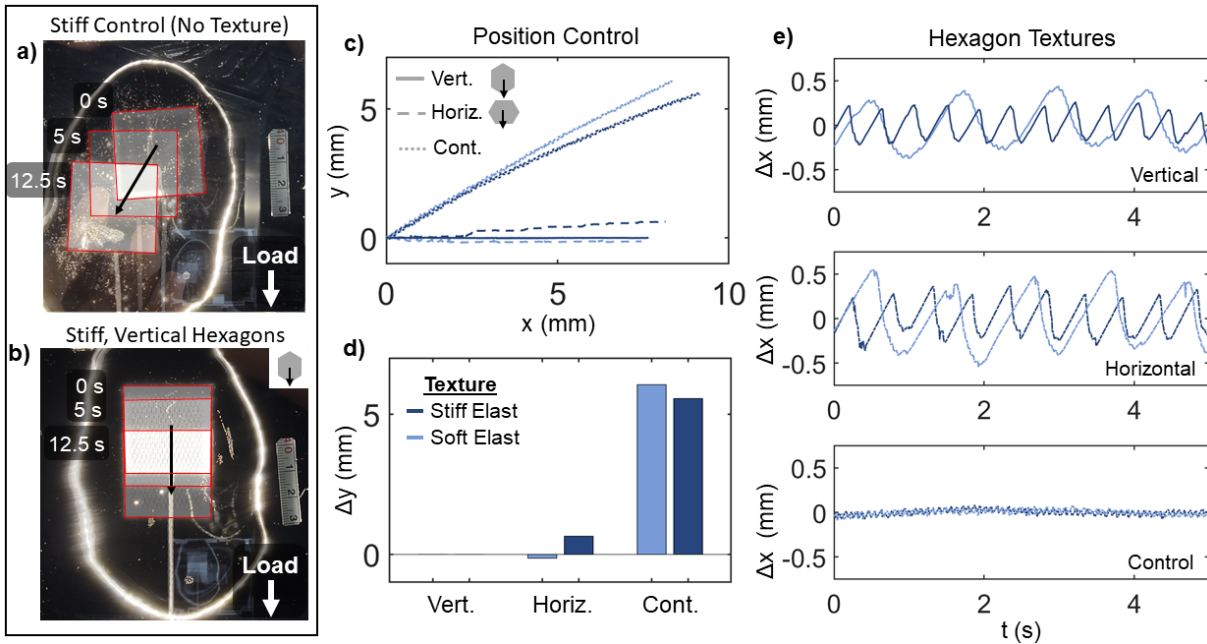
Figure 6.3: **Fluid channeling enabled position control, as visualized using FTIR. a)** A time series showing the drift of a control pad (stiffness, S5) when pulled in shear along a lubricated imaging surface. **b)** A time series demonstrating the ability of the stiff, vertically aligned hexagons to maintain a stable y-position when pulled in shear. **c)** Plot of the x- and y-positions of the textures when pulled in the x-direction for 7.5 mm. Position values were measured using motion tracking software. Light blue indicates a soft elastomeric texture. Dark blue indicates a stiff elastomeric texture. Vertically aligned textures are denoted by a solid line, horizontally aligned denoted by a dashed line. The control is denoted by a dotted line. **d)** Displacement of the y-position (Δy), which corresponded to drift, was quantified for the hexagonal textures (soft and stiff, vertical and horizontal orientations) and for the control pads. **e)** Fluid-mediated stick-slip response of the hexagonal textures that were vertically (top) and horizontally (middle) aligned and pulled along a lubricated surface. The motion of the texture was linearized and subtracted to study the time-dependent change in x-position (Δx). The control (bottom) did not exhibit an apparent sinusoidal, stick-slip behavior.

the points of contact, which can then be imaged by a camera [96]. The texture was preloaded to the imaging surface with a weight. Using a motion tracking software, we visually tracked the position of the texture when pulled in shear on a surface that was lubricated with glycerol (Fig. 6.3 a-c). We compared the effects of texture geometry and stiffness to the control friction pad, which did not have any textures.

To make this comparison, we quantified the position and displacement of the textures (Fig. 6.3 c-d). When pulled in shear along the x-axis, a texture with a greater degree of friction and

thus position control would have a negligible change in its *y*-position. The control pad exhibited a large drift in its *y*-position and thus performed worst at maintaining its position in comparison to all textured surfaces. The control surface hydroplaned upon a layer of glycerol which was trapped between its planar elastomeric surface and the imaging sheet. Across the different geometries and stiffnesses of the textures that were tested, we found that the presence of any texture was an improvement in the ability to maintain its position in comparison to a control surface.

For the textured surface, we found that its orientation influenced its ability to maintain a stable position when pulled in shear. Hexagonal textures aligned horizontally had a greater change in *y*-position in comparison to the vertically aligned textures. This trend was consistent for both soft and stiff textures. However, the softer of the horizontally oriented textures drifted comparably less than the stiffer hexagon (Fig. 6.3 d). Thus, the vertically aligned hexagonal texture provided greater position control in comparison to horizontal and was also influenced by its stiffness.

We then investigated the mechanics of motion during a shear pull. We linearized the motion of the texture to focus on the sinusoidal motion of its *x*-position in time. When the motion was subtracted, we observed a sinusoidal stick-slip behavior of the hexagonal textures on the lubricated surface. This stick-slip behavior was present for both vertically and horizontally oriented structures but was not present for the control pads. Additionally, the frequency of the sinusoidal behaviors corresponded predominantly with the stiffness of the texture, rather than their orientation, and hence the spatial frequency of their patterns. The soft elastomeric texture exhibited a sinusoidal stick-slip behavior with a period that was longer than that of the stiff texture.

By contrast, the stick-slip behavior described for the elastomeric textures on the lubricated surface was not dominant in a dry condition (Fig. 6.5). The dry condition for all surface textures did not exhibit any appreciable sinusoidal behavior in the changes to the *x*-position that was above the noise threshold.

6.3.4 Impact of shear and axial loads on contact area

We evaluated the effect of shear and axial loads on the contact area between a texture and a surface using FTIR. We investigated the effect of the stiffness, orientation, and pattern of a texture to resisting deformation caused by these loads. This investigation was performed under a dry condition, which allowed for better visualization of the contact area in comparison to the lubricated conditions.

When compressed to the imaging surface, the deformation of the texture was highly dependent on its stiffness. When the textures were compressed to the surface with a 200 g (1.96 N) preload, the area in contact increased by 350% and 110% for the soft and stiff elastomeric
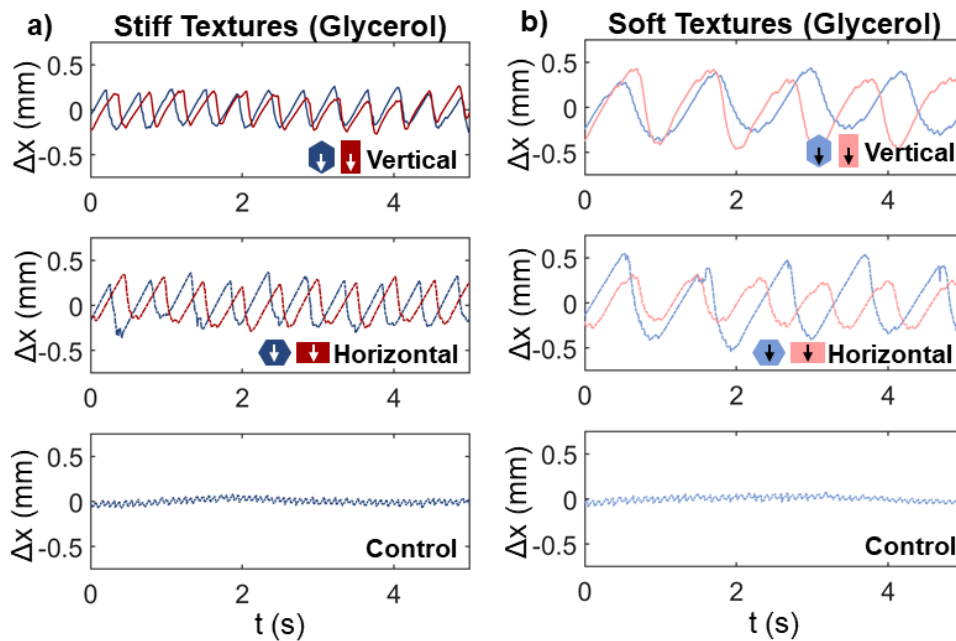
Figure 6.4: **A comparison of the stick-slip responses of the hexagonal and rectangular textures on a lubricated surface. a)** Fluid-mediated stick-slip behavior was present for both the vertically (top) and horizontally (middle) aligned stiff textures. Blue indicates a hexagonal geometry, whereas red indicates a texture composed of rectangular bars. The control (bottom), which was devoid of textures, did not exhibit a stick-slip behavior. **b)** Fluid-mediated stick-slip behavior for the soft elastomeric textures. The frequency of the stick-slip response corresponded with the stiffness of the texture, hence the longer periods for the soft textures with comparison to the stiff.
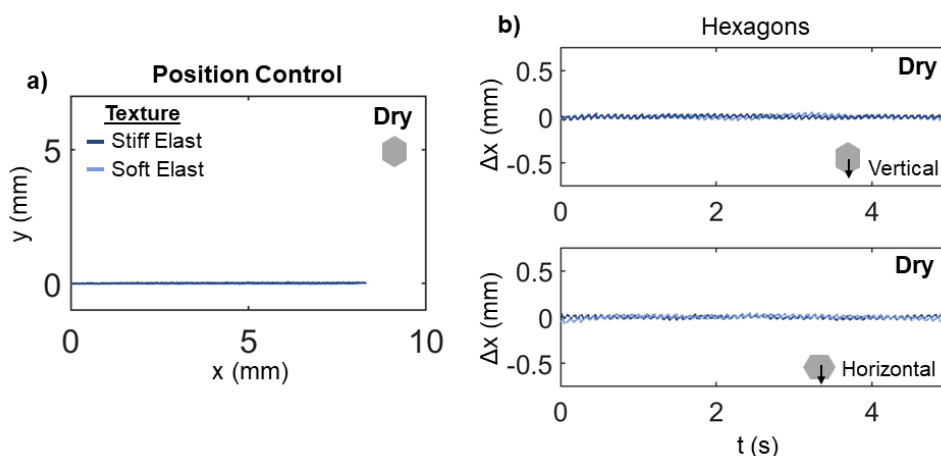
Figure 6.5: **Quantification of the position control of the hexagonal textures under dry conditions. a)** A representation of the *x*- and *y*-position of the stiff (dark blue) and soft (light blue) hexagonal textures when pulled in shear for 8 mm under a dry condition. Under a dry condition, the textures did not drift in the *y*-position. **b)** The change in *x*-position (Δx) of the vertically aligned hexagons when the linearized motion of the pull was removed. A stick-slip response was not observed for the dry condition, as it had been for the lubricated FTIR trials. **c)** The change in *x*-position of the horizontally aligned hexagons against a dry surface for both soft and stiff textures.

textures, respectively, from unloaded to loaded conditions. This result implied that the soft texture more evenly distributed the compressive load across the entire texture surface, in comparison to the stiff texture. When experiencing a shear load, the behavior of the texture was also dependent on its stiffness and orientation. The soft elastomeric texture deformed more than the stiff, and the resulting area of contact demonstrated a greater orientation dependence (Fig. 6.6). A horizontal orientation of the soft textures results in a higher degree of bending and deformation of the hexagonal structures, in comparison to the vertical orientation of the same stiffness. The higher degree of bending of the horizontal, soft textures led to a roughly 35% decrease in contact area when compared to its vertical orientation.

When comparing the differences in geometry between the hexagonal and rectangular bar textures, the hexagonal textures lost less contact area when pulled in shear, in comparison to the rectangular textures in both horizontal and vertical orientations for the soft elastomer (Fig. 6.7). The hexagonal textures also spread the contact more evenly across the experimental pad when
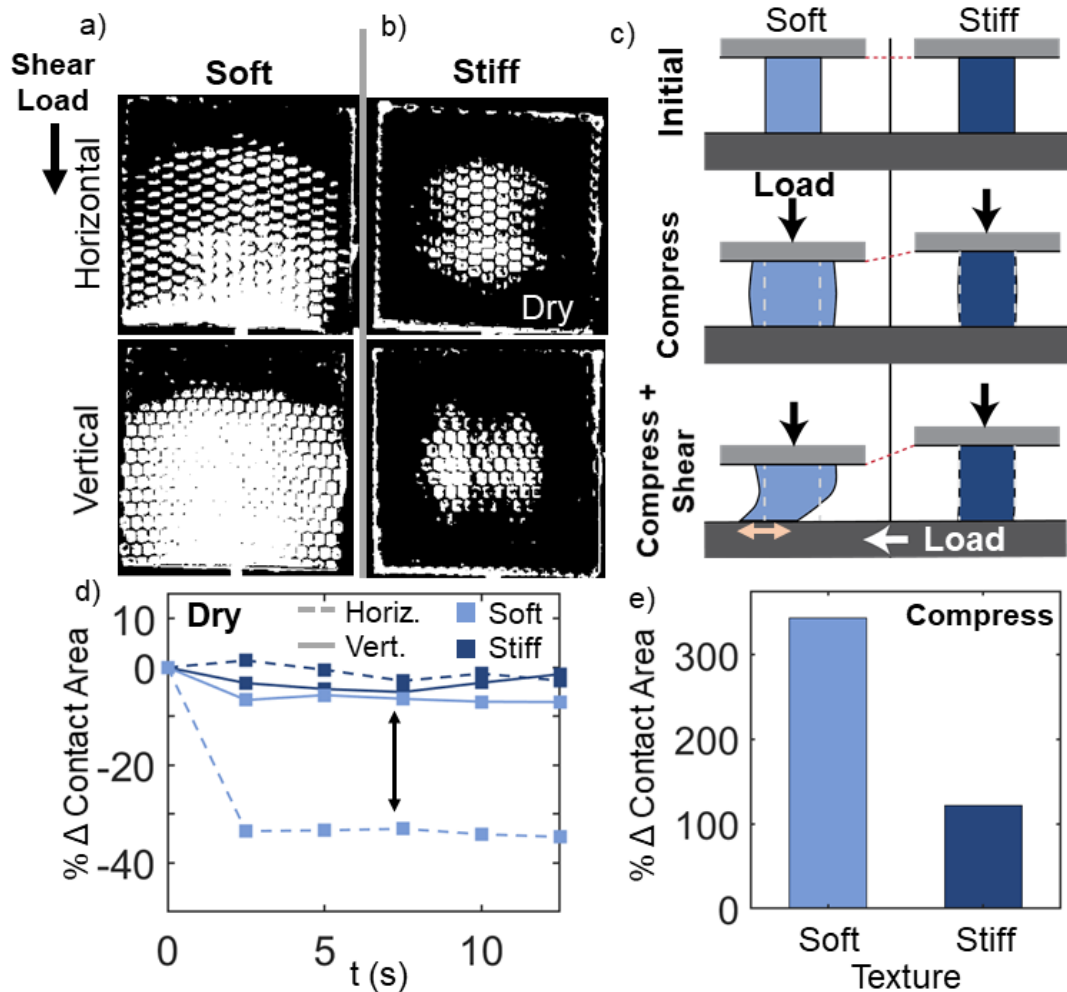
Figure 6.6: **FTIR analysis of the deformation of textures based on shear and axial loads.**
a) FTIR images of the horizontally (top) and vertically (bottom) aligned soft, hexagonal textures, when pressed to the surface with a 200 g weight and pulled in shear along a dry surface (t = 10 s). **b)** FTIR images of the horizontally (top) and vertically (bottom) aligned stiff elastomeric textures (t = 10 s). **c)** Schematic demonstrating the differing effects of compression and shear load on soft (left) and stiff (right) elastomeric textures. **d)** The percent change in contact area (%) was quantified for the soft (light blue) and stiff (dark blue) hexagonal textures that were horizontally (dashed line) and vertically (solid line) aligned. The percent change is reported as a function of time, from the start (t = 0 s) to the end (t = 10 s) of the shear pull. Arrow denotes the difference in behavior between the horizontally and vertically aligned soft texture. **e)** Measurement of the percent change of the area in contact with the FTIR surface for the textures when compressed with a 200 g weight. Percent change was quantified over the entire area of the texture (30 mm × 30 mm) from before to after compression.

166
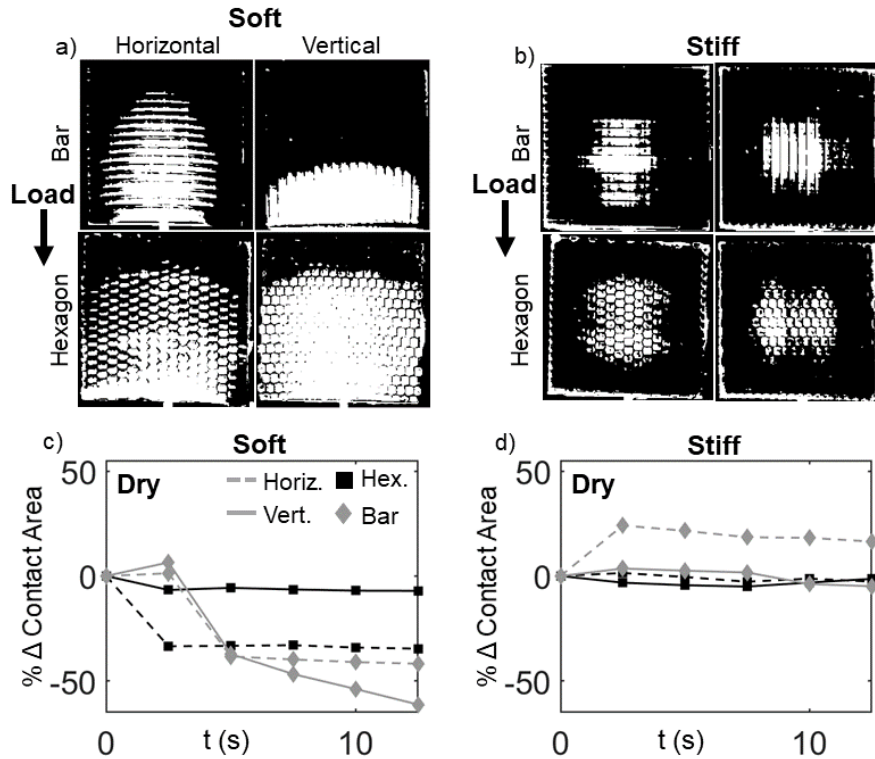
Figure 6.7: **Comparison of performance of the hexagonal and rectangular textures, as investigated using FTIR. a)** The soft, rectangular (top) and hexagonal (bottom) textures were compared while subjected to a constant shear load (imaged at t = 5 s) on a dry surface. We observed that the deformations of the textures differed between the horizontal and vertical orientations. **b)** The stiff, rectangular (top) and hexagonal (bottom) textures were compared while subjected to a constant shear load (imaged at t = 5 s) along a dry surface. **c)** The change in contact area (%) of the hexagonal and rectangular textures made of soft elastomer on a dry surface. The responses of textures in horizontal and vertical orientations are reported during time intervals of 12 s. **d)** The change in contact area (%) between the hexagonal and rectangular textures that were made of stiff elastomer on a dry surface.

first contacting the imaging plane in comparison to the rectangular textures, resulting in a higher total area of contact for the hexagonal textures. We concluded that the hexagonal textures best prevented loss of contact with the imaging surface in comparison to the rectangular texture.

6.3.5   Impact of texture and surface stiffness on compressive stress

We modeled the effect of the stiffness of the textures on the resulting contact stress when interacting with a soft surface using Finite Element Analysis (FEA). In setting up the simulation,

we used a single hexagonal pillar, representing one element along the texture, to press onto a flat, rectangular surface. We varied the stiffness of the surface in a range from soft to stiff (0.0065 to 0.445 MPa, respectively), which corresponded to our experimental shear stress surfaces. We evaluated the impact on compressive stress of a texture that was composed of either a soft elastomer, stiff elastomer, or rigid metal. We imparted a constant displacement of 0.25 mm, which was 1/4 of the height of the hexagonal pillar corresponding to an applied vertical strain of 0.125, to the back of the hexagonal texture. A constant displacement corresponded with previous work that modeled tissue damage by imparting a constant displacement or vertical strain to simulate grasping [169, 200].

We probed the maximum contact stress along the face of the hexagonal texture, as a metric of stress to be compared between the three texture types. For such a comparison, we used the same mesh, as the stress obtained using simulation would be dependent on mesh size. We acknowledge that the edge of the material would experience infinitely large stress, and thus the maximum stress reported in this work was solely used to judge performance between the three types of textures. We found that the maximum contact stress of the hexagonal texture increased with the stiffness of the surface for the rigid and stiff textures. The texture composed of rigid metal experienced the greatest slope, resulting in 82 kPa and 3327 kPa of contact stress for softest and stiffest surfaces, respectively. The stiff elastomeric texture experienced a modestly increasing slope in comparison to the rigid texture. The stiff texture resulted in a maximum contact stress of 53 kPa and 149 kPa against the softest and stiffest of the elastomeric surfaces tested. Conversely, the soft elastomeric texture maintained a similar contact stress across the entire range of surface stiffnesses that were tested. The maximum contact stress was found to average around 7 kPa across all trials for the soft elastomeric texture. For the stiffest of surfaces (S5), the textures resulted in at least an order of magnitude difference in resulting contact stress between the soft and stiff elastomeric textures and between the stiff and rigid textures (Fig. 6.9 d).

We modeled how stiffness influenced the change in contact area between the hexagonal
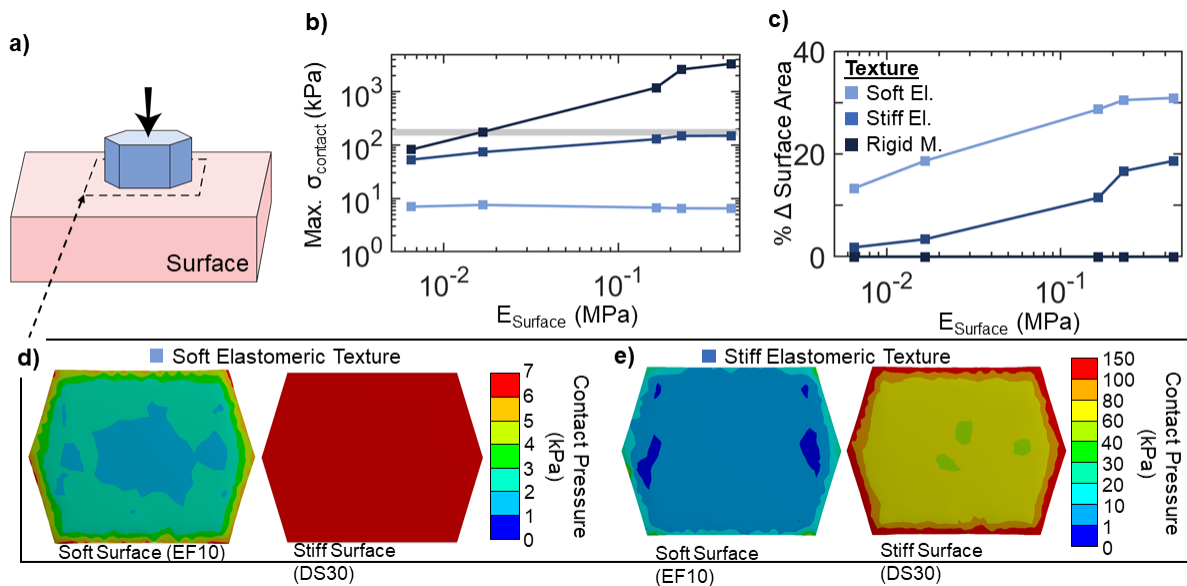
Figure 6.8: **Simulation of the contact stress due to a compressive load. a)** Schematic demonstrating the setup of the FEA simulation. A constant displacement was imparted to the back of a single hexagonal pillar of the texture. The stiffness of the surface was varied across the FEA trials. **b)** A representative, maximum contact stress (σ, kPa) was used to compare the texture types—soft elastomer (light blue), stiff elastomer (dark blue), and rigid metal (black)—across a range of surface stiffnesses (MPa). The gray line indicates a threshold of compressive stress reported by Chandler *et al.* (2017) and De *et al.* (2007) to help predict potential tissue trauma. **c)** The change in the surface area (%) was calculated per texture type across a range of surface stiffnesses. **d)** A map of contact stress (kPa) across the hexagonal surface for a soft elastomeric texture. The texture was compressed to the softest surface (S1, 0.0065 MPa; left) and to the stiffest surface (S5, 0.445 MPa; right). **e)** A map of the contact stress (kPa) across the hexagonal surface for a stiff elastomeric texture when compressed to a soft (S1, left) and stiff (S5, right) surface.

texture and surface. Perhaps intuitively, the soft elastomeric texture exhibited the greatest change in surface area in comparison to the stiff and rigid. The soft texture resulted in a 13.3% and 30.9% increase in surface area when compressed to a soft (S1; E$_{surface}$, 0.0065 MPa) and stiff surface (S5; E$_{surface}$, 0.445 MPa), respectively. The increase in surface area when compressed was consistent with lateral spreading of the hexagonal footprint due to deformation. On the other hand, the stiff texture deformed very little to a soft surface, which was approximately 68 times less stiff than the texture, resulting in a 1.8% increase in the surface area of the hexagon. This result is consistent with the conclusion that the soft surface would deform and interlock with
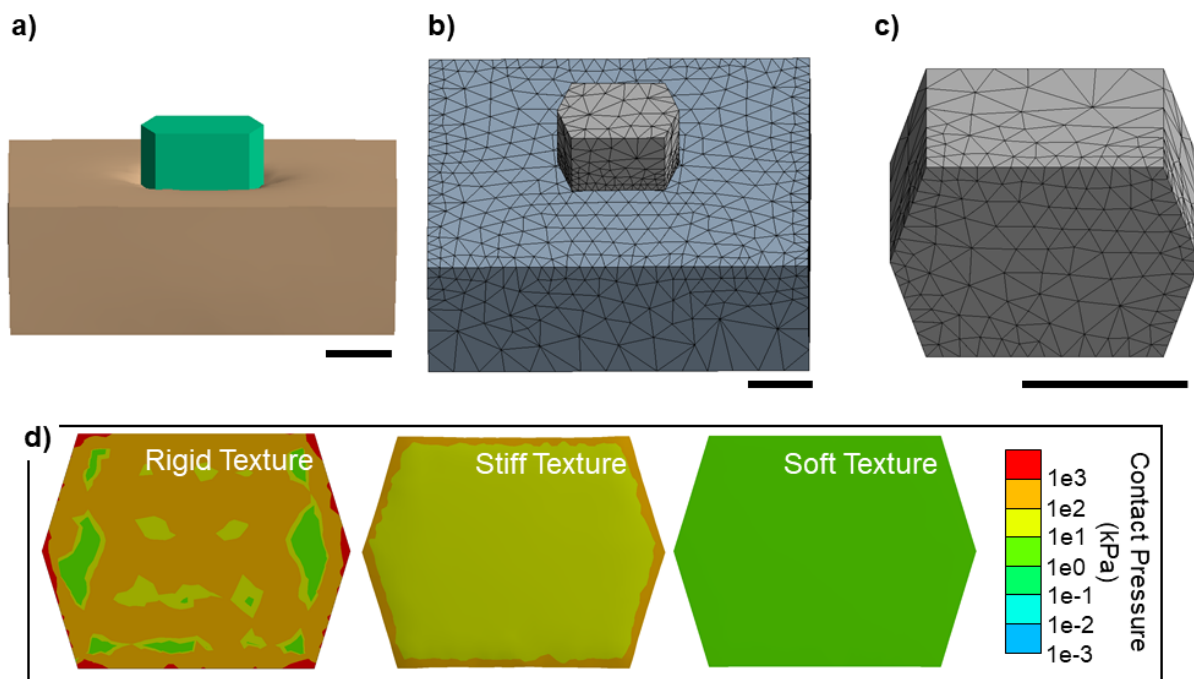
Figure 6.9: **Finite Element Analysis (FEA) comparing the contact stress between the different texture stiffnesses.** **a)** Isometric view of a rigid, hexagonal texture being compressed to a surface (S2) with a set displacement. **b)** Isometric view of the mesh used during the simulation. **c)** Isometric, bottom view of the hexagonal texture. A mesh refinement was used at the bottom face of the hexagon to yield a more detailed resolution of the contact pressure at the texture-surface interface. **d)** Comparison of the contact pressure between the surface (S5; stiffness, 0.445 MPa) and the rigid (left), stiff elastomeric (middle), and soft elastomeric (right) textures. Contact pressure was plotted logarithmically to encompass the broad range of contact pressures between the three texture types.

the stiff texture. Conversely, when the stiff texture was compressed to a surface of equivalent stiffness (S5), the stiff texture grew 18.7% in surface area. In a subsequent simulation, we found that when compressing the hexagonal pillars with a constant force (0.002 N) to a steel plate, the height of the texture decreased by roughly 2.7% for the soft texture and 0.14% for the stiff per 1 kPa of compressive stress applied (Fig. 6.10). The intrinsic nature of the elastomeric texture to compress and thus reduce its height and increase its surface area was therefore essential to allowing for contact spreading to occur.

We visualized the map of contact pressure of the soft and stiff textures, dependent on

170
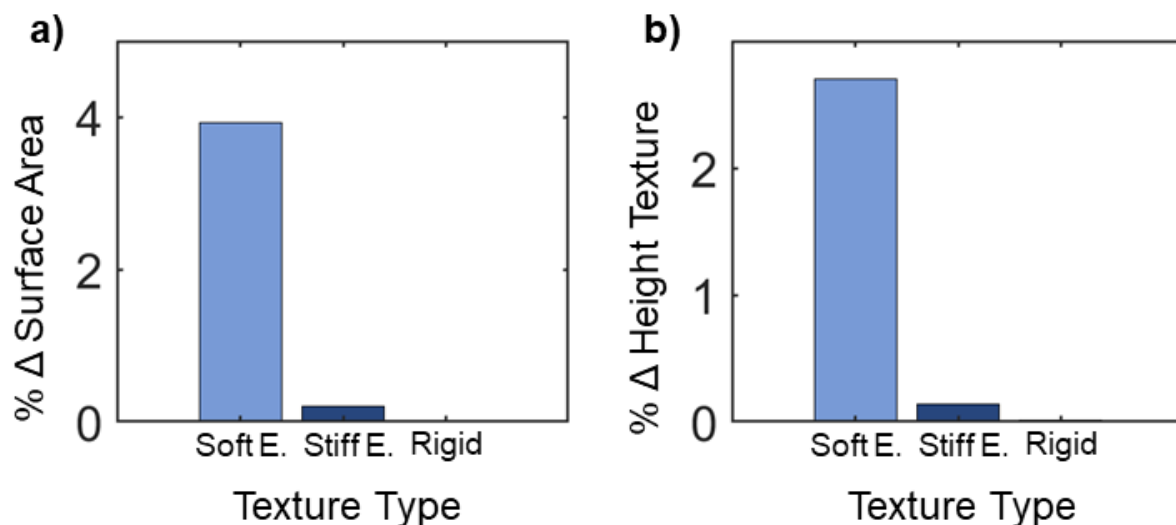
Figure 6.10: **Change in the structure of the hexagonal texture, when compressed to a rigid surface using a constant force, as modeled in FEA. a)** The soft, stiff, and rigid textures were pressed to a rigid (steel) surface using a constant force of 0.002 N, which corresponded to 1 kPa of pressure when calculated across the surface area of the undeformed hexagon. The change in surface area (%) at the interface of the texture and surface was reported. **b)** The change of the height of the texture (%) per 1 kPa of compression was reported for the three texture types.

surface type. Both the soft and stiff textures experience the maximum contact stress at the corners and along the perimeter of the hexagon (Fig. 6.8 d, e). For the soft texture against a stiff surface, we noticed a homogeneity of contact pressure, with minimum and maximum pressures of 6.03 and 6.51 kPa. This observation is consistent with a uniform distribution of load across the soft structure, which was not observed for the stiff texture.

6.3.6 Application of frictional textures to a soft robotic gripper

We applied the frictional textures to a soft robotic gripper, which was composed of fluidic elastomer actuators [190] that functioned to actively engage the friction textures with a surface (Fig. 6.11 a, b). The actuators were composed of a network of internal air chambers, which bent the actuator upon inflation due to the presence of an inextensible strain-limiting layer along the bottom of each actuator. Given that the organ surfaces that we aimed to manipulate were convex,
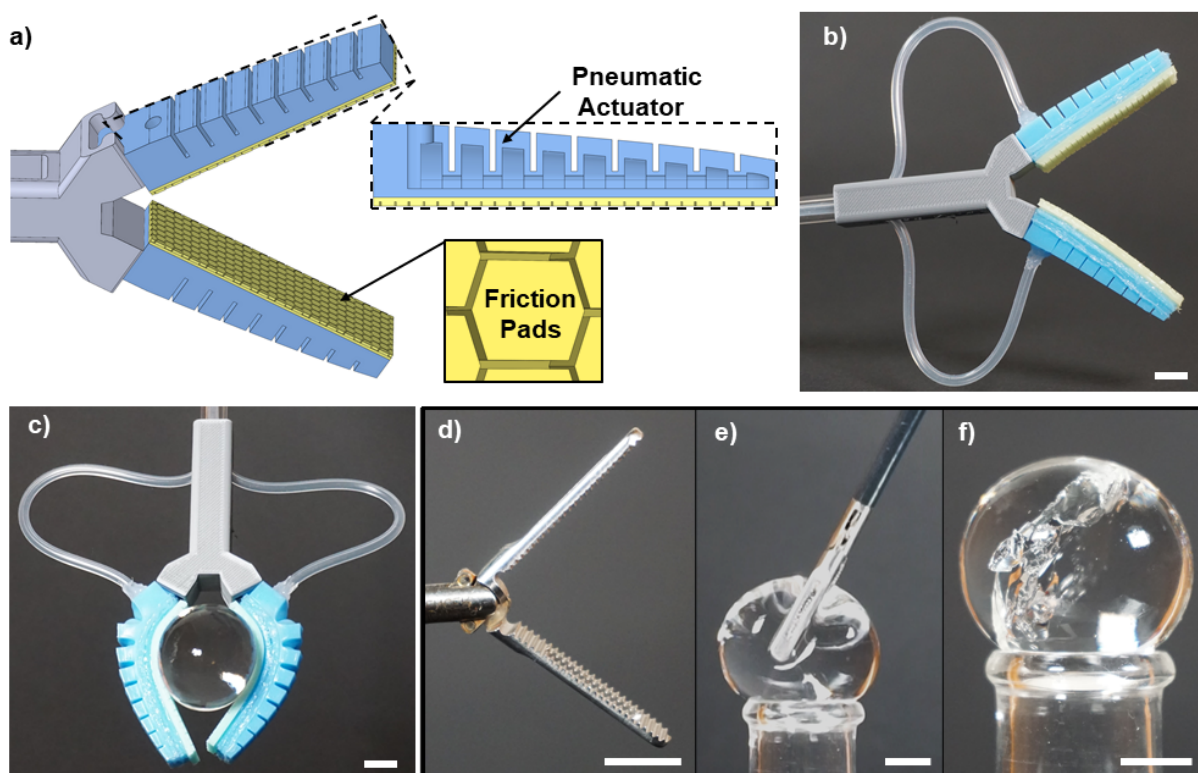
Figure 6.11: **Application of frictional textures to a pneumatic soft gripper. a)** A computer rendering of the soft gripper, which was composed of two fluidic elastomer actuators that were lined with frictional, elastomeric textures. The pneumatic actuator was composed of a network of air chambers with a parabolic decrease in internal area for more even surface conformation upon actuation [84]. **b)** Image of the textured gripper. **c)** The textured soft gripper successfully gripped and manipulated a clear hydrogel. **d)** Image of a commercially available surgical grasper composed of metal alloys. **e)** Image of an attempt at manipulation of the hydrogel with the metal surgical grasper. **f)** The resulting tear and damage of the hydrogel after attempted manipulation with the metal surgical grasper. All scale bars are 10 mm.

each actuator was positioned at an angle of 30 degrees relative to the central axis to better grip the surface. To engage all textures with the surface, a uniform conformation was critical. We used pneumatic actuators with a parabolic internal geometry, which had been previously reported to result in a non-uniform bending moment along the length of the actuator, to achieve an even surface conformation [84].

Using the textured pneumatic grippers, we were able to successfully, manually manipulate spherical hydrogels (diameter, 33 mm). Using the pneumatic grippers, we were able to pick

up, shake in multiple directions, and replace the spherical hydrogel without visible damage to the surface (Fig. 6.11 c). We compared the performance of the textured pneumatic gripper at manipulating the hydrogel with that of a commercially available, Dorsey-style, surgical grasper, which is commonly used in minimally invasive surgeries (Fig. 6.11 f). The surgical graspers featured serrations to help grip the surface. The surgical grasper was unable to grip the hydrogel, which would slip from the surface of the manipulator upon exertion of a normal force. Upon applying a larger preload to the hydrogel to help prevent it from slipping while gripping, the act of the surgical manipulator squeezing the surface triggered catastrophic damage to the brittle hydrogel, causing it to tear (Fig. 6.11 h). Overall, we were able to successfully demonstrate the ability of the textures to help stabilize the grip of the soft pneumatic grippers to a hydrogel surface without causing any visible damage.

6.4   Discussion

In this work, we provided an investigation into the role of stiffness for improving friction to lubricated soft surfaces. The biomimetic textures functioned to effectively shuttle fluid from the contact site and thus prevent excessive lubrication. We found two texture types that each demonstrated optimal performance depending on the stiffness of the surface. We highlighted the finding that the textures demonstrated two separate mechanisms to improve wet friction, also dependent on the stiffness of the textures. We implemented these elastomeric textures on soft robotic grippers to address the challenge of gripping wet, delicate objects and demonstrate their potential use applications during surgical manipulations.

6.4.1   The effect of surface stiffness on shear stress

We investigated the relationship between the stiffness of the texture and of the surface on shear stress. We surveyed surface stiffnesses across three orders of magnitude to address this

question. We found that a stiff elastomeric texture was most successful at generating high shear stress for the softest (order of magnitude, 0.001 MPa) of surfaces. Conversely, we found that a soft elastomeric texture resulted in the highest shear stress against surfaces on the orders of magnitude ranging from 0.01 to 0.1 MPa. The differences in the stiffness regimes in which the different textures dominated corresponded to the ways in which the textures were interacting with the surfaces.

We suggest that the high performance of stiff textures on the softest of the surfaces was a result of mechanical interlocking. The soft surface would deform more than the stiff texture, allowing the soft surface to recede into the space between the hexagonal textures. Given that the stiff texture still exhibited low contact stress when compressed against soft surfaces, we conclude that this type of mechanical interlocking would promote a higher frictional response while preventing damage to the surface.

Conversely, a soft texture, which had improved friction against stiffer surfaces, interacted in a different manner than its stiff counterpart. Upon compression to the surface, the soft elastomeric texture deformed, spreading laterally along the plane of the surface. This spreading of the texture increased the area in contact with the surface, which we observed in both the FEA and FTIR analyses. The increase in area that is in contact with the surface corresponded to the increase in friction, and thus a higher shear stress. From these results, we suggest that there may not exist a one-stiffness-fits-all approach to texturing. We concluded that, for manipulation of stiffer surfaces, a soft elastomeric texture would be preferred for gripping applications. Conversely, for manipulation of soft surfaces, a stiff elastomeric texture would fare better.

The effect of stiffness was uniform across both the hexagonal and rectangular patterns of the textures. We found that hexagonal surface textures exhibited far less orientation dependence than the rectangular bars. We concluded that for non-uniform, randomized shear loads, which would be expected during surgical manipulation, hexagonal surface textures would generate greater friction in comparison to textures composed of rectangular bars. Conversely, in scenarios

in which the direction of the shear load is known and predictable, an elongated rectangular bar would outperform the hexagonal textures.

6.4.2   Position control via fluid channeling

To design a texture to be applied to any form of manipulation, we would need to first quantify its ability to maintain its position while subjected to a disturbance. Using video tracking, we demonstrated the need for adequate fluid channeling to prevent unwanted drift in the position of the texture. Fluid channeling, which was achieved in the case of this study by the addition of channels between textures, removed fluid from the interfacial, lubricating layer between the surface and the textures. By channeling fluid, the height of the textures is reduced, allowing for a more intimate contact to be achieved with the surface and thus preventing drift in its position. Position stability is essential in the development of a gripper, where immediate fluid channeling would be required to achieve a stable grasp.

While the addition of a texture functioned to stabilize its position in comparison to the control, we observed an orientation dependence on fluid channeling and drift. The vertically aligned textures were better able to maintain their position, whereas horizontally aligned textures drifted. This orientation dependency was also observed in related work investigating the flow of fluid being channeled around hexagonal textures [147]. In this work, Chen *et al.* found that for horizontally aligned hexagons, fluid flushed onto the contact site, forming a partially lubricated layer across the hexagonal texture. This fluid flushing was not observed on the vertically aligned hexagonal structures. Chen *et al.* proposed that the angle formed by the channels in coordination with the sliding direction correlated with contact flushing and thus the reduction in overall friction.

We propose that, in this work, the drift observed in the horizontal hexagonal textures was in part due to this proposed mechanism of contact flushing, thus further lubricating the texture and resulting in a moderate loss of position control. Curiously, the shear stress resulting from experimental pull tests did not exhibit a dramatic difference in performance of the hexagonal

textures based on orientation. To further, the stiffness of the textures also influenced their orientation dependency, where the soft elastomeric textures managed to maintain their position better in the horizontal orientation in comparison to the stiff textures.

6.4.3 Mechanics of deformation of the textures

Using FTIR, we were able to monitor the deformation of the textures, which varied based on stiffness. On the FTIR imaging surface, which was lubricated in glycerol, we observed a stick-slip response when the textures were pulled in shear. The presence of surface lubrication resulted in a fluid-mediated stick-slip behavior that was not predominant in a dry environment. We propose that in a wet environment, the lubricating layer of fluid between the texture and the surface allows for restoration of the original shape and configuration of the hexagonal pillar of the texture. In a dry environment in which friction between the texture and a surface is greater, friction would anchor the face of the texture to the surface, preventing restoration of the original configuration and thus a stick-slip behavior.

For the fluid-mediated behavior, we found that the frequency of the stick-slip response strongly corresponded to the stiffness of the texture rather than its geometric spacing. Softer elastomeric textures were able to bend and deform for a longer duration of time when subjected to a shear stress in comparison to the stiff textures. This difference accounted for the longer period in the sinusoidal behavior of the soft textures.

In FTIR, we also observed the characteristics of the textures when deformed via compression and shear loading. The soft elastomeric textures were able to spread considerably during a compressive load in comparison to the stiff textures, resulting in a greater distribution of contact across the entirety of the texture. Correspondingly, when pulled in shear, the soft textures deformed more than the stiff textures. The soft textures that were horizontally oriented experienced the largest reduction in contact area when pulled in shear in comparison to those that were vertically oriented. We concluded that the vertically oriented soft texture had a greater

amount of bulk material in the direction of motion, which increased its effective material stiffness. Thus, with a higher effective material stiffness, the vertically oriented structures did not bend and deflect as greatly as the horizontally oriented textures. This reduction in contact area of the soft elastomers when pulled in shear was not observed in the stiff structures, suggesting that the stiffer textures did not significantly bend and deform laterally when disturbed in shear. Overall, from the quantifications of contact area, we concluded that the vertical orientation of the hexagonal textures of the soft elastomer resulted in the greatest contact with the surface, whereas orientation was less influential to the performance of the stiff textures.

We propose that in general a balance in behavior when subjected to shear loads would be necessary to achieve a stable frictional texture against stiff surfaces for gripping applications. We suggest that some deformation of the structures would act to increase the effective contact of the texture, as demonstrated in the soft, vertically aligned hexagonal structures. However, too much deformation would adversely affect the contact area, as seen with horizontally oriented soft textures, leading to a loss of position control. Too little deformation would also prevent a large increase in contact area when subjected to a shear load, as demonstrated in stiff textures, leading to lower friction against stiff surfaces.

6.4.4   The effect of stiffness during compression on contact stress

Using FEA, we were able to resolve the contribution of elastomeric textures in preventing tissue trauma due to high compressive stresses. We found that the use of elastomeric textures, regardless of soft or stiff, resulted in at least an order of magnitude reduction in the contact stress due to compression, when compared to the rigid texture. The soft elastomeric texture maintained a low contact stress across all surface textures, whereas stiff textures increased the contact stress with an increase in surface stiffness. We attributed the performance of the soft texture to its ability to spread laterally across the surface, which helped to dissipate the contact force over a larger area. The stiff texture deformed less with compression, resulting in higher contact stresses for the

177

same vertical displacement.

We compared the results from the simulation to the prediction of compressive stress known to cause tissue trauma (Fig. 6.8 b). Previous works have defined the threshold of compressive stress above which tissue trauma occurs in colonic tissue to be between 150 [170] and 200 (180 De 2007)[169] kPa. However, the type of tissue being manipulated also implies its susceptibility to damage, where some tissues are more robust to compression and manipulation. In comparing these biological limitations in compressive stress with our simulation, we found that the rigid texture quickly surpassed this threshold (contact stress, 176 kPa; $E_{surface}$, 0.017 MPa). On the other hand, the stiff texture reached this threshold for the stiffest of surfaces tested (contact stress, 149 kPa; $E_{surface}$, 0.445 MPa). This finding suggests that even the stiff elastomeric texture closely approached this threshold for tissue trauma for the stiffest of surfaces. However, given our finding that stiff textures functioned best in their manipulation of the softest of surfaces tested ($E_{surface}$ ~ 0.001 MPa), we would anticipate that the stiff elastomer would not damage the softest of the organ surfaces.

The soft texture was consistently at least an order of magnitude less than this threshold for tissue trauma across all surface stiffnesses tested. This finding suggests that the soft textures would be preferential for a wider range of tissue types and may prove beneficial at preventing tissue trauma due to excessive compression.

We acknowledge that while this simulation was helpful to demonstrate trends in the performance of the hexagonal structures based on stiffness, we did not expect it to accurately predict actual levels of tissue trauma. Instead, we would need to conduct compressive stress trials on living tissue and subsequently perform histological analyses to accurately assess for damage [171, 201]. However, as demonstrated in previous works, FEA can serve as a helpful tool for predicting tissue trauma when surveying the impact of design parameters of surgical grippers [169, 200].

We acknowledge that in our assessment of texture performance, we omitted the contribu-

tions of wet adhesion, which would provide viscosity-mediated, normal attachment. While this contribution was not accounted for, we expect that wet adhesion would play an important role in attachment and adhesion of the textures to the soft, wet surfaces.

6.4.5   Application to robotics

By applying the textures to a soft robotic gripper, we demonstrated the utility of coordinating friction and soft actuation to manipulate delicate, wet surfaces. We applied the gripper to the tasks of manipulating spherical hydrogels, which served as a proxy for organ tissue. Given that hydrogels are polymer networks that are swollen by water, these surfaces are notoriously difficult to manipulate due to the presence of a lubricating layer of water and the brittle nature of many hydrogels [202]. The manipulation of hydrogels was a successful demonstration of the ability of the textures to maintain a stable grasp of an object with a challenging surface without causing damage. The ability to shake and add additional disturbances while manipulating the hydrogel demonstrated a successful, stable grip. The inability of the metal surgical grasper to grip the hydrogel without catastrophic damage corresponded with the FEA results, in which the dissimilarity of the stiffnesses between the metal grasper and hydrogel resulted in high contact stresses and thus brittle failure of the hydrogel. Conversely, the soft nature of the pneumatic actuator also helped to prevent damage to the hydrogel due to the relative similarity in their stiffnesses.

We acknowledge that the development of our textured pneumatic gripper provided for purely open-loop manipulation, in which sensors were not used to detect surface contact. We suggest that the addition of sensors to this manipulation scheme would help to minimize potential damage to a delicate object during manipulation.

While we focused the efforts of this paper on surgical manipulation, the issue of gripping deformable, soft, and wet surfaces extends across a wide range of applications. We project that the use of surface textures, similar to these tested here, depending on the stiffness of the item to

be manipulated, could extend to robotic manipulation for manufacturing and agriculture, as two examples. We believe that the use of elastomeric textures would make a useful addition to soft robotics, in the areas of manipulation and locomotion. This work therefore can extend into many different aspects of robotics for enhanced friction in wet environments.

6.5   Materials and Methods

6.5.1   Fabrication of textures and gripper

We fabricated the frictional textures using silicone rubber, which was considered to be either "soft" (Young's modulus, 0.0167 MPa; Ecoflex 00-20, Smooth-On Inc.) or "stiff" (Young's modulus, 0.445 MPa; Dragon Skin 20, Smooth-On Inc.). The mold (Fig. 6.12) for the texture was etched into acrylic using a laser machining system (PLS6MW, Universal Laser Systems). The mold measured to a width, length, and height of approximately 1.6 mm, 2.1 mm, and 1.0 mm, respectively. Uncured silicone was added to the mold, degassed for 5 min, and cured for 6 hr.
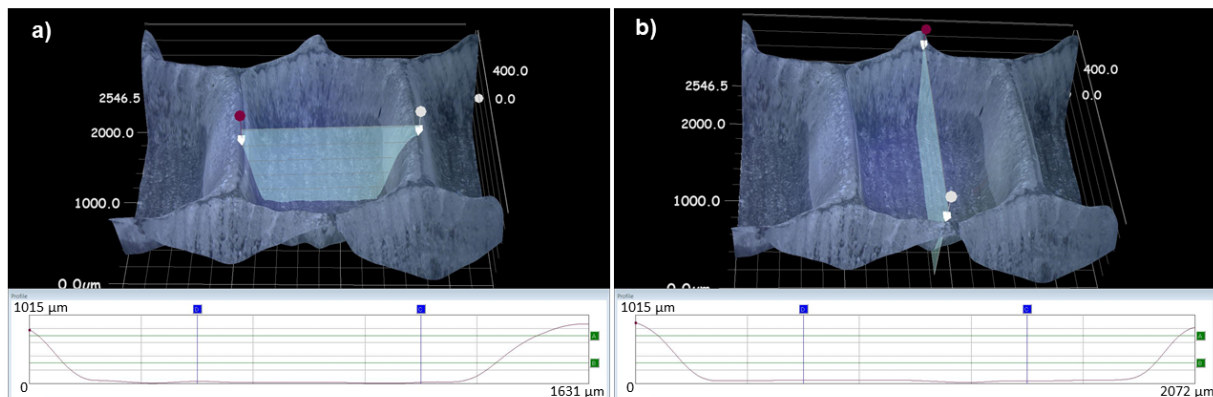
Figure 6.12:   **3D microscopy to measure the dimensions of the mold for the hexagonal texture.** The mold for the hexagonal textures was etched using laser micromachining into acylic. **a)** The width of the hexagonal feature of the mold was measured to ~ 1.6 mm, and the height was measured to ~ 1.0 mm. **b)** The length of the hexagonal feature was measured to ~ 2.1 mm.

All components of the gripper were modeled using computer-aided design (Solidworks, Dassault Systems). The support collar for the gripper, which served to mate together its silicone

digits, was fabricated from PLA using a 3D printer (Prusa i3 MK3S+). The support collar angled the actuators by 30° relative to the central axis and was bonded using cyanoacrylate adhesive to an acrylic rod.
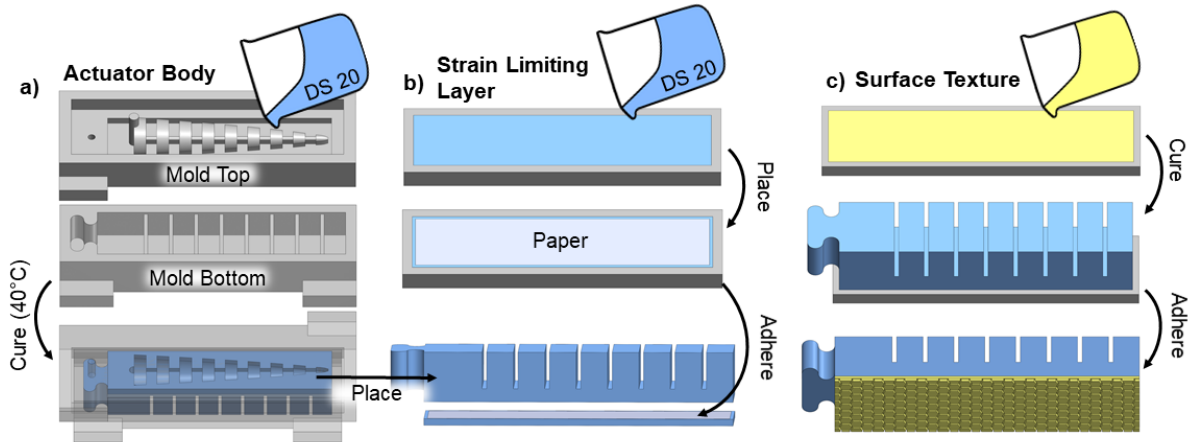
Figure 6.13: **Fabrication of the textured pneumatic actuator. a)** The body of the pneumatic actuator was fabricated using a stiff silicone (Dragon Skin 20) that was poured into a mold, degassed in a vacuum chamber, and cured at 40°C. **b)** The strain limiting layer was fabricated using an inextensible paper layer that was embedded in uncured silicone. The strain limiting layer was bonded to the body of the actuator using a silicone adhesive. **c)** The texture was molded and applied to the bottom of the pneumatic actuator using a silicone adhesive.

The actuators were designed with a length of 46 mm, width of 11 mm, and height of 10 mm. The pneumatic actuator was produced using a custom mold that was made of a hard resin (VeroClear, Stratasys Inc.) on a multimaterial 3D printer (Object 350 Connex3, Stratasys, Inc.). After printing, the mold for the pneumatic actuator was further aged for 4 h at 40°C to ensure that the resin fully cured. The actuators were molded using silicone rubber (stiffness, 0.231 MPa; Dragon Skin 20, Smooth-On, Inc.). Uncured silicone was added to the mold for the pneumatic network, degassed for 5 min, and cured for 4 hr (Fig. 6.13). Uncured silicone was added to the mold for the strain-limiting layer and degassed for 2 min. A strip of paper was embedded in the silicone to serve as the inextensible layer. Upon fully curing, the elastomeric body was bonded to the strain-limiting layer using a silicone adhesive (Sil-Poxy, Smooth-On, Inc.). The surface texture was then bonded to the strain-limiting layer also using silicone adhesive. The

pressure inside of the actuators was manually controlled using a syringe to push air into the internal chambers, causing a bending behavior.

6.5.2   Experimental setup for friction characterizations

We experimentally measured the friction of the textures using artificial mimics of organ surfaces. The testing surface was molded using silicones of different stiffnesses: 0.0065 MPa (Ecoflex 00-10, Smooth-On, Inc.), 0.165 MPa (Dragon Skin 10 Medium, Smooth-On, Inc.), and 0.445 MPa (Dragon Skin 30, Smooth-On, Inc.). The testing surface was lubricated with glycerol (viscosity, 1.4 Pa·s; Vegetable Glycerin, Essential Depot, Co.) which served as an analog to the secretions that coat organ tissue. The friction measurements were conducted using a universal testing machine with a force gauge (Max force, 100 N; Resolution, 0.2 N; M7-20, Mark-10 Co.). The experiments were performed using a motorized test stand (ESM303, Mark-10 Co.) at a rate of retraction of 100 mm·min^{-1}. The textures were preloaded to the surface using a weight of 200 g (1.96 N) placed on a rigid support backing. An inextensible cord was routed from the support backing, through a pulley, to the upper clamp of the motorized stage. The experiment was initiated upon retraction of the upper clamp and performed in triplicate.

6.5.3   FTIR and Drift Quantifications

We used FTIR to assess the contact and deformation of the textures when pulled along a surface. The FTIR imaging plate was composed of a 9.7 mm thick plate of acrylic, which was lined along its side with white light-emitting diodes (LEDs; 3528-24 VDC, Super Bright LEDs, Inc.). The light from the diodes was internally reflected within the acrylic plate and escaped when contacted by the texture. The FTIR plate was imaged from below using a camera (16 MP, 120 fps, Motorola, Inc.). The FTIR imaging plate was placed horizontally, acting as a runway for the texture, and was either dry or lubricated with glycerol for the trials.

To allow for better visualization, the texture was dyed using black silicone pigment (Silc Pig, Smooth-On, Inc.). A preload of 200 g (1.96 N) was applied to the back of the texture, pressing it to the surface of the FTIR plate. The texture was then pulled along the FTIR plate using a universal testing machine at a rate of retraction of 100 mm·min^{-1}. The images from FTIR were post-processed in MATLAB to convert the RGB image to a binary image.

Using video sequences captured during FTIR, we measured the distance that the textures drifted when pulled horizontally using an open-source video analysis software (Tracker; [203]). We quantified the drift using visual markers on the textures and measured the displacement of their position in the y-direction with respect to time.

6.5.4   Finite Element Analysis

We used Finite Element Analysis to measure the interaction of a hexagonal texture and a surface during compression. FEA was conducted using ANSYS 2021 R2. We experimentally determined the material properties of the silicone surfaces (Ecoflex 00-10, Ecoflex 00-20, Dragon Skin 10 Medium, Dragon Skin 20, Dragon Skin 30) via tensile tests using a universal testing machine and load cell (M7-20, Mark-10 Co.). The data from each tensile test was best fit to the Yoeh 3rd order hyperelastic model. We used triangular elements to mesh the surfaces and performed a mesh refinement at the interface between the hexagonal texture and the surface. The FE model had a total of 12,805 nodes and 7808 elements (Fig. 6.9 a-c).

A constant 0.25 mm displacement was imparted on the back of the hexagonal structure. We assumed the surface to be frictionless and in air. We measured the maximum contact stress at the interface between the hexagon and the surface, comparing across stiffnesses of the surface. We also quantified the change in surface area of the structure by exporting the deformed hexagonal texture and measuring the surface area of the contacting hexagonal face in a modeling program (SpaceClaim, Ansys Inc.).

6.5.5   Application to manipulation
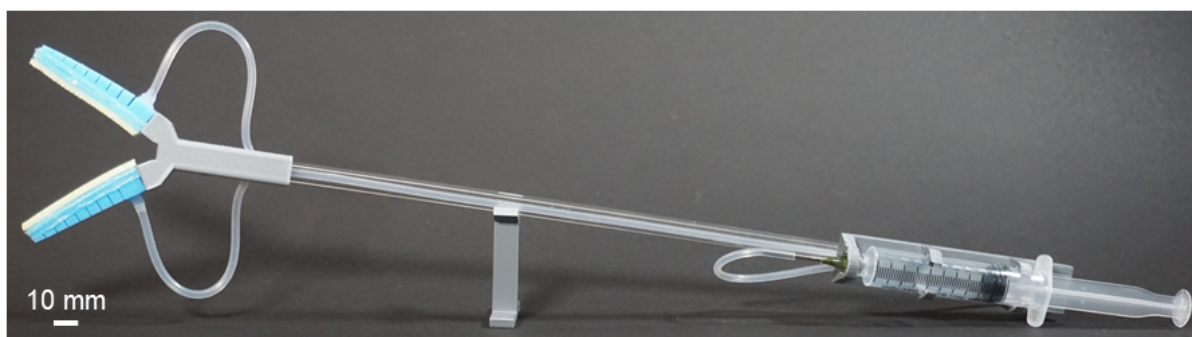
Figure 6.14: **The overall assembly of the textured pneumatic gripper, for use during hydrogel manipulations.** The pneumatic gripper was attached to a rigid rod for manual manipulation. The gripper was pneumatically actuated using an air-filled syringe.

The textured pneumatic gripper was applied to the tasks of manipulating hydrogels. To grip, a 10 mL syringe was used to manually inject air into the pneumatic actuators, which would in turn result in bending (Fig. 6.14). Spherical hydrogels (Jumbo Water Beads, Leeche) were submerged in water for 6 hr prior to manipulation to ensure adequate hydration and expansion. Both soft and stiff textures were used to successfully manipulate the hydrogel object. We compared the manipulation performance with a surgical, Dorsey-style, fenestrated grasper (25 mm jaw, 5 mm width; SP90-6378, Snowden-Pencer Diamond Line, BD Co.).

6.6   Acknowledgements

characterizations and friction measurements and post-processed the data. J.A.S. performed the FTIR trials and FEA simulation. J.A.S. and T.X. fabricated the textured gripper for demonstration of application. J.A.S. prepared the initial draft of the manuscript and all authors provided feedback during revisions.

Chapter 6, in part, is currently being prepared for submission for publication of the material. Sandoval, Jessica A.; Xu, Thomas; Tolley, Michael T. The dissertation author was the primary investigator and author of this material.

Chapter 7

Combining suction and friction to stabilize a soft gripper to shear and normal forces, for manipulation of soft objects in wet environments

Jessica A. Sandoval[1], Thomas Xu[2], Iman Adibnazari[1], Dimitri D. Deheyn[3], Michael T. Tolley[1]

[1]Department of Mechanical and Aerospace Engineering, University of California San Diego, 9500 Gilman Dr., La Jolla, CA 92093, United States

[2]Department of Mechanical Engineering, Carnegie Mellon University, 5000 Forbes Ave, Pittsburgh, PA 15213, United States.

[3]Marine Biology Research Division, Scripps Institution of Oceanography, 9500 Gilman Dr., La Jolla, CA 92093

7.1 Abstract

Soft robotic gripping in wet environments is generally limited by the presence of a liquid that lubricates the interface between the gripper and an object being manipulated. The use of soft grippers is particularly beneficial for manipulating soft, delicate objects, yet is further limited by low grip strengths. We propose the use of suction, a form of adhesion that functions well in wet environments, to enhance soft robotic grippers. We stabilized the suction against shear disturbances using soft actuated fingers decorated with fluid-channeling patterns to enhance friction, counteracting the interfacial lubrication experienced in wet environments. We therefore combined the uses of attachment via suction and shear stability via friction to create an adhesive soft gripper. We evaluated the contributions to attachment of each component to help stabilize it against dislodgement forces that act in parallel and normal to an object that it aimed to manipulate. By identifying these contributions, we envision that such an adhesive gripper can be used to benefit soft robotic manipulation in a variety of wet environments, from surgical to subsea applications.

7.2 Introduction

A wet environment poses a challenge for soft robotic gripping. The presence of water, or any other fluid, acts to lubricate a surface, thus reducing the friction needed to achieve a stable grasp [172, 173]. Soft grippers, like human hands, exert a force on an object, perpendicular to the surface in an effort to maintain its grasp [174]. This force is related to the amount of friction between the gripper and the object being manipulated [175]. For grippers with high coefficients of friction, the force required to maintain a stable grasp is reduced, allowing for more delicate manipulation [175]. Additionally, the use of elastomers in soft robotic grippers further enhances the ability to delicately manipulate a surface while minimizing the potential for damage [27].

A pneumatic soft gripper is composed of a series of internal chambers, that upon inflation,

187

results in a bending motion. When grasping objects, soft grippers face the challenge of generating sufficient grip forces to support a payload [27]. The design of the pneumatic channels have been tailored to improve load distribution [84], yet the generated force is still low compared to the forces generated by manipulators composed of rigid components. To yield a higher load capacity, adhesives, such as gecko-inspired adhesives, have been applied to soft grippers [84]. However, in the presence of water, dry adhesives are rendered ineffective [2]. Thus, alternative adhesive strategies that function within a wet environment must be used to enhance gripping in the case of interfacial lubrication.

One adhesive mechanism that works well in a wet environment is suction, which generates high adhesive forces normal to a surface, thus supporting the grip of a wetted object. Previous work has demonstrated that the use of suction at the end of robotic fingertips helps to increase the coefficient of friction and normal force of the robotic hand against wetted objects [204]. Suction has shown promise for its ability to grasp delicate, irregular, and even rough surfaces [65]. However, dependent on the design of the suction device, some designs have reported low coefficients of friction when used on wetted surfaces [205]. Enforcing the shear stability of a suction-based gripper would be crucial for preventing slippage along a wet surface.

Surface texturing has been demonstrated to improve coefficients of friction against wet objects. The use of textures to successfully grip in wet environments is not unique to robotic systems, however. Organisms such as the tree frog[11] and clingfish [60] all use surface textures to help stabilize their grip to wet surfaces. These organisms have inspired the development of biomimetic frictional textures that function based on the principles of wet adhesion and friction [139]. Surface textures act to shuttle fluid from beneath the area of contact into channels between the textures, resulting in greater contact and an improved coefficient of friction [147, 179]. Overall, these bioinspired textures have been demonstrated to improve the resistance to shear forces that act parallel to a surface.

In this work, we coordinated the advances of surface textures, suction, and soft actuation

to develop an adhesive gripper that is capable of attaching to wet surfaces. We investigated the relative contributions of each of these three components to successful attachment against disturbances that act parallel, or along the x-direction of the coordinate frame, and normal, along the z-direction, to a surface. Additionally, to narrow the scope of this study, we only considered gripping large objects that were too wide to envelop in an enclosing grasp.
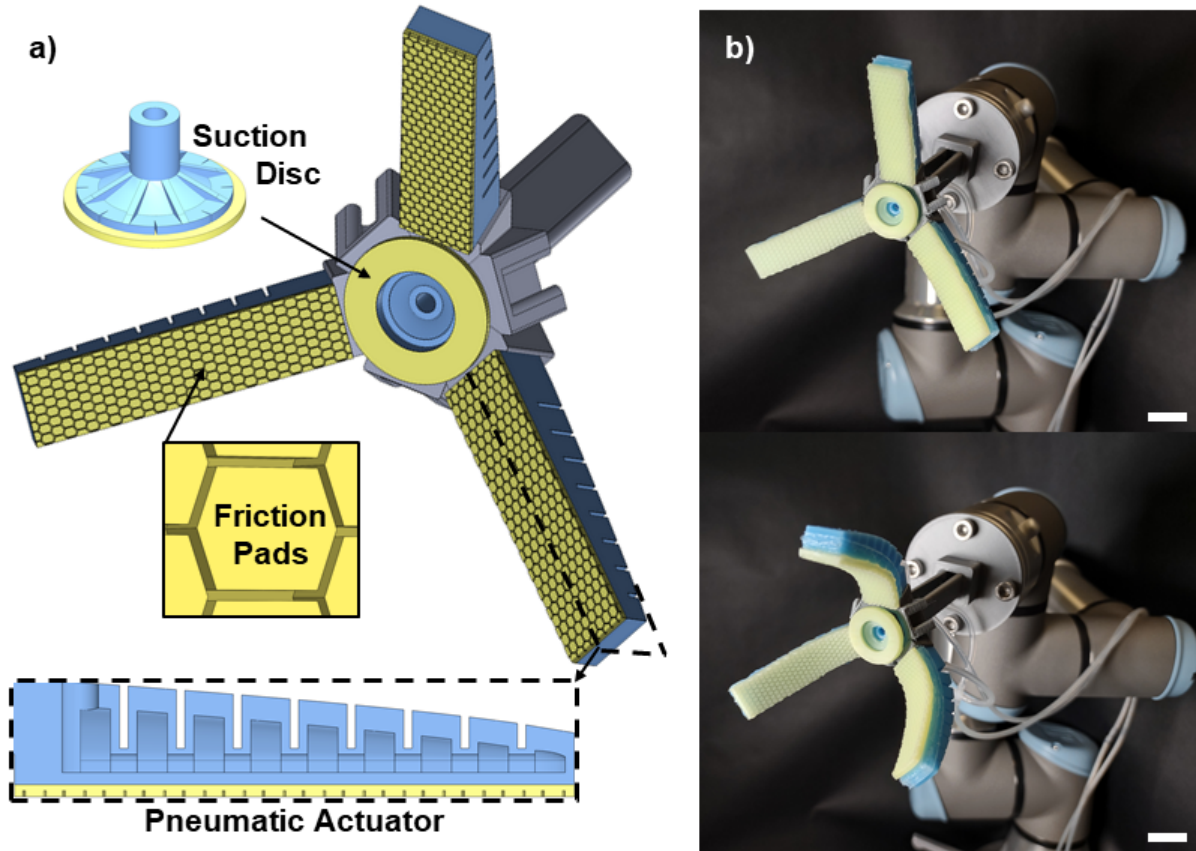
Figure 7.1: **Overview of the adhesive gripper. a)** Schematic of the adhesive gripper. A central suction disc is flanked by three fingers composed of fluidic elastomer actuators (FEAs), which bend to engage a frictional texture with the surface of a target object. The actuators have internal pneumatic chambers with parabolically decreasing internal geometry to achieve even surface conformation. **b)** Photographs of unactuated (top) and actuated (10 psi, bottom) states of the pneumatic fingers. The gripper is mounted to a commercial robotic arm. Scale bar, 20 mm.

7.3   Results

7.3.1   Design of an adhesive gripper

The adhesive gripper was designed to provide a stable, delicate grip by combining suction, friction, and soft actuation. The gripper was composed of three components: 1) a suction disc to provide strong adhesion normal to the surface, 2) friction pads to provide resistance to shear forces along the x-direction, and 3) fluidic elastomer actuators (FEAs) to engage the friction pads with the surface of a target object (Fig. 7.1). In this work, the FEAs combined with the friction pads are referred to as a unit as textured fingers.

At the center of the gripper, a suction disc, composed of soft elastomers consistent with our previous work [65] served to provide strong axial adhesion to wet surfaces. To stabilize against shear forces of dislodgement, three fingers composed of friction pads were equidistantly spaced around the central axis of the gripper. The friction pads consisted of a textured surface composed of elongated hexagons (aspect ratio: 1.3), which we found in previous work to increase the coefficient of friction when subjected to shear loads [60]. The hexagons were designed with a width, length, and height of 1.3, 2.1, and 1.0 mm, respectively.

We used soft actuators containing a network of pneumatic chambers [83] to bend upon inflation to engage the friction pads with a surface. We used an inextensible strain-limiting layer along the length of the actuator to enforce a bending behavior.

7.3.2   Simulation of surface conformation of the textured fingers

We aimed to engage as much of the friction pads as possible with the target surface. A greater amount of friction pads in contact with the surface would allow for a higher occurrence of fluid channeling, thus allowing for more intimate contact to be achieved with the surface [194]. Additionally, by increasing the amount of contact that the gripper made with a surface, we would reduce the compressive load on the object and distribute it over a larger surface area, thus enabling

a more delicate grip. Thus, a uniform surface conformation was critical. Using simulation, we tested the difference in contact between two geometries of the pneumatic chambers. We chose to investigate a rectangular and a parabolic geometry of the pneumatic chambers. The selection of a parabolic pneumatic chamber was based on previous work which found that this geometry resulted in a non-uniform bending moment along the length of the actuator [84].

Additionally, we simulated how the different geometries interacted with a cylindrical surface that varied in stiffness from soft to stiff (0.005, 0.05, and 0.5 MPa) to rigid (50 GPa) (Fig. 7.2 a). Please refer to the Materials and Methods section for further details of the setup of the simulation.

Across the four tested surface stiffnesses, we monitored the percentage of the actuator in contact with the surface of the cylinder (Fig. 7.3). The actuator with a parabolic internal geometry maintained consistently at least double the amount of contact with the simulated surface in comparison to the actuator with a rectangular internal geometry (Fig. 7.2 c). The actuator with parabolic chambers demonstrated greater surface contact with surfaces of a stiffness greater than 0.05 MPa (i.e. 83% and 79% for 0.05 and 0.5 MPa, respectively) in comparison with the softest of the surfaces (61%; 0.005 MPa). The actuator of a rectangular internal geometry maintained a significantly lower percentage of contact, at an average of 28%, with the simulated surface. The surface contact of the actuator with a rectangular internal geometry did not vary across the surface stiffnesses, where the softest and stiffest of surfaces tested exhibited a consistent, although low, area of contact.

The actuators of parabolic and rectangular pneumatic chambers differed in the distribution of contact and overall bending behavior. The parabolic internal geometry resulted in a greater distribution of contact, most specifically extending from the middle to the tip of the actuator (Fig. 7.3). The bending behavior of the actuator with a parabolic pneumatic chamber therefore demonstrated a higher degree of surface conformation (Fig. 7.2 a). The rectangular internal geometry resulted in a lower distribution of contact, which was instead concentrated at the base
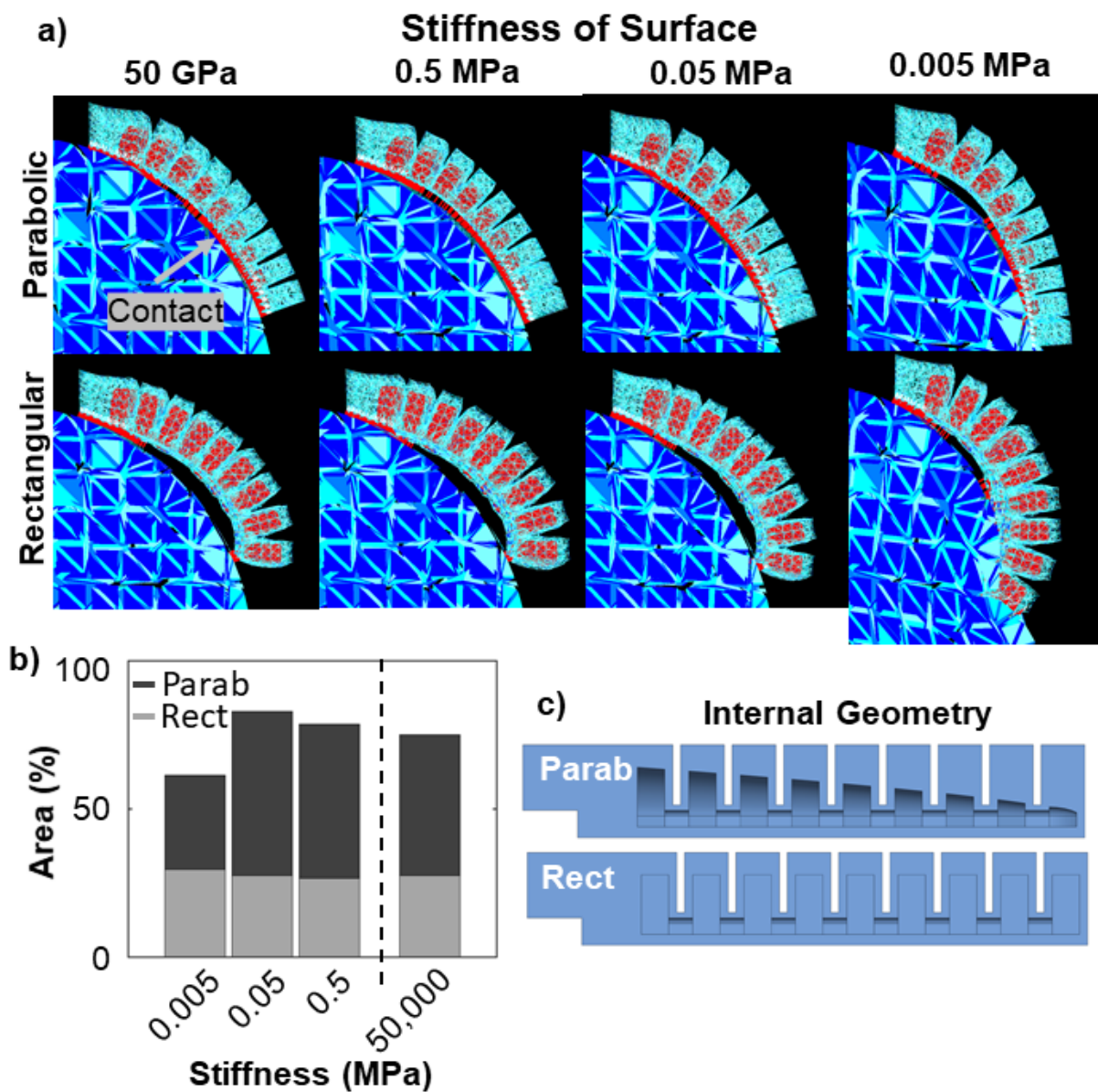
Figure 7.2: **Simulation of the contact made by an actuator against a cylindrical surface.**
a) Simulation of the contact made by an actuator of either parabolic (top row) or rectangular
(bottom row) internal geometries, against a cylindrical object that varied in stiffness (left to
right, 50 GPa, 0.5 MPa, 0.05 MPa, and 0.005 MPa). **b)** We measured the percentage of the total
surface area of the soft finger that was in contact with the simulated surface upon actuation. We
compared the contact area of the soft finger with parabolic (dark gray) and rectangular (light
gray) internal geometries. **c)** Cross-sectional view of the pneumatic chambers of the actuator.
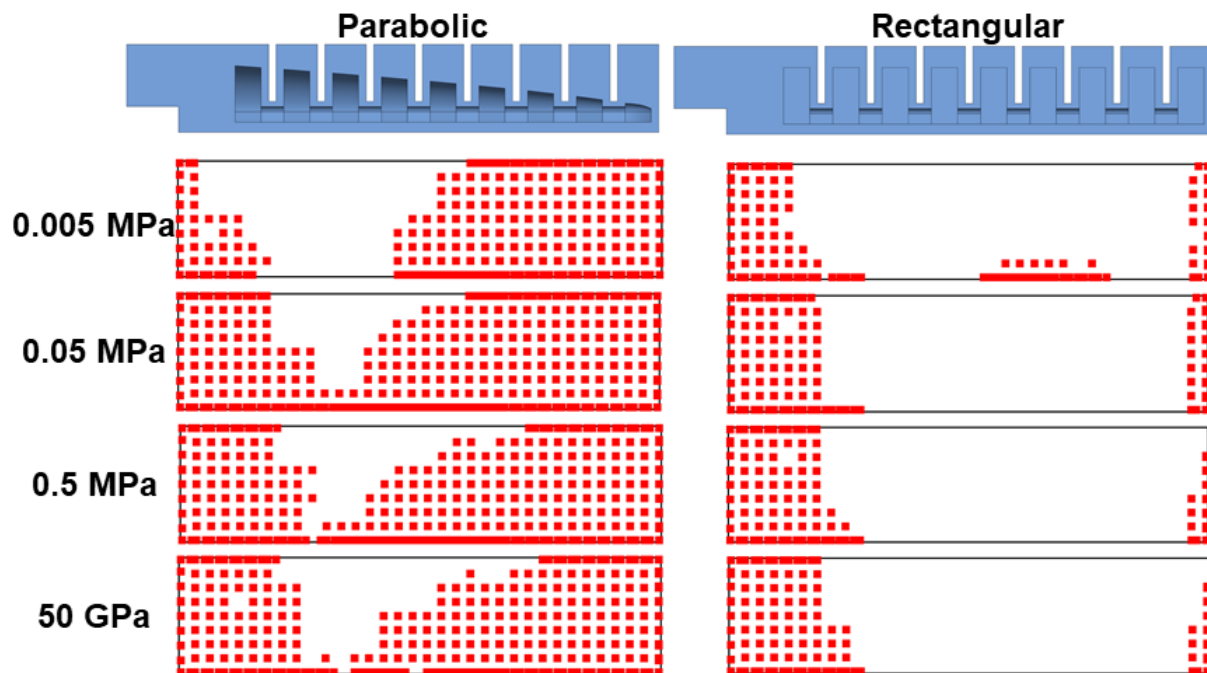
Figure 7.3: **Map of surface contact, as quantified in simulation. a)** A visual representation of the nodes in contact with the cylindrical surface upon actuation of the actuators with parabolic (left) and rectangular (right) internal geometries. We varied the stiffness of the surface from soft (0.005 MPa; top row) to rigid (50 GPa; bottom row).

and tip of the actuator (Fig. 7.3). As the actuator of a rectangular pneumatic chamber contacted the surface, the middle of its length buckled and bent away from the surface, leading to the concentration of contact in only its base and tip (Fig. 7.2 a). This buckling led to an apparent pinching behavior of the actuator and an overall loss of surface contact.

From the visualization of surface contact, we observed that the simulated behavior demonstrated some asymmetries. The body of the actuator would twist slightly, causing an asymmetric behavior. The twist was attributed to minor differences in the meshes of the body of the actuator and the internal air chambers, and to surface interactions with the highly deformable cylindrical surface.

Thus, we concluded that since the pneumatic chambers with parabolically decreasing internal area was most successful at engaging with the surface of a soft target object in simulation, we chose this design for our experimental investigations.

7.3.3 Resistance to shear forces in a wet environment

We tested the contributions of the components of the gripper to resisting shear disturbances (Fig. 7.4). To perform this characterization, we secured the gripper as an end effector to a robotic arm, which was used to record the forces from manipulation. We translated the gripper a distance of 30 mm in the x-direction, along a plane tangent to the top of a hemispherical surface, which was submerged in a bath of water (Fig. 7.4 a). We varied the stiffness of the hemispherical surface to quantify the effect of surface stiffness on the resistance to shear disturbances.

To elucidate the contribution of suction and friction to the magnitude of the aforementioned resistance to shear disturbances, we ran experiments with the gripper in one of four configurations– all components (suction and textured fingers) active (*S.T.*), only suction active (*S.* only), only the textured fingers active (*T.* only), or a control, in which all components were inactive (*Ctrl.*) (Fig. 7.4 b). Prior to the trial, the suction disc was preloaded to the surface by imparting a displacement on the back of 1 mm. For the reported adhesive forces per configuration type, we
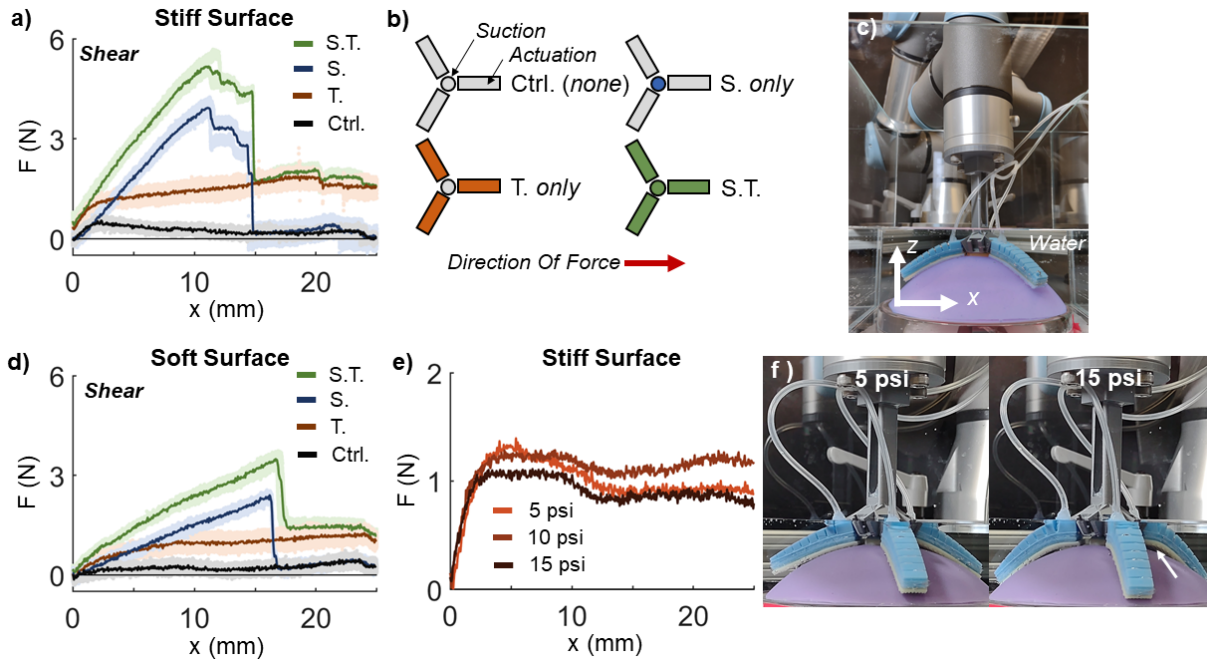
Figure 7.4: **Contribution of suction and friction to shear stability to soft surfaces. a)** Force measurements quantifying the contribution of suction and friction to resisting shear motions, while engaged with a stiff surface. The gripper was sheared for a total of 30 mm in the *x*-direction. The averaged, interpolated force-extension curve is shown as a dark line. The shaded region represents the standard deviation across three trials. Color coordination corresponds to subfigure b. **b)** The control (dark gray), in which neither the suction or actuation of the soft fingers were active. The suction only (S. only; blue) configuration, in which only the central suction chamber was active. The textured fingers only (T. only; orange) configuration, in which only the frictional actuators were active. The suction and soft fingers (S.T.; green) configuration, in which both the suction disc and the textured fingers were active. **c)** Experimental setup of force measurements. The gripper was attached as an end effector to a robotic arm. All tests took place in a bath of water, water line indicated in white. **d)** Force measurement quantifying resistance to shear (*x*-direction) motions of a gripper, against a soft surface. **e)** Quantification of actuation pressure of the pneumatic gripper. We tested the actuation pressures of 5 (light orange), 10, and 15 (darkest orange) psi. The test was performed on a stiff surface ($E_{surface}$, 0.165 MPa) . **f)** Gripper engaged with the surface with either 5 (left) or 15 (right) psi. The use of 15 psi to actuate the gripper caused disengagement with the surface (arrow).

linearly interpolated the raw data per trial to generate a trendline for the force-displacement curve that accounted for noise. We then averaged the interpolated adhesive curves, which are reported in (Fig. 7.4 c). We found that, when gripping a stiff elastomeric surface, the use of both suction and textured fingers resulted in the highest shear force (S.T.; 5.3 ± 0.3 N; Fig. 7.4 c), which was 1.3 times greater than the use of suction alone (S; 3.96 ± 0.16 N) and 2.75 greater than the use of the

textured fingers alone (F; 1.92 ± 0.17 N). The combined suction and textured fingers had a shear force that was 8.9 times greater than the control (0.59 ± 0.06 N). These results demonstrated that the effects of suction and actuated, textured fingers were linearly additive to the resulting shear force.

When comparing the resistance to shear motions between surface types, we found that using a soft surface ($E_{surface}$, 0.0065 MPa) that was about two orders of magnitude less stiff in comparison to the stiff ($E_{surface}$, 0.165 MPa) elastomeric surface resulted in a 32% reduction in shear force for the S.T. (3.6 ± 0.2 N) and T. (1.3 ± 0.2 N) configurations and a 39% reduction for the S. (2.4 ± 0.1 N) configuration. The force curves exhibited different behaviors, where the soft surface corresponded to sharp transitions in the force-displacement curves. The shear force for the stiff surface, by comparison, demonstrated a step-wise transition from the maximum force to a sharp vertical transition. This more gradual transition was attributed to an apparent stick-slip behavior of the suction disc as it was sheared, resulting in a buckling in the suction chamber while still attached, likely causing a temporary leak in its seal and thus lower adhesive force.

We quantified the effect of the pressurization of the pneumatic chambers to select the ideal operating pressures for the experiments. We found that while low pressures of the pneumatic chambers still served to adequately engage the frictional textures to the surface, over-pressurizing would result in a reduction of shear force. Pressurization of the textured fingers with 5 and 10 psi resulted in a consistent shear force of 1.4 ± 0.1 N across the two pressures. Pressurization to 15 psi resulted in a drop in shear force to 1.2 ± 0.2 N. Visually, we observed a buckling of the actuator from the surface at 15 psi that was not observed at 5 psi (Fig. 7.4 f).

To understand the variability in the shear force as a function of the rotation of the three-fingered gripper around its central axis, we quantified the effect of the orientation of the gripper on its shear force. The gripper was considered to be either in a "forward" orientation, when the gripper moved in a direction toward one of the fingers, or in a "trailing" orientation, when the gripper moved in a direction away from one of the fingers (see Fig. 7.5c).

We found that the orientation affected to a greater degree the shear force against a stiff surface. That is, a change in the orientation from Forward to Trailing on the stiff surface resulted in a 12% reduction in shear force for the suction and friction (S.T.) configuration, and a 27% reduction in performance for the textured finger (T.) configuration (Fig. 7.5 a).
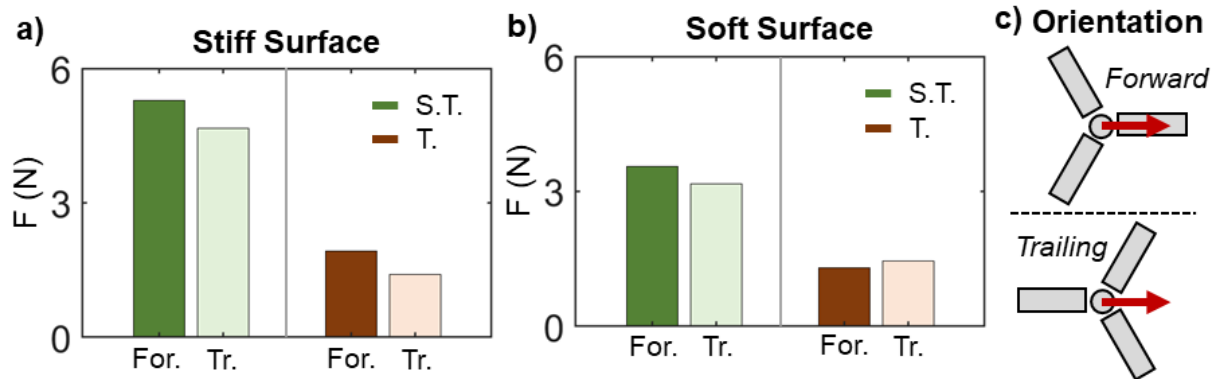
Figure 7.5: **Effect of orientation of the gripper on shear adhesion. a)** The difference in adhesive force of a gripper in the forward (For., dark shade) and trailing (Tr., light shade) orientations for the S.T. and T. configurations when tested against a stiff surface. **b)** The difference in adhesive force, dependent on orientation, when tested against a soft surface. **c)** Schematic of the orientations of the gripper.

Conversely, for the soft surface, the effect of the orientation was less apparent. The suction and textured finger orientation (S.T.) resulted in a 10% reduction in shear force by changing from forward to trailing configurations. Conversely, the configuration of only actuated textured fingers (T.) resulted in an 11% increase in shear force (Fig. 7.5 b).

7.3.4 Normal adhesion in a wet environment

We tested the contributions of the components of the gripper to resisting dislodgement normal to the testing surface. We retracted the arm in the *z*-direction at a constant rate for a total of 15 mm. Against a stiff elastomeric testing surface, the adhesive gripper generated higher normal forces than against a soft surface. The combination of active suction and textured fingers (S.T.) resulted in an adhesive force of 4.9 ± 0.2 N, followed by the suction only (S.) configuration, with
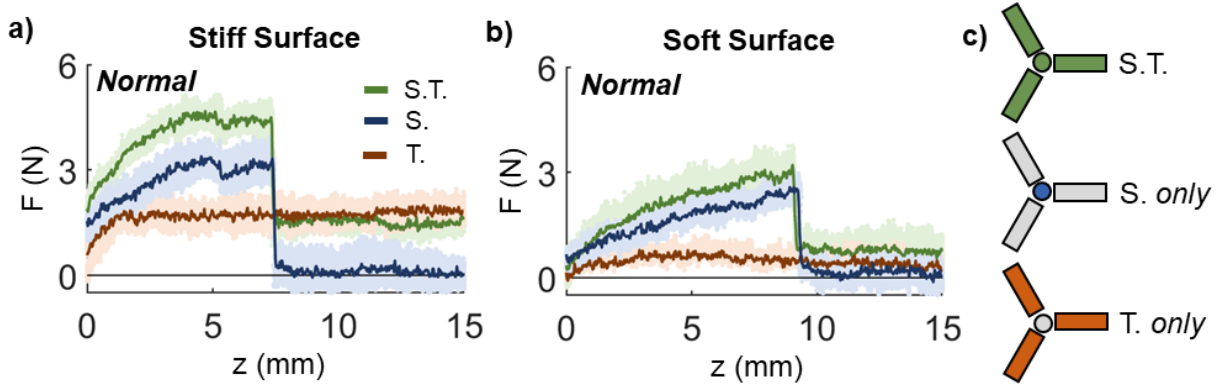
Figure 7.6: **Contribution of suction and friction to adhesion of the gripper normal to the surface.** **a)** Force of axial adhesion resulting from 15 mm displacement in the *z*-direction, against a stiff hemispherical surface in water. The data was linearly interpolated and averaged across three trials. The raw data from the three trials is indicated by the light shading. The averaged interpolated curve is indicated by the dark line, corresponding to the color of the configuration. Suction and textured fingers actuated (S.T.; green). Suction only activated (S.; blue). Textured fingers only actuated (T.; orange). **b)** Axial adhesion of gripper against a soft, hemispherical surface in water. **c)** Configuration of the gripper, the color of which corresponds to the plots.

an adhesive force of 3.6 ± 0.2 N. The actuated textured fingers alone (T.) resulted in a normal force of 2.2 ± 0.2 N. We observed a difference in normal force responses, dependent on the type of actuation involved. The suction disc resulted in a sharp vertical transition from the absolute maxima to 0 N. Conversely, the textured fingers alone resulted in a constant force which plateaued across the force-displacement curve. We attributed this plateau to the fact that a displacement of 15 mm in the *z*-direction was still less than the length of the finger, and thus while the fingers were still in contact with the surface, the resulting force would be predominantly due to friction.

Comparing the performance of the components, we investigated the effect of a soft surface on the resulting normal force. We found that the use of the gripper against a soft surface resulted in a reduction of adhesive force across all components tested, most significantly for the actuated textured fingers. For only the actuated fingers, changing from a stiff to a soft surface resulted in a 56% reduction in normal force (T. at soft surface; 1.0 ± 0.3 N). Suction was less affected by the change in surface stiffness, in comparison to the textured fingers, with a 23% reduction in normal

force for suction alone (S. on soft surface; 2.8 ± 0.2 N). The configuration of active suction and textured fingers resulted in a 32% reduction of adhesive force (S.T.; 3.3 ± 0.3 N).

7.4   Discussion

In this work, we evaluated the contribution of suction and friction to resist disturbances of forces that acted shear and normal to large, hemispherical surfaces. We performed these trials on large objects, such that the gripper was unable to achieve an enclosing grasp. By evaluating the effects of these components to the stability of a soft robotic gripper, we can aid in successful gripping of large, soft objects in wet environments.

We found that the each component (suction, friction) was linearly additive to the resulting force that acted to resist disturbances. That is, the frictional, textured fingers supplemented the adhesive strength of suction. This finding suggests that combining suction and frictional textures can benefit the stability of the grasp of a soft robotic gripper, thus enabling soft manipulators with a strong, yet delicate, grasp.

The use of adhesion, friction, and soft actuation benefits the objective of manipulation in wet and submerged environments while maintaining a delicate touch. This is especially important in the areas of surgical and subsea robotics. For surgical manipulations, the delicate organ tissue can easily be damaged by rigid manipulators, which are orders of magnitude stiffer than the tissue that they aim to manipulate [186]. While frictional textures have been previously demonstrated on surgical manipulators [147], our results suggest that coupling adhesion via suction would enhance the strength of the grip without the need to exert high compressive loads on the tissue. We anticipate that the coupling of suction and friction would also be beneficial to the field of subsea manipulations, in which a gentle touch is vital for specimen recovery.

7.5 Materials and Methods

7.5.1 Fabrication of the adhesive gripper

The adhesive gripper was composed of a suction chamber and pneumatic actuators, which were fabricated separately and combined using a modular support collar. All components of the gripper were modeled using computer-aided design (Solidworks, Dassault Systems). The support collar for the gripper was fabricated from PLA using a 3D printer (Prusa i3 MK3S+). The support collar angled the base of the actuators by $60°$ relative to the central axis of the suction disc. The pneumaic actuators were designed with a length of 46 mm, width of 11 mm, and height of 10 mm. The pneumatic actuator was produced using a custom mold that was made of a hard resin (VeroClear, Stratasys Inc.) on a multimaterial 3D printer (Object 350 Connex3, Stratasys, Inc.). After printing, the mold for the pneumatic actuator was aged for 4 h at 40°C to ensure that the resin had fully cured. The actuators were molded using silicone rubber (stiffness, 0.231 MPa; Dragon Skin 20, Smooth-On, Inc.). Uncured silicone was added to the mold for the pneumatic network, degassed for 5 min, and cured for 4 hr (Fig. 7.7). Uncured silicone was added to the mold for the strain-limiting layer and degassed for 2 min. A strip of paper was embedded in the silicone to serve as the inextensible layer. After fully curing, the elastomeric body was bonded to the strain-limiting layer using a silicone adhesive (Sil-Poxy, Smooth-On, Inc.).

We fabricated the frictional textures using soft silicone rubber (Young's modulus, 0.0167 MPa; Ecoflex 00-20, Smooth-On Inc.). The mold (Fig. 7.7 c) for the texture was etched into acrylic using a laser machining system (PLS6MW, Universal Laser Systems). The texture was composed of an array of elongated hexagons [60] with a width, length, and height of approximately 1.6 mm, 2.1 mm, and 1.0 mm, respectively. Uncured silicone was added to the mold, degassed for 5 min, and cured for 6 h. The frictional texture was then bonded to the strain-limiting layer using silicone adhesive.

We fabricated the suction discs using a 3D printed mold for the suction chamber. Uncured
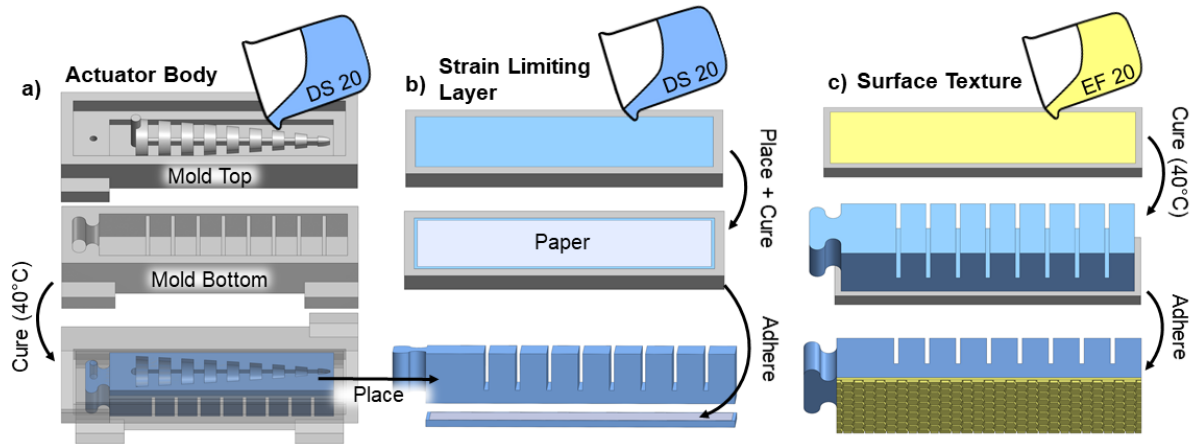
Figure 7.7: **Fabrication steps of the frictional, pneumatic actuators. a)** The body of the actuator was molded with a stiff elastomer (Dragon Skin 20; blue). **b)** The strain limiting layer was molded separately. A strip of paper served as the strain-limiting element of the layer. The body of the actuator and the strain limiting layer were adhered together using silicone adhesive. **c)** The surface texture was molded using a soft elastomer. The fully cured texture was applied to the bottom of the actuator using silicone adhesive.

silicone (Dragon Skin 20, Smooth-On, Inc.) was added to the mold of the suction chamber, degassed for 5 min, and cured at 40°C. A soft sealing layer (Ecoflex 00-20, Smooth-On Inc.) was added to the disc margin of the suction chamber. The uncured silicone was first added to a mold, partially cured at 40°C for 5 minutes, and bonded to the suction chamber using uncured silicone. These two components were allowed to cure together at 40°C for 1 hr.

7.5.2 Simulation of the contact made by an actuator

We simulated the contact of the actuator with a surface using an open-source physics simulation software (Simulation Open Framework Architecture, SOFA, v20.06). We first modeled using CAD (SolidWorks, Dassault Systems) the actuator and the test object. The test object was a cylindrical object (radius, 13 mm), for which we varied the stiffness across the trials from 0.005, 0.05, and 0.5 MPa and 50 GPa. From the CAD models, we generated the surface meshes of the objects which were used in SOFA for collision detection. We also generated volumetric meshes to model internal forces and object deformation, using an open-source mesh generation software
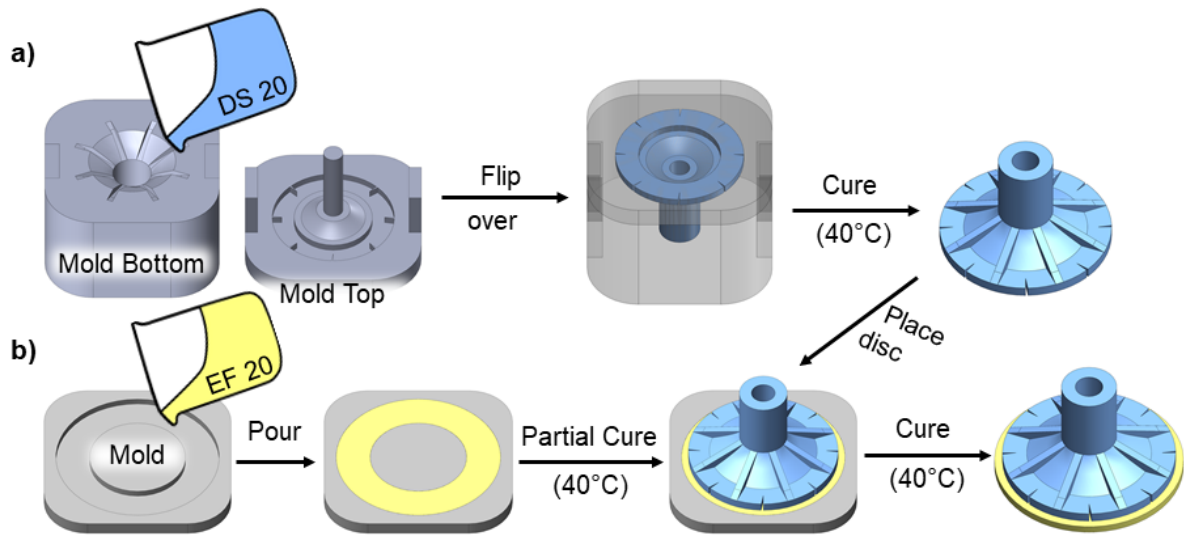
Figure 7.8: **Fabrication steps of the suction disc. a)** The suction chamber was molded from a stiff elastomer (DragonSkin 20; blue) and cured in the mold at 40°C. **b)** The sealing layer of the suction disc was molded using a soft elastomer (Ecoflex 00-20; yellow), and partially cured at 40°C. The fully cured suction chamber was applied to the back of the sealing layer, and subsequently fully cured together.

(Gmsh v4.5.6).

The simulation was set up using an implicit, first-order numerical integration scheme (module, "EulerImplicitSolver"), and was solved at each time step using LDL decomposition (module, "SparseLDLSolver"). Compliance matrices were also solved directly at each time step (module, "LinearSolverConstraintCorrection"). The simulated actuator was pressurized by applying pressure to the surface elements of the mesh of the pneumatic cavity (module, "SurfacePressureConstraint"). We then used a Barycentric mapping component to couple the motions of the cavity mesh and body mesh.

In the simulated environment, we assumed that the actuator and test object had diagonal mass matrices, Poisson ratios of 0.3, and a mutual coefficient of friction of 0.3. We assumed that their materials were linear and isotropic, providing the same resistance to strain in all directions.

The elastic modulus of the body of the actuator was 3.4 MPa, consistent with silicone elastomers. Additionally, the strain-limiting layer in the body of the actuator was modelled as a

202

layer that was 2 mm thick of a high elastic modulus (50 GPa).

Each test performed in the simulation was conducted in the absence of gravity, with a time step of 0.02 s, and with an average test duration of 7.5 s. The pressure within the pneumatic cavity was increased linearly at a rate of 0.001 MPa per 0.06 s, up to a maximum pressure of 0.06 MPa. The body of the actuator was angled 15° from horizontal and was offset from the centerline of the test object. The base of the actuator, as well as $\frac{3}{4}$ of the cylindrical object, were fixed in space during tests. We monitored the area of the actuator in contact with the test surface upon inflation.

7.6   Force measurements using a robotic arm

We measured the force of gripping a submerged, hemispherical, elastomeric surface using a robotic arm (UR3e, Universal Robots, Co). We used the robotic arm to record the force resulting from a displacement in either the *x*- or *z*-directions. We mounted the gripper as an end effector and submerged it in a bath of water which completely covered the experimental surface. The experimental surface was a hemisphere composed of silicone rubber. To understand the effect of surface stiffness on the forces, we varied the stiffness of the surface from stiff (stiffness, 0.165 MPa; Dragon Skin 10 Medium, Smooth-On, Inc.) to soft (stiffness, 0.0065 MPa; Ecoflex 00-10, Smooth-On, Inc.). Prior to the measurements, a starting position was established, defined by the location where the suction disc began to contact the apex of the hemispherical surface. To preload the disc slightly to the surface, we added an offset of 1 mm to the starting z-position.

During the shear measurements, the gripper translated in the *x*-direction for 30 mm at a rate of 0.5 mm · s^{-1}. During measurements of normal force, the gripper translated in the *z*-direction for 15 mm at a rate of 0.5 mm · s^{-1}. Each trial was run in triplicate and post-processed in MATLAB. We performed a linear interpolation on the data set from each trial, and averaged the interpolated force-displacement curves.

7.7 Acknowledgement

Chapter 8

Conclusion

Through this dissertation, I have explored concepts of biological adhesion and applied them to engineering tasks. By merging the fields of biology, materials science, and robotics, we covered topics that ranged from morphologically "intelligent" adhesives to attachment in challenging conditions (i.e., submerged, to coarse surfaces).

We have explored the use of fish-inspired adhesives as a way to achieve delicate manipulation in both surgical applications and subsea artifact recovery. We have demonstrated that the suction discs maintained high adhesive strength to coarse surfaces (which may be found on artifacts, for example), all the while delicate enough to prevent trauma to a surface (such as the tissue of a kidney and liver). We have investigated ways to tune the suction discs to achieve traction in locomoting underwater robots, all the while reducing complexity of control for successful walking schemes. We have developed fish-inspired textures to improve shear stability to robotic grip, which we demonstrated in an adhesive gripper. The adhesive gripper thus leveraged the advantages of suction, friction, and soft actuation to generate a truly delicate, yet robust, soft manipulator. To generalize more broadly, this dissertation has demonstrated that advancements in bioinspired wet adhesives can greatly benefit the field of robotics, most notably in the areas of manipulation and locomotion.

While I was explicitly focusing on clingfish-inspired adhesives, there exists a large breadth of biological adhesives yet to be explored. The natural world is a constantly evolving toolbox of fascinating biological designs that are objects of wonder and marvel. These designs serve as incredibly useful models off of which we can base our engineering innovations. As mentioned in earlier chapters, the diversity of biological adhesives have been further explored in terrestrial organisms, leaving much to be desired in the space of adhesion of aquatic organisms. While there exists exciting research into the reversible attachment strategies of the octopus, marine snails such as abalone, echinoderms such as sea stars, and even diving beetles, we pose that research has just begun to uncover and mimic these novel attachment strategies, especially given recent advancements in high-resolution imaging and testing systems, that yield a nanoscale resolution to adhesive structures. A greater understanding of and investigation into mimicking the adhesives used by aquatic organisms would serve to further enhance our toolbox of biomimetic designs.

While this work explicitly focused on the development of biomimetic devices based on the intertidal clingfish, fish that reside in high-velocity, uni-directional flow regimes, such as the waterfall-climbing goby or stream catfish, would be of considerable use for bioinspiration. The clingfish (intertidal) and remora (uni-directional flow), thus far, are the only two fish models used by research groups to inspire biomimetic devices. Thus, there exists a wide range of possibilities when considering the further exploration and development of fish-inspired adhesives for advanced attachment in a wet environment.

Overall, however, the trend in the increasing instance of research in bioinspired adhesives is promising. Given that there is still much to explore in terms of biological adhesives, there exists a large space for discovery and innovation of novel attachment devices that can attach in a reversible manner.

Bibliography

[1] P. M. Favi, S. Yi, S. C. Lenaghan, L. Xia, and M. Zhang, "Inspiration from the natural world: from bio-adhesives to bioinspired adhesives," *Journal of Adhesion Science and Technology*, vol. 28, no. 3–4, pp. 290–319, 2014.

[2] P. Ditsche and A. P. Summers, "Aquatic versus terrestrial attachment: Water makes a difference," *Beilstein Journal of Nanotechnology*, vol. 5, pp. 2424–2439, 2014.

[3] S. N. Gorb, "Biological attachment devices: exploring nature's diversity for biomimetics," *Philosophical Transactions of the Royal Society A*, vol. 366, pp. 1557–1574, 2008.

[4] P. Flammang and R. Santos, "Biological adhesives: from biology to biomimetics," *Interface Focus*, vol. 5, no. 1, p. 20140086, 2014.

[5] K. Autumn, Y. A. Liang, S. T. Hsieh, W. Zesch, W. P. Chan, T. W. Kenny, R. Fearing, and R. J. Full, "Adhesive force of a single gecko foot-hair," *Nature*, vol. 405, pp. 681–685, 2000.

[6] K. Autumn, A. Dittmore, D. Santos, M. Spenko, and M. Cutkosky, "Frictional adhesion: a new angle on gecko attachment," *Journal of Experimental Biology*, vol. 209, no. 18, pp. 3569–3579, 2006.

[7] A. B. Kesel, A. Martin, and T. Seidl, "Getting a grip on spider attachment: an afm approach to microstructure adhesion in arthropods," *Smart Materials and Structures*, vol. 13, no. 3, pp. 512–518, 2004.

[8] R. Hensel, K. Moh, and E. Arzt, "Engineering micropatterned dry adhesives: From contact theory to handling applications," *Advanced Functional Materials*, vol. 28, no. 28, p. 1800865, 2018.

[9] H. Jiang, E. W. Hawkes, C. Fuller, M. A. Estrada, S. A. Suresh, N. Abcouwer, A. K. Han, S. Wang, C. J. Ploch, A. Parness, and M. R. Cutkosky, "A robotic device using gecko-inspired adhesives can grasp and manipulate large objects in microgravity," *Science Robotics*, vol. 2, no. 7, p. eaan4545, 2017.

[10] M. R. Cutkosky, "Climbing with adhesion: from bioinspiration to biounderstanding," *Interface Focus*, vol. 5, p. 20150015, 2015.

[11] J. K. Langowski, D. Dodou, M. Kamperman, and J. L. van Leeuwen, "Tree frog attachment: mechanisms, challenges, and perspectives," *Frontiers in Zoology*, vol. 15, p. 32, 2018.

[12] W. Federle, M. Riehle, A. S. Curtis, and R. J. Full, "An integrative study of insect adhesion: Mechanics and wet adhesion in pretarsal pads in ants," *Integrative and Comparative Biology*, vol. 42, no. 6, pp. 1100–1106, 2002.

[13] M. Li, L. Shi, and X. Wang, "Physical mechanisms behind the wet adhesion: From amphibian toe-pad to biomimetics," *Colloids and Surfaces B: Biointerfaces*, vol. 199, p. 111531, 2021.

[14] M. Cui, S. Ren, S. Wei, C. Sun, and C. Zhong, "Natural and bio-inspired underwater adhesives: Current progress and new perspectives," *APL Materials*, vol. 5, no. 11, p. 116102, 2017.

[15] S. Sareh, K. Althoefer, M. Li, Y. Noh, F. Tramacere, P. Sareh, B. Mazzolai, and M. Kovac, "Anchoring like octopus: Biologically inspired soft artificial sucker," *Journal of the Royal Society Interface*, vol. 14, no. 135, p. 20170395, 2017.

[16] B. Mazzolai, A. Mondini, F. Tramacere, G. Riccomi, A. Sadeghi, G. Giordano, E. Del Dottore, M. Scaccia, M. Zampato, and S. Carminati, "Octopus-inspired soft arm with suction cups for enhanced grasping tasks in confined environments," *Advanced Intelligent Systems*, vol. 1, no. 6, p. 1900041, 2019.

[17] R. Blake, P. Kwok, and K. Chan, "The energetics of rheotactic behaviour in *Pterygoplichthys* spp. (teleostei: Loricariidae)," *Journal of Fish Biology*, vol. 71, no. 2, pp. 623–627, 2007.

[18] R. Britz and G. D. Johnson, "Ontogeny and homology of the skeletal elements that form the sucking disc of remoras (*Teleostei Echeneoidei, Echeneidae*)," *Journal of Morphology*, vol. 273, no. 12, pp. 1353–1366, 2012.

[19] Y. Wang, X. Yang, Y. Chen, D. K. Wainwright, C. P. Kenaley, Z. Gong, Z. Liu, H. Liu, J. Guan, T. Wang, J. C. Weaver, R. J. Wood, and L. Wen, "A biorobotic adhesive disc for underwater hitchhiking inspired by the remora suckerfish," *Science Robotics*, vol. 2, no. 10, p. eaan8072, 2017.

[20] Y.-C. Chuang, H.-K. Chang, G.-L. Liu, and P.-Y. Chen, "Climbing upstream: Multi-scale structural characterization and underwater adheison of the pulin river loach (sinogastromyzon puliensis)," *Journal of the Mechanical Behavior of Biomedical Materials*, vol. 73, pp. 76–85, 2017.

[21] H. L. Schoenfuss and R. W. Blob, "Kinematics of waterfall climbing in hawaiian freshwater fishes (gobiidae): Vertical propulsion at the aquatic-terrestrial interface," *Journal of Zoology*, vol. 261, pp. 191—-205, 2003.

[22] E. Arzt, "Biological and artificial attachment devices: Lessons for materials scientists from flies and geckos," *Materials Science and Engineering: C*, vol. 26, no. 8, pp. 1245–1250, 2006.

[23] B. Lengerer and P. Ladurner, "Properties of temporary adhesion systems of marine and freshwater organisms," *Journal of Experimental Biology*, vol. 221, no. 16, p. jeb182717, 2018.

[24] A. M. Peattie, "Functional demands of dynamic biological adhesion: An integrative approach," *Journal of Comparative Physiology B*, vol. 179, no. 231, pp. 231—-239, 2009.

[25] K. Kamino, "Molecular design of barnacle cement in comparison with those of mussel and tubeworm," *Journal of Adhesion*, vol. 86, no. 1, pp. 96–110, 2010.

[26] L. F. Boesel, C. Greiner, E. Arzt, and A. del Campo, "Gecko-inspired surfaces: A path to strong and reversible dry adhesives," *Advanced Materials*, vol. 22, no. 19, pp. 2125–2137, 2010.

[27] J. Shintake, V. Cacucciolo, D. Floreano, and H. Shea, "Soft robotic grippers," *Advanced Materials*, vol. 30, no. 29, p. 1707035, 2018.

[28] P. Chattopadhyay and S. K. Ghoshal, "Adhesion technologies of bio-inspired climbing robots: A survey," *International Journal of Robotics and Automation*, vol. 33, no. 6, pp. 654–661, 2018.

[29] W. P. Barnes, "Biomimetic solutions to sticky problems," *Science*, vol. 318, no. 5848, pp. 203–204, 2007.

[30] A. Kesel, A. Martin, and T. Seidl, "Adhesion measurements on the attachment devices of the jumping spider *Evarcha arcuata*," *Journal of Experimental Biology*, vol. 206, no. 16, pp. 2733–2738, 2003.

[31] W. Sun, P. Neuzil, T. S. Kustandi, S. Oh, and V. D. Samper, "The nature of the gecko lizard adhesive force," *Biophysical Journal*, vol. 89, no. 2, pp. PL14–PL17, 2005.

[32] W. Federle, "Why are so many adhesive pads hairy?," *Journal of Experimental Biology*, vol. 209, no. 14, pp. 2611–2621, 2006.

[33] E. Arzt, S. Gorb, and R. Spolenak, "From micro to nano contacts in biological attachment devices," *PNAS*, vol. 100, no. 19, pp. 10603–10606, 2003.

[34] J.-H. Dirks, "Principles of fluid-mediated insect attachment – shouldn't insects slip?," *Beilstein Journal of Nanotechnology*, vol. 5, pp. 1160–1166, 2014.

[35] K. Autumn, C. Majidi, R. Groff, A. Dittmore, and R. Fearing, "Effective elastic modulus of isolated gecko setal arrays," *Journal of Experimental Biology*, vol. 209, no. 18, pp. 3558–3568, 2006.

[36] D. Brodoceanu, C. Bauer, E. Kroner, E. Arzt, and T. Kraus, "Hierarchical bioinspired adhesive surfaces - a review," *Bioinspiration & Biomimetics*, vol. 11, no. 5, p. 051001, 2016.

[37] J. M. Bullock and W. Federle, "Division of labour and sex differences between fibrillar, tarsal adhesive pads in beetles: Effective elastic modulus and attachment performance," *Journal of Experimental Biology*, vol. 212, no. 12, pp. 1876–1888, 2009.

[38] H. Peisker, J. Michels, and S. N. Gorb, "Evidence for a material gradient in the adhesive tarsal setae of the ladybird beetle *Coccinella septempunctata*," *Nature Communications*, vol. 4, no. 1661, p. ncomms2576, 2013.

[39] M.-J. Moon, J.-G. Park, and W.-J. Choi, "Fine structural analysis of the fibrillar adhesion apparatus in ladybird beetle," *Entomological Research*, vol. 42, pp. 196–205, 2012.

[40] J. M. Bullock, P. Drechsler, and W. Federle, "Comparison of smooth and hairy attachment pads in insects: Friction, adhesion and mechanisms for direction-dependence," *Journal of Experimental Biology*, vol. 211, no. 20, pp. 3333–3343, 2008.

[41] Y. Chen, M.-C. Shih, M.-H. Wu, E.-C. Yang, and K.-J. Chi, "Underwater attachment using hairs: the functioning of spatula and sucker setae from male diving beetles," *Journal of the Royal Society Interface*, vol. 11, p. 20140273, 2014.

[42] L. Wang, Y. Hui, C. Fu, Z. Wang, M. Zhang, and T. Zhang, "Recent advances in gecko-inspired adhesive materials and application," *Journal of Adhesion Science and Technology*, vol. 34, no. 21, pp. 2275–2291, 2020.

[43] D. Sameoto and C. Menon, "Recent advances in the fabrication and adhesion testing of biomimetic dry adhesives," *Smart Materials and Structures*, vol. 19, no. 10, p. 103001, 2010.

[44] S. Kim, M. Spenko, S. Trujillo, B. Heyneman, D. Santos, and M. R. Cutkosky, "Smooth vertical surface climbing with directional adhesion," *IEEE Transactions on Robotics*, vol. 24, no. 1, pp. 65–74, 2008.

[45] Y. Wang, V. Kang, E. Arzt, W. Federle, and R. Hensel, "Strong wet and dry adhesion by cupped microstructures," *ACS Applied Materials and Interfaces*, vol. 11, no. 29, pp. 26483–26490, 2019.

[46] A. Lin, R. Brunner, P. Chen, F. Talke, and M. Meyers, "Underwater adhesion of abalone: The role of van der waals and capillary forces," *Acta Materialia*, vol. 57, no. 14, pp. 4178–4185, 2009.

[47] J. Li, Y. Zhang, S. Liu, and J. Liu, "Insights into adhesion of abalone: A mechanical approach," *Journal of the Mechanical Behavior of Biomedical Materials*, vol. 77, pp. 331–336, 2018.

[48] F. Tramacere, E. Appel, B. Mazzolai, and S. N. Gorb, "Hairy suckers: The surface microstructure and its possible functional significance in the *Octopus vulgaris* sucker," *Beilstein Journal of Nanotechnology*, vol. 5, pp. 561–565, 2014.

[49] G. Greco, F. Bosia, F. Tramacere, B. Mazzolai, and N. M. Pugno, "The role of hairs in the adhesion of octopus suckers: A hierarchical peeling approach," *Bioinspiration & Biomimetics*, vol. 15, no. 3, p. 035006, 2020.

[50] D. M. Green and D. L. Barber, "The ventral adhesive disc of the clingfish *Gobiesox maeandricus*: integumental structure and adhesive mechanisms," *Canadian Journal of Zoology*, vol. 66, no. 7, pp. 1610–1619, 1988.

[51] P. Ditsche, M. Hicks, L. Truong, C. Linkem, and A. Summers, "From smooth to rough, from water to air: The intertidal habitat of northern clingfish (*Gobiesox maeandricus*," *The Science of Nature*, vol. 104, p. 33, 2017.

[52] D. K. Wainwright, T. Kleinteich, A. Kleinteich, S. N. Gorb, and A. P. Summers, "Stick tight: suction adhesion on irregular surface in the northern clingfish," *Biology Letters*, vol. 9, no. 3, p. 20130234, 2013.

[53] P. Ditsche, D. K. Wainwright, and A. P. Summers, "Attachment to challenging substrates–fouling, roughness and limits of adhesion in the northern clingfish (*Gobiesox maeandricus*," *Journal of Experimental Biology*, vol. 217, no. 14, pp. 2548–2554, 2014.

[54] M. Offroy, A. Razafitianamaharavo, A. Beaussart, C. Pagnout, and J. F. Duval, "Fast automated processing of afm peakforce curves to evaluate spatially resolved young modulus and stiffness of turgescent cells," *RSC Advances*, vol. 10, no. 33, pp. 19258–19275, 2020.

[55] X. Wang, D. Tan, X. Zhang, Y. Lei, and L. Xue, "Effective elastic modulus of structured adhesives: From biology to biomimetics," *Biomimetics*, vol. 2, no. 3, p. 10, 2017.

[56] I. N. Sneddon, "The relation between load and penetration in the axisymmetric boussinesq problem for a punch of arbitrary profile," *International Journal of Engineering Science*, vol. 3, no. 1, pp. 47–57, 1965.

[57] W. Zhang, P. Soman, K. Meggs, X. Qu, and S. Chen, "Tuning the poisson's ratio of biomatierals for investigating cellular response," *Advanced Functional Materials*, vol. 23, no. 25, pp. 3226–3232, 2013.

[58] M. Menárguez, L. Pastor, and E. Odeblad, "Morphological characterization of different human cervical mucus types using light and scanning electron microscopy," *Human Reproduction*, vol. 18, no. 9, pp. 1782–1789, 2003.

[59] M. E. Cortés, F. González, and P. Vigil, "Crystallization of bovine cervical mucus at oestrus: An update," *Revista de Medicina Veterinaria*, vol. 28, no. 28, pp. 103–108, 2014.

[60] J. A. Sandoval, J. Sommers, K. R. Peddireddy, R. M. Robertson-Anderson, M. T. Tolley, and D. D. Deheyn, "Toward bioinspired wet adhesives: Lessons from assessing surface structures of the suction disc of intertidal clingfish," *ACS Applied Materials and Interfaces*, vol. 12, no. 40, pp. 45460–45475, 2020.

[61] A. M. Smith, "The role of suction in the adhesion of limpets," *Journal of Experimental Biology*, vol. 161, no. 1, pp. 151–169, 1991.

[62] S. Gorb, E. Gorb, and V. Kastner, "Scale effects on the attachment pads and friction forces in syrphid flies (diptera, syrphidae)," *Journal of Experimental Biology*, vol. 204, no. 8, pp. 1421–1431, 2001.

[63] K. Autumn, M. Sitti, Y. A. Liang, A. M. Peattie, W. R. Hansen, S. Sponberg, T. W. Kenny, R. Fearing, J. N. Israelachvili, and R. J. Full, "Evidence for van der waals adhesion in gecko setae," *PNAS*, vol. 99, no. 19, pp. 12252–12256, 2002.

[64] A. M. Peattie, C. Majidi, A. Corder, and R. J. Full, "Ancestrally high elastic modulus of gecko setal β-keratin," *Journal of the Royal Society Interface*, vol. 4, pp. 1071—-1076, 2007.

[65] J. A. Sandoval, S. Jadhav, H. Quan, D. D. Deheyn, and M. T. Tolley, "Reversible adhesion to rough surfaces both in and out of water, inspired by the clingfish suction disc," *Bioinspiration & Biomimetics*, vol. 14, no. 6, p. 066016, 2019.

[66] P. Ditsche and A. Summers, "Learning from northern clingfish (*Gobiesox maeandricus*): Bioinspired suction cups attach to rough surfaces," *Philosophical Transactions of the Royal Society B*, vol. 374, no. 1784, p. 20190204, 2019.

[67] C. A. Schneider, W. S. Rasband, and K. W. Eliceiri, "NIH Image to ImageJ: 25 years of image analysis," *Nature Methods*, vol. 9, pp. 671—675, 2012.

[68] H. Izadi and A. Penlidis, "Polymeric bio-inspired dry adhesives: van der waals or electrostatic interactions?," *Macromolecular Reaction Engineering*, vol. 7, pp. 588–608, 2013.

[69] R. Santos, S. Gorb, V. Jamar, and P. Flammang, "Adhesion of echinoderm tube feet to rough surfaces," *Journal of Experimental Biology*, vol. 208, no. 13, pp. 2555–2567, 2005.

[70] M. A. North, C. A. Del Grosso, and J. J. Wilker, "High strength underwater bonding with polymer mimics of mussel adhesive proteins," *ACS Applied Materials and Interfaces*, vol. 9, no. 8, pp. 7866–7872, 2017.

[71] L. Heepe and S. N. Gorb, "Biologically inspired mushroom-shaped adhesive microstructures," *Annual Review of Materials Research*, vol. 44, pp. 173–203, 2014.

[72] A. Smith, "Cephalopod sucker design and the physical limits to negative pressure," *Journal of Experimental Biology*, vol. 199, pp. 949–958, 1996.

[73] W. P. Barnes, "Functional morphology and design constraints of smooth adhesive pads," *MRS Bulletin*, vol. 32, no. 6, pp. 479–485, 2007.

[74] B. Persson, "Wet adhesion with application to tree frog adhesive toe pads and tires," *Journal of Physics: Condensed Matter*, vol. 19, no. 37, p. 3761104, 2007.

[75] S. Gorb, "The design of the fly adhesive pad: distal tenent setae are adapted to the delivery of an adhesive secretion," *Proceedings of the Royal Society B*, vol. 265, pp. 747—752, 1998.

[76] W. Federle, W. Barnes, W. Baumgartner, P. Drechsler, and J. Smith, "Wet but not slippery: boundary friction in tree frog adhesive toe pads," *Journal of the Royal Society Interface*, vol. 3, pp. 689—-697, 2006.

[77] M. Culler, K. A. Ledford, and J. H. Nadler, "The role of topology and tissue mechanics in remora attachment," *MRS Online Proceedings Library*, vol. 1648, no. 102, pp. mrsf13–1648–hh10–02, 2014.

[78] T. Kampowski, L. Eberhard, F. Gallenmüller, T. Speck, and S. Poppinga, "Functional morphology of suction discs and attachment performance of the mediterranean medicinal leech (*Hirudo verbana* carena)," *Journal of the Royal Society Interface*, vol. 13, no. 117, p. 20160096, 2016.

[79] Y. Li, J. Krahn, and C. Menon, "Bioinspired dry adhesive materials and their application in robotics: A review," *Journal of Bionic Engineering*, vol. 13, no. 2, pp. 181–199, 2016.

[80] M. Calisti, G. Picardi, and C. Laschi, "Fundamentals of soft robot locomotion," *Journal of the Royal Society Interface*, vol. 14, no. 130, p. 20170101, 2017.

[81] X. Zhou, C. Majidi, and O. M. O'Reilly, "Soft hands: an analysis of some gripping mechanisms in soft robot design," *International Journal of Solids and Structures*, vol. 64–65, pp. 155–165, 2015.

[82] K. A. Daltorio, T. E. Wei, A. D. Horchler, L. Southard, G. D. Wile, S. N. Gorb, R. E. Ritzmann, and R. D. Quinn, "Mini-whegs$^{(tm)}$ climbs steep surfaces using insect-inspired attachment mechanisms," *International Journal of Robotics Research*, vol. 28, no. 2, pp. 285–302, 2009.

[83] P. Polygerinos, N. Correll, S. A. Morin, B. Mosadegh, C. D. Onal, K. Petersen, M. Cianchetti, M. T. Tolley, and R. F. Shepherd, "Soft robotics: review of fluid-driven intrinsically soft devices; manufacturing, sensing, control, and applications in human-robot interaction," *Advanced Engineering Materials*, vol. 19, no. 12, p. 1700016, 2017.

[84] P. Glick, S. A. Suresh, D. Ruffatto, M. Cutkosky, M. T. Tolley, and A. Parness, "A soft robotic gripper with gecko-inspired adhesive," *IEEE Robotics and Automation Letters*, vol. 3, no. 2, pp. 903–910, 2018.

[85] S. Song, D.-M. Drotlef, C. Majidi, and M. Sitti, "Controllable load sharing for soft adhesive interfaces on three-dimensional surfaces," *PNAS*, vol. 114, no. 22, pp. E4344–E4353, 2017.

[86] P. Glass, H. Chung, N. R. Washburn, and M. Sitti, "Enhanced reversible adhesion of dopamine methacrylamide-coated elastomer microfibrillar structures under wet conditions," *Langmuir*, vol. 25, no. 12, pp. 6607—-6612, 2009.

[87] H. Yi, S. H. Lee, M. Seong, M. K. Kwak, and H. E. Jeong, "Bioinspired reversible hydrogel adhesives for wet and underwater surfaces," *Journal of Materials Chemistry B*, vol. 6, no. 48, pp. 8064–8070, 2018.

[88] H. Izadi, B. Zhao, Y. Han, N. McManus, and A. Penlidis, "Teflon hierarchical nanopillars with dry and wet adhesive properties," *Journal of Polymer Science Part B*, vol. 50, no. 12, pp. 846–851, 2012.

[89] M. Varenberg and S. Gorb, "A beetle-inspired solution for underwater adhesion," *Journal of the Royal Society Interface*, vol. 5, no. 20, pp. 383—-385, 2008.

[90] B. Mazzolai, L. Margheri, M. Cianchetti, P. Dario, and C. Laschi, "Soft-robotic arm inspired by the octopus: Ii. from artificial requirements to innovative technological solutions," *Bioinspiration & Biomimetics*, vol. 7, p. 025005, 2012.

[91] F. Tramacere, M. Follador, N. M. Pugno, and B. Mazzolai, "Octopus-like suction cups: from natural to artificial solutions," *Bioinspiration & Biomimetics*, vol. 10, no. 3, p. 035004, 2015.

[92] H. K. Yap, J. C. H. Goh, and R. C. H. Yeow, "Design and characterization of soft actuator for hand rehabilitation application," *6th European Conference of the International Federation for Medical and Biological Engineering Proceedings*, vol. 45, pp. 367–370, 2015.

[93] Y.-L. Park, C. Majidi, R. Kramer, P. Bérard, and R. J. Wood, "Hyperelastic pressure sensing with liquid-embedded elastomer," *Journal of Micromechanics and Microengineering*, vol. 20, no. 12, p. 125029, 2010.

[94] A. Parness, D. Soto, N. Esparza, N. Gravish, M. Wilkinson, K. Autumn, and M. Cutkosky, "A microfabricated wedge-shaped adhesive array displaying gecko-like dynamic adhesion, directionality and long lifetime," *Journal of the Royal Society Interface*, vol. 6, no. 41, pp. 1223–1232, 2009.

[95] M. M. Noor, K. Kadirgama, and M. M. Rahman, "Analysis of surface roughness for laser cutting on acrylic sheets using response surface method," *National Conference in Mechanical Engineering for Research & Postgraduate Studies*, vol. 1, pp. 24–31, 2010.

[96] J. Y. Han, "Low-cost multi-touch sensing through frustrated total internal reflection," *UIST Proceedings*, pp. 115–118, 2005.

[97] R. W. Hertzberg, R. P. Vinci, and J. L. Hertzberg, *Elastic response of solids*. Deformation and Fracture Mechanics of Engineering Materials, Wiley, 2013.

[98] K. TeleRobotics, *Predator: Force feedback manipulator*. Product Specification P505-1, 2005.

[99] R. Maruyama, T. Watanabe, and M. Uchida, "Delicate grasping by robotic gripper with incompressible fluid-based deformable fingertips," *IEEE/RSJ International Conference on Intelligent Robots and Systems*, pp. 5469–5474, 2013.

[100] J. M. Krahn, F. Fabbro, and C. Menon, "A soft-touch gripper for grasping delicate objects," *IEEE/ASME Transactions on Mechatronics*, vol. 22, no. 3, pp. 1276–1286, 2017.

[101] K. Kendall, "The adhesion and surface energy of elastic solids," *Journal of Physics D: Applied Physics*, vol. 4, no. 8, pp. 1186–1195, 1971.

[102] J. H. Lai, J. C. del Alamo, J. Rodríguez-Rodríguez, and J. C. Lasheras, "The mechanics of the adhesive locomotion of terrestrial gastropods," *Journal of Experimental Biology*, vol. 213, no. 22, pp. 3920—3933, 2010.

[103] S. Heydari, A. Johnson, O. Ellers, M. J. McHenry, and E. Kanso, "Sea star inspired crawling and bouncing," *Journal of the Royal Society Interface*, vol. 17, no. 162, p. 20190700, 2020.

[104] S. Kalouche, N. Wiltsie, H.-J. Su, and A. Parness, "Inchworm style gecko adhesive climbing robot," in *2014 IEEE/RSJ International Conference on Intelligent Robots and Systems (IROS)*, pp. 2319–2324, IEEE, 2014.

[105] P. Manoonpong, D. Petersen, A. Kovalev, F. Wörgötter, S. N. Gorb, M. Spinner, and L. Heepe, "Enhanced locomotion efficiency of a bio-inspired walking robot using contact surfaces with frictional anisotropy," *Scientific Reports*, vol. 6, p. 39455, 2016.

[106] J. Cao, L. Qin, J. Liu, Q. Ren, C. C. Foo, H. Wang, H. P. Lee, and J. Zhu, "Untethered soft robot capable of stable locomotion using soft electrostatic actuators," *Extreme Mechanics Letters*, vol. 21, pp. 9–16, 2018.

[107] S. D. de Rivaz, B. Goldberg, N. Doshi, K. Jayaram, J. Zhou, and R. J. Wood, "Inverted and vertical climbing of a quadrupedal microrobot using electroadhesion," *Science Robotics*, vol. 3, no. 25, p. eaau3038, 2018.

[108] Y. Hou, X. Deng, and C. Xie, "Biomaterial surface modification for underwater adhesion," *Smart Materials in Medicine*, vol. 1, pp. 77–91, 2020.

[109] M. A. Bell, I. Pestovski, W. Scott, K. Kumar, M. K. Jawed, D. A. Paley, C. Majidi, J. C. Weaver, and R. J. Wood, "Echinoderm-inspired tube feet for robust robot locomotion and adhesion," *IEEE Robotics and Automation Letters*, vol. 3, no. 3, pp. 2222–2228, 2018.

[110] X. Tang, D. Zhang, Z. Li, and J. Chen, "An omni-directional wall-climbing microrobot with magnetic wheels directly integrated with electromagnetic micromotors," *International Journal of Advanced Robotic Systems*, vol. 9, no. 16, 2012.

[111] Z. Ye, G. Z. Lum, S. Song, S. Rich, and M. Sitti, "Phase change of gallium enables highly reversible and switchable adhesion," *Advanced Materials*, vol. 28, pp. 5088–5092, 2016.

[112] W. P. Weston-Dawkes, I. Adibnazari, Y.-W. Hu, M. Everman, N. Gravish, and M. T. Tolley, "Gas-lubricated vibration-based adhesion for robotics," *Advanced Intelligent Systems*, p. 2100001, 2021.

[113] S. Kawasaki and K. Kikuchi, "Development of a small legged wall climbing robot with passive suction cups," in *The 3rd International Conference on Design Engineering and Science, ICDES*, vol. 2014, pp. 112–116, 2014.

[114] G. Lee, H. Kim, K. Seo, J. Kim, and H. S. Kim, "Multitrack: A multi-linked track robot with suction adhesion for climbing and transition," *Robotics and Autonomous Systems*, vol. 72, pp. 207–216, 2015.

[115] Y. Tang, Q. Zhang, G. Lin, and J. Yin, "Switchable adhesion actuator for amphibious climbing soft robot," *Soft Robotics*, vol. 5, no. 5, pp. 592–600, 2018.

[116] T. Miyake, H. Ishihara, and M. Yoshimura, "Basic studies on wet adhesion system for wall climbing robots," in *2007 IEEE/RSJ International Conference on Intelligent Robots and Systems (IROS)*, pp. 1920–1925, IEEE, 2007.

[117] D. Santos, S. Kim, M. Spenko, A. Parness, and M. Cutkosky, "Directional adhesive structures for controlled climbing on smooth vertical surfaces," in *Proceedings of the 2007 IEEE International Conference on Robotics and Automation*, pp. 1262–1267, IEEE, 2007.

[118] D. Santos, M. Spenko, A. Parness, S. Kim, and M. Cutkosky, "Directional adhesion for climbing: theoretical and practical considerations," *Journal of Adhesion Science and Technology*, vol. 21, no. 12-13, pp. 1317–1341, 2007.

[119] H. Hauser, A. J. Ijspeert, R. M. Fuchslin, R. Pfeifer, and W. Maass, "Towards a theoretical foundation for morphological computation with compliant bodies," *Biological Cybernetics*, vol. 105, pp. 355–370, 2011.

[120] M. McEnvoy and N. Correll, "Materials that couple sensing, actuation, computation, and communication," *Science*, vol. 347, no. 6228, p. 1261689, 2015.

[121] C. Laschi and B. Mazzolai, "Lessons from animals and plants: The symbiosis of morphological computation and soft robotics," *IEEE Robotics Automation Magazine*, vol. 23, no. 3, pp. 107–114, 2016.

[122] R. Pfeifer, M. Lungarella, and I. Fumiya, "Self-organization, embodiment, and biologically inspired robotics," *Science*, vol. 318, no. 5853, pp. 1088–1093, 2007.

[123] W. Federle and D. Labonte, "Dynamic biological adhesion: mechanisms for controlling attachment during locomotion," *Philosophical Transactions of the Royal Society B*, vol. 374, p. 20190199, 2019.

[124] H. Gai, X. Wang, H. Yao, S. Gorb, and E. Arzt, "Mechanics of hierarchical adhesion structures of geckos," *Mechanics of Materials*, vol. 37, pp. 275–285, 2005.

[125] G. C. Hill, D. R. Soto, A. M. Peattie, R. J. Full, and T. Kenny, "Orientation angle and the adhesion of single gecko setae," *Journal of the Royal Society Interface*, vol. 8, pp. 926–933, 2011.

[126] M. P. Murphy, B. Aksak, and M. Sitti, "Gecko-inspired directional and controllable adhesion," *Small*, vol. 5, no. 2, pp. 170–175, 2009.

[127] L. Heepe, A. E. Kovalev, and S. N. Gorb, "Direct observation of microcavitation in underwater adhesion of mushroom-shaped adhesive microstructure," *Beilstein Journal of Nanotechnology*, vol. 5, pp. 903–909, 2014.

[128] H. Lee, B. P. Lee, and P. B. Messersmith, "A reversible wet/dry adhesive inspired by mussels and geckos," *Nature*, vol. 448, pp. 338–341, 2007.

[129] D. Dodou, P. Breedveld, J. De Winter, J. Dankelman, and J. Van Leeuwen, "Mechanisms of temporary adhesion in benthic animals," *Biological Reviews*, vol. 86, no. 1, pp. 15–32, 2011.

[130] K. M. Gamel, A. M. Garner, and B. E. Flammang, "Bioinspired remora adhesive disc offers insight into evolution," *Bioinspiration & Biomimetics*, vol. 14, no. 5, p. 056014, 2019.

[131] H. Bagheri, A. Hu, S. Cummings, C. Roy, R. Casleton, A. Wan, N. Erjavic, S. Berman, M. M. Peet, D. M. Aukes, *et al.*, "New insights on the control and function of octopus suckers," *Advanced Intelligent Systems*, vol. 2, no. 6, p. 1900154, 2020.

[132] M. Elbadawi, G. Andrikopoulos, G. Nikolakopoulos, and T. Gustafsson, "Bio-inspired climbing robots in wet environments: Recent trends in adhesion methods and materials," in *2018 IEEE International Conference on Robotics and Biomimetics (ROBIO)*, pp. 2347–2353, IEEE, 2018.

[133] Z. Xie, A. G. Domel, N. An, C. Green, Z. Gong, T. Wang, E. M. Knubben, J. C. Weaver, K. Bertoldi, and L. Wen, "Octopus arm-inspired tapered soft actuators with suckers for improved grasping," *Soft robotics*, vol. 7, no. 5, pp. 639–648, 2020.

[134] S. Wang, L. Li, W. Sun, D. Wainwright, H. Wang, W. Zhao, B. Chen, Y. Chen, and L. Wen, "Detachment of the remora suckerfish disc: kinematics and a bio-inspired robotic model," *Bioinspiration & Biomimetics*, vol. 15, p. 056018, 2020.

[135] H. Tsukagoshi and Y. Osada, "Soft hybrid suction cup capable of sticking to various objects and environments," in *Actuators*, vol. 10, p. 50, Multidisciplinary Digital Publishing Institute, 2021.

[136] Z. Zhakypov, F. Heremans, A. Billard, and J. Paik, "An origami-inspired reconfigurable suction gripper for picking objects with variable shape and size," *IEEE Robotics and Automation Letters*, vol. 3, no. 4, pp. 2894–2901, 2018.

[137] A. Tiwari and B. Persson, "Physics of suction cups," *Soft Matter*, vol. 15, no. 46, pp. 9482–9499, 2019.

[138] T. Endlein and W. J. P. Barnes, *Wet adhesion in tree and torrent frogs*. Encyclopedia of Nanotechnology, Springer, 2015.

[139] F. Meng, Q. Liu, X. Wang, D. Tan, L. Xue, and W. J. P. Barnes, "Tree frog adhesion biomimetics: Opportunities for the development of new, smart adhesives that adhere under wet conditions," *Philosophical Transactions of the Royal Society A*, vol. 377, no. 2150, p. 20190131, 2019.

[140] H.-J. Butt, W. J. P. Barnes, A. del Campo, M. Kappla, and F. Schönfeld, "Capillary forces between soft, elastic spheres," *Soft Matter*, vol. 6, no. 23, pp. 5930–5936, 2010.

[141] W. J. P. Barnes, *Adhesion in wet environments: Frogs*. Encyclopedia of Nanotechnology, Springer, 2012.

[142] G. Amarpuri, C. Zhang, C. Diaz, B. D. Opell, T. A. Blackledge, and A. Dhinojwala, "Spiders tune glue viscosity to maximize adhesion," *ACS Nano*, vol. 9, no. 11, pp. 11472–11478, 2015.

[143] D. Shin, W. T. Choi, H. Lin, Z. Qu, V. Breedveld, and J. C. Meredith, "Humidity-tolerant rate-dependent capillary viscous adhesion of bee-collected pollen fluids," *Nature Communications*, vol. 10, p. 1379, 2019.

[144] X. Li, D. Tao, H. Lu, P. Bai, Z. Liu, L. Ma, Y. Meng, and Y. Tian, "Recent developments in gecko-inspired dry adhesive surfaces from fabrication to application," *Surface Topography: Metrology and Properties*, vol. 7, no. 2, p. 023001, 2019.

[145] M. P. Murphy, S. Kim, and M. Sitti, "Enhanced adhesion by gecko-inspired hierarchical fibrillar adhesives," *ACS Applied Materials and Interfaces*, vol. 1, no. 4, pp. 849–855, 2009.

[146] J. M. Smith, W. J. P. Barnes, J. R. Downie, and G. D. Ruxton, "Structural correlates of increased adhesive efficiency with adult size in the toe pads of hylid tree frogs," *Journal of Comparative Physiology A*, vol. 192, no. 11, pp. 1193–1204, 2006.

[147] H. Chen, L. Zhang, D. Zhang, P. Zhang, and Z. Han, "Bioinspired surface for surgical graspers based on the strong wet friction of tree frog toe pads," *ACS Applied Matierals and Interfaces*, vol. 7, no. 25, pp. 13987–13995, 2015.

[148] S. H. Lee, H. W. Song, B. S. Kang, and M. K. Kwak, "Remora-inspired reversible adhesive for underwater applications," *ACS Applied Materials and Interfaces*, vol. 11, no. 50, pp. 47571–47576, 2019.

[149] D. Das and T. C. Nag, "Adhesion by paired pectoral and pelvic fins in a mountain-stream catfish, *Pseudocheneis sulcatus* (sisoridae)," *Environmental Biology of Fishes*, vol. 71, pp. 1–5, 2004.

[150] W. De Crop, E. Pauwels, L. Van Hoorebeke, and T. Geerinckx, "Functional morphology of the andean climbing catfishes (astroblepidae, siluriformes): Alternative ways of respiration, adhesion, and locomotion using the mouth," *Journal of Morphology*, vol. 274, no. 10, pp. 1164–1179, 2013.

[151] J. Kuruvilla, D. Sukumaran, A. Sankar, and S. P. Joy, "A review on image processing and image segmentation," *2016 International Conference on Data Mining and Advanced Computing (SAPIENCE)*, pp. 198–203, 2016.

[152] C. R. White and R. S. Seymour, "Mammalian basal metabolic rate is proportional to body mass$^{2/3}$," *PNAS*, vol. 100, no. 7, pp. 4046–4049, 2003.

[153] S. K. Lai, Y.-Y. Wang, D. Wirtz, and J. Hanes, "Micro- and macrorheology of mucus," *Advanced Drug Delivery Reviews*, vol. 61, no. 2, pp. 86–100, 2009.

[154] R. Nagpal, A. Patel, and M. C. Gibson, "Epithelial topology," *BioEssays*, vol. 30, no. 3, pp. 260–266, 2008.

[155] J. Y. Chung and M. K. Chaudhury, "The role of discontinuities in bio-inspired adhesive pads," *Journal of the Royal Society Interface*, vol. 2, no. 2, pp. 55–61, 2005.

[156] S. Leroy and E. Charlaix, "Hydrodynamic interactions for the measurement of thin film elastic properties," *Journal of Fluid Mechanics*, vol. 674, pp. 389—-407, 2011.

[157] D. M. Green, "Treefrog toe pads: Comparative surface morphology using scanning electron microscopy," *Canadian Journal of Zoology*, vol. 57, no. 10, pp. 2033–2046, 1979.

[158] W. J. P. Barnes, M. Baum, H. Peisker, and S. N. Gorb, "Comparative cryo-sem and afm studies of hylid and rhacophorid tree frog toe pads," *Journal of Morphology*, vol. 274, no. 12, pp. 1384–1396, 2013.

[159] G. Hanna, W. Jon, and W. P. J. Barnes, "Attachment and detachment of the toe pads of tree frogs," *Journal of Experimental Biology*, vol. 155, no. 1, pp. 103–125, 1991.

[160] T. Endlein, W. J. P. Barnes, D. S. Samuel, N. A. Crawford, A. B. Biaw, and U. Grafe, "Sticking under wet conditions: The remarkable attachment abilities of the torrent frog, *Staurois guttatus*," *PLoS One*, vol. 8, no. 9, p. e73810, 2013.

[161] I. D. C. Hill, B. Dong, W. J. P. Barnes, A. Ji, and T. Endlein, "The biomechanics of tree frogs climbing curved surfaces: A gripping problem," *Journal of Experimental Biology*, vol. 221, no. 5, p. jeb168179, 2018.

[162] D. M. Drotlef, E. Appel, H. Peisker, K. Dening, A. del Campo, S. N. Gorb, and W. J. P. Barnes, "Morphological studies of the toe pads of the rock frog, *Staurois parvus* (family: Ranidae) and their relevance to the development of new biomimetically inspired reversible adhesives," *Interface Focus*, vol. 5, no. 1, p. 20140036, 2014.

[163] T. G. Mason, A. Dhople, and D. Wirtz, "Linear viscoelastic moduli of concentrated dna solutions," *Macromolecules*, vol. 31, no. 11, pp. 3600–3603, 1998.

[164] R. M. L. Evans, M. Tassieri, D. Auhl, and T. A. Waigh, "Direct conversion of rheological compliance measurements into storage and loss moduli," *Physical Review E*, vol. 80, p. 012501, 2009.

[165] M. Tassieri, R. M. L. Evans, R. L. Warren, N. J. Bailey, and J. M. Cooper, "Microrheology with optical tweezers: Data analysis," *New Journal of Physics*, vol. 14, p. 115032, 2012.

[166] J. D'Errico, "A suite of minimal bounding objects," *MATLAB FileExchange*, pp. https://www.mathworks.com/matlabcentral/fileexchange/34767–a–suite–of–minimal–bounding–objects (accessed Aug. 2019), 2019.

[167] P. Fricker, "getnearestneighbordistances.m," *MATLAB FileExchange*, pp. https://www.mathworks.com/matlabcentral/fileexchange/47964–getnearestneighbordistances–m (accessed Aug. 2019), 2019.

[168] C. Liu and L.-K. Pan, "Advances in minimally invasive surgery and clinical measurement," *Computer Assisted Surgery*, vol. 24, no. S1, p. 1560103, 2019.

[169] S. De, J. Rosen, A. Dagan, B. Hannaford, P. Swanson, and M. Sinanan, "Assessment of tissue damage due to mechanical stresses," *International Journal of Robotics Research*, vol. 26, no. 11–12, pp. 1159–1171, 2007.

[170] J. H. Chandler, F. Mushtaq, B. Moxley-Wyles, N. P. West, G. W. Taylor, and P. R. Culmer, "Real-time assessment of mechanical tissue trauma in surgery," *IEEE Transactions on Biomedical Engineering*, vol. 64, no. 10, pp. 2384–2393, 2017.

[171] W. Li, Z. Jia, J. Wang, L. Shi, and Z. Zhou, "Friction behavior at minimally invasive grasper/liver tissue interface," *Tribology International*, vol. 81, pp. 190–198, 2015.

[172] K. Mizushima, T. Nishimura, Y. Suzuki, T. Tsuji, and T. Watanabe, "Surface texture of deformable robotic fingertips for a stable grasp under both dry and wet conditions," *IEEE Robotics and Automation Letters*, vol. 2, no. 4, pp. 2048–2055, 2017.

[173] M. S. Li, D. Melville, E. Chung, and H. S. Stuart, "Milliscale features increase friction of soft skin in lubricated contact," *IEEE Robotics and Automation Letters*, vol. 5, no. 3, pp. 4781–4787, 2020.

[174] H. Kinoshita, L. Backstrom, J. R. Flanagan, and R. S. Johansson, "Tangential torque effects on the control of grip forces when holding objects with a precision grip," *Journal of Neurophysiology*, vol. 78, no. 3, pp. 1619–1630, 1997.

[175] M. R. Cutkosky and P. K. Wright, "Friction, stability and the design of robotic fingers," *International Journal of Robotics Research*, vol. 5, no. 4, pp. 20–37, 1986.

[176] E. Heijnsdijk, H. deVisser, J. Dankelman, and D. Gouma, "Slip and damage properties of jaws of laparoscopic graspers," *Surgical Endoscopy*, vol. 18, no. 6, pp. 974–979, 2004.

[177] J. Cartmill, A. Shakeshaft, W. Walsh, and C. Martin, "High pressures are generated at the tip of laparoscopic graspers," *Australian and New Zealand Journal of Surgery*, vol. 69, no. 2, pp. 127–130, 1999.

[178] Y. Huan, I. Tamadon, C. Scatena, V. Cela, A. G. Naccarato, A. Menciassi, and E. Sinibaldi, "Soft graspers for safe and effective tissue clutching in minimally invasive surgery," *IEEE Transactions on Biomedical Engineering*, vol. 68, no. 1, pp. 56–67, 2021.

[179] P. V. Nguyen and V. A. Ho, "Mechanics of wet adhesion in soft interaction with patterned morphology," *Bioinspiration & Biomimetics*, vol. 14, no. 1, p. 016005, 2019.

[180] M. Li, L. Shi, and X. Wang, "Physical mechanisms behind the wet adhesion: From amphibian toe-pad to biomimetics," *Colloids and Surfaces B: Biointerfaces*, vol. 199, p. 111531, 2021.

[181] P. Rao, T. L. Sun, L. Chen, R. Takahashi, G. Shinohara, H. Guo, D. R. King, T. Kurokawa, and J. P. Gong, "Tough hydrogels with fast, strong, and reversible underwater adhesion based on a multiscale design," *Advanced Materials*, vol. 30, no. 32, p. 1801884, 2018.

[182] M. Kang, K. Sun, M. Seong, I. Hwang, H. Jang, S. Park, G. Choi, S.-H. Lee, J. Kim, and H. E. Jeong, "Applications of bioinspired reversible dry and wet adhesives: A review," *Frontiers in Mechanical Engineering*, vol. 7, p. 668262, 2021.

[183] Q. Dai, Q. Chang, M. Li, W. Huang, and X. Wang, "Non-sticky and non-slippery biomimetic patterned surfaces," *Journal of Bionic Engineering*, vol. 17, no. 2, pp. 326–334, 2020.

[184] Z. Shi, D. Tan, Q. Liu, F. Meng, B. Zhu, and L. Xue, "Tree frog-inspired nanopillar arrays for enhancement of adhesion and friction," *Biointerphases*, vol. 16, no. 2, p. 021001, 2021.

[185] D. W. Kim, S. Baik, H. Min, S. Chun, H. J. Lee, K. H. Kim, J. Y. Lee, and C. Pang, "Highly permeable skin patch with conductive hierarchical architectures inspired by amphibians and octopi for omnidirectionally enhanced wet adhesion," *Advanced Functional Materials*, vol. 29, no. 13, p. 1807614, 2019.

[186] M. Cianchetti, C. Laschi, A. Menciassi, and P. Dario, "Biomedical applications of soft robotics," *Nature Reviews Materials*, vol. 3, no. 6, pp. 143–153, 2018.

[187] M. Runciman, A. Darzi, and G. P. Mylonas, "Soft robotics in minimally invasive surgery," *Soft Robotics*, vol. 6, no. 4, pp. 423–443, 2019.

[188] G. Rateni, M. Cianchetti, G. Ciuti, A. Menciassi, and C. Laschi, "Design and development of a soft robotic gripper for manipulation in minimally invasive surgery: a proof of concept," *Meccanica*, vol. 50, no. 11, pp. 2855–2863, 2015.

[189] J. Gafford, Y. Ding, A. Harris, T. McKenna, P. Polygerinos, D. Holland, C. Walsh, and A. Moser, "Shape deposition manufacturing of a soft, atraumatic, and deployable surgical grasper," *Journal of Mechanisms and Robotics*, vol. 7, no. 2, p. 021006, 2015.

[190] F. Ilievski, A. D. Mazzeo, R. F. Shepherd, X. Chen, and G. M. Whitesides, "Soft robotics for chemists," *Angewandte Chemie International Edition*, vol. 50, no. 8, pp. 1890–1895, 2011.

[191] T. Ranzani, G. Gerboni, M. Cianchetti, and A. Menciassi, "A bioinspired soft manipulator for minimally invasive surgery," *Bioinspiration & Biomimetics*, vol. 10, no. 3, p. 035008, 2015.

[192] E. Brown, N. Rodenberg, J. Amend, A. Mozeika, E. Steltz, M. R. Zakin, H. Lipson, and H. M. Jaeger, "Universal robotic gripper based on the jamming of granular material," *PNAS*, vol. 107, no. 44, pp. 18809–18814, 2010.

[193] K. P. Becker, N. W. Bartlett, M. J. D. Malley, P. M. Kjeer, and R. J. Wood, "Tunable friction through constrained inflation of an elastomeric membrane," *IEEE International Conference on Robotics and Automation*, pp. 4352–4357, 2017.

[194] P. V. Nguyen, Q. K. Luu, Y. Takamura, and V. A. Ho, "Wet adhesion of micro-patterned interfaces for stable grasping of deformable objects," *IEEE International Conference on Intelligent Robots and Systems*, pp. 9213–9219, 2020.

[195] C. F. Guimarães, L. Gasperini, A. P. Marques, and R. L. Reis, "The stiffness of living tissues and its implications for tissue engineering," *Nature Reviews Materials*, vol. 5, no. 5, pp. 351–370, 2020.

[196] D. Gandhi, P. Kalra, B. Raterman, X. Mo, H. Dong, and A. Kolipaka, "Magnetic resonance elastography-derived stiffness of the kidneys and its correlation with water perfusion," *NMR in Biomedicine*, vol. 33, no. 4, p. e4237, 2020.

[197] D. Roulot, S. Czernichow, H. L. Clésiau, J.-L. Costes, A.-C. Vergnaud, and M. Beaugrand, "Liver stiffness values in apparently healthy subjects: Influence of gender and metabolic syndrome," *Journal of Hepatology*, vol. 48, no. 4, pp. 606–613, 2008.

[198] I. Nenadic, L. Mynderse, D. Husmann, M. Mehrmohammadi, M. Bayat, A. Singh, M. Denis, M. Urban, A. Alizad, and M. Fatemi, "Noninvasive evaluation of bladder wall mechanical properties as a function of filling volume: Potential application in bladder compliance assessment," *PLoS ONE*, vol. 11, no. 6, p. e0157818, 2016.

[199] B. Spronck and J. D. Humphrey, "Arterial stiffness: Different metrics, different meanings," *Journal of Biomechanical Engineering*, vol. 141, no. 9, p. 091004, 2019.

[200] L. Cheng and B. Hannaford, "Evaluation of liver tissue damage and grasp stability using finite element analysis," *Computer Methods in Biomechanics and Biomedical Engineering*, vol. 19, no. 1, pp. 31–40, 2016.

[201] J. Barrie, L. Russell, A. J. Hood, D. G. Jayne, A. Neville, and P. R. Culmer, "An in vivo analysis of safe laparoscopic grasping thresholds for colorectal surgery," *Surgical Endoscopy*, vol. 32, no. 10, pp. 4244–4250, 2018.

[202] R. Long and C.-Y. Hui, "Fracture toughness of hydrogels: Measurement and interpretation," *Soft Matter*, vol. 12, no. 39, pp. 8069–8086, 2016.

[203] D. Brown, "Tracker," *Tracker Video Analysis*, p. http://physlets.org/tracker/, 2007.

[204] H. S. Stuart, M. Bagheri, S. Wang, H. Barnard, A. L. Sheng, M. Jenkins, and M. R. Cutkosky, "Suction helps in a pinch: Improving underwater manipulation with gentle suction flow," *IEEE/RSJ International Conference on Intelligent Robots and Systems*, pp. 2279–2284, 2015.

[205] T. Miyake, H. Ishihara, and M. Yoshimura, "Basic studies on wet adhesion system for wall climbing robots," *IEEE/RSJ International Conference on Intelligent Robots and Systems*, pp. 1920–1925, 2007.